Alcohol Oxidation over Supported Platinum-based Nanoparticles and Non-precious-metal Atoms

---

A Dissertation

Presented to
the faculty of the School of Engineering and Applied Science
University of Virginia

---

in partial fulfillment
of the requirements for the degree

Doctor of Philosophy

by

Jiahan Xie

December 2017

Abstract:

Selective oxidation of alcohols to aldehydes and acids is an important reaction in organic synthesis and will likely play a significant role in the development of a sustainable route to value-added chemicals from biomass. Under environmentally-friendly conditions (<400 K, dioxygen as oxidant, aqueous solution), platinum can efficiently catalyze the oxidation of biomass-derived alcohols, such as 5-hydroxymethylfurfural, glycerol and 1,6-hexanediol to the corresponding carbonyl compounds. However, the high cost of Pt as well as the severe deactivation during reaction limits the application of this process on large scale and distributed systems. Therefore, the motivation of this project is to rationally develop an efficient, stable and affordable catalyst based on the mechanistic understanding of the reaction and deactivation path.

During Pt-catalyzed 1,6-hexanediol oxidation, the initial rate decreases significantly with reaction time as the result of competitive adsorption of products and irreversible adsorption of unknown strongly-bonded species. To identify the poisoning species, in situ surface-enhanced Raman spectroscopy (SERS) and solid-state ^{13}C nuclear magnetic resonance (NMR) spectroscopy were applied in this work. In situ SERS during 1,6-hexanediol oxidation revealed an accumulation of di-σ-bonded olefinic species with features at ~1150 cm^{-1} and ~1460 cm^{-1} on the poisoned Pt surface. Consistent with SERS, results from ^{13}C NMR spectroscopy of a Pt catalyst deactivated from oxidation of ^{13}C-labeled 1,4-butanediol revealed a C=C feature associated with ethylene. Molecules containing olefinic groups are two orders of magnitude more effective at competing for Pt surface sites compared to the aldehyde and acid products from alcohol oxidation. The poisoning olefinic species were generated by decarbonylation of product aldehyde (as revealed by head space analysis) and could be easily removed from the deactivated catalyst by mild treatment in H_2.

In an attempt to suppress the deactivation and increase the rate of alcohol oxidation, a

series of carbon-supported bimetallic Bi-Pt catalysts with various Bi/Pt atomic ratios was prepared by selectively depositing Bi on Pt nanoparticles. The catalysts were evaluated for 1,6-hexanediol oxidation activity under different dioxygen pressures. The rate of diol oxidation based on Pt loading over a Bi-promoted catalyst was three times faster than an unpromoted Pt catalyst in 0.02 MPa O_2, whereas the unpromoted catalyst was more active than the promoted catalyst in 1 MPa O_2. After liquid-phase catalyst pretreatment and 1,6-hexanediol oxidation, migration of Bi on the carbon support was observed. The reaction order in O_2 was zero over Bi-promoted Pt/C compared to 0.75 over unpromoted Pt/C in the range of 0.02 – 0.2 MPa O_2. Under low O_2 pressure, rate measurements in D_2O instead of H_2O solvent revealed a moderate kinetic isotope effect ($rate_{H_2O}/rate_{D_2O}$) on 1,6-hexanediol oxidation over Pt/C (KIE = 1.4) whereas a negligible effect was observed on Bi-Pt/C (KIE = 0.9), indicating that the promotional effect of Bi could be related to the formation of surface hydroxyl groups from reaction of dioxygen and water. However, no significant change of product distribution or catalyst stability was observed with Bi promotion, regardless of the dioxygen pressure, which is likely related to the high mobility of Bi.

From the perspective of replacing the expensive Pt catalyst, an atomically-dispersed Fe catalyst on nitrogen-doped carbon (Fe-N-C) containing bio-mimic nitrogen-coordinated Fe sites (FeN_x) sites was provided by collaborators using inexpensive ferrous iron salt and nicarbazin as precursors, which exhibited modest activity in the oxidation of benzyl alcohol and 5-hydroxymethylfurfural by O_2 in the aqueous phase. Whereas deactivation was observed, the activity of the catalyst can be regenerated by a mild treatment in H_2. An observed kinetic isotope effect indicates β-H elimination from the alcohol is the kinetically-relevant step in the mechanism, which can be accelerated by substituting Fe with Cu. Dispersed Cr, Co and Ni also convert alcohols, demonstrating the general utility of metal-nitrogen-carbon materials for alcohol oxidation catalysis. Although oxidation of aliphatic alcohols was substantially slower than that of aromatic alcohols, addition of 2,2,6,6-tetramethyl-1-piperidinyloxy as a co-catalyst with Fe can significantly improve the reaction rate.

Among the series of M-N-C catalysts that we tested, highest reaction rates of benzyl alcohol oxidation were observed over Co-N-C and Cu-N-C. The selective poisoning of highly active Co sites allowed for the estimation of a turnover frequency, which was determined to be nearly the same as that over Pt nanoparticles under identical conditions. Whereas highly-active CuN_x sites also catalyze the reaction, they are approximately of an order of magnitude less active than the CoN_x moieties. Results from X-ray absorption spectroscopy suggest the active CoN_x sites are also coordinated to oxygen, which can be removed by H_2 at 523 K or higher. Since spectroscopy results showed that the CoN_x sites do not reduce up to 750 K, they were tested and shown to be active catalysts for propane dehydrogenation at 773 K. Characterization of CuN_x sites revealed that reduction of the Cu cations begins above 473 K, which indicates that the atomically-dispersed Cu catalysts can only be effective at low reaction temperature. The quantification and identification of active sites provides insights for the optimization of M-N-C catalysts in the future.

Acknowledgements

I feel lucky to have Prof. Robert J. Davis as my advisor throughout this project. He is a good chemist, a good engineer, a good scholar, a good leader, a good writer, a good driver, a good booster and a good laugher. This project would not have been possible without his guidance and encouragement as well as, mostly importantly, the financial support he obtained.

This material is based upon work supported by the National Science Foundation (NSF) under Award No. EEC-0813570 and CBET-1157829. Any opinions, findings, and conclusions or recommendations expressed in this material are those of the authors and do not necessarily reflect the views of the NSF. A portion of the microscopy research was conducted at the Center for Nanophase Materials Sciences in Oak Ridge National Lab, which is a DOE Office of Science User Facility. This research also used resources of the National Synchrotron Light Source I & II, a U.S. Department of Energy (DOE) Office of Science User Facility operated for the DOE Office of Science by Brookhaven National Laboratory under Contract No. DE-AC02-98CH10886 and DE-SC0012704.

I would like to acknowledge my committee members Prof. William Epling, Prof. David Green, Prof. Joshua Choi, Prof. Brent Gunnoe and Prof. Sen Zhang for assisting me in the completion of this PhD thesis. Richard White, Joe Thompson, Dr. Helge Heinrich, Dr. Matt Schneider and Dr. Michal Sabat are acknowledged for the training of XRD, Raman and TEM in nanoscale materials characterization facility on University of Virginia. The chemical engineering staff: Vickie Faulconer, Teresa Morris, Jennifer Davis, and Rich Buchanan are greatly appreciated for their tireless patience and attention to detail.

I am very grateful for all of the present and past Davis group members for the invaluable interactions. A special thanks to: Dr. Matthew S. Ide (the forerunner); Dr. Derek D. Falcone (my mentor), Kehua Yin (elder brother), Nick Kaylor and James Kammert (classmates and

coworkers) as well as Gordon Brezicki (officemate).

I would like to thank all collaborators from the Center for Biorenewable Chemicals, Brookhaven National Laboratory and Oak Ridge Laboratory, in particular: Jiajie Huo, Dr. Hien. Pham, Prof. Thomas Schwartz, Prof. Abhaya Datye and Prof. Matthew Neurock. Special thanks to Prof. Haichao Liu, my instructor in the undergraduate school, for introducing me to the study of alcohol oxidation catalysis and encouraging me to go to graduate school for further catalysis research.

Love thanks to my friends for their long-time support. I cherish all time spending with you. I would like to quote Dr. Falcone's words: "If it were not for you, I would have completed it two years earlier; however, the friendship and support that you continuously provide me make the completion of this degree significantly more rewarding."

Finally, my sincerest gratitude to my family for their endless love. Particularly, to my grandfather, Qu Wenxiang: You set a diligent and responsible example to me. I will always remember your words "One may distinguish himself in any field if he works hard enough"; to my mother and grandmother, Qu Li and Wang Yu: Thank you for spoiling me with all your love and supporting me unconditionally from 330 months ago; to my wife, Yanqin Tan: With flowers by the road, lyrics in the mind, stars in the sky, the place we are travelling to, will have beautiful scenes.

Table of Contents

Chapter 1. Introduction 1

1.1. Alcohol oxidation reaction 1

1.2. Supported metal catalysts for alcohol oxidation 2

1.3. Deactivation of supported metal catalysts in alcohol oxidation reaction 3

- 1.3.1. Characterization methods for deactivation study 3

- 1.3.2. Causes for catalyst deactivation 10

1.4. Strategies to suppress the deactivation 13

1.5. Alcohol oxidation over non-precious-metal catalysts 14

1.6. Objectives of this work 16

References for Chapter 1 17

Chapter 2. Deactivation of supported Pt catalysts during alcohol oxidation 40

2.1. Introduction 40

2.2. Experimental methods 42

- 2.2.1. Preparation and characterization of supported Pt nanoparticles 42

- 2.2.2. Preparation and characterization of Au and Au@Pt nanoshells 43

- 2.2.3. Oxidation of 1,6-hexanediol 45

- 2.2.4. SERS analysis of adsorbates 46

- 2.2.5. NMR spectroscopy of adsorbates 47

2.3. Results 48

- 2.3.1. Characterization of supported Pt nanoparticles 48

- 2.3.2. Competitive adsorption of oxidation products and generation of poisoning byproducts 50

- 2.3.3. Au@Pt nanoshells for SERS analysis 54

- 2.3.4. SERS of adsorbates during 1,6-hexanediol oxidation 59

2.3.5. Solid-state NMR spectroscopy of deactivated Pt catalyst 64

2.3.6. Influence of substrates containing olefinic groups 70

2.3.7. Formation of unsaturated species 73

2.3.8. Influence of other possible byproducts 76

2.3.9. Potential strategies to suppress the deactivation of Pt 76

2.4. Conclusion 78

References for chapter 2 79

Chapter 3. Oxidation of 1,6-hexanediol over bimetallic Bi-Pt catalysts 92

3.1. Introduction 92

3.2. Experimental methods 94

3.2.1. Catalyst preparation 94

3.2.2. Characterization of catalysts 95

3.2.3. Oxidation of 1,6-hexanediol 97

3.3. Results 99

3.3.1. Characterization of the Bi-promoted Pt catalysts 99

3.3.2. Oxidation of 1,6-hexanediol 115

3.3.3. Influence of Bi on the stability of Pt catalyst during 1,6-hexanediol oxidation 127

3.4. Discussion 129

3.5. Conclusions 131

References for chapter 3 131

Chapter 4. Alcohol oxidation reaction over non-precious metal atoms 141

4.1. Introduction 141

4.2. Experimental methods 142

4.2.1. Preparation of M-N-C catalysts 142

4.2.2. Characterization of M-N-C catalysts 143

4.2.3. Oxidation of benzyl alcohol over M-N-C....144

4.3. Results....145

4.3.1. Catalyst characterization....145

4.3.2. Benzyl alcohol oxidation over Fe-N-C....148

4.3.3. Benzyl alcohol oxidation over M-N-C (M = Cr, Co, Ni and Cu)....156

4.4. Conclusion....157

References for chapter 4....158

Chapter 5. Atomically-dispersed Co and Cu on N-doped Carbon for Reactions involving C-H activation....164

5.1. Introduction....164

5.2. Experimental methods....165

5.2.1. Preparation of M-N-C catalysts....165

5.2.2. Characterization of M-N-C catalysts....167

5.2.3. Oxidation of benzyl alcohol over M-N-C....168

5.2.4. Propane Dehydrogenation....169

5.3. Results....170

5.3.1. Optimization of Co-N-C and Cu-N-C for benzyl alcohol oxidation....170

5.3.2. Quantification of active sites for low-temperature C-H activation....176

5.3.3. Discrimination of active sites....179

5.3.4. Characterization of atomically-dispersed metal sites....182

5.3.5. Evolution of M-N-C under reducing condition at elevated temperature....192

5.3.6. Propane dehydrogenation over CoNx sites....193

5.4. Conclusion....194

References for chapter 5....195

Chapter 6: Concluding Remarks....204

6.1. Conclusions 204

6.2. Outlook 206

    6.2.1. Kinetics Study of Catalyst Deactivation in the Flow Reactor 206

    6.2.2. Bimetallic catalyst synthesis 206

    6.2.3. Mechanistic study of C-H activation over Co-N-C 207

    6.2.4. Optimization of M-N-C catalysts for C-H activation 208

References 208

Tables

Table 2. 1 Platinum metal particles sizes on Pt/C evaluated from electron microscopy, H_2-chemisorption and X-ray diffraction 49

Table 2. 2 Apparent adsorption coefficients (K) of different additives during oxidation of 1,6-hexanediol....................52

Table 2. 3 Turnover frequencies of 1,6-hexanediol oxidation over fresh, used and regenerated Pt/C in the mixture of alcohol, aldehyde and acid....................53

Table 2. 4 Initial turnover frequencies of 1,6-hexanediol oxidation over Pt/C in the presence of trace additives 72

Table 2. 5 Initial activity of 1,6-hexanediol oxidation over treated Pt/C with 1,5-pentanedial or adipic acid under reaction conditions 74

Table 2. 6 Production of CO_2 during oxidation reactions over Pt/C....................75

Table 3. 1 XPS curve fitting parameters used in Casa XPS(Version 2.3.16)……………..97

Table 3. 2. XPS binding energies (Pt, Bi) and surface compositions of 0.6Bi-Pt/C, 0.6Bi-Pt/C-P and 0.6Bi-Pt/C-R....................102

Table 3. 3 Elemental analysis of 0.6Bi-Pt/C and 0.6Bi-Pt/C-R....................103

Table 3. 4 Summary of results from H_2 chemisorption and electron microscopy of Pt/C and Bi-Pt/C catalysts....................106

Table 3. 5 Elemental compositions from EDS of 0.6Bi-Pt/C, 0.6Bi-Pt/C-P and 0.6Bi-Pt/C-R 110

Table 3. 6 Calculated Weisz-Prater parameters for 1,6-hexanediol and dioxygen 119

Table 3. 7 Reaction order and apparent activation energy of 1,6-hexanediol (HDO) oxidation over Pt/C and Bi-Pt/C 125

Table 3. 8 Effect of D_2O versus H_2O on the rate of 1,6-hexanediol oxidation over Pt/C and 0.6Bi-Pt/C 127

Table 4. 1. Metal loadings of M-N-C catalysts from XPS analysis 148

Table 4. 2. Elemental analysis of fresh and used Fe-N-C and the recovered reaction medium after alcohol oxidation reaction over Fe-N-C or Cu-N-C[a] 148

Table 4. 3. Rates of benzyl alcohol oxidation over fresh, used and regenerated M-N-C catalysts 150

Table 4. 4. Rates of benzyl alcohol oxidation over different materials 151

Table 4. 5. Kinetics isotope effect and orders of reaction for benzyl alcohol oxidation........152

Table 4. 6. Influence of radical trap addition on benzyl alcohol oxidation over Fe-N-C and Pt/C[a] 154

Table 4. 7. Influence of TEMPO of benzyl alcohol and 1,6-hexanediol oxidation over Fe-N-C[a] 156

Table 5. 1. Rates of benzyl alcohol oxidation over reference materials...........................173

Table 5. 2. Rates of benzyl alcohol oxidation over Co and Cu catalysts 174

Table 5. 3. Kinetic isotope effect for benzyl alcohol oxidation 176

Table 5. 4. Reaction rate of benzyl alcohol oxidation over M-N-C with additives 177

Table 5. 5. Amount of active sites from linear fit of alcohol oxidation rate with acid additives 179

Table 5. 6. Weight loadings of metal sites associated with atomically-dispersed Co and Cu catalysts 181

Table 5. 7. Rates of benzyl alcohol oxidation over Co-N-C before and after acid wash.......182

Table 5. 8. Core level binding energies and compositions determined by XPS 184

Table 5. 9. Results from the analysis of Co EXAFS from Co-N-C-HCl catalyst after H_2 treatment 191

Table 5. 10. Results from the analysis of Cu EXAFS from Cu-N-C catalyst........................191

Figures

Figure 1. 1. Reaction path of selective oxidation of primary alcohols to aldehydes and acids . 1

Figure 1. 2. The general scheme for primary alcohol to aldehyde and acid 3

Figure 1. 3. Flowchart of investigation on supported-metal catalyst deactivation during alcohol oxidation reaction. 13

Figure 2. 1. STEM image, particle size from STEM and XRD and fit curves from as-prepared Pt/C catalyst………………………………………………………………………….…….50

Figure 2. 2. Reaction profile of a) 1,6-hexanediol oxidation over Pt/C and b) 1,4-butanediol oxidation over Pt/silica.. 51

Figure 2. 3. Influence of aldehyde and acid additives on the initial rate of 1,6-hexanediol oxidation over Pt/C. 51

Figure 2. 4. UV-vis spectrum of gold shell growth on 120 nm silica nanospheres. 55

Figure 2. 5. TEM images and visible color of Au nanoshells prepared in 21 cm^{-3} of 293 μM K-gold solution and differnet amount of suspension of silica seeds covered with 2 nm Au nanoparticles. 55

Figure 2. 6. STEM-EDS mapping of Au@Pt nanoshells. 56

Figure 2. 7. SEM images of Au and Au@Pt nanoshells. 57

Figure 2. 8. Raman spectra of para-mercaptoaniline (PMA) chemisorbed on Au and Au@Pt nanoshells. 58

Figure 2. 9. The oxidation reaction of 1,6-hexanediol in the semi-batch reactor and the SERS analysis chamber under flow 59

Figure 2. 10. Raman spectra of chemical standards 60

Figure 2. 11. Surface-enhanced Raman spectra of backgrounds and after chemisorption of 1,6-hexanediol, 1,5-pentanedial, adipic acid, 4-pentenoic acid, 4-penten-1-ol and ethylene as well as residues after a 2 h treatment of O_2-saturated 1,5-pentanedial over Au@Pt nanoshells.

....62

Figure 2. 12. Waterfall plot and contour plot of time-resolved surface-enhanced Raman spectra gathered during the oxidation of 10 mM 1,6-hexanediol solution over Au@Pt nanoshells at 343 K and individual scans at 0, 300, and 590 min after injection of 1,6-hexanediol solution......63

Figure 2. 13. MultiCP ^{13}C NMR spectra of molecules derived from uniformly ^{13}C-enriched 1,4-butanediol (1,4-BD) after oxidation reaction on Pt/silica for 40 hours (thick red line) and adsorbed to silica (thin blue line)...66

Figure 2. 14. Solid-state ^{13}C NMR spectra of molecules derived from uniformly ^{13}C-enriched 1,4-butanediol (1,4-BD) after reaction under oxidative conditions on Pt/silica for 40 hours. 67

Figure 2. 15. Solid-state ^{13}C NMR spectra of molecules derived from uniformly ^{13}C-enriched 1,4-butanediol (1,4-BD) after reaction under oxidative conditions on Pt/silica for 40 hours, optimized to show broad components..68

Figure 2. 16. Solution ^{13}C NMR, recorded at 100 MHz with ^{1}H decoupling at 400 MHz, of molecules derived from uniformly ^{13}C-enriched 1,4-butanediol (1,4-BD) after reaction under oxidative conditions on Pt/silica for 40 hours...69

Figure 2. 17. Influence of 4-penten-1-ol on the initial activity of 1,6-hexanediol oxidation over Pt/C catalyst. 71

Figure 2. 18. Possible reaction paths for oxidation and side reactions of alcohols over Pt/C. 78

Figure 3. 1. SEM images, N_2 sorption isotherm, measured surface areas measured and pore size distribution curves of Pt/C as received, 0.6Bi-Pt/C as-prepared and 0.6Bi-Pt/C-R recovered after 4 h of 1,6-hexanediol oxidation under 0.02 MPa O_2 at 328 K……………..100

Figure 3. 2. The Bi $4f_{7/2}$ and the Pt $4f_{7/2}$ X-ray photoemission spectra of 0.6Bi-Pt/C, 0.6Bi-Pt/C-P and 0.6Bi-Pt/C-R...101

Figure 3. 3. Normalized XAS spectra at the Pt L_{III} edge, Normalized XANES spectra at the Pt L_{III} edge, k^3-weighted EXAFS data in k-space and r-space collected during exposure of Pt/C,

0.3Bi-Pt/C, Pt foil and $(NH_3)_4Pt(NO_3)_2$ to air. 104

Figure 3. 4. Dark-field STEM images of Pt/C, 0.3Bi-Pt/C, 0.6Bi-Pt/C and 0.6Bi-Pt/C-R recovered after 4 h of 1,6-hexanediol oxidation under 0.02 MPa O_2 at 328 K. 105

Figure 3. 5. Particle size distributions obtained from STEM of Pt/C, 0.3Bi-Pt/C, 0.6Bi-Pt/C and 0.6Bi-Pt/C-R recovered after 4 h of 1,6-hexanediol oxidation under 0.02 MPa O_2 at 328 K. 105

Figure 3. 6. XRD patterns, offset for clarity, of Pt/C and Bi-Pt/C bimetallic catalysts. 107

Figure 3. 7. H/Pt ratio of xBi-Pt/C catalyst (x = 0, 0.09, 0.18, 0.30, 0.45, 0.6). 108

Figure 3. 8. Regions for EDS analysis of 0.6Bi-Pt/C, 0.6Bi-Pt/C-P and 0.6Bi-Pt/C-R. 109

Figure 3. 9. STEM-EDS-map of 0.6Bi-Pt/C, 0.6Bi-Pt/C-P and 0.6Bi-Pt/C-R including including dark-field STEM images, EDS map of Pt, EDS map of Bi and the overlayed map of Pt and Bi 111

Figure 3. 10. Pt and Bi EDS mapping of 0.6Bi-Pt/C, 0.6Bi-Pt/C-P and 0.6Bi-Pt/C-R in large region. 112

Figure 3. 11. Effect of stirring rate on measured initial activity (TOF) of 1,6-hexanediol oxidation over 0.6Bi-Pt/C.. 116

Figure 3. 12. Dependence of initial activity (TOF (s^{-1})) of 1,6-hexanediol (HDO) oxidation over Pt/C and 0.6Bi-Pt/C on dioxygen pressure (MPa) and concentration of 1,6-hexanediol (HDO) (M) 117

Figure 3. 13. Performance of Bi-Pt/C with different Bi:Pt ratios in oxidation of 1,6-hexanediol. 120

Figure 3. 14. Reaction profiles for 1,6-hexanediol oxidation over Pt/C and 0.6Bi-Pt/C. 121

Figure 3. 15. Reaction profiles for 1,6-hexanediol oxidation over Pt/C, 0.3Bi-Pt/C and 0.6Bi-Pt/C under different dioxygen pressure 122

Figure 3. 16. Product distribution during 1,6-hexanediol oxidation over Pt/C, 0.3Bi-Pt/C and

0.6Bi-Pt/C (conversion ≈ 20%) under different dioxygen pressure....................................123

Figure 3. 17. Curve fitting of HDO oxidation deactivation model over Pt/C and 0.6Bi-Pt/C under different O_2 pressure. 128

Figure 3. 18. Deactivation factor (k_d) of 1,6-hexanediol oxidation over Pt/C and 0.6Bi-Pt/C under different O_2 pressure. 129

Figure 3. 19. Illustration of restructuring between as-prepared Bi-Pt/C and Bi-Pt/C after pretreatment or reaction. 130

Figure 4. 1. STEM image of Fe-N-C, Fe/C and particle size analysis of Fe/C……………..146

Figure 4. 2. Aberration-corrected STEM images of fresh Fe-N-C, used Fe-N-C, fresh Cu-N-C and used Cu-N-C-R..147

Figure 4. 3. Dependence of initial alcohol oxidation turnover frequencies (TOF (s^{-1})) on dioxygen pressure and alcohol concentration in the range of 0.3 – 2 MPa over Fe-N-C and Cu-N-C..153

Figure 4. 4. Conversion and product distribution from oxidation of benzyl alcohol, 5-hydroxymethylfurfural (HMF), glycerol and ethanol over Fe-N-C………………………155

Figure 5. 1. XRD patterns, offset for clarity of Cu and Co catalysts prepared under different conditions and the metal-free N-doped carbon pyrolyzed at 973 K……………………………………………………………………………………………… 171

Figure 5. 2. Normalized XANES at the Co K-edge of and the k2-weighted Fourier transform (not corrected for phase shift) of Co EXAFS associated with carbon-supported 1,10-phenanthroline Co complex (CoPhen/C) and Co catalysts prepared by pyrolysis at 873, 973 and 1073 K and c) cobalt standards (PcCo is Co(II) phthalocyanine)...........................172

Figure 5. 3. Dark-field STEM images of Cu-N-C (prepared by pyrolysis at 973 K followed by NH_3 treatement at 1223 K), Co-N-C (prepared by pyrolysis at 973 K) and Co-N-C-HCl (prepared by HCl treatment of Co-N-C). 175

Figure 5. 4. Influence of adsorbed acids on metal sites on the reaction rate of benzyl alcohol oxidation over Co-N-C and Cu-N-C catalysts. 178

Figure 5. 5. Dark-field STEM images and particle size distribtuion of Co/C and Cu/C 180

Figure 5. 6. Dark-field STEM image and k^2-weighted Fourier transform (not corrected for phase shift) of Co-K edge EXAFS associated with CoO_x-SiO_2 in air. 181

Figure 5. 7. Co $2p_{3/2}$ X-ray photoelectron spectrum of Co-N-C-HCl and Cu $2p_{3/2}$ X-ray photoelectron spectrum of Cu-N-C. 183

Figure 5. 8. N 1s X-ray photoelectron spectrum of N-C. 185

Figure 5. 9. Normalized XANES at the Cu K-edge of and the k2-weighted Fourier transforms (not corrected for phase shift) of Cu EXAFS associated with carbon-supported 1,10-phenanthroline Cu complex (CuPhen/C), Cu-N-C catalysts prepared by 973 K pyrolysis followed by NH_3 treatment at 1223 K and copper standards (PcCu is Cu(II) phthalocyanine); 187

Figure 5. 10. Normalized XANES and the k^2-weighted Fourier transform (not corrected for phase shift) associated with Co-N-C-HCl and Cu-N-C at room temperature, at 373 K under 10% O_2 and at 373 K under 5% H_2 188

Figure 5. 11. Normalized XANES and the k2-weighted Fourier transform (not corrected for phase shift) associated with Co-N-C-HCl under 5% H_2 flow from 373 to 750 K and Cu-N-C under 5% H_2 flow from 373 to 573 K 189

Figure 5. 12. The k, k^2 and k^3-weighted experimental and fitted Fourier transforms of the Co EXAFS associated with Co-N-C-HCl after the thermal treatment up to 750 K in H_2 and cooling to 313 K and the Cu EXAFS associated with as-synthesized Cu-N-C at room temperature. 190

Figure 5. 13. Conversion of propane and nominal TOF during propane dehydrogenation over 0.05 g Co-N-C-HCsl and 0.1 g CoO_x-SiO_2. 194

Chapter 1. Introdsuction

1.1. Alcohol oxidation reaction

The oxidation of alcohols is widely applied in many fields, such as synthesis of chemicals,[1] production of electricity[2,3] and treatment of wastes.[4] In the field of chemical synthesis, selective oxidation of hydroxyl groups to corresponding carbonyl groups (Figure 1.1) is important in the production of bulk chemicals that are used in industry and agriculture[5,6] as well as fine chemicals such as pharmaceuticals and cosmetics.[7,8] Alcohols, such as methanol, ethanol, ethylene glycol and glycerol, also exhibit high volumetric energy density and are easy to store and transport, which makes alcohol a promising source of carbon and hydrogen for fuel cells.[2,3] In the direct alcohol fuel cells, alcohols are oxidized to CO, CO_2, acids or aldehydes over the anode, while dioxygen is reduced to water or OH^- over the cathode to generate electric power. Additionally, as an organic component commonly detected in waste water, alcohols are usually removed by a wet oxidation process during the waste water treatment.[4,9]

$$R\text{-}CH_2OH + 1/2\ O_2 \rightarrow R\text{-}CHO + H_2O$$

$$R\text{-}CHO + 1/2\ O_2 \rightarrow R\text{-}COOH$$

Figure 1. 1. Reaction path of selective oxidation of primary alcohols to aldehydes and acids

Notably, alcohol oxidation reactions will also likely play a significant role in the development of a sustainable route to value-added chemicals from biomass.[10] In this process, biomass raw materials, such as starch, cellulose and fatty oils, are usually converted to some versatile platform molecules, which are further converted to valuable chemicals or intermediates.[10] Among these platform molecules, biomass-derived alcohols, such as 5-hydroxymethylfurfural (HMF), glycerol, ethanol and 1,6-hexanediol,[11] can be converted to the valuable corresponding carbonyl compounds via alcohol oxidation reaction.

1.2. Supported metal catalysts for alcohol oxidation

The use of stoichiometric reagents to oxidize alcohols, though decreasing, is still widespread in the field.[12] These strong oxidizing reagents, which commonly contain chromium, manganese, oxalyl chloride or hyper-valent iodine, are usually toxic and can cause severe environmental problems.[13,14] In contrast, the catalytic oxidation of alcohol can use molecular oxygen as oxidant, which only generates water as the by-product.[14–16] Although homogeneous transition metal complex have demonstrated remarkableactivity selectivity and stability in this reaction,[17] heterogeneous supported catalysts are preferred on industrial scale because they are easier to recover, reuse and usually do not have corrosion problems on the reactor wall.[18–20]

Alcohol oxidation over supported noble metal nanoparticles, such as Pd, Pt, Au, Ru and Rh, has been thoroughly investigated and summarized in several reviews.[17–20] These nanoparticles with great redox activity, can readily activate the dioxygen and alcohol molecules under mile reaction conditions, usually under 400 K. A generally-accepted mechanism of alcohol oxidation is shown in Figure 1.2. In the first step, a reversible deprotonation of the alcohol to form alkoxide species happens on metal surface or in the solution. The extent of this step can be represented by the pKa of the alcohol, which is approximately in 14-16, and is closely related to the pH of the solution.[20] When the alkoxide species is in proximity with the surface of the nanoparticle, the α-H will be eliminated from the alkoxide by metal sites themselves or adsorbed hydroxyl group, negatively-charge oxygen or peroxides on the metal, depending on the nature of the metals and reaction conditions.[21] This step is well-recognized to be kinetically-relevant, as evidenced by a kinetic isotope effect, usually of ~2, when replacing the α-H with a deuterium.[20] After the two dehydrogenation steps, the resulting aldehyde or ketone can desorb from the catalytic surface or be hydrated to germinal diol, which may be oxidized to acids with similar dehydrogenation steps.[20–22] At last, the residual hydrogens or hydroxyl species on catalytic surface would be removed by activated oxygen to close the redox cycle.[23]

Alcohol oxidation

$$R-CH_2OH + * + \otimes \rightleftharpoons R-CH_2O* + H\otimes$$
$$R-CH_2O* + \otimes \rightarrow R-CHO* + H\otimes$$
$$R-CHO* \rightleftharpoons R-CHO + *$$
$$O_2 + 4H\otimes \rightleftharpoons 2H_2O + 4\otimes$$

Aldehyde oxidation

$$R-CHO + H_2O + * + \otimes \rightleftarrows R-CH(OH)O* + H\otimes$$
$$R-CH(OH)O* + \otimes \rightarrow R-C(OH)O* + H\otimes$$
$$R-C(OH)O* \rightleftharpoons R-COOH + *$$
$$O_2 + 4H\otimes \rightleftharpoons 2H_2O + 4\otimes$$

Figure 1. 2. The general scheme for primary alcohol to aldehyde and acid. * represents the metal active sites and ⊗ represents the metal sites or adsorbed oxygen, hydroxyl group or peroxides on metal.

1.3. Deactivation of supported metal catalysts in alcohol oxidation reaction

Although supported precious metal nanoparticles efficiently catalyze the selective alcohol oxidation reaction, activity loss during reaction is widely recognized, making it one of the main barriers to the large-scale application of this process.[19,20,24] Therefore, it is imperative to elucidate the deactivation path, based upon which catalysts with better stability can be ration designed. The common characterization methods and reported deactivation causes are summarized below.

1.3.1. Characterization methods for deactivation study

Kinetics

Reaction kinetics is widely used to elucidate the deactivation path.[25,26] After measuring the reaction rates under different reaction conditions with varying substrate concentration, temperature, additives and reaction time, kinetic models with elementary steps, which usually evidenced by spectroscopic or computational results, can be established and evaluated by comparing fitted results with experimental data. With the well-fitted kinetic model, deactivation path can be illustrated. For example, during Pt-catalyzed aerobic oxidation of methylglucoside, the deactivation mode was significantly dependent on partial pressure of O_2. A kinetic model including mass transfer, adsorption, desorption, surface reaction and transformation of Pt to PtO_x, which was established and fitted well with the experimental results, suggests the formation of PtO_x as the cause of deactivation.[27–30]

Computational simulation

Benefitting from increasing computational calculation capacity, complicated many-body system can be simulated with reasonable accuracy. In the case of heterogeneous catalysis, the density functional theory (DFT) is widely adopted to calculate the energy barriers of elementary steps.[31] Since the uncertainty of energy barrier calculated from DFT can be as high as 10 kJ mol^{-1}, DFT is usually combined with Monte Carlo methods or microkinetics to derive observable kinetic parameters,[32,33] which can be verified by experimental kinetic measurements. Computational simulation can be used to verify the proposed reaction mechanism as well as provide detailed interpretation of each elementary steps that are difficult to be experimentally measured. A recent work by Chibani *et al.* investigated the deactivation path of ethanol oxidation over Pt and proposed the decarbonylation of aldehyde intermediates likely caused the decrease of reaction rate based on DFT calculation.[34]

Infrared Spectroscopy (IR)

Infrared spectroscopy measures the vibrational and rotational modes in a system. Based on the characteristic vibrational modes, reaction intermediates with corresponding functional groups can be determined. Different techniques has been developed to measure the IR of adsorbed species on heterogeneous catalysts under reaction conditions, such as diffuse reflectance infrared fourier transform spectroscopy (DRIFTS), attenuated total reflection infrared spectroscopy (ATR-IR) and polarization modulation infrared reflection-absorption spectroscopy (PM-IRRAS).[35–37] The IR spectra of adsorbed probe molecules are able to provide information about electronic and geometric properties of active sites. Additionally, the in situ IR spectra also shows capacity to illustrate the molecular structure of intermediates and poisoning residuals.[38–46]

Raman spectroscopy

The vibrational and rotational modes can also be measured by Raman spectroscopy, which has a different selection rule from IR. Under some circumstances, intermediates or poisoning species with functional groups that has negligible IR signal can be detected by Raman, such as C=C bond. Additionally, some strong IR features, such as hydroxyl group from water, are very weak in Raman spectroscopy, making it possible to avoid the noisy background. For example, Lucarelli *et al.* detected the Raman fingerprints of carbonaceous compounds on the deactivated Au/CeO_2 catalyst after aldehyde synthesis.[47] Moreover, a significant enhancement effect with a factor up to 10^{11} in Raman spectroscopy has been observed when using Au or Ag as the substrate, which makes it possible to detect poisoning species even at a low concentration.[48] The Au nanoshells (with or without Pd layers), for example, has been successfully reported by Heck and co-workers to investigate the trace adsorbates during catalytic oxidation of glycerol and hydrodechlorination of 1,1-dichloroethene in the aqueous phase.[49,50]

High resolution electron energy loss spectroscopy (HREELS)

Commonly used in surface science study, HREELS measures the inelastic scattering process of electrons related to the vibrational modes of adsorbates on the surface. Ultra-high vaccum are required for HREELS measurement, limiting the application of this characterization method under reaction conditions. However, HREELS can still provide insights in the transformation of substrates or intermediates on the surface of catalyst. A study in 2013 by Besson's group successfully measured the transformation of ethanol to CO and hydrocarbon residuals over Pt by HREELS, which supported that decarbonylation is likely the side reaction causing the deactivation.[34]

Metastable de-excitation spectroscopy (MDS)

MDS utilizes the energy associated with the metastable states of rare-gas atoms to induce electron emission from adsorbates and is very surface sensitive.[51] Similar to HREELS, the technique also requires ultra-high vacuum. MDS has been successfully applied by Wilson's group to probe the oxidation of crotyl alcohol over Pd(111).[51] The propylidyne, which was generated from decarbonylation of crotonaldehyde, was observed by MDS and attributed to the deactivation of Pd.

Nuclear magnetic resonance (NMR)

Another method to identify organic molecular species with high specificity is NMR, which measures the nuclear magnetic resonance and is characteristic of specific chemical environment of molecules. Detecting poisoning species on metal is challenging, considering that the metal-bound species would be too small in concentration to give detectable signals and furthermore broadened or shifted too strongly for useful spectroscopic analysis.[52–55] Developments in two-dimensional NMR, multiple cross polarization and chemical-shift-anisotropy filter, however, significantly promoted the sensitivity of NMR.[56,57] For example, evidence from NMR helped identify the carbonaceous species over deactivated MnO_2/CeO_2, which was proposed to cause the deactivation.[58]

X-ray photoelectron spectroscopy (XPS)

XPS measures the kinetic energy and counts of emitted electrons activated by X-ray photons. The kinetic energy of electrons, which can be derived from measured kinetic energy, is characteristic of specific element and closed related to the chemical state of the element. Additionally, the measured counts of emitted electrons are proportional to the amount of the elements. Therefore, XPS spectra can be used to analytically identify the oxidation state of element and its surrounding chemical environment as well as quantitively analyze the relative amount of each species. For deactivation study, XPS is commonly used to analyze the oxidation state of deactivated metal nanoparticles as well as the chemical state of carbon and oxygen in the poisoning residuals.[42,44,59–70] Recently, ambient-pressure XPS has been developed and enabled the XPS measurements under reactive atmosphere,[71] which provided an opportunity to investigate the evolution of catalysts in situ.

Electrochemical analysis

Electrochemical analysis methods, such as potentiometry and cyclic voltammetry, have successfully been applied by Baiker's lab in deactivation study.[60,72,73] The in situ potentiometry measurement showed the increase of Pt potential after the deactivation happened. The results indicated that the active Pt was transformed into platinum oxide but not the main cause of deactivation. The subsequent cyclic voltammetry results on deactivated catalyst showed a significant decrease in area of hydrogen sorption region, suggesting that the active sites were likely covered by some irreversibly adsorbed products.

Electron paramagnetic resonance spectroscopy (EPR)

EPR is generated from the spinning of unpaired electrons and has been used by Pan *et al.* in the deactivation of TiO_2 during photocatalytic oxidation of benzyl alcohols.[67] The EPR signal at g = 2.004 over the used sample was assigned to the electrons trapped on the oxygen vacancy, which was attributed to the loss of photocatalytic activity.

Temperature programmed desorption (TPD)

TPD is a general method to investigate the desorption or transformation of poisoning residuals on the deactivated catalysts.[40,42,44,47,59,62,63,74–80] Under reducing, oxidizing or invert environment, the solids with adsorbed molecules are treated in temperature-programmed process. To detect the desorption or transformation of adsorbed molecules, TPD is usually coupled with other characterization methods. Thermal conductivity detector and mass spectroscopy are commonly used to detect the composition of gas flow. Highly sensitive balance can be used to measure the change of mass, which is also known as thermogravimetric analysis when coupled with TPD. Various spectroscopic characterization techniques mentioned above, such as IR, UV-vis, XPS, XAS, Raman spectroscopy, MDS, HREELS and NMR, are also applied to study the chemical environment of catalyst and molecular structure of adsorbates during temperature-programmed processes.

Electron microscopy

Electron microscopy, including scanning electron microscopy (SEM) and (scanning) transmission electron microscopy ((S)TEM) is an important tool to measure the size and structure of catalysts. The size distribution of metal nanoparticles is a direct evidence to determine whether aggregation happened during the reaction, which has been proposed to be responsible for the deactivation.[42,44,64–66,81–85] Additionally, high-resolution (S)TEM can be coupled with energy-dispersive X-ray spectroscopy, electron energy loss spectroscopy and high-resolution electron energy loss spectroscopy and special cells have been developed for in situ microscopy study.[86] The higher resolution, in situ capacity and coupled spectroscopic information make microscopy a promising tool to investigate the deactivation path in the near future.

X-ray absorption spectroscopy (XAS)

In contrast to the electron beam that requires high vacuum, X-ray has better penetration properties. Therefore, XAS has been widely applied to investigate the evolution of catalyst in situ. The size of nanoparticles is reflected by coordination number from extended X-ray absorption fine structure (EXAFS).[62,63,69,87,88] Additionally, the X-ray absorption near edge structure (XANES) reflects the chemical state of the metals, which is powerful to determine whether over-oxidation happened.[89,90]

Ultraviolet–visible spectroscopy (UV-Vis)

The UV-vis measures the scattering and adsorption of light pass through a sample. The UV-vis adsorption band of nanoparticles depend strongly on the shape and size of nanoparticles, which can be used to monitor the structural change of catalytically-active nanoparticles under reactions. For example, Bΰrgi observed an increasing intensity of absorption band at 330 nm during alcohol oxidation over Pd/Al_2O_3 and attributed the irreversible change to the Pd corrosion.[40]

Atomic spectroscopy

Atomic spectroscopy measures the electromagnetic radiation absorbed or immitted by atoms.

Because of the characteristic atomic spectra of different elements, the atomic spectroscopy is applied for identifying and quantifying the element. The atomic absorption spectroscopy (AAS) and atomic emission spectroscopy (AES) have been commonly used to determine whether catalytically-active sites leached during the reaction and caused the deactivation.[60,83,84,91–93]

1.3.2. Causes for catalyst deactivation

Leaching

Acid, as an oxidation product from alcohol, is a strong chelating ligand that can lead to the leaching of metals. In fact, leaching of active components has been frequently reported during liquid-phased alcohol oxidation reaction over different catalysts, including supported Au, Pt, Pd and Ru as well as vanadium silicate molecular sieves.[65,70,83,84,91–94] Leaching of catalytically active components can be easily detected by AAS or AES, as introduced above. Also, since leaching is usually irreversible, the loss of reaction activity in the recycle experiments is another indication.

Restructuring

A common restructuring type observed during alcohol oxidation is the aggregation of metal nanoparticles because of their high surface energy. The growth of particle size decreases the amount of exposed surface sites, which can cause the loss of activity.[62,81,83–85,87,88] Additionally, in some structure-sensitive catalytic systems, the change of coordination environment can lead to significantly different reaction rate and product distribution.[95] To determine metal aggregation, (S)TEM characterization on fresh and used samples is commonly used. The in situ EXAFS has also been reported to monitor the change of particle size during the alcohol oxidation reaction.

Other types of catalyst restructuring have also been reported and attributed to the deactivation. For example, during photocatalytic ethanol oxidation over CdS, Nasalevich *et al.* reported the transformation of surface sulfur ions to SO_4^{2-} groups.[96] In gas-phase oxidation of benzyl alcohol over Ag-Ni, the formation of carbide was observed and attributed.[77] In another case of catalytic benzyl alcohol oxidation, Liu *et al.* reported the reduction of immobilized active Pd^{2+} complex to Pd particles associated with a significant decrease of rate.[68] Since the restructuring only occurred on the surface with small amount, characterization methods with high sensitivity, such as XPS, ESR and UV-vis, are required to demonstrate the process.

Over-oxidation

Under alcohol oxidation reaction conditions, catalysts are exposed to both reducing and oxidizing agent. With the consumption of alcohol and increasing oxidizing potential, the adsorbed oxygenate species can saturate the metal surface and even irreversibly oxidize nano-sized metal to metal oxides,[97] which has been observed in several studies[58,60,88–90,98–101] and attributed to the gradual loss of activity during the reaction.[27,30,58,75,88,89,99–108] The reversible adsorption of oxygenate groups can be removed by treating the catalysts in alcohol oxidation under oxygen-free conditions and activity can be recovered.[109] The formation of bulk metal oxides, however, usually lead to the irreversible deactivation. The formation of adsorbed oxygenates can be detected by potentiometry and the bulk metal oxides can be characterized by XAS, TEM and XPS. Additionally, water, as the product of oxidation of adsorbed hydrogen, has been proposed to be an indicator of over-oxidation, which can be detected by IR.[100] Kinetic model containing over-oxidation steps of Pt also fitted well with the deactivation behavior during alcohol oxidation reaction.[27–30]

Strongly-adsorbed species

The strong adsorption of species can block the active sites, which leads to the decrease of activity. Poisoning species have been proposed to be oxidation products, impurities and byproducts generated from agglomeration, decomposition of substrates or oxidation products.[24,38,41,42,45–47,51,58–61,63,72,76,78,89,98,100,103,107,110–130] Loss of activity from competitive adsorption of oxidation products are easy to discriminate by kinetic measurement with addition of known chemicals.[118,119,126,128] The oxidation products have also been detected on deactivated catalyst by IR and Raman.[38,128] And kinetic measurement of alcohol oxidation reaction using purified substrate can determine whether the deactivation is from impurities.[127] The identification of poisoning byproducts is quite challenging because of their trace amount and vulnerability when exposed. Therefore, in situ characterization methods with ultra-high sensitivity combined with other indirect experimental evidence are required to identify the poisoning species. For example, carbon monoxide, generated from decarbonylation of aldehydes or acids, has been identified by in situ IR during alcohol oxidation reaction under O_2 transfer-limiting region.[39,44,100] And unsaturated residuals from aldehyde decarbonylation was proposed to cause the deactivation as evidenced by kinetics measurements, solid-state NMR, TPD, in situ IR and in situ Raman.[44,128]

Procedures to investigate deactivation during alcohol oxidation reaction

Catalyst deactivation during alcohol oxidation reaction depends significantly on the reaction conditions, substrates and catalysts. Therefore, all possible causes for deactivation mentioned above need to be examined to reach an unambiguous conclusion. A recommended process for deactivation study on alcohol oxidation over supported metal catalysts is briefly summarized in Figure 1.3. Deactivation caused by impurities can be easily determined by purifying the reagents. Characterization on metal concentration in filtered reaction medium and size distribution after reaction is able to discriminate whether leaching or aggregation causes the deactivation. The characterization of deactivated catalysts can also examine whether irreversible over-oxidation happens. To differentiate chemical poisoning from reversible over-oxidation poisoning, deactivated catalyst can be pre-treated in alcohol oxidation under oxygen-free conditions. If this pretreatment regenerates the activity, the deactivation is likely caused by reversible oxidation. If not, the strongly-adsorbed poisoning species can be characterized by methods introduced above.

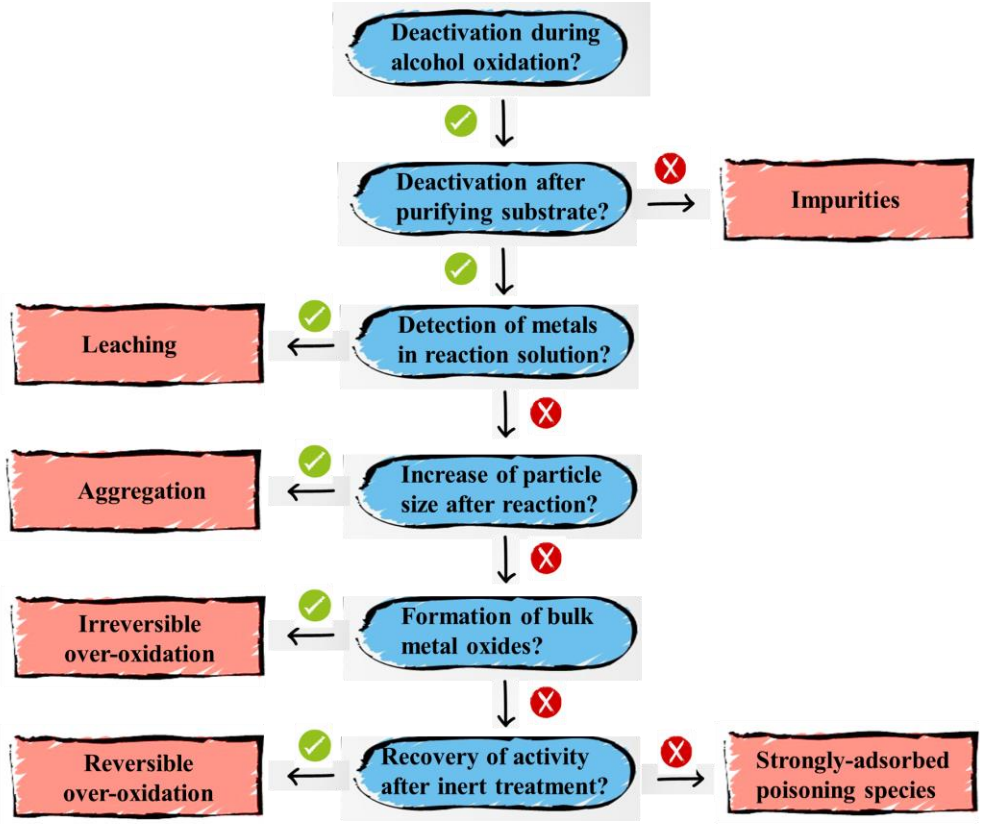

Figure 1. 3. Flowchart of investigation on supported-metal catalyst deactivation during alcohol oxidation reaction.

1.4. Strategies to suppress the deactivation

Based on the results of deactivation investigation, catalyst can be modified rationally with better stability. The deactivation caused by leaching and aggregation of metals can be inhibited by strong metal-support interactions, as shown in the case of benzyl alcohol oxidation over TiO_2-supported Pd.[131] Another approach is to encapsulate active metal nanoparticles by SiO_2, Al_2O_3, zeolites or metal organic frameworks. Through the tunnels, oxygen and substrates can still transport to the active sites and the encapsulation can eliminate the aggregation of nanoparticles.[132,133] To avoid the over-oxidation of catalyst, a simple way is to tune the rate of oxygen feed. When the reaction rate of metal reduction by alcohol is not slower than the metal oxidation rate, the catalytically-active metal components will keep reduced.[60,73,99,100,109]

If the deactivation is caused by strongly-adsorbed byproducts, catalysts needs to be modified to suppress the rate of side reaction or adsorption of poisoning species while catalyzing alcohol oxidation reaction. Therefore, the strategy of catalyst modification depends on the reaction path of alcohol oxidation and the certain side reaction over specific catalysts. For example, during alcohol oxidation over Pt-group catalysts, strongly-adsorbed species has been recognized to be generated from decarbonylation of aldehyde.[44,128] Different steps are involved in these two reactions. The activation of O-H and C-H bonds is required for the alcohol oxidation whereas the activation of a C-C bond is additionally required for the decarbonylation reaction. The rates of these steps are very sensitive to the ensemble size and coordination number of metal.[134–137] To suppress the C-C cleavage path, Medlin's group modified the surface environment of Pt-group catalysts by self-assembly of thiol monolayers, which has been proven to inhibit the deactivation during the alcohol oxidation reaction.[46,138,139] Another promising approach is to develop bimetallic catalysts that can tune the ensemble size and electronic properties. Compared to monometallic Pd catalysts, the PdAu catalysts with alloyed structure have demonstrated much better stability during oxidation of benzyl alcohol and glycerol.[140,141]

1.5. Alcohol oxidation over non-precious-metal catalysts

Heterogeneous precious-metal catalysts have been long recognized as possessing the features needed to catalyze alcohol oxidation by air under mild temperatures (usually <400 K).[19] However, the high cost limits their application on large scale and distributed systems.[142] Therefore, a strong motivation exists to discover or engineer earth-abundant elements in chemical environments that catalyze desired chemical transformations similar to those typical of precious metals.

Recently, non-precious metal catalysts confined in a nitrogen-containing carbon matrix, which were prepared by pyrolysis or a ball milling method, exhibited decent activity in electrochemical reactions[143–148] and organic synthesis.[149–154] For example, the efficient activation of dioxygen has been reported with Fe-containing, nitrogen-doped carbon (Fe-N-C) in the electrochemical O_2 reduction reaction (ORR), with a comparable activity to the well-known Pt ORR catalysts.[146] Alcohol oxidation reactions can also be catalyzed by the Fe-based catalysts, such as Fe-containing polyoxometalates,[155] nano-Fe_2O_3 particles[156,157] and encapsulated or supported Fe complexes,[158–162] but these catalysts often require the addition of peroxides, which is likely the consequence of the poor ability of the catalyst to activate dioxygen. Since an Fe-N-C catalyst has previously demonstrated excellent ORR performance, we hypothesized that it might also be a promising catalyst for the aerobic oxidation of alcohols. Compared to Fe-N-C, M-N-C with other metal centers are less active to activate oxygen but exhibited reasonable activity in several organic reactions involving oxidative C-H activation at mild temperature,[149,150,163–171] which is well recognized as the kinetically-relevant step in alcohol oxidation reaction.

The M-N-C catalysts usually produces a variety of metal environments simultaneously, such as exposed or encapsulated metal nanoparticles. Moreover, the atomically-dispersed metals can be found in a variety of coordination environments. The co-existence of these sites complicates the investigation into the nature of the catalytically active sites. Catalysts containing predominantly atomically-dispersed Fe and Co, which also exhibited catalytic activity in ORR or C-H activation, were utilized to study the coordination environment and chemical state around the metal.[144,147,165,167,169,172–188] Atomic dispersion of the metals on these catalysts has been demonstrated by aberration-corrected scanning transmission electron microscopy (AC-STEM) and XAS. The chemical state and coordination environment were probed by XAS, along with XPS, Mössbauer spectroscopy, EELS and DFT.[147,165,167,177–179,183,184,186,188,189] Although the existence of nitrogen-coordinated metal (MN_x) sites has been well documented, the coordination number of N atoms to the active metal center is still unresolved.[170,185,186,188,190] Therefore, the M-N-C catalysts are promising to replace precious metal in the alcohol oxidation reaction and it would be quite advantageous to identify the atomic and electronic structure of active MN_x sites and relate those characteristics to catalytic performance in alcohol oxidation, based on which the catalysts can be rationally optimized.

1.6. Objectives of this work

The motivation of this project is to rationally develop an efficient and affordable catalyst based on mechanistic understanding for alcohol oxidation under environmentally friendly conditions (water as solvent; dioxygen/air as oxidant; relatively low temperature (<373 K); without base addition). Although supported Pt exhibits highest activity to oxidize alcohols among various supported metals under such conditions,[20] the severe deactivation observed during the reaction[44] as well as high price and limited amount are potential drawbacks for its large-scale application. Therefore, the goals of the dissertation are to:

1) Understand the deactivation path of supported Pt catalyst during the alcohol oxidation reaction;
2) Promote the catalytic performance of Pt catalyst by synthesizing bimetallic nanoparticles;

3) Explore the application of non-precious-metal heterogeneous catalysts in alcohol oxidation reaction;
4) Investigate the chemical structure of active sites of non-precious-metal catalysts for alcohol oxidation reaction.

In this dissertation, Chapter 2 discusses the deactivation path of supported Pt catalysts investigated by kinetic measurements, comprehensive characterization on fresh and used Pt catalyst, and in situ surface-enhanced Raman spectroscopy. To promote catalytic performance of Pt, bimetallic Bi-Pt catalysts was explored for alcohol oxidation in Chapter 3 and the promotional effect of Bi addition was studied by kinetic isotope effect and detailed characterization. Chapter 4 introduces the application of non-precious metal catalysts in aerobic alcohol oxidation reaction and preliminary mechanistic study. Subsequently, in Chapter 5, the chemical structure of active sites was probed by extensive *ex-situ* characterization methods and the evolution of active sites under different reaction conditions was revealed by in situ XAS. To conclude, Chapter 6 remarks on the research works that are presented throughout all chapters and presents thought for further researches.

References for Chapter 1

(1) Monson, R. S. *Advanced Organic Synthesis : Methods and Techniques*; Academic Press: New York, 1971.

(2) Bianchini, C.; Shen, P. K. Palladium-Based Electrocatalysts for Alcohol Oxidation in Half Cells and in Direct Alcohol Fuel Cells. *Chem. Rev.* **2009**, *109*, 4183–4206.

(3) Antolini, E. Catalysts for Direct Ethanol Fuel Cells. *Journal of Power Sources*, 2007, *170*, 1–12.

(4) Bhargava, S. K.; Tardio, J.; Prasad, J.; Föger, K.; Akolekar, D. B.; Grocott, S. C. Wet Oxidation and Catalytic Wet Oxidation. *Ind. Eng. Chem. Res.* **2006**, *45*, 1221–1258.

(5) Tiwari, A.; Syvajarvi, M. *Advanced Materials for Agriculture, Food, and Environmental Safety*; Wiley-VCH, 2014.

(6) Weissermel, K.; Arpe, H.-J. *Industrial Organic Chemistry, 6th Ed.*; Wiley-VCH, 2007.

(7) Tao, J. A.; Lin, G.-Q.; Liese, A. *Biocatalysis for the Pharmaceutical Industry: Discovery, Development, and Manufacturing*; John Wiley & Sons, Ltd: Chichester, UK, 2009.

(8) Surburg, H.; Panten, J. *Common Fragrance and Flavor Materials: Preparation, Properties and Uses, 5th, Completely Revised and Enlarged Edition*; Wiley-VCH, 2006.

(9) Jungclaus, G.; Avila, V.; Hites, R. Organic Compounds in an Industrial Wastewater: A Case Study of Their Environmental Impact. *Environ. Sci. Technol.* **1978**, *12*, 88–96.

(10) Corma, A.; Sara Iborra, A.; Velty, A.; Corma, A.; Iborra, S.; Velty, A.; Corma Canos, A.; Iborra, S.; Velty, A. Chemical Routes for the Transformation of Biomass into Chemicals. *Chem. Rev.* **2007**, *107*, 2411–2502.

(11) Werpy, T.; Petersen, G.; Aden, A.; Bozell, J.; Holladay, J.; White, J.; Mandeim, A.; Eloit, D.; Lasure, L.; Jones, S. *Top Value Added Chemicals from Biomass: Volume I -- Results of Screening for Potential Candidates from Sugars and Synthesis Gas. Office of Scientific and Technical Information (OSTI)*; 2004.

(12) Mallat, T.; Baiker, A. Oxidation of Alcohols with Molecular Oxygen on Solid Catalysts. *Chem. Rev.* **2004**, *104*, 3037–3058.

(13) Fallis, A. . *March's Advanced Organic Chemistry*; Wiley, 2013; Vol. 53.

(14) Marko, I. E.; Giles, P. R.; Tsukazaki, M.; Brown, S. M.; Urch, C. J. Copper-Catalyzed Oxidation of Alcohols to Aldehydes and Ketones: An Efficient, Aerobic Alternative. *Science.* **1996**, *274*, 2044–2046.

(15) Henry, W. Experiments on the Quantity of Gases Absorbed by Water, at Different

Temperatures, and under Different Pressures. *Philos. Trans. R. Soc. London* **1803**, 29–42.

(16) Corma, A.; Iborra, S.; Velty, A. Chemical Routes for the Transformation of Biomass into Chemicals. *Chem. Rev.* **2007**, *107*, 2411–2502.

(17) Parmeggiani, C.; Cardona, F. Transition Metal Based Catalysts in the Aerobic Oxidation of Alcohols. *Green Chem.* **2012**, *14*, 547–564.

(18) Matsumoto, T.; Ueno, M.; Wang, N.; Kobayashi, S. Recent Advances in Immobilized Metal Catalysts for Environmentally Benign Oxidation of Alcohols. *Chem. - An Asian J.* **2008**, *3*, 196–214.

(19) Mallat, T.; Baiker, A. Oxidation of Alcohols with Molecular Oxygen on Solid Catalysts. *Chem. Rev.* **2004**, *104*, 3037–3058.

(20) Davis, S. E.; Ide, M. S.; Davis, R. J. Selective Oxidation of Alcohols and Aldehydes over Supported Metal Nanoparticles. *Green Chem.* **2013**, *15*, 17–45.

(21) Zope, B. N.; Hibbitts, D. D.; Neurock, M.; Davis, R. J. Reactivity of the Gold/Water Interface During Selective Oxidation Catalysis. *Science (80-.).* **2010**, *330*, 74–78.

(22) Davis, S. E.; Zope, B. N.; Davis, R. J. On the Mechanism of Selective Oxidation of 5-Hydroxymethylfurfural to 2,5-Furandicarboxylic Acid over Supported Pt and Au Catalysts. *Green Chem.* **2012**, *14*, 143–147.

(23) Nie, J.; Xie, J.; Liu, H. Efficient Aerobic Oxidation of 5-Hydroxymethylfurfural to 2,5-Diformylfuran on Supported Ru Catalysts. *J. Catal.* **2013**, *301*, 83–91.

(24) Besson, M.; Gallezot, P. Selective Oxidation of Alcohols and Aldehydes on Metal Catalysts. *Catal. Today* **2000**, *57*, 127–141.

(25) Kumbilieva, K.; Petrov, L.; Alhamed, Y.; Alzahrami; A. Reaction Mechanism and Deactivation Modes of Heterogeneous Catalytic Systems. *Chinese Journal of Catalysis*, 2011, *32*, 387–404.

(26) Ostrovskii, N. M. Catalyst Deactivation Kinetics: An Apparent Delay in Decreasing of Catalyst Activity, “ Inflection Point ” and Data Interpretation. *Russ. J. Phys. Chem.* **2011**, *85*, 2336–2343.

(27) Kluytmans, J. H. .; Markusse, a. .; Kuster, B. F. .; Marin, G. .; Schouten, J. . Engineering Aspects of the Aqueous Noble Metal Catalysed Alcohol Oxidation. *Catal. Today* **2000**, *57*, 143–155.

(28) Gangwal, V. R.; van Wachem, B. G. M.; Kuster, B. F. M.; Schouten, J. C. Platinum Catalysed Aqueous Alcohol Oxidation: Model-Based Investigation of Reaction Conditions and Catalyst Design. *Chem. Eng. Sci.* **2002**, *57*, 5051–5063.

(29) Gangwal, V. R.; Van Der Schaaf, J.; Kuster, B. F. M.; Schouten, J. C. Catalyst Performance for Noble Metal Catalysed Alcohol Oxidation: Reaction-Engineering Modelling and Experiments. *Catal. Today* **2004**, *96*, 223–234.

(30) Tschentscher, R.; Nijhuis, T. A.; Van Der Schaaf, J.; Schouten, J. C. Glucose Oxidation in Slurry Reactors and Rotating Foam Reactors. *Ind. Eng. Chem. Res.* **2012**, *51*, 1620–1634.

(31) Nørskov, J. K.; Bligaard, T.; Rossmeisl, J.; Christensen, C. H. Density Functional Theory in Surface Chemistry and Catalysis. *Nat. Chem.* **2009**, *1*, 37–46.

(32) Stamatakis, M. Kinetic Modelling of Heterogeneous Catalytic Systems. *J. Phys. Condens. Matter* **2015**, *27*, 13001.

(33) Rudd, D.; Dumesic, J. *The Microkinetics of Heterogeneous Catalysis*; American Chemical Society: Washington, DC, 1993.

(34) Chibani, S.; Michel, C.; Delbecq, F.; Pinel, C.; Besson, M. On the Key Role of Hydroxyl Groups in Platinum-Catalysed Alcohol Oxidation in Aqueous Medium. *Catal. Sci. Technol.* **2013**, *3*, 339–350.

(35) Che, M. (Michel); Védrine, J. C.; Wiley InterScience (Online service).

Characterization of Solid Materials and Heterogeneous Catalysts : From Structure to Surface Reactivity; Wiley-VCH, 2012.

(36) Andanson, J.-M.; Baiker, A. Exploring Catalytic Solid/liquid Interfaces by in Situ Attenuated Total Reflection Infrared Spectroscopy. *Chem. Soc. Rev.* **2010**, *39*, 4571.

(37) Lamberti, C.; Zecchina, A.; Groppo, E.; Bordiga, S. Probing the Surfaces of Heterogeneous Catalysts by in Situ IR Spectroscopy. *Chem. Soc. Rev.* **2010**, *39*, 4951.

(38) Pillai, U. R.; Sahle-Demessie, E. Selective Oxidation of Alcohols in Gas Phase Using Light-Activated Titanium Dioxide. *J. Catal.* **2002**, *211*, 434–444.

(39) Keresszegi, C.; Bürgi, T.; Mallat, T.; Baiker, A. On the Role of Oxygen in the Liquid-Phase Aerobic Oxidation of Alcohols on Palladium. *J. Catal.* **2002**, *211*, 244–251.

(40) Burgi, T. Combined in Situ Attenuated Total Reflection Infrared and UV-Vis Spectroscopic Study of Alcohol Oxidation over Pd/Al2O3. *J. Catal.* **2005**, *229*, 55–63.

(41) Burgener, M.; Tyszewski, T.; Ferri, D.; Mallat, T.; Baiker, A. Palladium-Catalyzed Oxidation of Geraniol in Dense Carbon Dioxide. *Appl. Catal. A Gen.* **2006**, *299*, 66–72.

(42) Yu, H.; Zhang, Y.; Fu, X.; Peng, F.; Wang, H.; Yang, J. Deactivation and Regeneration of RuO2·xH2O/CNT Catalyst for Aerobic Oxidation of Benzyl Alcohol. *Catal. Commun.* **2009**, *10*, 1752–1756.

(43) Meier, D. M.; Urakawa, A.; Baiker, A. In Situ PM-IRRAS Study of Liquid-Phase Benzyl Alcohol Oxidation on Palladium. *J. Phys. Chem. C* **2009**, *113*, 21849–21855.

(44) Ide, M. S.; Falcone, D. D.; Davis, R. J. On the Deactivation of Supported Platinum Catalysts for Selective Oxidation of Alcohols. *J. Catal.* **2014**, *311*, 295–305.

(45) Villa, A.; Ferri, D.; Campisi, S.; Chan-Thaw, C. E.; Lu, Y.; Kröcher, O.; Prati, L. Operando Attenuated Total Reflectance FTIR Spectroscopy: Studies on the Different

Selectivity Observed in Benzyl Alcohol Oxidation. *ChemCatChem* **2015**, *7*, 2534–2541.

(46) Hao, P.; Pylypenko, S.; Schwartz, D. K.; Medlin, J. W. Application of Thiolate Self-Assembled Monolayers in Selective Alcohol Oxidation for Suppression of Pd Catalyst Deactivation. *J. Catal.* **2016**, *344*, 722–728.

(47) Lucarelli, C.; Lolli, A.; Giugni, A.; Grazia, L.; Albonetti, S.; Monticelli, D.; Vaccari, A. Efficient and Ecofriendly Route for the Solvent-Free Synthesis of Piperonal and Aromatic Aldehydes Using Au/CeO2 Catalyst. *Appl. Catal. B Environ.* **2017**, *203*, 314–323.

(48) Le Ru, E. C.; Blackie, E.; Meyer, M.; Etchegoin, P. G. Surface Enhanced Raman Scattering Enhancement Factors: A Comprehensive Study. *J. Phys. Chem. C* **2007**, *111*, 13794–13803.

(49) Heck, K. N.; Janesko, B. G.; Scuseria, G. E.; Halas, N. J.; Wong, M. S. Observing Metal-Catalyzed Chemical Reactions in Situ Using Surface-Enhanced Raman Spectroscopy on Pd-Au Nanoshells. *J. Am. Chem. Soc.* **2008**, *130*, 16592–16600.

(50) Heck, K. N.; Janesko, B. G.; Scuseria, G. E.; Halas, N. J.; Wong, M. S. Using Catalytic and Surface-Enhanced Raman Spectroscopy-Active Gold Nanoshells to Understand the Role of Basicity in Glycerol Oxidation. *ACS Catal.* **2013**, *3*, 2430–2435.

(51) Naughton, J.; Pratt, A.; Woffinden, C. W.; Eames, C.; Tear, S. P.; Thompson, S. M.; Lee, A. F.; Wilson, K. Metastable de-Excitation Spectroscopy and Density Functional Theory Study of the Selective Oxidation of Crotyl Alcohol over Pd(111). *J. Phys. Chem. C* **2011**, *115*, 25290–25297.

(52) Zilm, K. W.; Bonneviot, L.; Hamilton, D. M.; Webb, G. G.; Haller, G. L. Carbon-13 NMR Studies of Supported Platinum and Palladium Catalysts Using Magic Angle

Sample Spinning. *J. Phys. Chem.* **1990**, *94*, 1463–1472.

(53) Pruski, M.; Kelzenberg, J. C.; Gerstein, B. C.; King, T. S. Solid-State NMR of Carbon-13 in Ethylene Adsorbed on Silica-Supported Ruthenium. *J. Am. Chem. Soc.* **1990**, *112*, 4232–4240.

(54) Pruski, M.; Wu, X.; Smale, M. W.; Gerstein, B. C.; King, T. S. The Conversion of Ethylene to Coke on Supported Platinum Catalysts Investigated by 13C Nmr. *Stud. Surf. Sci. Catal.* **1991**, *68*, 699–706.

(55) Gay, I. Chemisorption of Ethylene on Supported Platinum Studied by High-Resolution Solid-State NMR. *J. Catal.* **1987**, *108*, 15–23.

(56) Mao, J.-D.; Schmidt-Rohr, K. Separation of Aromatic-Carbon 13C NMR Signals from Di-Oxygenated Alkyl Bands by a Chemical-Shift-Anisotropy Filter. *Solid State Nucl. Magn. Reson.* **2004**, *26*, 36–45.

(57) Johnson, R. L.; Schmidt-Rohr, K. Quantitative Solid-State 13C NMR with Signal Enhancement by Multiple Cross Polarization. *J. Magn. Reson.* **2014**, *239*, 44–49.

(58) Keresszegi, C.; Grunwaldt, J.-D.; Mallat, T.; Baiker, A. Liquid Phase Oxidation of Alcohols with Oxygen: In Situ Monitoring of the Oxidation State of {Bi}-Promoted {Pd}/{Al}_2{O}_3. *Chem. Commun.* **2003**, *18*, 2304–2305.

(59) Mallat, T.; Baiker, A.; Patscheider, J. Liquid Phase Oxidation of 1-Methoxy-2-Propanol with Air. II. Structure and Chemical Properties of Lead-Promoted Palladium Catalysts. *Appl. Catal. A, Gen.* **1991**, *79*, 59–75.

(60) Mallat, T.; Bodnar, Z.; Maciejewski, M.; Baiker, A. Partial Oxidation of Cinnamyl Alcohol on Bimetallic Catalysts of Improved Resistance to Self-Poisoning. *Stud. Surf. Sci. Catal.* **1994**, *82*, 561–570.

(61) Wenkin, M.; Ruiz, P.; Delmon, B.; Devillers, M. The Role of Bismuth as Promoter in Pd-Bi Catalysts for the Selective Oxidation of Glucose to Gluconate. *J. Mol. Catal. A*

Chem. **2002**, *180*, 141–159.

(62) Lee, A. F.; Wilson, K. Structure-reactivity Correlations in the Selective Aerobic Oxidation of Cinnamyl Alcohol: In Situ XAFS. *Green Chem.* **2004**, *6*, 37.

(63) Lee, A. F.; Chang, Z.; Ellis, P.; Hackett, S. F. J.; Wilson, K. Selective Oxidation of Crotyl Alcohol over Pd (111). *Society* **2007**, 18844–18847.

(64) Maity, P.; Gopinath, C. S.; Bhaduri, S.; Lahiri, G. K. Applications of a High Performance Platinum Nanocatalyst for the Oxidation of Alcohols in Water. *Green Chem.* **2009**, *11*, 554–561.

(65) Liu, G.; Li, G.; Song, H. Direct Synthesis of Methyl Propionate from N-Propyl Alcohol and Methanol Using Gold Catalysts. *Catal. Letters* **2009**, *128*, 493–501.

(66) Delidovich, I. V.; Taran, O. P.; Matvienko, L. G.; Simonov, A. N.; Simakova, I. L.; Bobrovskaya, A. N.; Parmon, V. N. Selective Oxidation of Glucose over Carbon-Supported Pd and Pt Catalysts. *Catal. Letters* **2010**, *140*, 14–21.

(67) Pan, X.; Zhang, N.; Fu, X.; Xu, Y.-J. Selective Oxidation of Benzyl Alcohol over TiO2 Nanosheets with Exposed {001} Facets: Catalyst Deactivation and Regeneration. *Appl. Catal. A Gen.* **2013**, *453*, 181–187.

(68) Liu, K.; Chen, Z.; Hou, Z.; Wang, Y.; Dai, L. Sulfur-Modified SBA-15 Supported Amorphous Palladium with Superior Catalytic Performance for Aerobic Oxidation of Alcohols. *Catal. Letters* **2014**, *144*, 935–942.

(69) Parlett, C. M. A.; Durndell, L. J.; Machado, A.; Cibin, G.; Bruce, D. W.; Hondow, N. S.; Wilson, K.; Lee, A. F. Alumina-Grafted SBA-15 as a High Performance Support for Pd-Catalysed Cinnamyl Alcohol Selective Oxidation. *Catal. Today* **2014**, *229*, 46–55.

(70) Wu, G.; Brett, G. L.; Cao, E.; Constantinou, A.; Ellis, P.; Kuhn, S.; Hutchings, G. J.; Bethell, D.; Gavriilidis, A. Oxidation of Cinnamyl Alcohol Using Bimetallic Au–

Pd/TiO 2 Catalysts: A Deactivation Study in a Continuous Flow Packed Bed Microreactor. *Catal. Sci. Technol.* **2016**, *6*, 4749–4758.

(71) SALMERON, M.; SCHLOGL, R. Ambient Pressure Photoelectron Spectroscopy: A New Tool for Surface Science and Nanotechnology. *Surf. Sci. Rep.* **2008**, *63*, 169–199.

(72) Mallat, T.; Bodnar, Z.; Baiker, A. Partial Oxidation of Water - Insoluble Alcohols over Bi - Promoted Pt on Alumina . Electrochemical Characterization of the Catalyst in Its Working State. *Stud. Surf. Sci. Catal.* **1993**, *78*, 377–384.

(73) Mallat, T.; Baiker, A. Catalyst Potential: A Key for Controlling Alcohol Oxidation in Multiphase Reactors. *Catal. Today* **1995**, *24*, 143–150.

(74) Markusse, A. P.; Kuster, B. F. M.; Koningsberger, D. C.; Marin, G. B. Platinum Deactivation: In Situ EXAFS during Aqueous Alcohol Oxidation Reaction. *Catal. Letters* **1998**, *55*, 141–145.

(75) Markusse, A. P.; Kuster, B. F. M.; Schouten, J. C. Catalyst Deactivation and Reactivation during Aqueous Alcohol Oxidation in a Redox-Cycle Reactor. *Stud. Surf. Sci. Catal.* **1999**, *126*, 273–280.

(76) Wang, R.; Li, J. Effects of Precursor and Sulfation on OMS-2 Catalyst for Oxidation of Ethanol and Acetaldehyde at Low Temperatures. *Environ. Sci. Technol.* **2010**, *44*, 4282–4287.

(77) Deng, M.; Zhao, G.; Xue, Q.; Chen, L.; Lu, Y. Microfibrous-Structured Silver Catalyst for Low-Temperature Gas-Phase Selective Oxidation of Benzyl Alcohol. *Appl. Catal. B Environ.* **2010**, *99*, 222–228.

(78) Hao, Y.; Hao, G. P.; Guo, D. C.; Guo, C. Z.; Li, W. C.; Li, M. R.; Lu, A. H. Bimetallic Au-Pd Nanoparticles Confined in Tubular Mesoporous Carbon as Highly Selective and Reusable Benzyl Alcohol Oxidation Catalysts. *ChemCatChem* **2012**, *4*, 1595–1602.

(79) Heidkamp, K.; Aytemir, M.; Vorlop, K.-D.; Prüße, U. Ceria Supported Gold–platinum

Catalysts for the Selective Oxidation of Alkyl Ethoxylates. *Catal. Sci. Technol.* **2013**, *4*, 2984–2992.

(80) D'Agostino, C.; Ryabenkova, Y.; Miedziak, P. J.; Taylor, S. H.; Hutchings, G. J.; Gladden, L. F.; Mantle, M. D. Deactivation Studies of a Carbon Supported AuPt Nanoparticulate Catalyst in the Liquid-Phase Aerobic Oxidation of 1,2-Propanediol. *Catal. Sci. Technol.* **2014**, *4*, 1313–1322.

(81) Heidkamp, K.; Decker, N.; Martens, K.; Prüe, U.; Vorlop, K. D.; Franke, O.; Stankowiak, A. Oxidation of a Tensidic Alcohol to Its Corresponding Carboxylic Acid via Au Catalysts. *Eur. J. Lipid Sci. Technol.* **2010**, *112*, 51–57.

(82) Heeskens, D.; Aghaei, P.; Kaluza, S.; Strunk, J.; Muhler, M. Selective Oxidation of Ethanol in the Liquid Phase over Au/TiO 2. *Phys. Status Solidi* **2013**, *250*, 1107–1118.

(83) Chan-Thaw, C.; Campisi, S.; Wang, D.; Prati, L.; Villa, A. Selective Oxidation of Raw Glycerol Using Supported AuPd Nanoparticles. *Catalysts* **2015**, *5*, 131–144.

(84) Sha, J.; Zheng, E. J.; Zhou, W. J.; Liebens, A.; Pera-Titus, M. Selective Oxidation of Fatty Alcohol Ethoxylates with H2O2 over Au Catalysts for the Synthesis of Alkyl Ether Carboxylic Acids in Alkaline Solution. *J. Catal.* **2016**, *337*, 199–207.

(85) Gómez-Villarraga, F.; Radnik, J.; Martin, A.; Köckritz, A. Synergistic Effect in the Oxidation of Benzyl Alcohol Using Citrate-Stabilized Gold Bimetallic Nanoparticles Supported on Alumina. *J. Nanoparticle Res.* **2016**, *18*, 141–158.

(86) Taheri, M. L.; Stach, E. A.; Arslan, I.; Crozier, P. A.; Kabius, B. C.; LaGrange, T.; Minor, A. M.; Takeda, S.; Tanase, M.; Wagner, J. B.; *et al.* Current Status and Future Directions for in Situ Transmission Electron Microscopy. *Ultramicroscopy*, 2016, *170*, 86–95.

(87) Hsieh, C. C.; Lee, J. F.; Liu, Y. R.; Chang, J. R. Structural Investigation of Catalyst Deactivation of Pt/SDB for Catalytic Oxidation of VOC-Containing Wastewater.

Waste Manag. **2002**, *22*, 739–745.

(88) Zhao, Z.; Miller, J. T.; Wu, T.; Schweitzer, N. M.; Wong, M. S. EXAFS Characterization of Palladium-on-Gold Catalysts Before and After Glycerol Oxidation. *Top. Catal.* **2015**, *58*, 302–313.

(89) Keresszegi, C.; Grunwaldt, J.-D.; Mallat, T.; Baiker, A. In Situ EXAFS Study on the Oxidation State of Pd/Al2O3 and Bi-Pd/Al2O3 during the Liquid-Phase Oxidation of 1-Phenylethanol. *J. Catal.* **2004**, *222*, 268–280.

(90) Wang, L.; Lavacchi, A.; Bellini, M.; D’Acapito, F.; Benedetto, F. Di; Innocenti, M.; Miller, H. A.; Montegrossi, G.; Zafferoni, C.; Vizza, F. Deactivation of Palladium Electrocatalysts for Alcohols Oxidation in Basic Electrolytes. *Electrochim. Acta* **2015**, *177*, 100–106.

(91) Singh, A. P.; Selvam, T. Liquid Phase Oxidation of Para-Chlorotoluene to Para-Chlorobenzaldehyde Using Vanadium Silicate Molecular Sieves. *Appl. Catal. A Gen.* **1996**, *143*, 111–124.

(92) Frassoldati, A.; Pinel, C.; Besson, M. Aerobic Oxidation of Secondary Pyridine-Derivative Alcohols in the Presence of Carbon-Supported Noble Metal Catalysts. *Catal. Today* **2013**, *203*, 133–138.

(93) Zhang, Y.; Chu, R.; Zhang, H.; Zhao, J. Synthesis of a Polymer–ruthenium Complex Ru(pbbp)(pydic) and Its Catalysis in the Oxidation of Secondary Alcohols with TBHP as Oxidant. *Transit. Met. Chem.* **2017**, *42*, 105–116.

(94) Biella, S.; Prati, L.; Rossi, M. Selective Oxidation of D-Glucose on Gold Catalyst. *J. Catal.* **2002**, *206*, 242–247.

(95) Haneda, M.; Bonne, M.; Duprez, D.; Ozawa, M. Effect of Y-Stabilized ZrO2 as Support on Catalytic Performance of Pt for N-Butane Oxidation. *Catal. Today* **2013**, *201*, 25–31.

(96) Nasalevich, M. A.; Kozlova, E. A.; Lyubina, T. P.; Vorontsov, A. V. Photocatalytic Oxidation of Ethanol and Isopropanol Vapors on Cadmium Sulfide. *J. Catal.* **2012**, *287*, 138–148.

(97) Van Dam, H. E.; Kieboom, A. P. G.; Van Bekkum, H. Pt/C Oxidation Catalysts. Part 1. Effect of Carrier Structure on Catalyst Deactivation during the Oxidation of Glucose 1-Phosphate into Glucuronic Acid 1-Phosphate. *Appl. Catal.* **1987**, *33*, 361–372.

(98) Hirofumi, H.; Nishiyama, S.; Tsuruya, S.; Masai, M. The Effect of Alkali Promoters on Cu-Na-ZSM-5 Catalysts in the Oxidation of Benzyl Alcohol. *Journal of Catalysis*, 1995, *153*, 254–264.

(99) Markusse, A. P.; Kuster, B. F. M.; Schouten, J. C. Platinum Catalysed Aqueous Alcohol Oxidation: Experimental Studies and Reaction Model Discrimination. *J. Mol. Catal. A Chem.* **2000**, *158*, 215–222.

(100) Ferri, D.; Baiker, A. Advances in Infrared Spectroscopy of Catalytic Solid-Liquid Interfaces: The Case of Selective Alcohol Oxidation. *Top. Catal.* **2009**, *52*, 1323–1333.

(101) Mondelli, C.; Grunwaldt, J.; Ferri, D.; Baiker, A. Role of Bi Promotion and Solvent in Platinum-Catalyzed Alcohol Oxidation Probed by in Situ X-Ray Absorption and ATR-IR Spectroscopy. *Phys. Chem. Chem. Phys.* **2010**, *12*, 5307–5316.

(102) Crozon, A. B.; Besson, M.; Gallezot, P. Oxidation of 9-Decen-1-Ol (Rosalva) by Air in Aqueous Media on Platinum Catalysts. *New J. Chem.* **1998**, *22*, 269–273.

(103) Markusse, A. P.; Kuster, B. F. M.; Schouten, J. C. Platinum Catalysed Aqueous Methyl Alpha-D-Glucopyranoside Oxidation in a Multiphase Redox-Cycle Reactor. *Catal. Today* **2001**, *66*, 191–197.

(104) Gläser, R.; Josl, R.; Williardt, J. Selective Oxidation of 1- and 2-Propanol with Molecular Oxygen by Noble Metal Catalysis in “supercritical” Carbon Dioxide. *Top.*

Catal. **2003**, *22*, 31–39.

(105) Gangwal, V. R.; Van Der Schaaf, J.; Kuster, B. F. M.; Schouten, J. C. Noble-Metal-Catalysed Aqueous Alcohol Oxidation: Reaction Start-up and Catalyst Deactivation and Reactivation. *J. Catal.* **2005**, *232*, 432–443.

(106) Beier, M. J.; Grunwaldt, J.-D.; Tsivintzelis, I.; Jensen, A. D.; Kontogeorgis, G. M.; Baiker, A. Selective Oxidation of Benzyl Alcohol in Dense CO2: Insight by Phase Behavior Modeling. *J. Supercrit. Fluids* **2012**, *63*, 199–207.

(107) Villa, A.; E-Chan-Thaw, C.; Schiavoni, M.; Campisi, S.; Wang, D.; Prati, L. Fragrances by Selective Oxidation of Long-Chain Alcohols. *Chinese J. Catal.* **2014**, *35*, 945–951.

(108) Ablasser, C.; Hilger, A.; Hinrichsen, O. Kinetic Study of Heterogeneously Catalyzed Glucose Oxidation in a Stirred Cell. *Chemie-Ingenieur-Technik* **2014**, *86*, 1948–1953.

(109) Ayude, A.; Cechini, J.; Cassanello, M.; Martínez, O.; Haure, P. Trickle Bed Reactors: Effect of Liquid Flow Modulation on Catalytic Activity. *Chem. Eng. Sci.* **2008**, *63*, 4969–4973.

(110) Nicoletti, J.; Whiteside, G. Liquid-Phase Oxidation of 2-Propanol to Acetone by Dioxygen Using Supported Platinum Cataiysts. *J. Phys. Chem.* **1989**, *93*, 759–767.

(111) Mallat, T.; Baiker, A. Liquid-Phase Oxidation of 1-Methoxy-2-Propanol with Air. I. Lead and Bismuth Promotion and Deactivation of Palladium Catalysts. *Appl. Catal. A, Gen.* **1991**, *79*, 41–58.

(112) Luo, S.; Falconer, J. L. Acetone and Acetaldehyde Oligomerization on TiO2 Surfaces. *J. Catal.* **1999**, *185*, 393–407.

(113) Önal, Y.; Schimpf, S.; Claus, P. Structure Sensitivity and Kinetics of D-Glucose Oxidation to D-Gluconic Acid over Carbon-Supported Gold Catalysts. *J. Catal.* **2004**, *223*, 122–133.

(114) Kim, S.-K.; Ihm, S.-K. Nature of Carbonaceous Deposits on the Alumina Supported Transition Metal Oxide Catalysts in the Wet Air Oxidation of Phenol. *Top. Catal.* **2005**, *33*, 171–179.

(115) Bavykin, D. V.; Lapkin, A. A.; Plucinski, P. K.; Friedrich, J. M.; Walsh, F. C. TiO2 Nanotube-Supported ruthenium(III) Hydrated Oxide: A Highly Active Catalyst for Selective Oxidation of Alcohols by Oxygen. *J. Catal.* **2005**, *235*, 10–17.

(116) Li, X.; Qiu, X.; Yuan, H.; Chen, L.; Zhu, W. Size-Effect on the Activity of Anodic Catalysts in Alcohol and CO Electrooxidation. *J. Power Sources* **2008**, *184*, 353–360.

(117) Mounzer, H. N.; Wood, J.; Stitt, E. H. Heterogeneous Oxidation of 2-Octanol on 5wt%Pt–1wt%Bi/Carbon Catalyst. *Chem. Eng. Sci.* **2010**, *65*, 179–185.

(118) Dhakshinamoorthy, A.; Alvaro, M.; Garcia, H.; Valencia, D. Aerobic Oxidation of Benzylic Alcohols Catalyzed by Metal - Organic Frameworks Assisted by TEMPO. *ACS Catal.* **2011**, *1*, 48–53.

(119) Zope, B. N.; Davis, R. J. Inhibition of Gold and Platinum Catalysts by Reactive Intermediates Produced in the Selective Oxidation of Alcohols in Liquid Water. *Green Chem.* **2011**, *13*, 3484–3491.

(120) Hammond, C.; Schümperli, M. T.; Conrad, S.; Hermans, I. Hydrogen Transfer Processes Mediated by Supported Iridium Oxide Nanoparticles. *ChemCatChem* **2013**, *5*, 2983–2990.

(121) Oberhauser, W.; Lavacchi, A.; Vizza, F.; Capozzoli, L.; Lee, H. M. Aerobic Diol Lactonization by Au-Nanoparticles Supported onto an Anion-Exchange Resin. *Appl. Catal. A Gen.* **2013**, *451*, 58–64.

(122) Skupien, E.; Berger, R.; Santos, V.; Gascon, J.; Makkee, M.; Kreutzer, M.; Kooyman, P.; Moulijn, J.; Kapteijn, F. Inhibition of a Gold-Based Catalyst in Benzyl Alcohol Oxidation: Understanding and Remediation. *Catalysts* **2014**, *4*, 89–115.

(123) Mannel, D. S.; Stahl, S. S.; Root, T. W. Continuous Flow Aerobic Alcohol Oxidation Reactions Using a Heterogeneous Ru(OH)x/Al2O3 Catalyst. *Org. Process Res. Dev.* **2014**, *18*, 1503–1508.

(124) Li, Y.; Zaera, F. Factors Affecting Activity and Selectivity in the Oxidation of Glycerol Promoted by Platinum Catalysts. *Catal. Sci. Technol.* **2015**, *5*, 3773–3781.

(125) Arena, F.; Gumina, B.; Cannilla, C.; Spadaro, L.; Patti, A.; Spiccia, L. Nanostructured MnOx Catalysts in the Liquid Phase Selective Oxidation of Benzyl Alcohol with Oxygen. Part II. Reaction Mechanism, Kinetics and Deactivation Pattern. *Appl. Catal. B Environ.* **2015**, *170–171*, 233–240.

(126) He, Y.; Feng, J.; Brett, G. L.; Liu, Y.; Miedziak, P. J.; Edwards, J. K.; Knight, D. W.; Li, D.; Hutchings, G. J. Oxidation of Aliphatic Alcohols by Using Precious Metals Supported on Hydrotalcite under Solvent- and Base-Free Conditions. *ChemSusChem* **2015**, *8*, 3314–3322.

(127) Chan-Thaw, C. E.; Chinchilla, L. E.; Campisi, S.; Botton, G. A.; Prati, L.; Dimitratos, N.; Villa, A. AuPt Alloy on TiO2: A Selective and Durable Catalyst for L-Sorbose Oxidation to 2-Keto-Gulonic Acid. *ChemSusChem* **2015**, *8*, 4189–4194.

(128) Xie, J.; Duan, P.; Kaylor, N.; Yin, K.; Huang, B.; Schmidt-Rohr, K.; Davis, R. J. Deactivation of Supported Pt Catalysts during Alcohol Oxidation Elucidated by Spectroscopic and Kinetic Analyses. *ACS Catal.* **2017**, *7*, 6745–6756.

(129) Brazier, J. B.; Hellgardt, K.; Hii, K. K. (Mimi). Catalysis in Flow: O_2 Effect on the Catalytic Activity of $Ru(OH)_x/\gamma\text{-}Al_2O_3$ during the Aerobic Oxidation of an Alcohol. *React. Chem. Eng.* **2017**, *2*, 60–67.

(130) Du, Z. T.; Liu, J. X.; Lu, T. L.; Ma, Y. Y.; Xu, J. Studies on the Roles of Vanadyl Sulfate and Sodium Nitrite in Catalytic Oxidation of Benzyl Alcohol with Molecular Oxygen. *Sci. China-Chemistry* **2015**, *58*, 114–122.

(131) Wang, J.; Rao, P.; An, W.; Xu, J.; Men, Y. Boosting Photocatalytic Activity of Pd Decorated TiO2 Nanocrystal with Exposed (001) Facets for Selective Alcohol Oxidations. *Appl. Catal. B Environ.* **2016**, *195*, 141–148.

(132) Sadjadi, S.; Heravi, M. M. Pd(0) Encapsulated Nanocatalysts as Superior Catalytic Systems for Pd-Catalyzed Organic Transformations. *RSC Adv.* **2016**, *6*, 88588–88624.

(133) Ren, N.; Yang, Y. H.; Shen, J.; Zhang, Y. H.; Xu, H. L.; Gao, Z.; Tang, Y. Novel, Efficient Hollow Zeolitically Microcapsulized Noble Metal Catalysts. *J. Catal.* **2007**, *251*, 182–188.

(134) Neurock, M.; Janik, M.; Wieckowski, A. A First Principles Comparison of the Mechanism and Site Requirements for the Electrocatalytic Oxidation of Methanol and Formic Acid over Pt. *Faraday Discuss.* **2009**, *140*, 363–378.

(135) Basaran, D.; Genest, A.; Lercher, J. A.; Rösch, N. Formation of CO 2 and Ethane from Propionyl over Platinum: A Density Functional Theory Study. *ACS Catal.* **2013**, *3*, 1730–1738.

(136) Chen, Y.; Vlachos, D. G. Hydrogenation of Ethylene and Dehydrogenation and Hydrogenolysis of Ethane on Pt (111) and Pt (211): A Density Functional Theory Study. *J. Phys. Chem. C* **2010**, *114*, 4973–4982.

(137) Wang, H. F.; Liu, Z. P. Comprehensive Mechanism and Structure-Sensitivity of Ethanol Oxidation on Platinum: New Transition-State Searching Method for Resolving the Complex Reaction Network. *J. Am. Chem. Soc.* **2008**, *130*, 10996–11004.

(138) Kahsar, K. R.; Schwartz, D. K.; Medlin, J. W. Control of Metal Catalyst Selectivity through Speci Fi c Noncovalent Molecular Interactions. *J. Am. Chem. Soc.* **2014**, *134*, 520–526.

(139) Schoenbaum, C. A.; Schwartz, D. K.; Medlin, J. W. Controlling the Surface Environment of Heterogeneous Catalysts Using Self-Assembled Monolayers. *Acc.*

Chem. Res. **2014**, *47*, 1438–1445.

(140) Deplanche, K.; Mikheenko, I. P.; Bennett, J. A.; Merroun, M.; Mounzer, H.; Wood, J.; MacAskie, L. E. Selective Oxidation of Benzyl-Alcohol over Biomass-Supported Au/Pd Bioinorganic Catalysts. *Top. Catal.* **2011**, *54*, 1110–1114.

(141) Zhao, Z.; Arentz, J.; Pretzer, L. A.; Limpornpipat, P.; Clomburg, J. M.; Gonzalez, R.; Schweitzer, N. M.; Wu, T.; Miller, J. T.; Wong, M. S. Volcano-Shape Glycerol Oxidation Activity of Palladium-Decorated Gold Nanoparticles. *Chem. Sci.* **2014**, *5*, 3715.

(142) Vesborg, P. C. K.; Jaramillo, T. F. Addressing the Terawatt Challenge: Scalability in the Supply of Chemical Elements for Renewable Energy. *RSC Adv.* **2012**, *2*, 7933–7947.

(143) Zheng, X.; Deng, J.; Wang, N.; Deng, D.; Zhang, W. H.; Bao, X.; Li, C. Podlike N-Doped Carbon Nanotubes Encapsulating FeNi Alloy Nanoparticles: High-Performance Counter Electrode Materials for Dye-Sensitized Solar Cells. *Angew. Chemie - Int. Ed.* **2014**, *53*, 7023–7027.

(144) Cui, X.; Xiao, J.; Wu, Y.; Du, P.; Si, R.; Yang, H.; Tian, H.; Li, J.; Zhang, W. H.; Deng, D.; *et al.* A Graphene Composite Material with Single Cobalt Active Sites: A Highly Efficient Counter Electrode for Dye-Sensitized Solar Cells. *Angew. Chemie - Int. Ed.* **2016**, *100190*, 6708–6712.

(145) Zou, X.; Huang, X.; Goswami, A.; Silva, R.; Sathe, B. R.; Mikmeková, E.; Asefa, T. Cobalt-Embedded Nitrogen-Rich Carbon Nanotubes Efficiently Catalyze Hydrogen Evolution Reaction at All pH Values. *Angew. Chemie Int. Ed.* **2014**, *53*, 4372–4376.

(146) Shao, M.; Chang, Q.; Dodelet, J.-P.; Chenitz, R. Recent Advances in Electrocatalysts for Oxygen Reduction Reaction. *Chem. Rev.* **2016**, *116*, 3594–365.

(147) Serov, A.; Artyushkova, K.; Niangar, E.; Wang, C.; Dale, N.; Jaouen, F.; Sougrati,

M.-T.; Jia, Q.; Mukerjee, S.; Atanassov, P. Nano-Structured Non-Platinum Catalysts for Automotive Fuel Cell Application. *Nano Energy* **2015**, *16*, 293–300.

(148) Wang, J.; Wu, H.; Gao, D.; Miao, S.; Wang, G.; Bao, X. High-Density Iron Nanoparticles Encapsulated within Nitrogen-Doped Carbon Nanoshell as Efficient Oxygen Electrocatalyst for Zinc-Air Battery. *Nano Energy* **2015**, *13*, 387–396.

(149) Jagadeesh, R. V; Junge, H.; Pohl, M.; Radnik, J.; Brückner, A.; Beller, M. Selective Oxidation of Alcohols to Esters Using Heterogeneous Co3O4–N@C Catalysts under Mild Conditions. *J. Am. Chem. Soc.* **2013**, *135*, 10776–10782.

(150) Cui, X.; Li, Y.; Bachmann, S.; Scalone, M.; Surkus, A. E.; Junge, K.; Topf, C.; Beller, M. Synthesis and Characterization of Iron-Nitrogen-Doped Graphene/Core-Shell Catalysts: Efficient Oxidative Dehydrogenation of N-Heterocycles. *J. Am. Chem. Soc.* **2015**, *137*, 10652–10658.

(151) Jagadeesh, R. V; Stemmler, T.; Surkus, A.; Junge, H.; Junge, K.; Beller, M. Hydrogenation Using Iron Oxide – Based Nanocatalysts for the Synthesis of Amines. *Nat. Protoc.* **2015**, *10*, 548–557.

(152) Matanovic, I.; Babanova, S.; Iii, P.; Serov, A. Bio-Inspired Design of Electrocatalysts for Oxalate Oxidation : A Combined Experimental and Computational Study of Mn – N – C Catalysts †. *Phys. Chem. Chem. Phys.* **2015**, *17*, 13235–13244.

(153) Jagadeesh, R. V.; Surkus, A.-E.; Junge, H.; Pohl, M.; Radnik, J.; Rabeah, J.; Huan, H.; Schunemann, V.; Bruckner, A.; Beller, M. Nitroarenes to Anilines. *Science.* **2013**, *342*, 1073–1076.

(154) Deng, D.; Chen, X.; Yu, L.; Wu, X.; Liu, Q.; Liu, Y.; Yang, H.; Tian, H.; Hu, Y.; Du, P.; *et al.* A Single Iron Site Confined in a Graphene Matrix for the Catalytic Oxidation of Benzene at Room Temperature. *Sci. Adv.* **2015**, *1*, e1500462.

(155) Farsani, M. R.; Yadollahi, B. Synthesis, Characterization and Catalytic Performance of

a Fe Polyoxometalate/silica Composite in the Oxidation of Alcohols with Hydrogen Peroxide. *J. Mol. Catal. A Chem.* **2014**, *392*, 8–15.

(156) Shi, F.; Tse, M. K.; Pohl, M. M.; Brückner, A.; Zhang, S.; Beller, M. Tuning Catalytic Activity between Homogeneous and Heterogeneous Catalysis: Improved Activity and Selectivity of Free Nano-Fe2O3 in Selective Oxidations. *Angew. Chemie - Int. Ed.* **2007**, *46*, 8866–8868.

(157) Gao, Y.; Ma, D.; Hu, G.; Zhai, P.; Bao, X.; Zhu, B.; Zhang, B.; Su, D. S. Layered-Carbon-Stabilized Iron Oxide Nanostructures as Oxidation Catalysts. *Angew. Chem. Int. Ed. Engl.* **2011**, *50*, 10236–10240.

(158) Modak, A.; Mondal, J.; Bhaumik, A. Porphyrin Based Porous Organic Polymer as Bi-Functional Catalyst for Selective Oxidation and Knoevenagel Condensation Reactions. *Appl. Catal. A Gen.* **2013**, *459*, 41–51.

(159) Fidalgo-Marijuan, A.; Barandika, G.; Bazán, B.; Urtiaga, M. K.; Larrea, E. S.; Iglesias, M.; Lezama, L.; Arriortua, M. I. Heterogeneous Catalytic Properties of Unprecedented μ-O-[FeTCPP]2 Dimers (H2TCPP = Meso-tetra(4-Carboxyphenyl)porphyrin): An Unusual Superhyperfine EPR Structure. *Dalt. Trans.* **2015**, *44*, 213–222.

(160) Bilis, G.; Christoforidis, K. C.; Deligiannakis, Y.; Louloudi, M. Hydrocarbon Oxidation by Homogeneous and Heterogeneous Non-Heme Iron (III) Catalysts with H2O2. *Catal. Today* **2010**, *157*, 101–106.

(161) Rahimi, R.; Ghoreishi, S. Z.; Dekamin, M. G. Immobilized Metalloporphyrins on 3-Aminopropyl-Functionalized Silica Support as Heterogeneous Catalysts for Selective Oxidation of Primary and Secondary Alcohols. *Monatshefte für Chemie* **2012**, *143*, 1031–1038.

(162) Oveisi, A. R.; Zhang, K.; Khorramabadi-Zad, A.; Farha, O. K.; Hupp, J. T. Stable and Catalytically Active Iron Porphyrin-Based Porous Organic Polymer: Activity as Both a

Redox and Lewis Acid Catalyst. *Sci. Rep.* **2015**, *5*, 10621.

(163) Jagadeesh, R. V; Stemmler, T.; Surkus, A. E.; Bauer, M.; Pohl, M. M.; Radnik, J.; Junge, K.; Junge, H.; Bruckner, A.; Beller, M. Cobalt-Based Nanocatalysts for Green Oxidation and Hydrogenation Processes. *Nat. Protoc.* **2015**, *10*, 916–926.

(164) Jagadeesh, R. V; Junge, H.; Beller, M. Green Synthesis of Nitriles Using Non-Noble Metal Oxides-Based Nanocatalysts. *Nat. Commun.* **2014**, *5*, 4123.

(165) Zhang, L.; Wang, A.; Wang, W.; Huang, Y.; Liu, X.; Miao, S.; Liu, J.; Zhang, T. Co-N-C Catalyst for C-C Coupling Reactions: On the Catalytic Performance and Active Sites. *ACS Catal.* **2015**, *5*, 6563–6572.

(166) Slot, T. K.; Eisenberg, D.; van Noordenne, D.; Jungbacker, P.; Rothenberg, G. Cooperative Catalysis for Selective Alcohol Oxidation with Molecular Oxygen. *Chem. - A Eur. J.* **2016**, *22*, 12307–12311.

(167) Liu, W.; Zhang, L.; Liu, X. X.; Liu, X. X.; Yang, X.; Miao, S.; Wang, W.; Wang, A.; Zhang, T. Discriminating Catalytically Active FeNx Species of Atomically Dispersed Fe-N-C Catalyst for Selective Oxidation of the C-H Bond. *J. Am. Chem. Soc.* **2017**, *139*, 10790–10798.

(168) Li, M.; Wu, S.; Yang, X.; Hu, J.; Peng, L.; Bai, L.; Huo, Q.; Guan, J. Highly Efficient Single Atom Cobalt Catalyst for Selective Oxidation of Alcohols. *Appl. Catal. A Gen.* **2017**, *543*, 61–66.

(169) Nakatsuka, K.; Yoshii, T.; Kuwahara, Y.; Mori, K.; Yamashita, H. Controlled Synthesis of Carbon-Supported Co Catalysts from Single-Sites to Nanoparticles: Characterization of the Structural Transformation and Investigation of Their Oxidation Catalysis. *Phys. Chem. Chem. Phys.* **2017**, *19*, 4967–4974.

(170) Cheng, T.; Yu, H.; Peng, F.; Wang, H.; Zhang, B.; Su, D. Identifying Active Sites of CoNC/CNT from Pyrolysis of Molecularly Defined Complexes for Oxidative

Esterification and Hydrogenation Reactions. *Catal. Sci. Technol.* **2016**, *6*, 1007–1015.

(171) Serov, A.; Robson, M. H.; Halevi, B.; Artyushkova, K.; Atanassov, P. Highly Active and Durable Templated Non-PGM Cathod Catalysts Derived from Iron and Amino. *Electrochem. commun.* **2012**, *22*, 53–56.

(172) Kattel, S.; Atanassov, P.; Kiefer, B. Stability, Electronic and Magnetic Properties of in-Plane Defects in Graphene: A First-Principles Study. *J. Phys. Chem. C* **2012**, *116*, 8161–8166.

(173) Kattel, S.; Atanassov, P.; Kiefer, B. Catalytic Activity of Co-N(x)/C Electrocatalysts for Oxygen Reduction Reaction: A Density Functional Theory Study. *Phys. Chem. Chem. Phys.* **2013**, *15*, 148–153.

(174) Kamiya, K.; Koshikawa, H.; Kiuchi, H.; Harada, Y.; Oshima, M.; Hashimoto, K.; Nakanishi, S. Iron-Nitrogen Coordination in Modified Graphene Catalyzes a Four-Electron-Transfer Oxygen Reduction Reaction. *ChemElectroChem* **2014**, *1*, 877–884.

(175) Liang, W.; Chen, J.; Liu, Y.; Chen, S. Density-Functional-Theory Calculation Analysis of Active Sites for Four-Electron Reduction of O2 on Fe/N-Doped Graphene. *ACS Catal.* **2014**, *4*, 4170–4177.

(176) Serov, A.; Artyushkova, K.; Atanassov, P. Fe-N-C Oxygen Reduction Fuel Cell Catalyst Derived from Carbendazim: Synthesis, Structure, and Reactivity. *Adv. Energy Mater.* **2014**, *4*, 1–7.

(177) Zhou, J.; Duchesne, P. N.; Hu, Y.; Wang, J.; Zhang, P.; Li, Y.; Regier, T.; Dai, H. Fe-N Bonding in a Carbon Nanotube-Graphene Complex for Oxygen Reduction: An XAS Study. *Phys. Chem. Chem. Phys.* **2014**, *16*, 15787–15791.

(178) Artyushkova, K.; Serov, A.; Rojas-Carbonell, S.; Atanassov, P. Chemistry of Multitudinous Active Sites for Oxygen Reduction Reaction in Transition

Metal-Nitrogen-Carbon Electrocatalysts. *J. Phys. Chem. C* **2015**, *119*, 25917–25928.

(179) Jia, Q.; Ramaswamy, N.; Hafiz, H.; Tylus, U.; Strickland, K.; Wu, G.; Barbiellini, B.; Bansil, A.; Holby, E. F.; Zelenay, P.; *et al.* Experimental Observation of Redox-Induced Fe-N Switching Behavior as a Determinant Role for Oxygen Reduction Activity. *ACS Nano* **2015**, *9*, 12496–12505.

(180) Kabir, S.; Artyushkova, K.; Kiefer, B.; Atanassov, P. Computational and Experimental Evidence for a New TM–N 3 /C Moiety Family in Non-PGM Electrocatalysts. *Phys. Chem. Chem. Phys.* **2015**, *17*, 17785–17789.

(181) Cui, X.; Ren, P.; Deng, D.; Deng, J.; Bao, X. Single Layer Graphene Encapsulating Non-Precious Metals as High-Performance Electrocatalysts for Water Oxidation. *Energy Environ. Sci.* **2016**, *9*, 123–129.

(182) Jia, Q.; Ramaswamy, N.; Tylus, U.; Strickland, K.; Li, J.; Serov, A.; Artyushkova, K.; Atanassov, P.; Anibal, J.; Gumeci, C.; *et al.* Spectroscopic Insights into the Nature of Active Sites in Iron–nitrogen–carbon Electrocatalysts for Oxygen Reduction in Acid. *Nano Energy* **2016**, *29*, 65–82.

(183) Liu, W.; Zhang, L.; Yan, W.; Liu, X.; Yang, X.; Miao, S.; Wang, W.; Wang, A.; Zhang, T. Single-Atom Dispersed Co–N–C Catalyst: Structure Identification and Performance for Hydrogenative Coupling of Nitroarenes. *Chem. Sci.* **2016**, *7*, 5758–5764.

(184) Artyushkova, K.; Matanovic, I.; Halevi, B.; Atanassov, P. Oxygen Binding to Active Sites of Fe-N-C ORR Electrocatalysts Observed by Ambient-Pressure XPS. *J. Phys. Chem. C* **2017**, *121*, 2836–2843.

(185) Chen, X.; Yu, L.; Wang, S.; Deng, D.; Bao, X. Highly Active and Stable Single Iron Site Confined in Graphene Nanosheets for Oxygen Reduction Reaction. *Nano Energy* **2017**, *32*, 353–358.

(186) Chung, H. T.; Cullen, D. A.; Higgins, D.; Sneed, B. T.; Holby, E. F.; More, K. L.; Zelenay, P. Direct Atomic-Level Insight into the Active Sites of a High-Performance PGM-Free ORR Catalyst. *Science.* **2017**, *357*, 479–484.

(187) Guo, S.; Yuan, P.; Zhang, J.; Jin, P.; Sun, H.; Lei, K.; Pang, X.; Xu, Q.; Cheng, F. Atomic-Scaled Cobalt Encapsulated in P,N-Doped Carbon Sheaths over Carbon Nanotubes for Enhanced Oxygen Reduction Electrocatalysis under Acidic and Alkaline Media. *Chem. Commun.* **2017**, *53*, 9862–9865.

(188) Shen, H.; Gracia-Espino, E.; Ma, J.; Tang, H.; Mamat, X.; Wagberg, T.; Hu, G.; Guo, S. Atomically FeN2 Moieties Dispersed on Mesoporous Carbon: A New Atomic Catalyst for Efficient Oxygen Reduction Catalysis. *Nano Energy* **2017**, *35*, 9–16.

(189) Artyushkova, K.; Kiefer, B.; Halevi, B.; Knop-Gericke, A.; Schlogl, R.; Atanassov, P. Density Functional Theory Calculations of XPS Binding Energy Shift for Nitrogen-Containing Graphene-like Structures. *Chem. Commun.* **2013**, *49*, 2539.

(190) Liu, W.; Zhang, L.; Liu, X.; Liu, X.; Yang, X.; Miao, S.; Wang, W.; Wang, A.; Zhang, T. Discriminating Catalytically Active FeNx Species of Atomically Dispersed Fe-N-C Catalyst for Selective Oxidation of the C-H Bond. *J. Am. Chem. Soc.* **2017**, *139*, 10790–10798.

Chapter 2. Deactivation of supported Pt catalysts during alcohol oxidation

A portion of this thesis was previously published as Xie, J. et al. Deactivation of Supported Pt Catalysts during Alcohol Oxidation Elucidated by Spectroscopic and Kinetic Analyses. ACS Catal. 7, 6745–6756 (2017).

2.1. Introduction

For catalytic alcohol oxidation reaction, Pt has demonstrated promising activity under environmentally-friendly conditions (O_2 as oxidant, aqueous phase, mild temperature (<373 K), without base addition).[1,2] However, the deactivation of Pt catalysts can be a significant barrier to the large-scale application of this process.[3–21] Although sintering,[6,11] leaching,[7,10,11] and over-oxidation[3,5,10,14,16] have been commonly proposed to account for the deactivation behavior, our recently published paper has excluded these as factors for the severe loss of Pt activity during oxidation reaction of alcohols under mild reaction conditions.[20] Indeed, results from thermogravimetric analysis and regeneration studies indicate some strongly adsorbed species on the active Pt sites,[20] which has also been reported by others based on electrochemical characterization, spectroscopy, and kinetics studies.[5,8–13,15,17,18,22] The in situ attenuated-total-reflectance infrared spectroscopy further excluded CO as the poisoning species by demonstrating that CO can be readily removed by O_2.[20] To the best of our knowledge, however, the poisoning species have not been identified yet and the deactivation pathway is still not clear.

To investigate poisoning species generated during reaction, an in situ characterization method is preferential because of the possible change of poisoning species when exposed to different conditions. Discovered in 1977,[23,24] surface-enhanced Raman spectroscopy (SERS) has been widely used to monitor the surface adsorbates under reaction conditions.[25–34] Because of the weak Raman signal of water, SERS is well-suited for aqueous-phase catalysis study.[29,35] Roughened Pt has demonstrated SERS activity,[25,36–47] but with much weaker enhancements than typically observed for Au and Ag.[29] One promising approach to enhance the Raman signals on Pt is the "borrowed SERS" technique, wherein the SERS-active Au or Ag core is fabricated with a thin layer of Pt.[33,34,48–62] The Pt-coated Au or Ag exhibited both catalytic activity from Pt layer and an enhancement effect on Raman signals from Au or Ag cores. To reach enough sensitivity to detect trace amount of adsorbates, a core with particularly high Raman-enhanced factors inside Pt layer is required. Efforts have been made to engineer the shape of Au or Ag, such as rods, rings, gaps, bowties and shells, which increased the Raman-enhanced factor to up to nine orders of magnitude.[63–67] For example, Heck and co-workers successfully applied Au nanoshells with or without a Pd layer as SERS substrates to investigate catalytic oxidation of glycerol and hydrodechlorination of 1,1-dichloroethene in aqueous phase.[35,68]

An alternative method for identifying organic molecular species with high specificity is ^{13}C nuclear magnetic resonance spectroscopy (NMR). While the adsorption of ^{13}C-enriched molecules, such as CO and ethylene, on various transition-metal catalysts have been studied by ^{13}C magic-angle spinning NMR in some detail,[69–72] relatively few examples of NMR studies of the poisoning of transition-metal catalysts have been published.[73] This may have been due to concerns that the metal-bound species would be too small in concentration to give detectable signals and furthermore broadened or shifted too strongly[70–72,69] for useful spectroscopic analysis. A recent study of ^{13}C-enriched methionine on Pd[73] has shown that the shifts and broadening are moderate, in fact very suitable to identify the bound species, if the metal and the carbon observed are separated by at least one atom.[74]

In this study, Pt-coated Au (Au@Pt) nanoshells were synthesized and applied in the in situ SERS, which provides information of adsorbed chemicals on Pt surface with a flow of O_2-saturated HDO solution. Additionally, deactivated Pt catalyst after oxidation reaction of

^{13}C-labled diol was recovered and characterized by solid-state NMR. Detailed analysis of reaction products in liquid and gas phase under different conditions were performed to investigate the influence of proposed poisoning species deduced from SERS and NMR results as well as to investigate its formation pathway.

2.2. Experimental methods

2.2.1. Preparation and characterization of supported Pt nanoparticles

A carbon-supported 3 wt% Pt catalyst (Pt/C) was synthesized using a $NaBH_4$ reduction method.[75,76] Activated carbon (2 g, Norit, Ultra SX) was dispersed ultrasonically in 150 cm^3 of 1 mM NaOH solution (Sigma-Aldrich, >98%) for 1 h. Then 0.30 mmol of H_2PtCl_6 (Sigma-Aldrich, 99.995%) were dissolved in 25 cm^3 of 1 mM NaOH solution and the mixture was added to the carbon slurry with vigorous stirring. The Pt was subsequently reduced by the rapid addition of 10 cm^3 of a freshly prepared 0.3 M $NaBH_4$ solution (Sigma-Aldrich, 98%). The slurry was left under vigorous stirring for 2 h. Finally, the slurry was filtered, washed thoroughly with distilled, deionized water (D.I. water) and dried in air at room temperature. For the solid-state NMR study, 1 wt% Pt/silica was synthesized by incipient wetness impregnation using aqueous solution of H_2PtCl_6 and Davisil 636 silica support (Sigma-Aldrich). After impregnation, the catalyst was dried overnight in an oven at 393 K and finally reduced in flowing dihydrogen (GTS-Welco, 99.999%) at 923 K for 3 h after heating with a 1 K min^{-1} ramp rate.

The fraction of available Pt on the surface (dispersion) of Pt/C and Pt/silica was estimated by H_2 chemisorption using a Micromeritics ASAP 2020 automated adsorption analyzer. The catalysts were heated to 473 K at 4 K min^{-1} under flowing H_2 and reduced for 2 h. The samples were then evacuated for 2 h at 473 K before being cooled to 308 K for analysis in the pressure range of 1.33 – 59.9 kPa. The amount of exposed Pt was evaluated by the total amount of

H_2 adsorbed, extrapolated to zero pressure, assuming a stoichiometry (H/Pt_{surf}) equal to unity.

The X-ray diffraction (XRD) patterns of Pt/C were recorded using a PANalytical X'Pert Pro MPD (Multi-Purpose Diffractometer) instrument with Cu Kα radiation (45 kV, 40 mA) and scanning of 2θ from 20° to 80° with a step size of 0.0025° at a rate of 0.125° min^{-1}.

Scanning transmission electron microscopy (STEM) of Pt/C was performed on an FEI Titan 80-300 operating at 300 kV. To prepare a sample, ~1 mg of sample was suspended in 10 cm^3 of ethanol by agitating the mixture for 30 min in a sonication bath. Subsequently, a copper grid with a holey carbon film (Ted Pella, 400 mesh) was dipped into the suspension to capture the particles.

2.2.2. Preparation and characterization of Au and Au@Pt nanoshells

The Au nanoshells were prepared by a slightly modified approach based on the method developed by Halas and co-workers.[67,68] Briefly, 1 cm^3 of aminated silica nanospheres (Nanocomposix, 120 nm diameter, 10 mg cm^{-3}) was diluted in 200 cm^3 ethanol (Sigma-Aldrich, 99.8%). Then, 7.5 cm^3 of diluted aminated silica nanospheres were added to 150 cm^3 of a solution of 1-2 nm Au nanoparticles, which were previously prepared via the Duff method [77] and aged at 277 K for at least one week. The silica–Au seeds were aged overnight, centrifuged, and re-dispersed in D.I. water three times, leaving a final seed volume of 7.5 cm^3. The solution of seeds (volume ranging from zero to 3.92 cm^3) was added to 21 cm^3 of 293 μM K-gold solution (0.050g K_2CO_3 (Sigma-Aldrich, >99%) and 0.062 g 30 wt% $HAuCl_4$ (Sigma-Aldrich, 99.99%) in 200 cm^3 D.I. water, aged overnight) to find the optimum Au nanoshell thickness. Under vigorous shaking, 0.14 cm^3 of formaldehyde solution (Sigma-Aldrich, 36.5-38% in water) was added dropwise to the mixture of silica–Au seeds and K-gold solution to form the Au nanoshells. After 15 min, the sample was centrifuged and re-dispersed in D.I. water three times to give a final volume of 2 cm^3.

The Pt layer was coated on the Au nanoshells by reducing an aqueous solution of H_2PtCl_6 with ascorbic acid (Sigma-Aldrich, 99%).[34] Briefly, 1 cm^3 solution of previously-prepared Au nanoshells and 0.0176 cm^3 of 1 mM H_2PtCl_6 solution was added to 9 cm^3 of D.I. water and heated to 353 K. Subsequently, 1 cm^3 of 1 mM ascorbic acid was added dropwise while stirring and kept for 20 min. After the sample was cooled to room temperature, it was centrifuged and re-dispersed in D.I. water three times to give a final volume of 1 cm^3.

The Au or Au@Pt nanoshells were immobilized on a silicon wafer (Ted Pella, 5 mm × 5 mm) for SERS analysis using a similar method as reported by Lu et al. [48] The silicon wafers were cleaned for 20 min in a freshly prepared Piranha solution (3:1 H_2SO_4:30% H_2O_2) and then rinsed three times with D.I. water and ethanol, respectively. The cleaned silicon wafers were submerged overnight in a dilute solution of 0.3 cm^3 3-aminopropyltrimethoxysilane (APTMS) (Sigma-Aldrich, 97%) in 3 cm^3 methanol. The APTMS-coated silicon wafers were subsequently rinsed three times with ethanol and D.I. water. Finally, 30 μL of solution of Au or Au@Pt nanoshells were pipetted onto the APTMS-coated wafers for 3 h to immobilize the nanoshells.

The ultraviolet–visible spectra (UV-vis, 450 to 850 nm) of the Au nanoshell solutions with different thicknesses were obtained using a UV-vis spectrophotometer (Varian CARY 3E) with D.I. water as reference.

Transmission electron microscopy (TEM), scanning transmission electron microscopy (STEM) and energy dispersive spectroscopy (EDS) of Au or Au@Pt nanoshells were performed on an FEI Titan 80-300 operating at 300 kV that is equipped with a Gatan 794 Multi-scan Camera (EFTEM) and an energy dispersive spectrometer for elemental X-ray analysis. To prepare a sample, a copper grid with a holey carbon film (Ted Pella, 400 mesh) was dipped into the solution of Au or Au@Pt nanoshells and dried.

Scanning electron microscopy (SEM) of SERS analysis chips immobilized with Au or

Au@Pt nanoshells was performed on an FEI Quanta 650 FEG-SEM operated at 15 kV and a working distance of 10 mm under the secondary electron imaging mode. The sample was prepared by adhering the prepared SERS analysis chips to a carbon conductive tape on a sample stage.

2.2.3. Oxidation of 1,6-hexanediol

Semi-batch alcohol oxidation reactions were performed in a 50 cm^3 Parr Instrument Company 4592 batch reactor with a 30 cm^3 glass liner. The Pt/C, Pt/silica, Au or Au@Pt nanoshells and 12 cm^3 of D.I. water were added to the glass liner. The glass liner was inserted into the reactor, sealed, purged with 0.3 MPa H_2 (GTS-Welco, 99.999%), heated to 343 K and held for 20 min. The reactor was then flushed with He (GTS-Welco, 99.999%). The reaction was initiated by adding calculated amounts of 1,4-butanediol (Sigma-Aldrich, 99%), 1,6-hexanediol (Sigma-Aldrich, 99%), 5-hydroxypentanal (Ark Pharm, 97%), 1,5-pentanedial (Sigma-Aldrich, Grade I, 25% in water), 6-hydroxyhexanoic acid (Alfa-Aesar, 95%), adipic acid (Sigma-Aldrich, 99.5%), 3-hydroxybutanal (Sigma-Aldrich), mesityl oxide (Sigma-Aldrich, 98%), polyvinyl alcohol (Sigma-Aldrich, M_w 89,000-98,000, 99+% hydrolyzed), 4-penten-1-ol (Sigma-Aldrich, 99%), 4-pentenoic acid (Sigma-Aldrich, 97%), 3-pentenoic acid (Sigma-Aldrich, 95%), 2-pentenoic acid (Sigma-Aldrich, 98%) and/or allyl alcohol (Sigma-Aldrich, 99%) followed by pressurizing the reactor with 1 MPa of O_2 (GTS-Welco, 99.993%). Liquid samples were periodically removed and the catalyst was filtered using a 0.2 µm PTFE filter before product analysis with a Waters e2695 high performance liquid chromatograph (HPLC). The HPLC was equipped with refractive index detector. Product separation in the HPLC was accomplished on an Aminex HPX-87H column (Bio-Rad) operating at 318 K with an aqueous 5 mM H_2SO_4 solution as mobile phase flowing at 5 cm^3 min^{-1}. The retention times and calibration curves were determined by injecting known concentrations of standards. Carbon balances were always greater than 90%. Under reaction conditions, the oxidation reaction rate was not limited by the mass transfer of O_2 or alcohol substrate, which was examined in our previously published work.[78] The initial turnover frequency (TOF) [mol alcohol converted (mol Pt_{surf})$^{-1}$ s^{-1}] was calculated from the initial conversion of the alcohol, usually within the first 30 min of the reaction. The fraction of Pt_{surf} to total Pt atoms was determined from H_2 chemisorption. Headspace gas composition was analyzed using an HP 5890 Series II gas chromatograph equipped with a thermal conductivity detector (TCD) and a ShinCarbon 80/100 packed column.

2.2.4. SERS analysis of adsorbates

A prepared SERS chip was adhered to the bottom of a sealed analysis chamber with inlet and outlet ports (Warner Instruments, RC-43, 213 μL volume without analysis chips) that was mounted on a heater connected to a temperature controller (Omega). Prior to the acquisition of spectra, O_2-saturated (0.1 MPa) and H_2-saturated (0.1 MPa) D.I. water flowing at a rate of 0.1 cm^3 min^{-1} was passed over the sample for 30 min at 343 K, respectively.

To determine the SERS effectiveness of the prepared Au and Au@Pt nanoshells, 10μL of 440 μM para-mercaptoaniline in ethanol was added to SERS analysis chips and aged overnight, which has been used previously to determine SERS efficiency.[67,68] The samples were then rinsed with ethanol prior to SERS analysis using a Renishaw inVia micro-Raman spectrometer with a 785 nm excitation laser and a 50× working distance objective. Spectra were obtained using 7.6 mW power and 10 s integration times. For each sample, five spectra were acquired at different spots. The standard deviation between spectra for each sample was less than 5%.

For chemisorption experiments, Raman spectra ranging from 100 to 2500 cm^{-1} were recorded with a 785 nm laser operating at 7.6 mW and using a 10 s integration time. Three spectra were obtained at a single spot to establish a baseline. A He-saturated (0.1 MPa) solution of 0.05 M 1,6-hexanediol, 1,5-pentanedial, adipic acid, 4-penten-1-ol, or 4-pentenoic acid was passed through the SERS chamber at a flow rate of 0.1 cm^3 min^{-1} for 10 min followed by collection of Raman spectra at the same spot where the background was acquired. In a different experiment, water that was saturated with ethylene (0.1 MPa, Sigma-Aldrich, 99.9%) was passed through the chamber (0.1 cm^3 min^{-1} for 10 min) prior to spectral acquisition. Additionally, a Raman spectrum was acquired after flowing an aqueous solution of 0.05 M 1,5-pentanedial saturated with 0.1 MPa O_2 at a flow rate of 0.05 cm^3 min^{-1} for 2 h.

The oxidation reaction of 1,6-hexanediol was also monitored by in situ SERS. Raman spectra ranging from 100 to 2500 cm^{-1} were obtained using 0.76 mW to minimize the influence of localized heating during reaction. As described above, three spectra were obtained at a single spot to establish a baseline. A 10 mM 1,6-hexanediol solution saturated with 0.1 MPa O_2 was passed through the SERS chamber at the flow rate of 0.05 cm^3 min^{-1}. After 500 min, D.I. water was purged through the SERS chamber at the rate of 0.2 cm^3 min^{-1} for 90 min. Raman spectra were collected throughout the process at the same spot where the background was acquired. The samples of the reaction medium after different reaction times were collected and analyzed by HPLC to measure the conversion and product distribution.

2.2.5. NMR spectroscopy of adsorbates

To prepare samples for solid-state NMR spectroscopy, we ran the oxidation reaction of isotope-enriched 1,4-butanediol-$^{13}C_4$ (Toronto Research Chemicals) over the Pt/silica catalyst for 40 h in the Parr reactor as described in Section 2.3. The used catalyst was then recovered, washed thoroughly with D.I. water, dried in air at room temperature for 1 h and packed into a 2.9-mm inner diameter zirconia NMR rotor under Ar atmosphere in a glove box. To provide a Pt-free reference material, the filtered reaction solution containing 1,4-butanediol-$^{13}C_4$ and all of its products and byproducts after 40 h of reaction was utilized to treat Pt-free silica support for another 2 h at 343 K under 1 MPa O_2. The treated silica sample was then recovered, washed with D.I. water, dried in air and packed into a rotor for solid-state NMR analysis. NMR rotors, caps, and the packing tool used were brand new and were not opened in the NMR laboratory to avoid any potential contamination with ^{13}C-enriched compounds previously used in this space.

Solid-state NMR experiments were performed on a Bruker (Billerica, MA) DSX-400 spectrometer at a resonance frequency of 100 MHz for ^{13}C with high-power ^{1}H decoupling using a double-resonance magic-angle spinning (MAS) probe for 4-mm rotors. Typical ^{1}H and ^{13}C 90° pulse lengths were 4.2 μs. The multiCP pulse sequence[79] under 14 kHz MAS was used to obtain signals from both mobile and bound molecules at ambient temperature. Considering the low concentration of carbon-containing molecules in the sample, parameters were set to maximize the signal-to-noise ratio. A 1.25-s recycle delay and three cross polarization periods (2 × 1.1-ms and 0.55-ms) with two 0.5-s ^{1}H recovery periods and a measuring time of 2 days. Corresponding spectra of nonprotonated C and mobile segments were obtained after 68 μs recoupled ^{1}H-^{13}C dipolar dephasing before detection.[80] Direct polarization (DP) spectra with 0.5-s and 2-s recycle delays were measured under 14 kHz MAS at 300 K, 310 K and 320 K to document changes in the amount of weakly adsorbed ethylene.

2.3. Results

2.3.1. Characterization of supported Pt nanoparticles

The carbon supported Pt catalyst (Pt/C) was characterized by STEM, H_2-chemisorption and XRD for metal particle size analysis. As shown in Figures 2.1a and 2.1b, the dark-field STEM showed a relatively narrow size distribution of the supported Pt nanoparticles, with an average size of 3.4±1.0 nm according to a Gaussian fit of the size distribution of more than 300 particles (Table 2.1). The surface-weighted and volume-weighted average diameters are 4.0 nm and 4.5 nm, respectively, as derived from a statistical analysis of the STEM images of Pt/C.

Chemisorption of H_2 measured the ratio of adsorbed hydrogen atoms to total Pt atoms as 0.21, which indicates a surface-weighted average diameter as 4.7 nm.[81] In addition, a line broadening analysis of the X-ray diffraction peaks associated with Pt (111) and Pt (200) (Figure 2.1c) gives an volume-weighted average diameter of 5.2 nm (Table 2.1). The size of Pt nanoparticles on Pt/C determined by H_2 chemisorption, TEM and XRD is quite consistent. The dispersion of Pt/silica was also characterized by H_2 chemisorption, which had an H/Pt ratio of 0.40, indicating the Pt particles on Pt/silica are about half the size of those on Pt/C.

Table 2. 1 Platinum metal particles sizes on Pt/C evaluated from electron microscopy, H_2-chemisorption and X-ray diffraction

Avg. Diameter (nm)	Surface-weighted Avg. Diameter (nm)		Volume-weighted Avg. Diameter (nm)	
TEM[a]	TEM[b]	H_2 chemisorption[c]	TEM[d]	XRD[e]
3.4±1.0	4.0	4.7	4.5	5.2

a: Obtained from a Gaussian fit to the size distribution.

b: Obtained from $\Sigma d^3/\Sigma d^2$.

c: Estimated from the inverse of the dispersion of Pt, which was determined from H_2-chemisorption, assuming a nominal loading of Pt and a H:Pt ratio of 1:1. [124]

d: Obtained from $\Sigma d^4/\Sigma d^3$.

e: Estimated from the width of the Pt (111) X-ray diffraction peak using the Scherrer equation.

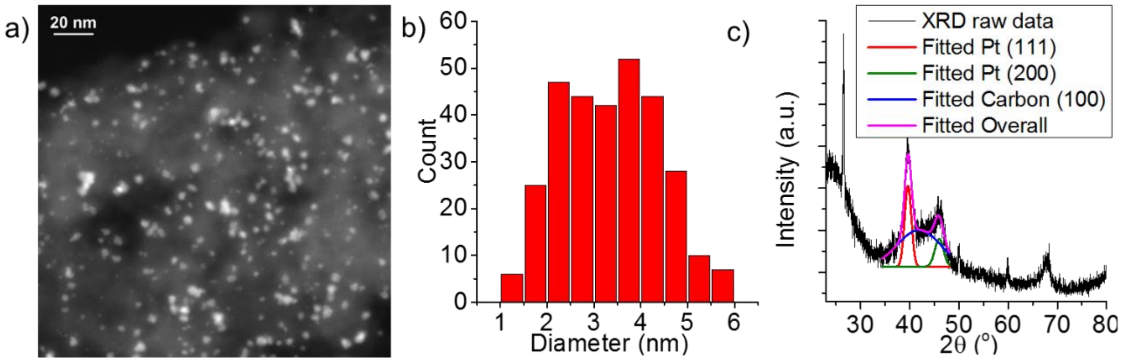

Figure 2. 1. a) STEM image, b) particle size from STEM and c) XRD and fit curves from as-prepared Pt/C catalyst.

2.3.2. Competitive adsorption of oxidation products and generation of poisoning byproducts

As shown in Figure 2.2, carbon- or silica-supported Pt catalysts efficiently catalyzed 1,6-hexanediol oxidation initially but gradually lost activity during the reaction. During the oxidation of α,ω-diols, ω-hydroxy aldehydes, ω-hydroxy acids, α,ω-dialdehydes, ω-oxo acids and α,ω-diacids were produced. To investigate the influence of oxidation products on the reaction rate, the initial rate of 1,6-hexanediol oxidation over Pt/C in the presence of different concentrations of aldehydes or acids was measured. As shown in Figure 2.3, the initial TOF of 1,6-hexanediol oxidation decreased with increasing concentration of added aldehydes or acids in the range of 0 to 0.04 M, which is likely related to the competitive adsorption of additives. The influence of competitive adsorption can be modeled simply as:

$$\mathrm{TOF} = \frac{\mathrm{TOF_0}}{1+\mathrm{K}\times[\mathrm{Additive}]} \qquad (1)$$

where TOF is the initial 1,6-hexanediol oxidation rate in the presence of aldehydes or acids, $\mathrm{TOF_0}$ is the initial 1,6-hexanediol oxidation rate without any additive, K represents an equilibrium adsorption constant and [Additive] is the concentration of additive. As shown in Figure 2.3, the experimental results could be well fitted by the competitive adsorption model. The equilibrium adsorption constants (K) of the different additives are fairly similar, varying from 27 M^{-1} (for ω-hydroxy aldehyde) to 82 M^{-1} (for ω-hydroxy acid), as summarized in Table 2.2.

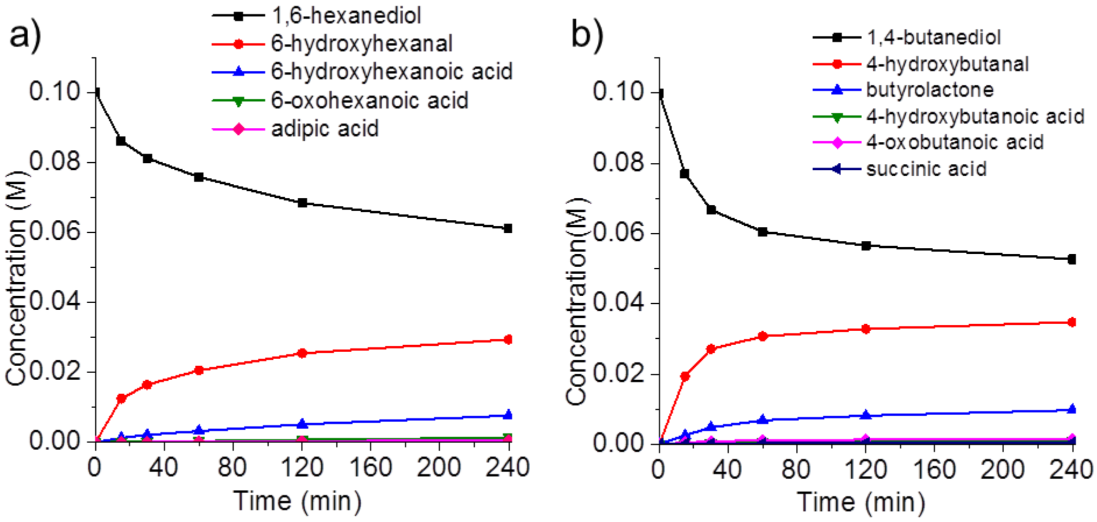

Figure 2. 2. Reaction profile of a) 1,6-hexanediol oxidation over Pt/C and b) 1,4-butanediol oxidation over Pt/silica. Reaction conditions: 343 K, 1 MPa O_2, 12 cm^{-3} aqueous solution of 0.1 M 1,6-hexanediol or 1,4-butanediol, Pt:substrate = 1:1000.

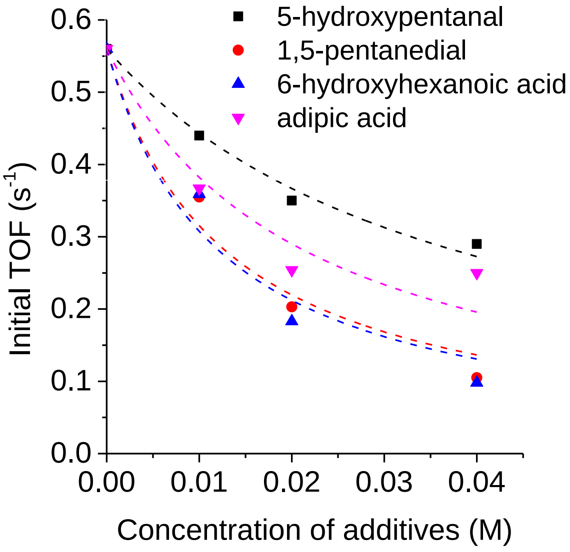

Figure 2. 3. Influence of aldehyde and acid additives on the initial rate of 1,6-hexanediol

oxidation over Pt/C. Individual points represent the measured initial TOFs and the dashed lines are the fitted results from Equation 1. Reaction conditions: 343 K, 1 MPa O_2, 12 cm^3 aqueous solution of 0.1 M 1,6-hexanediol, Pt:1,6-hexanediol = 1:1000.

Table 2. 2 Apparent adsorption coefficients (K) of different additives during oxidation of 1,6-hexanediol[a]

Additive	K (M^{-1})
5-Hydroxypentanal	27 ±2
1,5-Pentanedial	77 ± 11
6-Hydroxyhexanoic acid	82 ± 15
Adipic acid	46 ± 08
4-Penten-1-ol	$(1.0 \pm 0.2)\times10^4$

a: The values of K were fitted from the initial turnover frequencies of 1,6-hexanediol oxidation over Pt/C by $\mathrm{TOF} = \frac{\mathrm{TOF_0}}{1+\mathrm{K}\times[\mathrm{Additive}]}$. The experimental results are presented in Figure 2.3 and Figure 2.17. Reaction conditions: 343 K, 1 MPa O_2, 12 cm^3 aqueous solution of 0.1 M 1,6-hexanediol, Pt: 1,6-hexanediol = 1: 1000.

In addition to the competitive adsorption of oxidation products, byproducts from the side reactions of aldehyde and acid products could be strongly bonded to the Pt surface, leading to the observed loss of activity with time. To differentiate the influence of trace byproducts from that of major products, we measured the initial rate of alcohol oxidation over fresh and used Pt/C. As shown in Table 2.3, the TOF of 1,6-hexanediol oxidation over used Pt/C dropped to 0.035 s^{-1} after 4 h of reaction, compared to the initial TOF of 0.54 s^{-1}. We also measured the TOF of 1,6-hexanediol oxidation over fresh Pt/C in a reaction medium that also contained aldehydes and acids at a similar composition as the reaction medium after 4 h of 1,6-hexanediol oxidation reaction. In this case, only competitive adsorption of aldehydes and acid could influence the activity. The activity was measured to be 0.090 s^{-1}, which was three times greater than the activity over used Pt/C after 4 h of reaction (0.035 s^{-1}). The significant difference between the initial oxidation rate in the presence of aldehydes and acids and the rate after 4 h of oxidation reaction (which produced a similar amount of aldehydes and acids) indicates that poisoning byproducts that are not detected in solution deactivated the catalyst. Treatment of a deactivated Pt/C catalyst in the composite reaction medium with 0.3 MPa H_2 at 343 K for 30 min regenerated the catalyst to give a rate of 0.081 s^{-1}, which was quite similar to that over fresh Pt/C in the presence of aldehydes and acids (0.090 s^{-1}), indicating the poisoning species was removed by H_2. In previously published work, we also reported that the activity of deactivated Pt/C could be regenerated by a H_2 treatment at 473 K.[20]

Table 2. 3 Turnover frequencies of 1,6-hexanediol oxidation over fresh, used and regenerated Pt/C in the mixture of alcohol, aldehyde and acid[a]

Catalyst	TOF (s^{-1})
Fresh Pt/C	0.090
Used Pt/C[b]	0.035
Regenerated Pt/C[c]	0.081

a) Reaction conditions: 343 K, 1 MPa O_2, 12 cm^{-3} aqueous solution of 0.061 M HDO, 0.031 M ω-hydroxy aldehyde and 0.008 M ω-hydroxy acid products, 0.0078 g Pt/C. Turnover frequencies were calculated based on the measured conversion of 1,6-hexanediol within the first 30 min.

b) The Pt/C after 4 h of 1,6-hexanediol oxidation reaction at 343 K under 1 MPa O_2 is denoted as used Pt/C.

c) The reaction mixture after 4 h of 1,6-hexanediol oxidation reaction was treated under 0.3

MPa H_2 at 343 K for 30 min. The catalyst was denoted as regenerated Pt/C.

2.3.3. Au@Pt nanoshells for SERS analysis

To investigate the trace amount of poisoning byproduct on Pt, Au@Pt nanoshells were prepared for in situ SERS analysis. The size of our Au nanoshells was first optimized by varying the volume of silica–Au seeds while holding constant the amount of Au salt and formaldehyde. As indicated by the black line in Figure 2.4, in the absence of seeds, Au salt was reduced directly by formaldehyde to colloidal Au nanoparticles with a peak at ~550 nm in UV-vis spectrum. By increasing the amount of silica–Au seeds in the solution, a higher fraction of the Au salt was reduced to form nanoshells on the silica. Simultaneously, less Au salt was available to deposit on each seed particle. As shown in Figure 2.5, the diameter of the resulting Au nanoshells decreased from 180 nm to 146 nm when the volume of the seed solution increased from 0.49 cm^3 to 1.47 cm^3. The UV-vis peak positions and the observed colors of the nanoshell solutions varied simultaneously with the change of Au thickness. The optimized seed volume was determined to be 0.98 cm^3, corresponding to a 20 nm thickness of the nanoshells (Figure 2.5b). The absorption peak of the optimized Au nanoshells was observed at 748 nm (Figure 2.4d), which is close to the wavelength of the laser (785 nm) used for Raman spectroscopy.

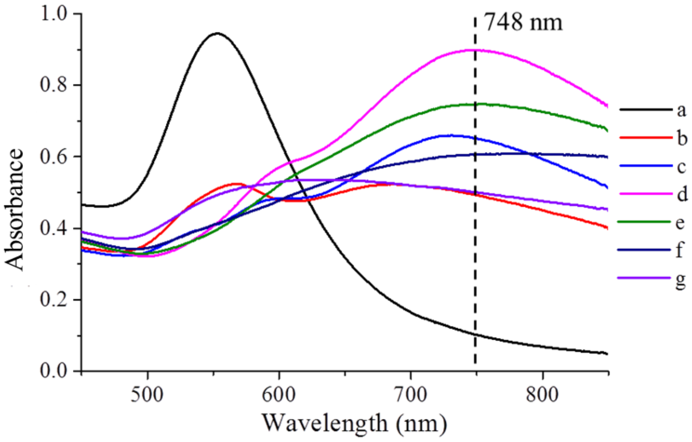

Figure 2. 4. UV-vis spectrum of gold shell growth on 120 nm silica nanospheres. a) 0, b) 0.49, c) 0.70, d) 0.98, e) 1.19, d) 1.47 and f) 1.96 cm^{-3} Au-adsorbed silica seeds were added to 21 cm^{-3} of 293 μM K-gold and the gold salt was reduced by formaldehyde.

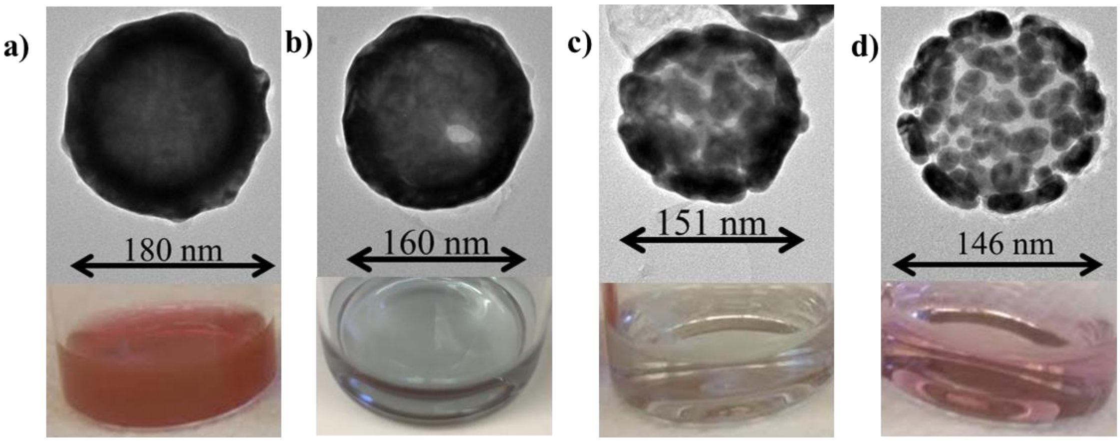

Figure 2. 5. TEM images and visible color of Au nanoshells prepared in 21 cm^{-3} of 293 μM K-gold solution and a) 0.49, b) 0.70, c) 0.98 and d) 1.47 cm^{-3} suspension of silica seeds covered with 2 nm Au nanoparticles.

Approximately, 1-2 Pt layers (nominal loading) were deposited on the optimized Au nanoshells, as demonstrated by the STEM-EDS study in Figure 2.6. In the EDS mapping area indicated by the red square in Figure 2.6a, both Au (Figure 2.6b) and Pt (Figure 2.6c) EDS signals appeared simultaneously. Additionally, as shown in Figure 2.6d, the EDS spectrum of the area labeled by the star in Figure 2.6a revealed the characteristic X-ray emission of Pt-L$_{III}$M$_{V}$ (9.44 KeV) and Au-L$_{III}$M$_{V}$ (9.71 KeV).[82] The Au and Au@Pt nanoshells assembled on the APTMS-modified silicon were also characterized by SEM. As shown in Figure 2.7, both Au and Au@Pt nanoshells were well dispersed on the silicon wafer.

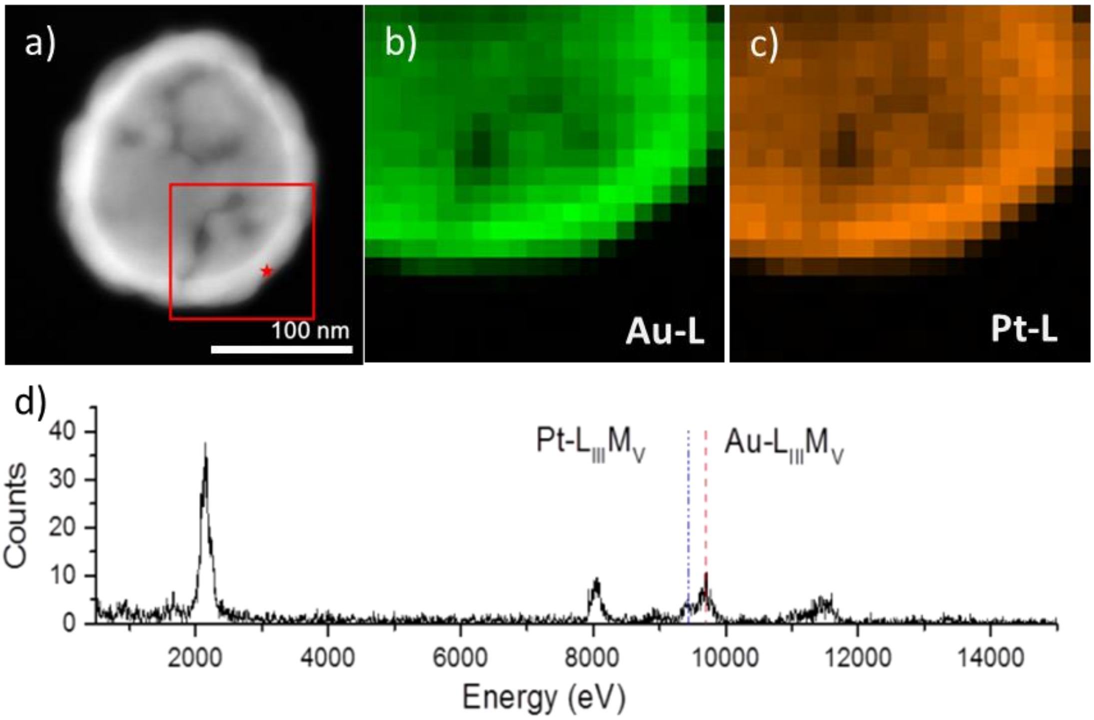

Figure 2. 6. STEM-EDS mapping of Au@Pt nanoshells. a) STEM image of Au@Pt nanoshells, with the EDS-mapping area outlined by the red square; L-edge EDS-mapping of b) Au and c) Pt and d) EDS spectrum taken at the star-labeled position in Figure 2.6a.

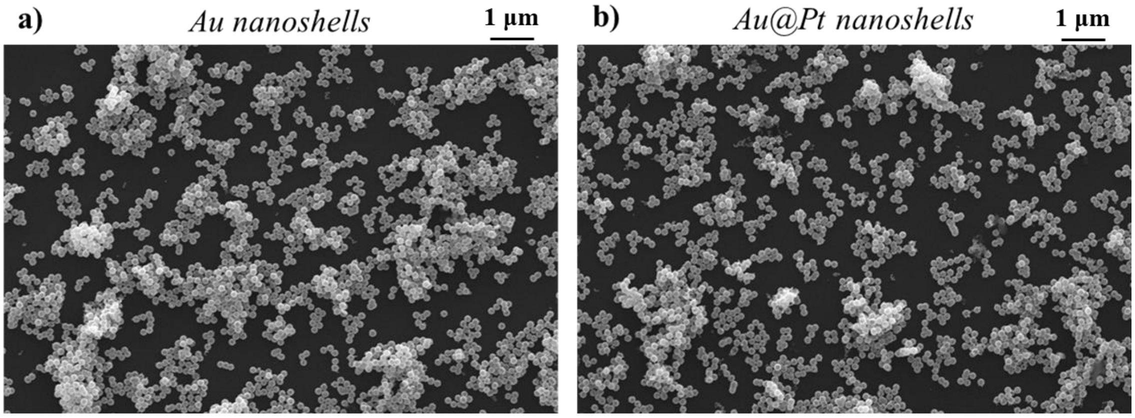

Figure 2. 7. SEM images of a) Au and b) Au@Pt nanoshells.

The SERS effectiveness of Au and Au@Pt nanoshells was characterized by the chemisorption of para-mercaptoaniline. As shown in Figure 2.8, a feature near 400 cm^{-1} was observed over both Au and Au@Pt nanoshells, which was attributed to the coupling between the metal-sulfur bond stretch and a para-mercaptoaniline ring deformation.[83] The intensity of the para-mercaptoaniline SERS spectrum over Au@Pt nanoshells was significantly lower compared to that over Au nanoshells without Pt. The decrease in Raman enhancement after the Pt deposition has been attributed to the damping of the plasmon resonance of Au.[34,68] The intensity of the para-mercaptoaniline SERS spectra taken at different places (more than 5 points) on the SERS chip were within an error of 5% over Au or Au@Pt nanoshells, indicating the nanoshells were well distributed on the silicon wafer.

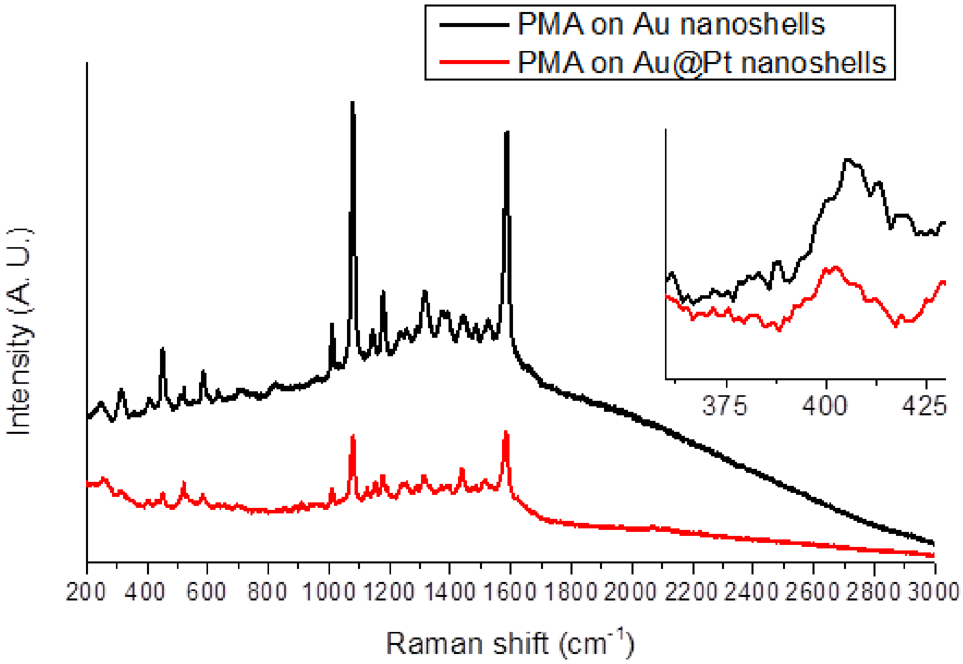

Figure 2. 8. Raman spectra of para-mercaptoaniline (PMA) chemisorbed on Au and Au@Pt nanoshells.

The Pt layers on the Au@Pt nanoshells exhibited similar catalytic performance to Pt/C. The initial TOF of 1,6-hexanediol oxidation over Au@Pt nanoshells was measured to be 0.57 s^{-1} and a similar deactivation pattern as Pt/C was observed, as shown in Figure 2.9a. The Au nanoshells without a Pt layer were also tested in the semi-batch reactor under the same reaction conditions, and negligible conversion (<0.1%) of 1,6-hexanediol was observed, even after 4 h of reaction. Additionally, the catalytic performance of Au@Pt nanoshells was investigated in the SERS analysis chamber under a flow of O_2-saturated (0.1 MPa) 1,6-hexanediol solution. After an induction period of 30 min, a conversion of 2.7% was observed over Au@Pt nanoshells (Figure 2.9b). The conversion over Au@Pt nanoshells then started to decrease with time on stream. After 3 h, the conversion of 1,6-hexanediol decreased to less than 0.5%. Considering the similar rate and deactivation pattern of 1,6-hexanediol oxidation over Au@Pt nanoshells and Pt/C, we conclude that the Au@Pt nanoshells are suitable materials to investigate the deactivation of Pt under reaction conditions by SERS.

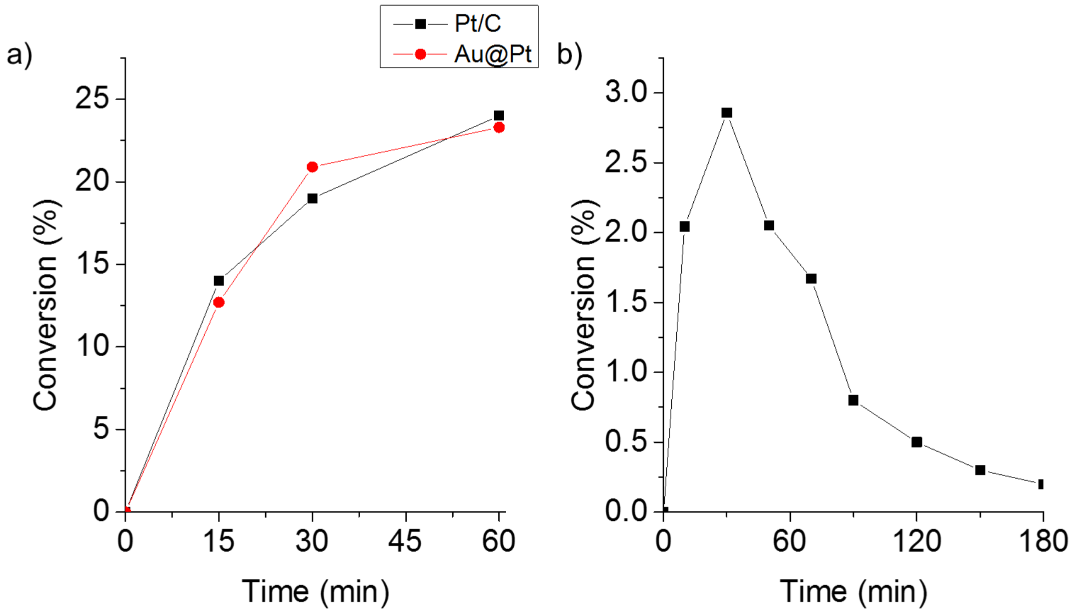

Figure 2. 9. The oxidation reaction of 1,6-hexanediol in the a) semi-batch reactor (Reaction conditions: Pt/C and Au@Pt nanoshells with the surface Pt amount of 2.5×10^{-7} mol, 12 cm^{-3} 0.1 M HDO solution, 1 MPa O_2, 343 K); and b) the SERS analysis chamber under flow (Reaction conditions: 0.88×10^{-8} mol Pt on silicon wafer, flowing 10 mM HDO solution at a flow rate of 0.05 cm^{-3} min^{-1}, 0.1 MPa O_2, 343 K).

2.3.4. SERS of adsorbates during 1,6-hexanediol oxidation

Raman spectra of standard chemicals with hydroxyl, carbonyl, carboxylic and olefinic groups were first acquired as references (Figure 2.10). Raman peaks at ~1430, ~1290 and ~1070 cm^{-1} were observed for alcohols, aldehydes and acids and were attributed to the CH_2 scissoring, CH_2 wagging and C-C stretching modes from the carbon backbone, respectively.[68,84] In addition, the Raman spectra of 4-penten-1-ol, 4-pentenoic acid, adipic acid, butyric acid and 5-hydroxypentanal exhibited features of C=O and C=C at ~1650 and ~1630 cm^{-1}, respectively.[35,68]

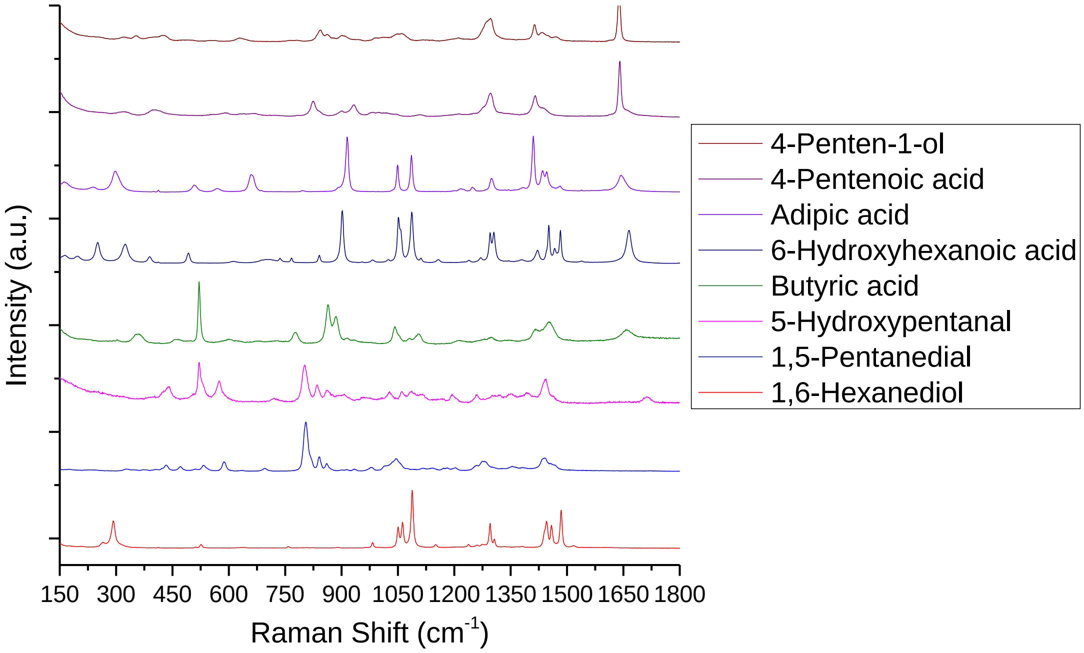

Figure 2. 10. Raman spectra of 4-penten-1-ol, 4-pentenoic acid, adipic acid, 6-hydroxyhexanoic acid, butyric acid, 5-hydroxypentanal, 1,5-pentanediald and 1,6-hexanediol.

The chemisorption of alcohols, aldehydes and acids on the Pt surface was also investigated by SERS. A relatively flat background was first obtained by flowing O_2- then H_2-saturated D.I. water over Au@Pt nanoshells, as shown in Figure 2.11. Subsequently, the He-saturated 1,6-hexanediol, 1,5-pentanedial or adipic acid solution was pumped into the SERS analysis cell for 10 min and Raman spectra were acquired. Raman features at ~1430 and ~1260 cm^{-1} were observed, representing the CH_2 scissoring and CH_2 wagging of the carbon backbones of 1,6-hexanediol, 1,5-pentanedial and adipic acid. However, the Raman peak at ~1650 cm^{-1}, associated with C=O, was not observed when 1,5-pentanedial and adipic acid were introduced to the Pt surface. Instead, Raman features in the range of 1500-1600 cm^{-1} were observed with adsorbed aldehyde and acid (Figures 2.11b and 2.11c) and were attributed to the C-O stretching mode of a carboxylate group.[35] The appearance of the carboxylate feature on aldehyde-treated Au@Pt nanoshells was likely the result of the oligomerization of aldehyde or dehydrogenation of aldehyde hydrate.[22] This feature was also observed when a He-saturated (0.1 MPa) solution of 1,6-hexanediol was in contact with the Pt surface (Figure 2.11a). It is likely that over the Pt surface, the alcohol was first dehydrogenated to form an aldehyde, which could subsequently generate carboxylate species.

We further investigated the adsorbates on the deactivated Pt by in situ SERS. As shown in Figure 2.9b, severe deactivation of Pt@Au nanoshells was observed under a continuous flow of O_2-saturated 1,6-hexanediol solution through the SERS analysis chamber. Simultaneously, the intensity of Raman peaks at ~1530, ~1460, ~1150cm^{-1} gradually increased (Figure 5). The Raman band at 1530 cm^{-1} in the carboxylate species region was attributed to acid products or oligomerization products from aldehydes. The sharp Raman peaks at ~1460 and ~1150 cm^{-1}, which were not observed for chemisorbed alcohols, aldehydes or acids, were likely from species that deactivated the catalysts. After flowing O_2-saturated (0.1 MPa) 1,6-hexanediol for 500 min, pure D.I. water was passed over Au@Pt nanoshells for 90 min to remove any weakly-adsorbed species. The peak in the range of 1500 – 1600 cm^{-1} decreased significantly, indicating the removal of weakly-adsorbed carboxylate species. However, the Raman peak at 1142 cm^{-1} remained strong and a Raman signal at 1470 cm^{-1} was still observed after purging the system with water (Figure 2.12c).

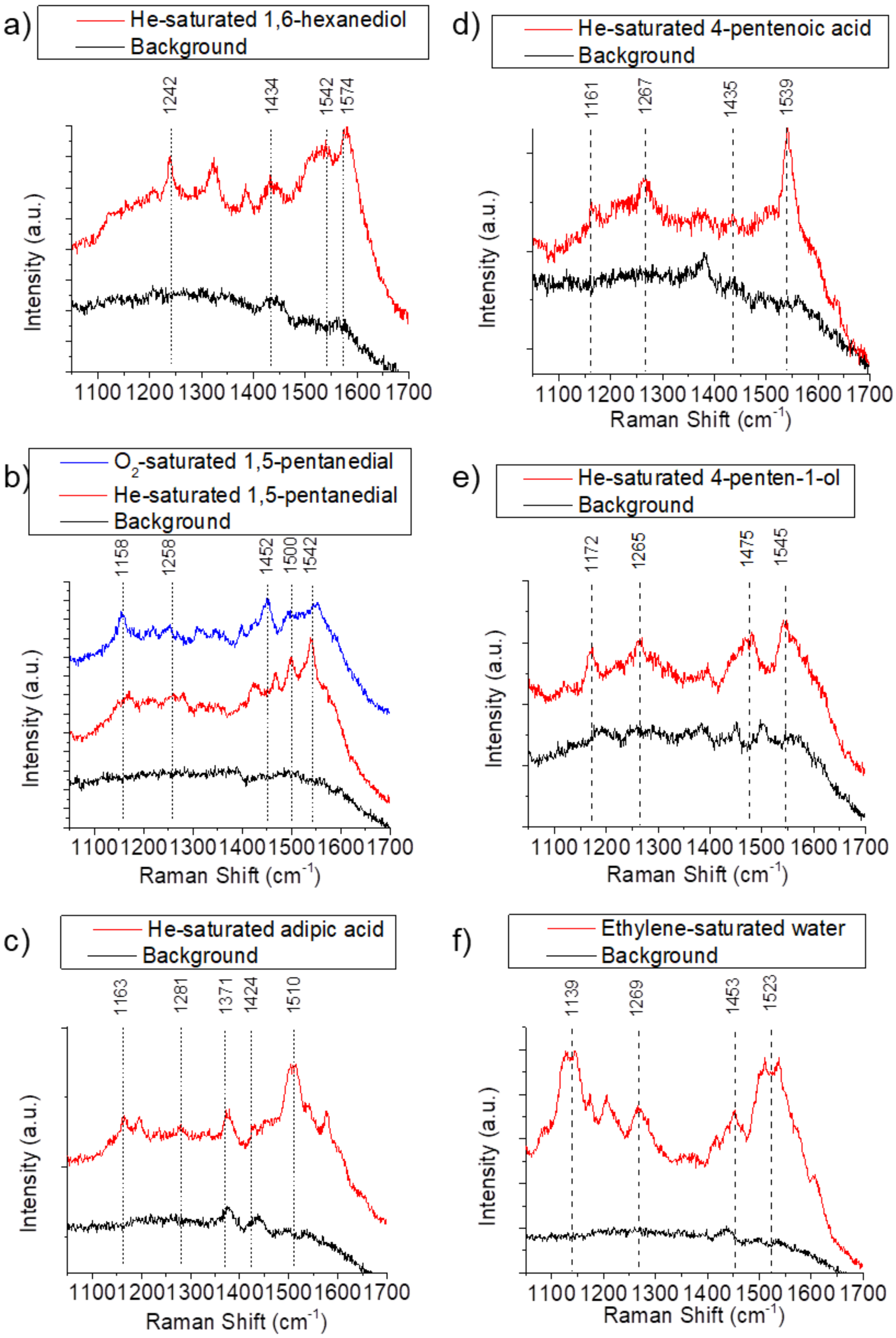

Figure 2. 11. Surface-enhanced Raman spectra of backgrounds and after chemisorption of a) 1,6-hexanediol, b) 1,5-pentanedial, c) adipic acid, d) 4-pentenoic acid, e) 4-penten-1-ol and f) ethylene as well as b) residues after a 2 h treatment of O$_2$-saturated 1,5-pentanedial over

Au@Pt nanoshells. The H_2-saturated and O_2-saturated D.I. water was passed over Au@Pt nanoshells separately to obtain a featureless background. The Raman spectra of chemisorbed compounds were acquired after flowing 0.05 M He-saturated solution or ethylene-saturated water for 10 min. A Raman spectrum was also acquired after flowing 0.05 M O_2-saturated 1,5-pentanedial solution for 2 h.

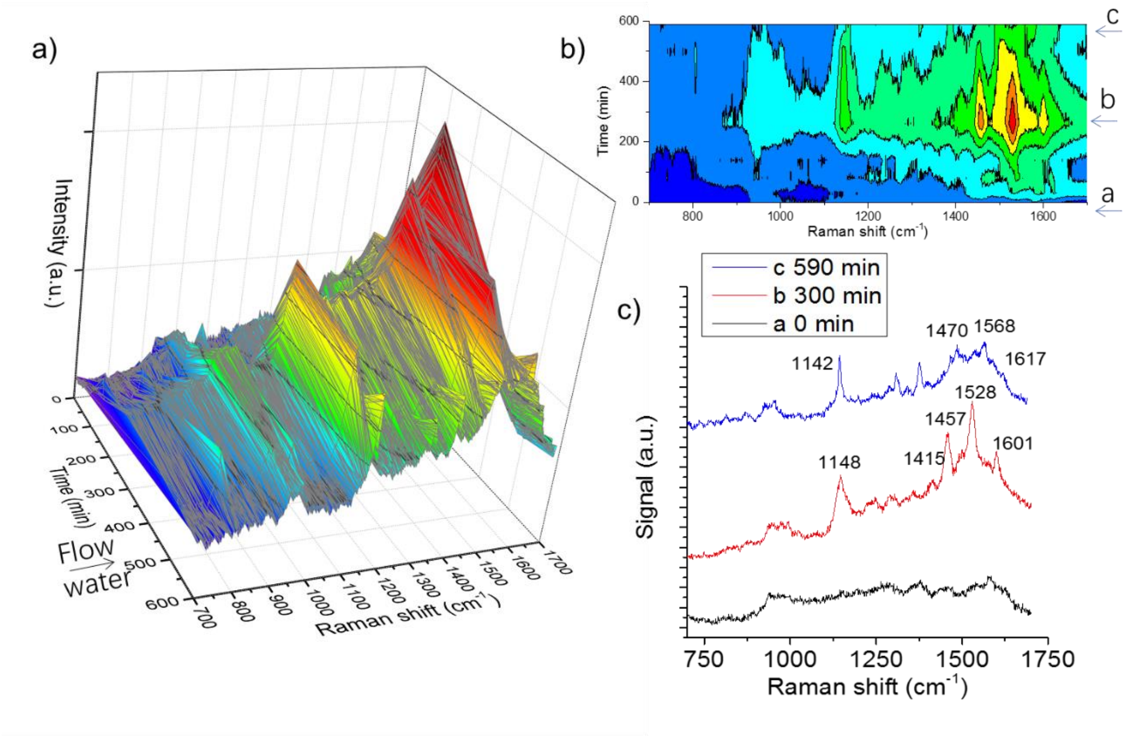

Figure 2. 12. a) Waterfall plot and b) contour plot of time-resolved surface-enhanced Raman spectra gathered during the oxidation of 10 mM 1,6-hexanediol solution over Au@Pt nanoshells at 343 K and c) individual scans at 0, 300, and 590 min after injection of 1,6-hexanediol solution. The 10 mM 1,6-hexanediol solution was saturated with 0.1 MPa O_2 before injection into the Raman cell. After 500 min of reaction, the cell was purged with D.I. water for 90 min.

The Raman features at ~1460 and ~1150 cm^{-1} from strongly-adsorbed species on the deactivated Pt surface are attributed to di-σ-bonded olefinic groups based on reported assignments for chemisorbed ethylene [85] and 1,1-dichloroethene.[68] This assignment is consistent with our reference spectra shown in Figure 2.11, in which adsorbed 4-penten-1-ol, 4-pentenoic acid and ethylene on Pt gave Raman shifts at ~1530, ~1460, ~1260 and ~1150 cm^{-1}. The CH_2 scissoring and CH_2 wagging modes of π-bonded olefins have features at ~1530 and ~1260 cm^{-1}.[68,85] And Raman features at ~1460 and ~1150 cm^{-1} were attributed to the CH_2 scissoring and CH_2 wagging modes of di-σ-bonded olefinic group. Considering the appearance of Raman bands at ~1460 and ~1150 cm^{-1} on both the deactivated Pt surface after oxidation reaction and adsorbed reference compounds with olefinic groups on Au@Pt nanoshells, we propose that species containing olefinic groups are likely the strongly-adsorbed poisons formed during the oxidation of alcohols over Pt.

2.3.5. Solid-state NMR spectroscopy of deactivated Pt catalyst

A deactivated Pt/silica catalyst recovered after oxidation of ^{13}C-labeled 1,4-butanediol was characterized by solid-state ^{13}C NMR spectroscopy. The ^{13}C NMR spectrum in Figure 2.13 showed a single, prominent, sharp signal in the C=C spectral region, which ranges from 105 to 150 ppm (conservatively assessed). In the reference spectrum of a silica sample without Pt nanoparticles that was contacted with the recovered reaction medium, a C=C peak was not observed (see Figures 2.13), confirming that the C=C feature results from the presence of Pt. Since a C=C moiety always involves two carbon atoms and there is only one peak in the C=C region, the molecule must be symmetric with identical chemical shifts for both carbon atoms. This excludes the possibility that asymmetric molecules such as 3-buten-1-ol or 3-butenoic acid are responsible for the C=C feature in Figure 2.13. In addition, no signals of similar intensity and narrow line width of other carbon atoms potentially bonded to the C=C moiety are observed, and the other large peaks have larger heteronuclear Overhauser enhancements (see Figure 2.14). Therefore, we can confidently assign the 125-ppm signal in Figure 2.13 to ethylene. Since changes in chemical shift of a few ppm are typical for weakly adsorbed molecules, the chemical shift of C=C in Figure 2.13 (125 ppm) is consistent with that of ethylene (123 ppm) as reported in the literature.[71] The ethylene detected in the NMR spectrum of Figure 2.13 is undergoing large-amplitude motions, as evidenced by its small line width, weak C-H dipolar couplings, and short ^{13}C spin lattice relaxation time of ~0.1 s, which indicates that it is only weakly adsorbed. It may be in equilibrium with strongly Pt-bound ethylene, which could be invisible to high-resolution NMR due to line broadening.[71] Support for this interpretation comes from two observations: the intensity of the ethylene peak increased by more than 60% after temperature cycling (to 320 K and back to ambient) and a week of NMR experiments (Figure 2.14), indicating the presence of an invisible pool of ethylene in the sample. Secondly, an experiment with cross polarization optimized for detecting immobilized hydrogen-bonded carbons with wide lines showed a broad band between 200 and 0 ppm (see Figure 2.15) with a maximum between 40 and 80 ppm,[72] which is distinct from probe-head background (Figure 2.15) and could be due to di-σ-bonded ethylene on Pt.

Other sharp NMR signals of Pt-associated molecules are observed in Figure 2.13 near 29 and 177 ppm and assigned to -CH_2-COO in weakly bound molecules, while a broader band near 173 ppm may arise from more strongly Pt-adsorbed COO groups. Aldehydes or ketones (resonating between 190 and 215 ppm) were insignificant in either sample. Liquid-state ^{13}C NMR spectra of the reaction medium after 40 h of reaction (see Figure 2.16) also showed little aldehyde but instead a prominent 98-ppm peak of a lactol (oxolan-2-ol) formed by cyclization of 4-hydroxybutanal.

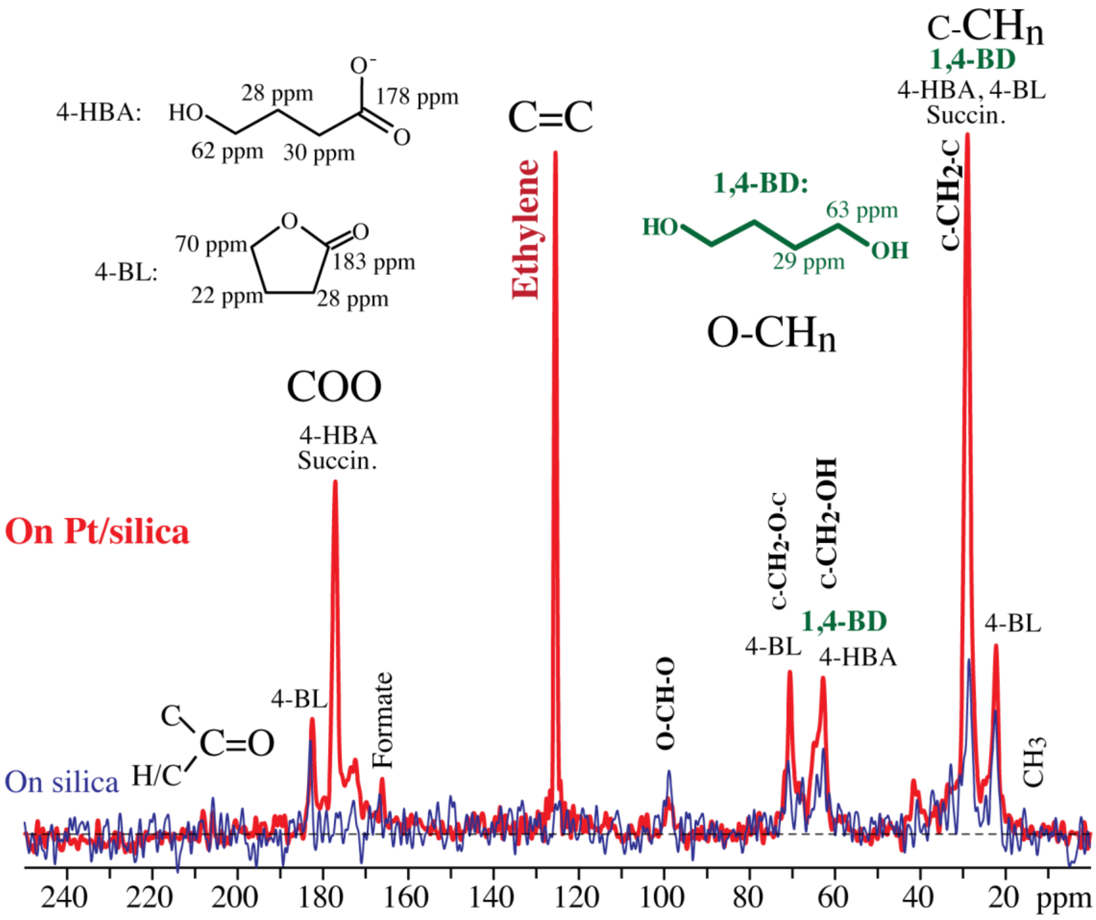

Figure 2. 13. MultiCP ^{13}C NMR spectra of molecules derived from uniformly ^{13}C-enriched 1,4-butanediol (1,4-BD) after oxidation reaction on Pt/silica for 40 hours (thick red line) and adsorbed to silica (thin blue line). Peak assignments to 4-hydroxybutyric acid (4-HBA), 4-butyrolactone (4-BL), succinic acid, and ethylene (~ 2 μg) are indicated (see also Figure 2.16). Reaction conditions: 343 K, 1 MPa O_2, 12 cm^3 aqueous solution of 0.1 M 1,4-butanediol-$^{13}C_4$, 0.050 g 1 wt% Pt/silica.

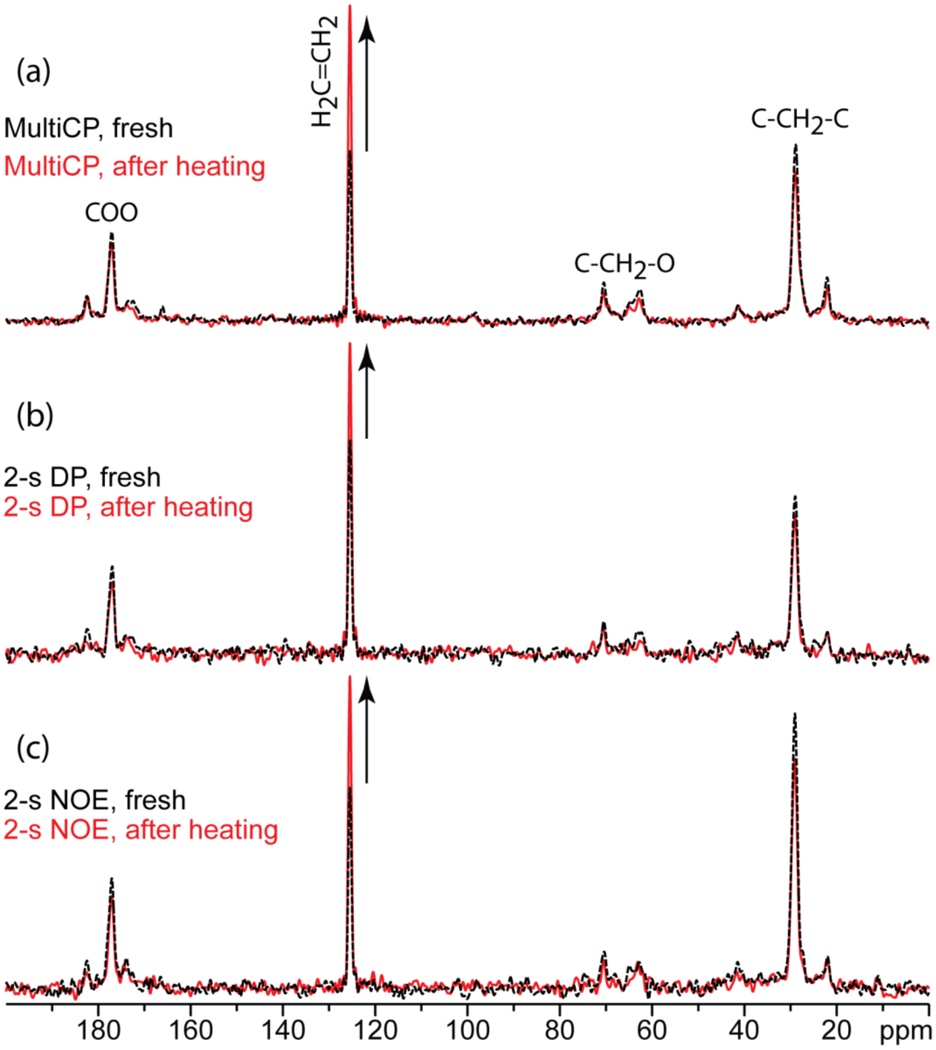

Figure 2. 14. Solid-state ^{13}C NMR spectra of molecules derived from uniformly ^{13}C-enriched 1,4-butanediol (1,4-BD) after reaction under oxidative conditions on Pt/silica for 40 hours. Initial spectra (dashed black line) are compared with spectra taken after heating to 50°C about a week later (solid red line). (a) MultiCP spectra. (b) Direct-polarization spectra with 2-s recycle delay. (c) Direct-polarization spectra with saturation of 1H during the recycle delay, giving rise to heteronuclear NOE. All spectra show a significant increase in the ethylene peak and a decrease in the other signal intensities.

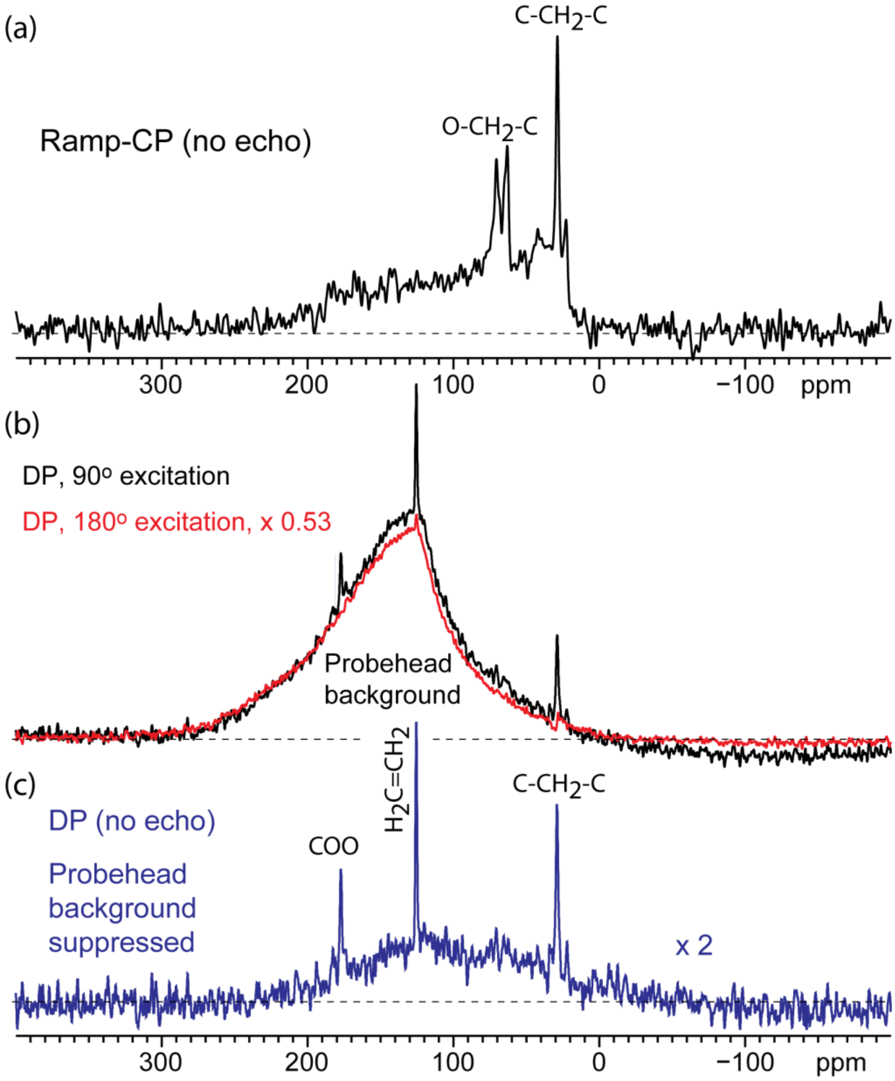

Figure 2. 15. Solid-state ^{13}C NMR spectra of molecules derived from uniformly ^{13}C-enriched 1,4-butanediol (1,4-BD) after reaction under oxidative conditions on Pt/silica for 40 hours, optimized to show broad components. (a) Spectrum after 0.5-ms ramp-CP at 7 kHz MAS, without a Hahn spin echo before detection. (b) Spectra after direct polarization (one-pulse excitation) with differing durations of the excitation pulse. The spectrum after a 180° pulse, which was scaled vertically by 0.53, shows pronounced probe-head background signal (from polymers used in the probe head).[86] (c) Difference of the two spectra in (b), which is nearly free of probe-head background.[86] The broad signals observed in (a) and (c) are quite distinct from the probe-head background in (b) and likely due to Pt-adsorbed molecules.

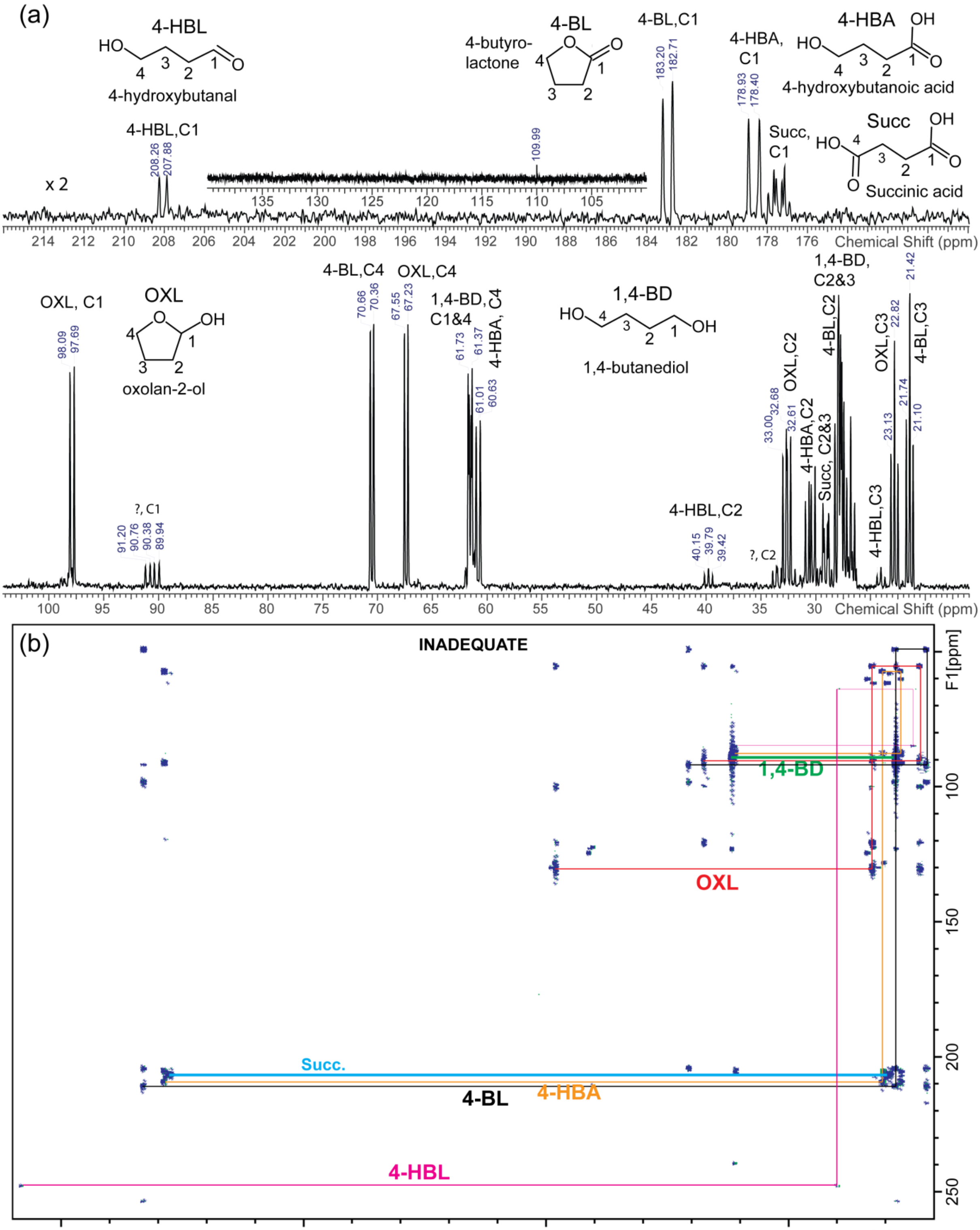

Figure 2. 16. Solution ^{13}C NMR, recorded at 100 MHz with ^{1}H decoupling at 400 MHz, of molecules derived from uniformly ^{13}C-enriched 1,4-butanediol (1,4-BD) after reaction under oxidative conditions on Pt/silica for 40 hours. The Pt/silica was filtered out of the solution

whose spectrum is shown here. (a) 1D spectrum (with nuclear Overhauser enhancement (NOE)). The inset shows no signal between 110 and 140 ppm, where solid-state NMR of the filtered-out Pt/silica exhibits a prominent ethylene peak. Conversely, the signals of oxolan-2-ol, e.g. at 98 ppm, are much larger than in the solid-state NMR spectrum. (b) 2D INADEQUATE spectrum for peak assignments (in particular C1 of 4-BL vs. 4-HBA). The nearest-neighbor connectivities are traced. Secondary cross peaks confirm the assignments.

2.3.6. Influence of substrates containing olefinic groups

The results of SERS and NMR spectroscopy consistently indicate that molecular species with olefinic groups are likely responsible for deactivating the Pt catalyst during alcohol oxidation. Thus, kinetic studies were performed on the influences of additives containing olefinic groups on the initial rate of 1,6-hexanediol oxidation. As shown in Table 2.4, a small amount of 4-penten-1-ol addition ([4-penten-1-ol]:[1,6-hexanediol] = 1 mM:100 mM) significantly inhibited the activity of the catalyst, with a decrease of 87% in the initial TOF. The initial rates of 1,6-hexanediol oxidation with different concentrations of 4-penten-1-ol were evaluated, as shown in Figure 2.17, and the results were used to estimate an equilibrium adsorption constant of 4-penten-1-ol. The calculated value of 1.0×10^{4} M^{-1} is 2 orders of magnitude greater than that estimated for aldehyde and acid products as reported in Table 2.4. Other molecules with an olefinic group, such as 4-pentenoic acid, 3-pentenoic acid, 2-pentenoic acid, 3-penten-1-ol and allyl alcohol decreased the initial rate of 1,6-hexanediol oxidation by more than 70% when added in small amount to the reaction, indicating that a broad range of molecules with an olefinic group can strongly adsorb on Pt/C.

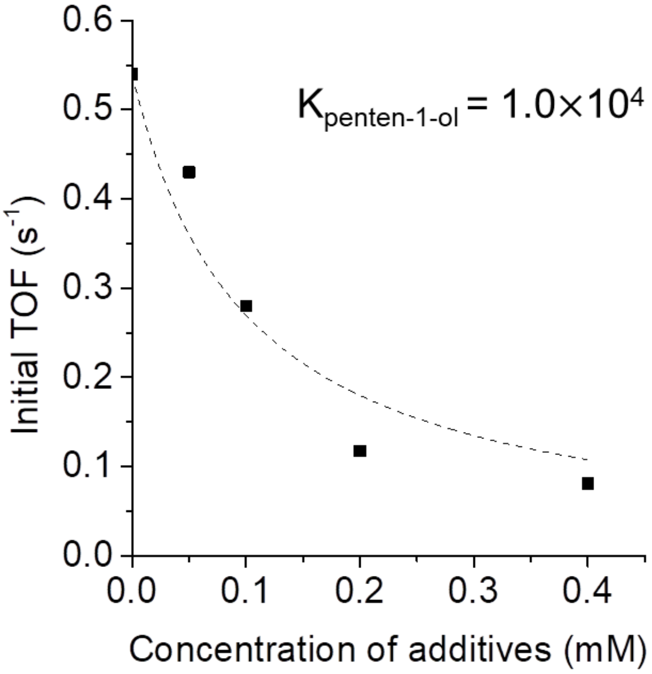

Figure 2. 17. Influence of 4-penten-1-ol on the initial activity of 1,6-hexanediol oxidation over Pt/C catalyst. The points represent the measured initial TOF and the dotted line are the fitted results from equation 1 based on a competitive adsorption model. The fitted adsorption coefficients are present in Table 2.2. Reaction conditions: 343 K, 1 MPa O_2, 12 cm^{-3} aqueous solution of 0.1 M 1,6-hexanediol, Pt:1,6-hexanediol = 1:1000.

Table 2. 4 Initial turnover frequencies of 1,6-hexanediol oxidation over Pt/C in the presence of trace additives[a]

Additive	TOF (s^{-1})	% Decrease in TOF
None	0.54	--
3-Hydroxybutanal	0.50	7.4
Mesityl oxide	0.49	9.3
Polyvinyl alcohol	0.53	1.9
4-Penten-1-ol	0.071	87
4-Penten-1-ol (+H_2)[b]	0.53	1.9
4-Pentenoic acid	0.068	87
4-Pentenoic acid (+H_2)[b]	0.48	11
3-Pentenoic acid	0.16	70
2-Pentenoic acid	0.10	81
Allyl alcohol	0.10	81

a) Reaction conditions: 343 K, 1 MPa O_2, 12 cm^3 aqueous solution of 0.1 M 1,6-hexanediol and 0.001 M additive, Pt:additive: 1,6-hexanediol = 1:10:1000.

b) Catalyst and additives in water were treated under 0.3 MPa H_2 at 343 K for 30 min followed by He flush, addition of 1,6-hexanediol, and pressurization with 1 MPa O_2.

As discussed previously, treatment in H_2 can effectively remove the poisoning species present on a used catalyst (Table 2.3). If species containing olefinic groups are responsible for deactivation, it may be possible to hydrogenate those species off of the catalyst under mild conditions. As shown in Table 2.4, H_2 treatment at 343 K for 30 min is capable of recovering the activity of Pt in the presence of 1 mM 4-penten-1-ol and 4-pentenoic acid. Since the hydrogenation of olefins over Pt is generally fast and zero-order in olefin,[87] we propose that the H_2 treatment efficiently saturated the strongly adsorbed species which can then desorb from the Pt and recover catalytic activity.

2.3.7. Formation of unsaturated species

Since olefins can be produced from the decarbonylation of aldehydes and acids,[88–98] the effect of aldehyde and acid pretreatment on the activity of 1,6-hexanediol oxidation was investigated, assuming byproducts of aldehyde and acid reaction would accumulate with time. As shown in Table 2.5, the initial TOF of 1,6-hexanediol oxidation after 0, 1 and 4 h of adipic acid pretreatment was 0.25, 0.23, and 0.24 s^{-1}, respectively, indicating a negligible amount of poisoning species was generated from exposure of Pt to adipic acid. In contrast, the influence of pretreatment time with 1,5-pentanedial on initial oxidation rate was significant. The initial TOF of 1,6-hexanediol oxidation over Pt/C that was treated with 1,5-pentanedial for 0 h was 0.20 s^{-1}, which further decreased to 0.10 s^{-1} and 0.033 s^{-1} after 1 h and 4 h of pretreatment, respectively. The significant decrease of initial rate with increasing pretreatment time in 1,5-pentanedial indicates that the poisoning species were likely generated from intermediate aldehydes produced during alcohol oxidation reaction.

Table 2. 5 Initial activity of 1,6-hexanediol oxidation over treated Pt/C with 1,5-pentanedial or adipic acid under reaction conditions[a]

Additive	Treatment time (h)	TOF (s^{-1})
1,5-Pentanedial	0	0.20
	1	0.10
	4	0.033
Adipic acid	0	0.25
	1	0.23
	4	0.24

a: The Pt/C was treated in 0.02 M 1,5-pentanedial or adipic acid at 343 K under 1 MPa O_2 for 0, 1, or 4 h. The 1,6-hexanediol and the mixture was subsequently treated at 343 K under 0.2 MPa He for 20 min. The reactor was then pressurized with 1MPa O_2 to start the reaction. Reaction conditions: 343 K, 1 MPa O_2, 12 cm^3 aqueous solution of 0.1 M 1,6-hexanediol and, Pt:additive:1,6-hexanediol = 1:200:1000.

In addition to producing olefinic species, the decarbonylation of aldehydes also generates CO (or CO_2 under oxidative reaction conditions).[20,88–98] To measure the amount of CO or CO_2 generated during reaction, the head space of the reactor was analyzed by gas chromatography. As shown in Table 2.6, 8.3×10^{-6} mol of CO_2 was generated after 16 h of oxidation reaction and no CO was detected. This observation is consistent with previous results, which showed that CO on Pt sites can be quickly and thoroughly oxidized by O_2 under oxidative reaction conditions.[35,36] The oxidation of various aldehydes and acids (5-hydroxypentanal, 1,5-pentanedial, butanal, butyric acid and adipic acid) was performed under the same conditions used for alcohol oxidation (343 K, 1 MPa O_2). After 16 h, the amount of CO_2 generated was approximately 1×10^{-5} mol when aldehydes were oxidized whereas negligible

CO_2 was generated during acid oxidation. Clearly, the production of CO_2 under the conditions of this study is from C-C cleavage of aldehydes. As a comparison, the amount of Pt surface atoms in the reactor was 7.8×10^{-6} mol. The similar amount of generated CO_2 and surface Pt suggests that Pt catalysts are readily poisoned after about one turnover of the aldehyde decarbonylation reaction by a strongly-adsorbed olefinic species.

Table 2. 6 Production of CO_2 during oxidation reactions over Pt/C[a]

Substrate	Production of CO_2 (10^{-6} mol)
1,6-Hexanediol	8.3
5-Hydroxypentanal	13
1,5-Pentanedial	11
Butanal	9.0
Butyric acid	0
Adipic acid	0

a: The CO_2 in the headspace of the reactor was quantified by GC after Pt/C was treated in 0.1 M solution of 1,6-hexanediol, 5-hydroxypentanal, 1,5-pentanedial, butanal, butyric acid or adipic acid for 16 h. Reaction conditions: 343 K, 1 MPa O_2, 12 cm^3 aqueous solution of 0.1 M substrate, Pt: substrate = 1: 250.

The SERS results on aldehyde-treated Au@Pt nanoshells also support the assumption that aldehydes can generate poisoning olefinic groups. After flowing the O_2-saturated 1,5-pentanedial over Au@Pt nanoshells for 2 h, a Raman spectrum was acquired and compared with the spectral pattern of chemisorbed aldehyde on the Pt surface. As shown in Figure 2.11b, Raman features at ~1150 cm^{-1} and ~1460 cm^{-1} associated with di-σ-bonded olefinic groups were observed, indicating the generation of poisoning species from aldehyde products.

2.3.8. Influence of other possible byproducts

In addition to decarbonylation, other side reactions of aldehydes have been proposed to cause the deactivation of catalyst, such as polymerization, aldol addition and aldol condensation.[22,99–103] Polyvinyl alcohol, 3-hydroxybutanal and mesityl oxide were selected as representatives of the byproducts from the potential side reactions mentioned above and the influence of these representative molecules on the initial rate of 1,6,-hexanediol oxidation was evaluated. As shown in Table 2.4, the addition of small amounts of 3-hydroxybutanal, mesityl oxide and polyvinyl alcohol resulted in decreases in initial oxidation rate by 1.9%, 7.4% and 9.3%, respectively. Compared to the original rate of 1,6-hexanediol oxidation when a small amount of olefinic molecules was added, the results suggest the products from aldehyde polymerization, aldol addition and aldol condensation reactions are only weakly adsorbed and are likely not responsible for the deactivation of Pt catalyst.

2.3.9. Potential strategies to suppress the deactivation of Pt

Combining the results from prior and current kinetic and spectroscopic studies, we propose the following pathways of alcohol conversion over Pt catalyst, as summarized in Figure 2.18:

1) Alcohols are converted to aldehyde products via oxidative dehydrogenation;
2) Acids are produced by hydration of aldehydes followed by oxidative dehydrogenation;
3) Aldehydes undergo slow decarbonylation reactions to produce adsorbed olefinic molecules and CO;
4) Adsorbed CO is rapidly oxidized on Pt in the presence of O_2;
5) Strongly-adsorbed olefinic species produced by aldehyde decarbonylation deactivate

the Pt catalyst, which can be regenerated by mild treatment in H_2.

Different steps are involved in the overall selective alcohol oxidation reaction and the minor aldehyde decarbonylation reaction. The activation of O-H and C-H bonds is required for the oxidation reaction, whereas the activation of a C-C bond is additionally required for the decarbonylation reaction, which generates the poisoning olefinic species. Our previous work has already shown that the alcohol oxidation reaction is structure-insensitive over supported Pt nanoparticles in the range of 2 to 6 nm.[2] Neurock et al. also demonstrated by density-functional-theory methods that the oxidation of alcohol over Pt is not structure-sensitive, requiring only 1-2 metal atoms.[104] The decarbonylation of aldehydes over Pt, however, has been shown to occur on highly stepped surfaces (low-coordinated Pt sites) by both experimental and computational methods.[105–107] Additionally, the adsorption energies of olefinic species were reported to be higher over Pt with lower coordination number by Paul and Sautet.[108] By minimizing the fraction of low-coordinated Pt sites that facilitate C-C breaking and adsorb poisoning olefinic species strongly, it may be possible to suppress the formation and/or adsorption of poisoning olefinic species while maintaining the activity for alcohol oxidation.

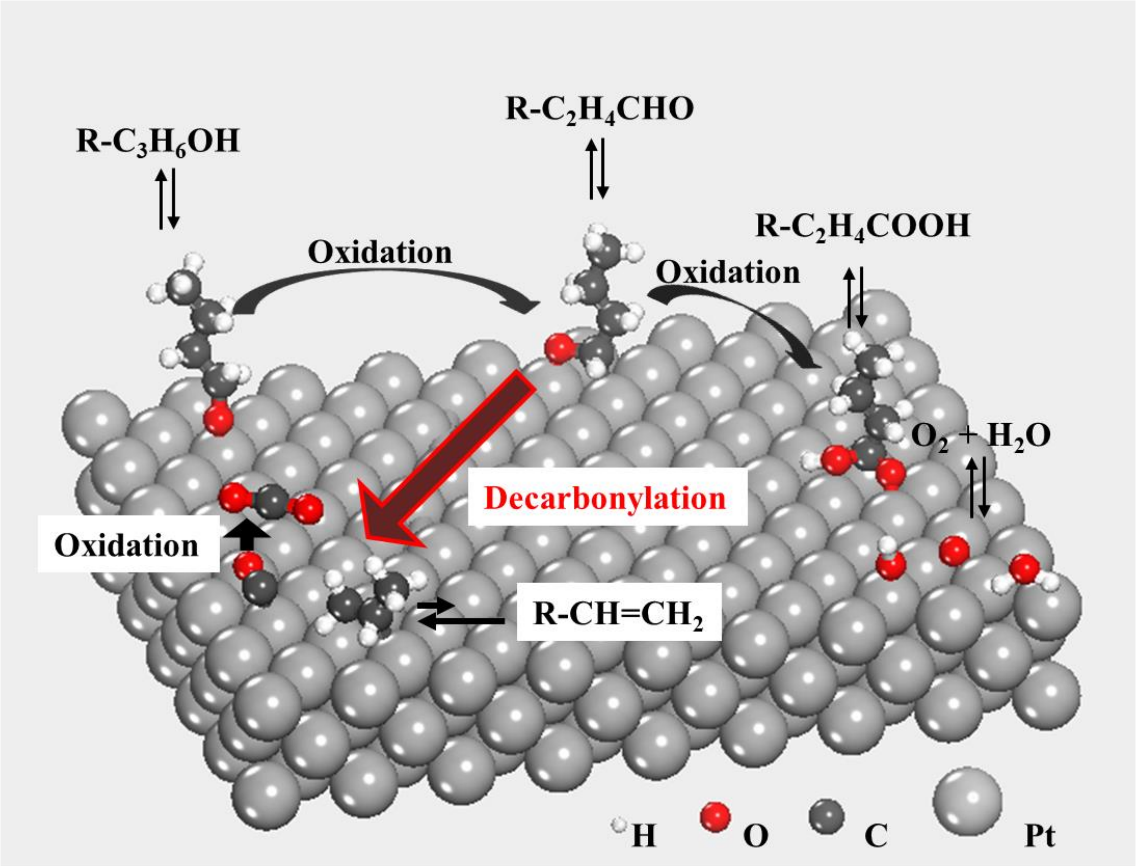

Figure 2. 18. Possible reaction paths for oxidation and side reactions of alcohols over Pt/C.

2.4. Conclusion

Carbon-supported Pt nanoparticles with an average size of 3.4 nm were prepared and utilized in a kinetic study of the deactivation of Pt during the alcohol oxidation reaction. The kinetic measurements indicate that product aldehydes and acids competitively adsorb on the catalyst but there is also generation of strongly-adsorbed poisoning species. In situ surface-enhanced Raman spectroscopy of adsorbates produced during 1,6-hexanediol oxidation over Pt revealed features at ~1150 cm-1 and ~1460 cm-1 that were attributed to a di-σ-bonded olefinic species. Consistent with SERS, solid-state 13C NMR spectroscopy of deactivated Pt/silica after oxidation of 13C-enriched 1,4-butanediol showed a single C=C signal at 125 ppm, which was assigned to ethylene. The observed weakly bound ethylene was likely derived from strongly adsorbed species on Pt, which would give only a non-distinct broad and low-intensity NMR feature. Kinetic measurements with various additives demonstrated that species containing olefinic groups were strongly adsorbed on Pt and significantly inhibited the alcohol oxidation reaction. The performance of deactivated catalyst after alcohol oxidation and of catalyst poisoned by unsaturated hydrocarbon species could be regenerated by a mild H2 treatment at 343 K for 30 min. The poisoning olefinic species are likely generated from the decarbonylation of aldehyde products, as evidenced by significant decrease of activity after aldehyde pretreatment as well as the similar amount of CO2 generated after alcohol oxidation reaction and aldehyde pretreatment.

References for Chapter 2

(1) Zope, B. N.; Davis, S. E.; Davis, R. J. Influence of Reaction Conditions on Diacid Formation During Au-Catalyzed Oxidation of Glycerol and Hydroxymethylfurfural. *Top. Catal.* **2012**, *55*, 24–32.

(2) Ide, M. S.; Davis, R. J. Perspectives on the Kinetics of Diol Oxidation over Supported Platinum Catalysts in Aqueous Solution. *J. Catal.* **2013**, *308*, 50–59.

(3) Dirkx, J. M. H.; van der Baan, H. S. The Oxidation of Gluconic Acid with Platinum on Carbon as Catalyst. *J. Catal.* **1981**, *67*, 14–20.

(4) Hronec, M.; Cvengrosova, Z.; Tuleja, J.; Ilavsky, J. New Developments in Selective Oxidation. *Stud. Surf. Sci. Catal.* **1990**, *55*, 169–176.

(5) Mallat, T.; Baiker, A.; Botz, L. Liquid-Phase Oxidation of 1-Methoxy-2-Propanol with Air III. *Appl. Catal. A Gen.* **1992**, *86*, 147–163.

(6) Schuurman, Y.; Kuster, B. F. M.; van der Wiele, K.; Marin, G. B. Selective Oxidation of Methyl α-D-Glucoside on Carbon Supported Platinum. *Appl. Catal. A Gen.* **1992**, *89*, 47–68.

(7) Venema, F. R.; Peters, J. A.; van Bekkum, H. Platinum-Catalyzed Oxidation of

Aldopentoses to Aldaric Acids. *J. Mol. Catal.* **1992**, *77*, 75–85.

(8) Mallat, T.; Bodnar, Z.; Baiker, A. Partial Oxidation of Water - Insoluble Alcohols over Bi - Promoted Pt on Alumina . Electrochemical Characterization of the Catalyst in Its Working State. *Stud. Surf. Sci. Catal.* **1993**, *78*, 377–384.

(9) Mallat, T.; Bodnar, Z.; Baiker, A. Promotion and Deactivation of Platinum Catalysts in Liquid-Phase Oxidation of Secondary Alcohols. *ACS Symp. Ser.* **1993**, *523*, 308–317.

(10) Baiker, A.; Bodnar, Z.; Mallat, T.; Bronnimann, C.; Hug, P. Direct Oxidation of L-Sorbose to 2-Keto-L-Gulonic Acid with Molecular Oxygen on Platinum- and Palladium-Based Catalysts. *J. Catal.* **1994**, *150*, 199–211.

(11) Mallat, T.; Baiker, A. Oxidation of Alcohols with Molecular Oxygen on Platinum Metal Catalysts in Aqueous Solutions. *Catal. Today* **1994**, *19*, 247–283.

(12) Mallat, T.; Bodnar, Z.; Maciejewski, M.; Baker, A.; Baiker, A. Partial Oxidation of Cinnamyl Alcohol on Bimetallic Catalysts of Improved Resistance to Self-Poisoning. *Stud. Surf. Sci. Catal.* **1994**, *82*, 561–570.

(13) Mallat, T.; Bronnimann, C.; Baiker, A. Platinum-Catalyzed Oxidation of Alcohols in Aqueous Solutions. The Role of Bi-Promotion in Suppression of Catalyst Deactivation. *Stud. Surf. Sci. Catal.* **1994**, *88*, 385–392.

(14) Gallezot, P. Selective Oxidation with Air on Metal Catalysts. *Catal. Today* **1997**, *37*, 405–418.

(15) Gootzen, J. F. E.; Wonders, A. H.; Cox, A. P.; Visscher, W.; Van Veen, J. A. R. On the Adsorbates Formed during the Platinum Catalyzed (Electro) Oxidation of Ethanol, 1,2-Ethanediol and Methyl-Alpha-D-Glucopyranoside at High pH. *J. Mol. Catal. A Chem.* **1997**, *127*, 113–131.

(16) Markusse, A. P.; Kuster, B. F. M.; Koningsberger, D. C.; Marin, G. B. Platinum Deactivation: In Situ EXAFS during Aqueous Alcohol Oxidation Reaction. *Catal.*

Letters **1998**, *55*, 141–145.

(17) Mavrikakis, M.; Barteau, M. A. Oxygenate Reaction Pathways on Transition Metal Surfaces. *J. Mol. Catal. A Chem.* **1998**, *131*, 135–147.

(18) Mallat, T.; Baiker, A. Oxidation of Alcohols with Molecular Oxygen on Solid Catalysts. *Chem. Rev.* **2004**, *104*, 3037–3058.

(19) Nie, J.; Xie, J.; Liu, H. Efficient Aerobic Oxidation of 5-Hydroxymethylfurfural to 2,5-Diformylfuran on Supported Ru Catalysts. *J. Catal.* **2013**, *301*, 83–91.

(20) Ide, M. S.; Falcone, D. D.; Davis, R. J. On the Deactivation of Supported Platinum Catalysts for Selective Oxidation of Alcohols. *J. Catal.* **2014**, *311*, 295–305.

(21) Besson, M.; Gallezot, P. Selective Oxidation of Alcohols and Aldehydes on Metal Catalysts. *Catal. Today* **2000**, *57*, 127–141.

(22) Hao, P.; Pylypenko, S.; Schwartz, D. K.; Medlin, J. W. Application of Thiolate Self-Assembled Monolayers in Selective Alcohol Oxidation for Suppression of Pd Catalyst Deactivation. *J. Catal.* **2016**, *344*, 722–728.

(23) Jeanmaire, D. L.; Van Duyne, R. P. Surface Raman Spectroelectrochemistry. *J. Electroanal. Chem. Interfacial Electrochem.* **1977**, *84*, 1–20.

(24) Albrecht, M. G.; Creighton, J. A. Anomalously Intense Raman Spectra of Pyridine at a Silver Electrode. *J. Am. Chem. Soc.* **1977**, *99*, 5215–5217.

(25) Tian, Z.-Q.; Ren, B. Adsorption and Reaction At Electrochemical Interfaces As Probed By Surface-Enhanced Raman Spectroscopy. *Annu. Rev. Phys. Chem.* **2004**, *55*, 197–229.

(26) Kudelski, A. Analytical Applications of Raman Spectroscopy. *Talanta* **2008**, *76*, 1–8.

(27) Wu, D.-Y.; Li, J.-F.; Ren, B.; Tian, Z.-Q. Electrochemical Surface-Enhanced Raman Spectroscopy of Nanostructures. *Chem. Soc. Rev.* **2008**, *37*, 1025–1041.

(28) Weaver, M. Raman and Infrared Spectroscopies as in Situ Probes of Catalytic

Adsorbate Chemistry at Electrochemical and Related Metal–gas Interfaces: Some Perspectives and Prospects. *Top. Catal.* **1999**, *8*, 65–73.

(29) Kim, H.; Kosuda, K. M.; Van Duyne, R. P.; Stair, P. C. Resonance Raman and Surface- and Tip-Enhanced Raman Spectroscopy Methods to Study Solid Catalysts and Heterogeneous Catalytic Reactions. *Chem. Soc. Rev.* **2010**, *39*, 4820–4844.

(30) Sharma, B.; Frontiera, R. R.; Henry, A.-I.; Ringe, E.; Van Duyne, R. P. SERS: Materials, Applications, and the Future. *Mater. Today* **2012**, *15*, 16–25.

(31) Campion, A.; Kambhampati, P. Surface-Enhanced Raman Scattering. *Chem. Soc. Rev.* **1998**, *27*, 241–250.

(32) Tian, Z.; Ren, B.; Wu, D. Surface-Enhanced Raman Scattering : From Noble to Transition Metals and from Rough. *J. Phys. Chemsitry* **2002**, *106*, 9463–9483.

(33) Weaver, M. J. Surface-Enhanced Raman Spectroscopy as a Versatile in Situ Probe of Chemisorption in Catalytic Electrochemical and Gaseous Environments. *J. Raman Spectrosc.* **2002**, *33*, 309–317.

(34) Tian, Z.-Q.; Ren, B.; Li, J.-F.; Yang, Z.-L. Expanding Generality of Surface-Enhanced Raman Spectroscopy with Borrowing SERS Activity Strategy. *Chem. Commun.* **2007**, 3514–3534.

(35) Heck, K. N.; Janesko, B. G.; Scuseria, G. E.; Halas, N. J.; Wong, M. S. Using Catalytic and Surface-Enhanced Raman Spectroscopy-Active Gold Nanoshells to Understand the Role of Basicity in Glycerol Oxidation. *ACS Catal.* **2013**, *3*, 2430–2435.

(36) Tian, Z. Q.; Ren, B.; Mao, B. W. Extending Surface Raman Spectroscopy to Transition Metal Surfaces for Practical Applications. 1. Vibrational Properties of Thiocyanate and Carbon Monoxide Adsorbed on Electrochemically Activated Platinum Surfaces. *J. Phys. Chem. B* **1997**, *101*, 1338–1346.

(37) Xiao, X.; Sun, S.; Yao, J.; Wu, Q. Surface-Enhanced Raman Spectroscopic Studies of Dissociative Adsorption of Amino Acids on Platinum and Gold Electrodes in Alkaline Solutions. *Langmuir* **2002**, 6274–6279.

(38) Cao, P.; Zhong, Q.; Sun, Y.; Gu, R. Dissociation and Electrooxidation of Formic Acid at Platinum in Nonaqueous Solutions as Probed by in Situ Surface-Enhanced Raman Spectroscopy. *Chem. Phys. Lett.* **2003**, *376*, 806–811.

(39) Solla-Gullón, J.; Gómez, R.; Aldaz, A.; Pérez, J. M. A Combination of SERS and Electrochemistry in Pt Nanoparticle Electrocatalysis: Promotion of Formic Acid Oxidation by Ethylidyne. *Electrochem. commun.* **2008**, *10*, 319–322.

(40) Panikkanvalappil, S. R.; Mahmoud, M. A.; MacKey, M. A.; El-Sayed, M. A. Surface-Enhanced Raman Spectroscopy for Real-Time Monitoring of Reactive Oxygen Species-Induced DNA Damage and Its Prevention by Platinum Nanoparticles. *ACS Nano* **2013**, *7*, 7524–7533.

(41) Huang, Q. J.; Li, X. Q.; Yao, J. L.; Ren, B.; Cai, W. B.; Gao, J. S.; Mao, B. W.; Tian, Z. Q. Extending Surface Raman Spectroscopic Studies to Transition Metals for Practical Applications III . E Ff Ects of Surface Roughening Procedure on Surface-Enhanced Raman Spectroscopy from Nickel and Platinum Electrodes. *Surf. Sci.* **1999**, *427–428*, 162–166.

(42) Zhong, Q.; Zhang, B.; Zhang, L.; Yang, X.; Huang, P. In situ SERS of Dissociative Adsorption and Oxidation of Ethanol on Roughed Platinum Electrodes. *ACTA Physicochim. Sin.* **2004**, *20*, 1163–1166.

(43) Cao, P.; Sun, Y.; Gu, R. Investigations of Chemisorption and Reaction at Non-Aqueous Electrochemical Interfaces by in Situ Surface-Enhanced Raman Spectroscopy. *J. Raman Spectrosc.* **2005**, *36*, 725–735.

(44) Gómez, R.; Solla-Gullón, J.; Pérez, J. M.; Aldaz, A. Nanoparticles-on-Electrode

Approach for in Situ Surface-Enhanced Raman Spectroscopy Studies with Platinum-Group Metals: Examples and Prospects. *J. Raman Spectrosc.* **2005**, *36*, 613–622.

(45) Ding, Y. M.; Liu, Y. L.; Rao, G. S.; Wang, G. F.; Zhong, Q. L.; Ren, B.; Tian, Z. Q. Electrooxidation Mechanism of Methanol at Pt-Ru Catalyst Modified GC Electrode in Electrolytes with Different pH Using Electrochemical and SERS Techniques. *Chinese J. Chem.* **2007**, *25*, 1617–1621.

(46) Liu, G. K.; Ren, B.; Gu, R. A.; Tian, Z. Q. Effect of the Intrinsic Properties of Metals on the Adsorption Behavior of Molecules - Competitive and Cooperative Adsorption of Benzene and Other Species on Pt and Rh Surfaces. *J. Phys. Chem. C* **2007**, *111*, 3417–3426.

(47) Vidal-Iglesias, F. J.; Solla-Gullón, J.; Orts, J. M.; Rodes, A.; Pérez, J. M.; Feliu, J. M. SERS on (111) Surface Nanofacets at Pt Nanoparticles: The Case of Acetaldehyde Oxime Reduction. *J. Phys. Chem. C* **2012**, *116*, 10781–10789.

(48) Lu, L.; Sun, G.; Zhang, H.; Wang, H.; Xi, S.; Hu, J.; Tian, Z.; Chen, R. Fabrication of Core-Shell Au-Pt Nanoparticle Film and Its Potential Application as Catalysis and SERS substrateElectronic Supplementary Information (ESI) Available: AFM Image and Line Scans of Core-Shell Au-Pt Nanoparticle Film (Colour Version of Fig. 4). *J. Mater. Chem.* **2004**, *14*, 1005–1009.

(49) Williams, C. T.; Chan, H. Y. H.; Tolia, A. A.; Weaver, M. J.; Takoudis, C. G. In Situ Real-Time Studies of Heterogeneous Catalytic Mechanisms at Ambient Pressures As Probed by Surface-Enhanced Raman and Mass Spectroscopies. *Ind. Eng. Chem. Res.* **1998**, *37*, 2307–2315.

(50) Zeng, J.; Jean, D.; Ji, C.; Zou, S. In Situ Surface-Enhanced Raman Spectroscopic Studies of Nafion Adsorption on Au and Pt Electrodes. *Langmuir* **2012**, *28*, 957–964.

(51) Lai, S. C. S.; Kleyn, S. E. F.; Rosca, V.; Koper, M. T. M. Mechanism of the Dissociation and Electrooxidation of Ethanol and Acetaldehyde on Platinum as Studied by SERS. *J. Phys. Chem. C* **2008**, *112*, 19080–19087.

(52) Guerrini, L.; Lopez-Tobar, E.; Garcia-Ramos, J. V; Domingo, C.; Sanchez-Cortes, S. New Insights on the Au(core)/Pt(shell) Nanoparticle Structure in the Sub-Monolayer Range: SERS as a Surface Analyzing Tool. *Chem. Commun.* **2011**, *47*, 3174–3176.

(53) Zhang, P.; Cai, J.; Chen, Y.; Tang, Z.; Chen, D.; Yang, J.; Wu, D.; Ren, B.; Tian, Z. Potential-Dependent Chemisorption of Carbon Monoxide at a Gold Core - Platinum Shell Nanoparticle Electrode : A Combined Study by Electrochemical in Situ Surface-Enhanced Raman Spectroscopy and Density Functional Theory. *J. Phys. Chem.* **2009**, *113*, 17518–17526.

(54) Zhang, P.; Cai, J.; Chen, Y. X.; Tang, Z. Q.; Chen, D.; Yang, J.; Wu, D. Y.; Ren, B.; Tian, Z. Q. Potential-Dependent Chemisorption of Carbon Monoxide at a Gold Core-Platinum Shell Nanoparticle Electrode: A Combined Study by Electrochemical in Situ Surface-Enhanced Raman Spectroscopy and Density Functional Theory. *J. Phys. Chem. C* **2010**, *114*, 403–411.

(55) Cui, Q.; Shen, G.; Yan, X.; Li, L.; Mo, H. Qianling Cui, Guizhi Shen, Xuehai Yan, Lidong Li, Helmuth Mohwald, and Matias Bargheer. *Appl. Mater. Interfaces* **2014**, *6*, 17075–17081.

(56) Liu, R.; Liu, J. F.; Zhang, Z. M.; Zhang, L. Q.; Sun, J. F.; Sun, M. T.; Jiang, G. Bin. Submonolayer-Pt-Coated Ultrathin Au Nanowires and Their Self-Organized Nanoporous Film: SERS and Catalysis Active Substrates for Operando SERS Monitoring of Catalytic Reactions. *J. Phys. Chem. Lett.* **2014**, *5*, 969–975.

(57) LeBlanc, R. J.; Chu, W.; Williams, C. T. Surface Raman Characterization of Cinchonidine-Modified Platinum in Ethanol: Effects of Liquid-Phase Concentration

and Co-Adsorbed Hydrogen. *J. Mol. Catal. A Chem.* **2004**, *212*, 277–289.

(58) Luo, H.; Weaver, M. J. Surface-Enhanced Raman Scattering as a Versatile Vibrational Probe of Transition-Metal Interfaces: Thiocyanate Coordination Modes on Platinum-Group versus Coinage-Metal Electrodes. *Langmuir* **1999**, *15*, 8743–8749.

(59) Jebaraj, A. J. J.; De Godoi, D. R. M.; Scherson, D. The Oxidation of Hydroxylamine on Pt-, and Pd-Modified Au Electrodes in Aqueous Electrolytes: Electrochemical and in Situ Spectroscopic Studies. *Catal. Today* **2013**, *202*, 44–49.

(60) Zou, S.; Chan, H. Y. H.; Williams, C. T.; Weaver, M. J. Formation and Stability of Oxide Films on Platinum-Group Metals in Electrochemical and Related Environments as Probed by Surface-Enhanced Raman Spectroscopy: Dependence on the Chemical Oxidant. *Langmuir* **2000**, *16*, 754–763.

(61) Yang, H.; Yang, Y.; Zou, S. In Situ Surface-Enhanced Raman Spectroscopic Studies of CO Adsorption and Methanol Oxidation on Ru-Modified Pt Surfaces. *J. Phys. Chem. C* **2007**, *111*, 19058–19065.

(62) Ahn, M.; Kim, J. Insights into the Electrooxidation of Formic Acid on Pt and Pd Shells on Au Core Surfaces via SERS at Dendritic Au Rod Electrodes. *J. Phys. Chem. C* **2013**, *117*, 24438–24445.

(63) Fromm, D. P.; Sundaramurthy, A.; Kinkhabwala, A.; Schuck, P. J.; Kino, G. S.; Moerner, W. E. Exploring the Chemical Enhancement for Surface-Enhanced Raman Scattering with Au Bowtie Nanoantennas. *J. Chem. Phys.* **2006**, *124*, 61101.

(64) Ward, D. R.; Grady, N. K.; Levin, C. S.; Halas, N. J.; Wu, Y.; Nordlander, P.; Natelson, D. Electromigrated Nanoscale Gaps for Surface-Enhanced Raman Spectroscopy. *Nano Lett.* **2007**, *7*, 1396–1400.

(65) Aizpurua, J.; Hanarp, P.; Sutherland, D. S.; Käll, M.; Bryant, G. W.; García de Abajo, F. J. Optical Properties of Gold Nanorings. *Phys. Rev. Lett.* **2003**, *90*, 57401.

(66) Lal, S.; Grady, N. K.; Kundu, J.; Levin, C. S.; Lassiter, J. B.; Halas, N. J. Tailoring Plasmonic Substrates for Surface Enhanced Spectroscopies. *Chem. Soc. Rev.* **2008**, *37*, 898–911.

(67) Oldenburg, S. J.; Averitt, R. D.; Westcott, S. L.; Halas, N. J. Nanoengineering_resonances.pdf. *Chem. Phys.* **1998**, *288*, 243–247.

(68) Heck, K. N.; Janesko, B. G.; Scuseria, G. E.; Halas, N. J.; Wong, M. S. Observing Metal-Catalyzed Chemical Reactions in Situ Using Surface-Enhanced Raman Spectroscopy on Pd-Au Nanoshells. *J. Am. Chem. Soc.* **2008**, *130*, 16592–16600.

(69) Gay, I. Chemisorption of Ethylene on Supported Platinum Studied by High-Resolution Solid-State NMR. *J. Catal.* **1987**, *108*, 15–23.

(70) Zilm, K. W.; Bonneviot, L.; Hamilton, D. M.; Webb, G. G.; Haller, G. L. Carbon-13 NMR Studies of Supported Platinum and Palladium Catalysts Using Magic Angle Sample Spinning. *J. Phys. Chem.* **1990**, *94*, 1463–1472.

(71) Pruski, M.; Kelzenberg, J. C.; Gerstein, B. C.; King, T. S. Solid-State NMR of Carbon-13 in Ethylene Adsorbed on Silica-Supported Ruthenium. *J. Am. Chem. Soc.* **1990**, *112*, 4232–4240.

(72) Pruski, M.; Wu, X.; Smale, M. W.; Gerstein, B. C.; King, T. S. The Conversion of Ethylene to Coke on Supported Platinum Catalysts Investigated by 13C Nmr. *Stud. Surf. Sci. Catal.* **1991**, *68*, 699–706.

(73) Johnson, R. L.; Schwartz, T. J.; Dumesic, J. A.; Schmidt-Rohr, K. Methionine Bound to Pd/γ-Al2O3 Catalysts Studied by Solid-State 13C NMR. *Solid State Nucl. Magn. Reson.* **2015**, *72*, 64–72.

(74) Tedsree, K.; Kong, A. T. S.; Tsang, S. C. Formate as a Surface Probe for Ruthenium Nanoparticles in Solution ^{13}C NMR Spectroscopy. *Angew. Chemie Int. Ed.* **2009**, *48*, 1443–1446.

(75) Kim, J. H.; Choi, S. H. M.; Nam, S. H.; Seo, M. H.; Choi, S. H. M.; Kim, W. B. Influence of Sn Content on PtSn/C Catalysts for Electrooxidation of C1-C3 Alcohols: Synthesis, Characterization, and Electrocatalytic Activity. *Appl. Catal. B Environ.* **2008**, *82*, 89–102.

(76) Xie, J.; Falcone, D. D.; Davis, R. J. Restructuring of Supported PtSn Bimetallic Catalysts during Aqueous Phase Oxidation of 1,6-Hexanediol. *J. Catal.* **2015**, *332*, 38–50.

(77) Duff, D. G.; Baiker, A.; Edwards, P. P. A New Hydrosol of Gold Clusters. *J. Chem. Soc. Chem. Commun.* **1993**, *272*, 96.

(78) Xie, J.; Huang, B.; Yin, K.; Pham, H. N.; Unocic, R. R.; Datye, A. K.; Davis, R. J. Influence of Dioxygen on the Promotional Effect of Bi during Pt-Catalyzed Oxidation of 1,6-Hexanediol. *ACS Catal.* **2016**, *6*, 4206–4217.

(79) Johnson, R. L.; Schmidt-Rohr, K. Quantitative Solid-State 13C NMR with Signal Enhancement by Multiple Cross Polarization. *J. Magn. Reson.* **2014**, *239*, 44–49.

(80) Mao, J.-D.; Schmidt-Rohr, K. Separation of Aromatic-Carbon 13C NMR Signals from Di-Oxygenated Alkyl Bands by a Chemical-Shift-Anisotropy Filter. *Solid State Nucl. Magn. Reson.* **2004**, *26*, 36–45.

(81) Pabst, W.; Gregorova, E. Characterization of Particles and Particle Systems. *ICT Prague* **2007**, 1–122.

(82) Bearden, J. A. X-Ray Wavelengths. *Rev. Mod. Phys.* **1967**, *39*, 78–124.

(83) Oldenburg, S. J.; Oldenburg, S. J.; Westcott, S. L.; Westcott, S. L.; Averitt, R. D.; Averitt, R. D.; Halas, N. J.; Halas, N. J. Surface Enhanced Raman Scattering in the near Infrared Using Metal Nanoshell Substrates. *Chem. Phys.* **1999**, *111*, 4729–4735.

(84) Weaver, M. J.; Kizhakevariam, N.; Jiang, X.; Villegas, I.; Stuhlmann, C.; Tolia, A.; Gao, X. Vibrational Spectroscopy at Metal-Solution Interfaces: Some Perspectives and

Prospects for Electrochemical Surface Science. *J. Electron Spectros. Relat. Phenomena* **1993**, *64–65*, 351–362.

(85) Bandy, B. J.; Chesters, M. A.; James, D. I.; Mcdougall, G. S.; Pemble, M. E.; Sheppard, D. R. . Electron Energy Loss Spectrosocpy of Adsorbed Ethylene. *Phil. Trans. R. Soc. Lond. A* **1986**, *318*, 141–161.

(86) Chen, Q.; Hou, S. S.; Schmidt-Rohr, K. A Simple Scheme for Probehead Background Suppression in One-Pulse 1H NMR. *Solid State Nucl. Magn. Reson.* **2004**, *26*, 11–15.

(87) Falcone, D. D.; Hack, J. H.; Davis, R. J. Aqueous-Phase Hydrogenation of Saturated and Unsaturated Ketones and Aldehydes over Supported Platinum-Rhenium Catalysts. *ChemCatChem* **2016**, *8*, 1074–1083.

(88) Zhao, H.; Kim, J.; Koel, B. E. Adsorption and Reaction of Acetaldehyde on Pt(1 1 1) and Sn/Pt(1 1 1) Surface Alloys. *Surf. Sci.* **2003**, *538*, 147–159.

(89) De Jesús, J. C.; Zaera, F. Double-Bond Activation in Unsaturated Aldehydes: Conversion of Acrolein to Propene and Ketene on Pt(111) Surfaces. *J. Mol. Catal. A Chem.* **1999**, *138*, 237–240.

(90) Burgener, M.; Wirz, R.; Mallat, T.; Baiker, A. Nature of Catalyst Deactivation during Citral Hydrogenation: A Catalytic and ATR-IR Study. *J. Catal.* **2004**, *228*, 152–161.

(91) Murillo, L. E.; Chen, J. G. Adsorption and Reaction of Propanal, 2-Propenol and 1-Propanol on Ni/Pt(111) Bimetallic Surfaces. *Surf. Sci.* **2008**, *602*, 2412–2420.

(92) Kliewer, C. J.; Bieri, M.; Somorjai, G. A. Hydrogenation of the ??,??-Unsaturated Aldehydes Acrolein, Crotonaldehyde, and Prenal over Pt Single Crystals: A Kinetic and Sum-Frequency Generation Vibrational Spectroscopy Study. *J. Am. Chem. Soc.* **2009**, *131*, 9958–9966.

(93) Mondelli, C.; Grunwaldt, J.; Ferri, D.; Baiker, A. Role of Bi Promotion and Solvent in Platinum-Catalyzed Alcohol Oxidation Probed by in Situ X-Ray Absorption and

ATR-IR Spectroscopy. *Phys. Chem. Chem. Phys.* **2010**, *12*, 5307–5316.

(94) Chibani, S.; Michel, C.; Delbecq, F.; Pinel, C.; Besson, M. On the Key Role of Hydroxyl Groups in Platinum-Catalysed Alcohol Oxidation in Aqueous Medium. *Catal. Sci. Technol.* **2013**, *3*, 339–350.

(95) Peng, B.; Zhao, C.; Mejía-centeno, I.; Fuentes, G. A.; Jentys, A.; Lercher, J. A. Comparison of Kinetics and Reaction Pathways for Hydrodeoxygenation of C 3 Alcohols on Pt / Al 2 O 3. *Catal. Today* **2012**, *183*, 3–9.

(96) Mäki-Arvela, P.; Snåre, M.; Eränen, K.; Myllyoja, J.; Murzin, D. Y. Continuous Decarboxylation of Lauric Acid over Pd/C Catalyst. *Fuel* **2008**, *87*, 3543–3549.

(97) Kaylor, N.; Xie, J.; Kim, Y.-S.; Pham, H. N.; Datye, A. K.; Lee, Y.-K.; Davis, R. J. Vapor Phase Deoxygenation of Heptanoic Acid over Silica-Supported Palladium and Palladium-Tin Catalysts. *J. Catal.* **2016**, *344*, 202–212.

(98) Lopez-Ruiz, J. A.; Davis, R. J.; Wallace, R.; Miller, J. T.; Fuller, T. F.; Jones, C. W.; Mäki-Arvela, P.; Salmi, T.; Yu, D.; Murzin, D. Y. Decarbonylation of Heptanoic Acid over Carbon-Supported Platinum Nanoparticles. *Green Chem.* **2014**, *16*, 683–694.

(99) Balu, A. M.; Lin, C. S. K.; Liu, H.; Li, Y.; Vargas, C.; Luque, R. Iron Oxide Functionalised MIL-101 Materials in Aqueous Phase Selective Oxidations. *Appl. Catal. A Gen.* **2013**, *455*, 261–266.

(100) Figueiredo, M. C.; Santasalo-aarnio, A.; Vidal-Iglesias, F. J.; Solla-Gullón, J.; Feliu, J. M.; Kontturi, K.; Kallio, T. Tailoring Properties of Platinum Supported Catalysts by Irreversible Adsorbed Adatoms toward Ethanol Oxidation for Direct Ethanol Fuel Cells. *Appl. Catal. B Environ.* **2013**, *140–141*, 378–385.

(101) Fan, S.; Luan, Y.; Wang, J.; Gao, H.; Zhang, X.; Wang, G. Journal of Molecular Catalysis A : Chemical Monodispersed Poly (4-Vinylpyridine) Spheres Supported Fe (III) Material : An Efficient and Reusable Catalyst for Benzylic Oxidation. *J. Mol.*

Catal. A. Chem. **2015**, *404–405*, 186–192.

(102) Schoenbaum, C. A.; Schwartz, D. K.; Medlin, J. W. Controlling the Surface Environment of Heterogeneous Catalysts Using Self-Assembled Monolayers. *Acc. Chem. Res.* **2014**, *47*, 1438–1445.

(103) Mallat, T.; Bodnar, Z.; Hug, P.; Baiker, A. Selective Oxidation of Cinnamyl Alcohol to Cinnamaldehyde with Air over Bi-Pt/Alumina Catalysts. *Journal of Catalysis*, 1995, *153*, 131–143.

(104) Neurock, M.; Janik, M.; Wieckowski, A. A First Principles Comparison of the Mechanism and Site Requirements for the Electrocatalytic Oxidation of Methanol and Formic Acid over Pt. *Faraday Discuss.* **2009**, *140*, 363–378.

(105) Pushkarev, V. V.; Musselwhite, N.; An, K.; Alayoglu, S.; Somorjai, G. A. High Structure Sensitivity of Vapor-Phase Furfural Decarbonylation/hydrogenation Reaction Network as a Function of Size and Shape of Pt Nanoparticles. *Nano Lett.* **2012**, *12*, 5196–5201.

(106) Wang, H.-F.; Liu, Z.-P. Comprehensive Mechanism and Structure-Sensitivity of Ethanol Oxidation on Platinum: New Transition-State Searching Method for Resolving the Complex Reaction Network. *J. Am. Chem. Soc.* **2008**, *130*, 10996–11004.

(107) Basaran, D.; Genest, A.; Lercher, J. A.; Rösch, N. Formation of CO 2 and Ethane from Propionyl over Platinum: A Density Functional Theory Study. *ACS Catal.* **2013**, *3*, 1730–1738.

(108) Paul, J.-F.; Sautet, P. Influence of the Surface Atom Metallic Coordination in the Adsorption of Ethylene on a Platinum Surface: A Theoretical Study. *J. Phys. Chem.* **1994**, *98*, 10906–10912.

Chapter 3. Oxidation of 1,6-hexanediol over bimetallic Bi-Pt catalysts

A portion of this thesis was previously published as Xie, J. et al. Influence of Dioxygen on the Promotional Effect of Bi during Pt-Catalyzed Oxidation of 1,6-Hexanediol. ACS Catal. 6, 4206–4217 (2016).

3.1. Introduction

Selective oxidation of alcohols to carbonyl compounds is an important reaction in organic synthesis[1,2] and will likely play a significant role in the development of value-added chemicals from biomass.[3] In particular, the oxidation of biomass-derived alcohols such as 5-hydroxymethylfurfural (HMF), glycerol and 1,6-hexanediol (HDO), using supported metal catalysts and dioxygen has received attention because it offers a green and sustainable path to value-added chemicals.[2,4–18] Among supported metal catalysts, Au has demonstrated the highest activity for alcohol oxidation under basic conditions.[16] The use of base, however, is not attractive because of the cost and waste involved in neutralizing the product stream to recover the free acid. In contrast, alcohol oxidation over Pt does not require high concentrations of base.[19,15] Unfortunately, severe deactivation was observed during the oxidation of HDO over Pt catalysts.[20]

Previous work has shown that the addition of Bi can promote the catalytic performance of Pt catalysts. Bismuth-promoted Pt catalysts have demonstrated enhanced rate, stability and/or selectivity, compared to monometallic Pt catalysts.[21–31] For example, enhancements in activity by a factor of 1.5 to 66 have been reported for the oxidation of various primary alcohols, secondary alcohols and polyols over Bi-promoted Pt catalysts.[21,23–25,27,28,31] Addition of Bi to Pt has also been claimed to make a catalyst more resistant to deactivation.[23,25,32] During glycerol oxidation over Pt, the presence of Bi promoted the oxidation of the secondary hydroxyl group.[29,31,33] Based on a kinetic model proposed by Wörz et al., the theoretical yield of dihydroxyacetone (DHA) can be as high as 70%,[29] but only 4% DHA selectivity was obtained at 37% conversion over unpromoted Pt/C.[34]

The promotional effects of Bi are often attributed to preventing the over-oxidation of Pt and the leaching of Pt into solution,[1,23,25,28,31,35] suppressing the production and adsorption of poisoning species,[1,23,24,36–38] favoring the formation of adsorbed hydroxyl species[23,25,27,28,36,39,40] and forming complexes of Bi with reaction intermediates.[27,31,33] Mallat et al. used electrochemical methods to investigate the in situ catalyst potential of Bi-Pt and Pt catalysts during the oxidation of various alcohols and found that the Pt in the Bi-promoted catalyst remained reduced under conditions that would oxidize an unpromoted Pt catalyst.[24,25,27] Results from in situ X-ray absorption spectroscopy (XAS) further confirmed that addition of Bi helped maintain Pt in a metallic state.[28] The enhanced stability of a Bi-Pt catalyst was also attributed to small ensembles of Pt atoms in the promoted catalyst,[21,23–25,27,28] which suppressed the formation and adsorption of hydrocarbon fragments and CO generated from C-C cleavage.[23,25,27,28,36,38] Another role of Bi might be to form new active centers. Using a laser-induced temperature jump method, Feliu et al. studied the interaction between water and the Bi-Pt surface and proposed that Bi might induce a surface dipole that leads to a reorientation of water and favors the formation of surface hydroxyl groups.[39,40] The presence of surface hydroxyl groups might participate in the activation of alcohol, and the removal of adsorbed remnants on the surface,[10,15,18] thus promoting the activity and stability of the alcohol oxidation reaction.[21,23,25,27,36,41,42] During polyol oxidation, Bi has been proposed to form complexes with the substrate and promote the selective oxidation of the secondary hydroxyl group, altering the product distribution compared to an unpromoted Pt catalyst.[29,31,33]

One potential complication with investigating the promotional effects of multi-component catalysts is restructuring under reaction conditions. In fact, changes in the structure of PtM (M = Rh,[43,44] Ru,[45] Pd,[46,47] Co,[48,49] Au[46] and Sn[50–52]) bimetallic catalysts have been reported during reaction, as revealed by in situ or ex-situ characterization using X-ray absorption spectroscopy (XAS), X-ray photoelectron spectroscopy (XPS), sum frequency generation vibrational spectroscopy (SFG), (scanning) transmission electron microscopy ((S)TEM) and infrared spectroscopy (IR). Although leaching of Pt and Bi from supported Bi-Pt catalysts was not detected under alcohol oxidation conditions,[27,31] the structure of Bi-Pt particles under reaction conditions is still a matter of debate. Therefore, it is necessary to examine the influence of the catalytic reaction on catalyst structure to elucidate the promotional effect of Bi on Pt oxidation catalysts.

In this study, a series of carbon-supported, Bi-promoted Pt catalysts was prepared and evaluated in the oxidation of HDO in liquid water under different dioxygen pressures without the addition of base. Extensive characterization of as-prepared and used catalysts was performed in an attempt to correlate reactivity results to catalyst structure. In addition, the influence of reaction conditions (HDO concentration, dioxygen pressure, temperature) and the kinetic isotope effect of deuterated oxide solvent were investigated over Pt/C and Bi-Pt/C.

3.2. Experimental methods

3.2.1. Catalyst preparation

The 2.69 wt% Pt/C (Sigma-Aldrich) catalyst was used as received. The Bi-promoted Pt catalysts were prepared by the selective deposition of Bi on Pt nanoparticles.[27] First, 2 g of Pt/C was pre-reduced by H_2 (GT&S 99.999%) flow (100 cm^3 min^{-1}) in 250 cm^3 distilled and deionized water stirred at 600 rpm at room temperature. After 30 min, 0.429 cm^3 acetic acid (Sigma-Aldrich, 99.9%) was added and an appropriate amount of $Bi(NO_3)_3 \cdot 5H_2O$ (Sigma-Aldrich, 99.999%) in 2 wt% aqueous acetic acid solution was dropped into the slurry within 30 min under H_2 flow. After waiting an additional 15 min, the catalysts were filtered, washed thoroughly with distilled and deionized water, and dried at room temperature. The as-prepared catalysts were denoted as xBi-Pt/C, where x is the nominal atomic ratio of Bi to Pt.

To study the effect of reaction conditions on xBi-Pt/C, a catalyst was recovered after HDO oxidation at 328 K under 0.02 MPa O_2 in 0.1 M HDO solution, washed with distilled and deionized water and dried at room temperature. The used catalyst after reaction was denoted as xBi-Pt/C-R. To study the effect of the pretreatment of the catalyst prior to reaction, fresh xBi-Pt/C that was treated at 328 K under He atmosphere in 0.1 M HDO solution for 30 min was recovered, washed and dried at room temperature and was denoted as xBi-Pt/C-P.

3.2.2. Characterization of catalysts

The specific surface area was measured by N_2 sorption using a Micromeritics ASAP 2020. The samples were evacuated for 600 min at 393 K prior to the N_2 sorption, after which adsorption isotherms were measured at 77 K. The Brunauer–Emmett–Teller (BET) method was used to determine the specific surface area.

The fraction of available Pt on the surface of a catalyst was estimated by H_2 chemisorption using the Micromeritics ASAP 2020. The catalysts were heated to 473 K at 4 K min^{-1} under flowing H_2 (GTS Welco 99.999%) and reduced for 2 h. The samples were then evacuated for 2 h at 473 K before being cooled to 308 K for analysis in the pressure range of 1.33 – 59.9 kPa. The amount of exposed Pt was evaluated by the total amount of H_2 adsorbed, extrapolated to zero pressure, assuming a stoichiometry (H/Pt_{surf}) equal to unity.

The X-ray diffraction (XRD) patterns were recorded using a PANalytical X'Pert Pro MPD (Multi-Purpose Diffractometer) instrument with Cu Kα radiation (45 kV, 40 mA) and scanning of 2θ from 10° to 70° with a step size of 0.0025° at a rate of 1° min^{-1}.

To estimate the metal particle sizes, scanning transmission electron microscopy (STEM) was performed on an FEI Titan 80-300 operating at 300 kV. A sample was also characterized with a JEOL 2010 F operating at 200 kV that is equipped with an Oxford Aztec energy dispersive spectrometer (EDS) system for single nanoparticle EDS and with an Hitachi HF-3300 that is equipped with a Bruker SDD-EDS system for elemental mapping. To prepare a sample, ~1 mg of catalyst was suspended in 10 cm^3 of ethanol by agitating the mixture for 30 min in a sonication bath. A copper grid was dipped into the solution to capture the particles and the ethanol was thoroughly evaporated before microscopy.

Scanning electron microscopy (SEM) was performed on an FEI Quanta 650 FEG-SEM operated at 2 kV and a working distance of 10 mm under the secondary electron imaging mode. The sample was prepared by adhering the catalyst powders to a copper conductive tape on a sample stage.

The X-ray photoelectron spectroscopy (XPS) was carried out at the Nanomaterials Core Characterization Facility of the Virginia Commonwealth University (Richmond, VA), utilizing a Thermo Scientific ESCALAB 250 spectrometer equipped with a focused monochromatic Al Kα X-ray radiation source (1486.6 eV) and a hemispherical analyzer with a 6-element multichannel detector. The incident X-ray beam was 45° off normal to the sample while the X-ray photoelectron detector was normal to the sample. A large area magnetic lens with a 500 μm spot size in constant analyzer energy mode was utilized with a pass energy of 20 eV for region scans. Charge compensation was employed during data collection with an internal electron flood gun (2 eV) and a low energy external Ar ion flood gun. All spectra were deconvoluted with a curve fitting routine in CasaXPS software. The background was corrected using the linear method and the binding energy of the C 1s peak assigned at 284.5 eV, which is attributed to the support, was used to reference the peak positions.[53] The integral of each peak was calculated after subtracting the background and fitting with a combination of Gaussian and Lorentzian curves of variable proportion. The Pt:Bi surface atomic ratios were calculated from peak areas normalized by atomic subshell photoionization cross sections of the corresponding element[54]. The detailed XPS curve fitting parameters are listed in Table 3.1.

Table 3. 1 XPS curve fitting parameters used in Casa XPS(Version 2.3.16)

Species	Pt(0)	Bi(0)	Bi(III)
Position (eV)	70.3 – 71.3	156.5 – 157.8	158.8 – 160.0
FWHM	0.3 – 1.5	0.2 – 1.2	1 – 2.5
Line shape	LA(1.2,85,70)	LA(1.2,85,70)	GL(30)

Elemental analysis was used to determine some of the Pt and Bi weight loadings on the catalysts and the concentration of leached Pt and Bi in the reaction solution after 4 h of HDO oxidation. Elemental analysis was performed by Galbraith Laboratories (2323 Sycamore Drive, Knoxville, TN 37921) using inductively coupled plasma – atomic emission spectroscopy (ICP-AES).

X-ray absorption spectroscopy at the Pt L_{III} and Bi L_{III} edges was collected at beamline X-18B at the National Synchrotron Light Source, Brookhaven National Laboratory. The storage ring was operated at 2.8 GeV and 300 mA. The $(NH_3)_4Pt(NO_3)_2$ (Sigma-Aldrich, 99.995%), $Bi(NO_3)_3$ (Sigma-Aldrich, 99.999%), Pt/C and Bi-Pt/C samples were ground into fine powders and spread over Kapton tape. The XAS data were processed using the Demeter software package.[55]

3.2.3. Oxidation of 1,6-hexanediol

The high-pressure, semi-batch alcohol oxidation reactions were performed in a 50 cm^3 Parr Instrument Company 4592 batch reactor with a 30 cm^3 glass liner. An aqueous 0.1 M HDO solution (10 mL) and 0.0132 g catalyst were added to the glass liner. The glass liner was inserted into the reactor, sealed, purged with He (GTS Welco, 99.999%), heated to 328 K, and held for 20 min. The reaction was initiated by pressurizing the reactor with O_2 (GTS Welco, 99.993%) in the range of 0.2 – 1 MPa. In the low O_2 pressure region (0.02 – 0.1 MPa), the reactions were performed in a 100 mL flask reactor equipped with gas inlet and outlet, reflux condenser, thermometer and magnetic stir bar. In a typical run, an aqueous 0.1 M HDO solution (50 mL) and 0.0660 g catalyst were added to the reactor, heated to 328 K under He flow (100 mL min^{-1}) and held for 20 min. The reaction was initiated by the flow of a He and O_2 mixture with a total flow rate of 100 mL min^{-1}. The O_2 pressure in the reactor was adjusted by varying the flow rates of He and O_2. Liquid samples were periodically removed and the catalyst was removed using a 0.2 μm PTFE filter before product analysis with a Waters e2695 high performance liquid chromatograph (HPLC) equipped with refractive index detector. Product separation in the HPLC was accomplished on an Aminex HPX-87H column (Bio-Rad) operating at 318 K with an aqueous 5 mM H_2SO_4 solution as the mobile phase flowing at 5 cm^3 min^{-1}. The retention times and calibration curves were determined by injecting known concentrations of standards. Carbon balances were always greater than 90%.

The maximum O_2 transport rate from the gas phase to the aqueous phase in the pressurized reaction system was determined by the sulfite oxidation method.[56] The amount of catalyst added to the reactor was chosen so that the alcohol oxidation rate would not be limited by O_2 mass transfer from the gas to the liquid. Selectivity to a specific product is defined as moles of that product formed divided by moles of all products produced. The initial turnover frequency (TOF) [mol alcohol converted $(\text{mol metal}_{\text{surface}})^{-1}$ s^{-1}] was calculated from the initial conversion of the alcohol, usually within the first 5 min of the reaction. A sample was also taken at 10 min to confirm that significant deactivation had not occurred in the initial rate determination. An estimate of surface Pt is needed to calculate a turnover frequency because Bi is not active for oxidation catalysis. Since Bi is highly mobile under reaction conditions (to be discussed later) whereas Pt nanoparticles are stable, we normalized the initial rate of HDO conversion to the estimated fraction of Pt atoms that can be exposed to the surface during reaction, which is determined from H_2-chemisorption of Pt/C before the Bi deposition.

3.3. Results

3.3.1. Characterization of the Bi-promoted Pt catalysts

3.3.1.1 As-synthesized materials

During the preparation of Bi-Pt/C catalysts, the goal was to selectively deposit Bi on carbon-supported Pt nanoparticles in the presence of H_2 via spillover of adsorbed hydrogen.[57] To study the structure of Bi-Pt/C prepared in this study, commercial Pt/C and Bi-promoted Pt/C were extensively characterized.

The Pt/C and as-prepared 0.6Bi-Pt/C samples were examined by SEM and N_2 sorption to explore whether the carbon support was stable under conditions used for Bi incorporation. As shown in Figures 3.1a and 3.1b, the size of the carbon support particles was approximately the same for Pt/C and 0.6Bi-Pt/C. The majority of carbon particles were below 15 μm while some larger particles (~25μm) were still observed. The surface area of Pt/C and 0.6Bi-Pt/C was 1.15×10^3 and 1.10×10^3 m^2 g^{-1}, respectively, indicating that the porous structure of the carbon support was maintained after the deposition of Bi on Pt/C.

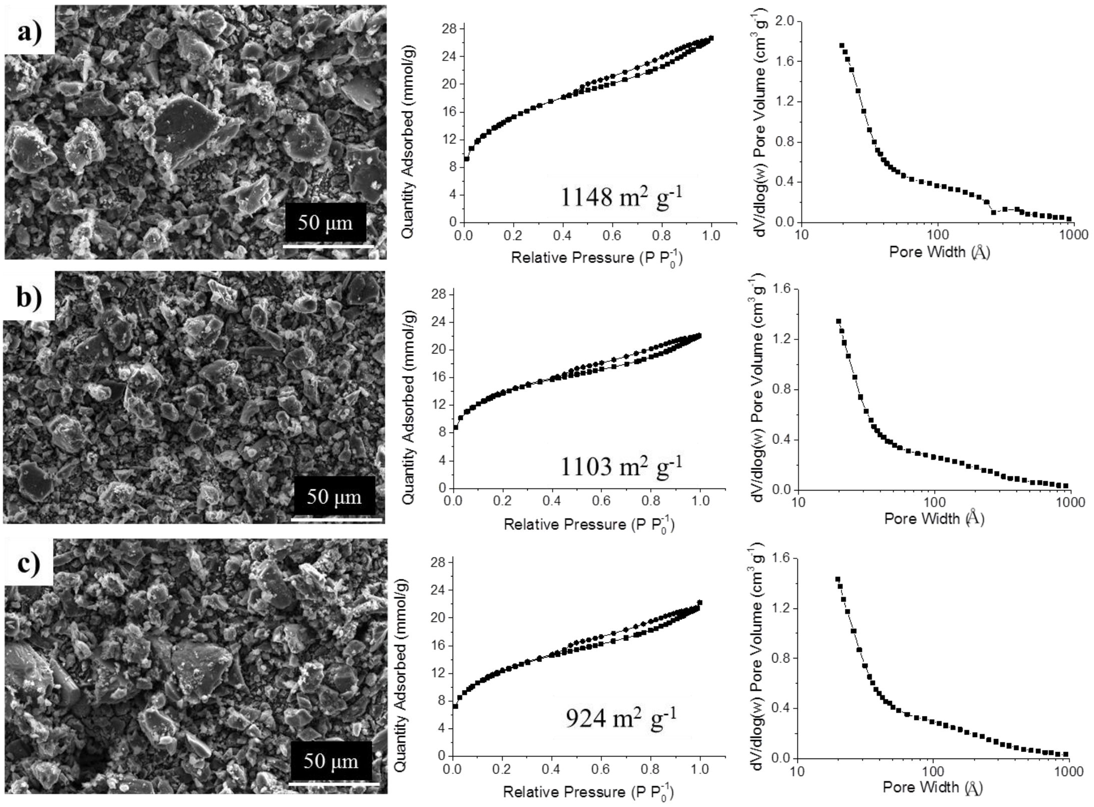

Figure 3. 1. SEM images, N_2 sorption isotherm, measured surface areas measured and pore size distribution curves of a) Pt/C as received; b) 0.6Bi-Pt/C as-prepared and c) 0.6Bi-Pt/C-R recovered after 4 h of 1,6-hexanediol oxidation under 0.02 MPa O_2 at 328 K.

The Pt/C and Bi-Pt/C catalysts were also characterized by XPS to investigate the oxidation states and distributions of Pt and Bi throughout the carbon support particles. The Pt $4f_{7/2}$ and Bi $4f_{7/2}$ spectra of 0.6Bi-Pt/C are shown Figure 3.2 and the fitting results are summarized in Table 3.2. The average Bi:Pt atomic ratio from XPS (2.4) is much higher than that from ICP-AES analysis (0.63) as shown in Table 3.3, suggesting an enrichment of Bi in the surface region of the carbon support particles. The XPS analysis also revealed the oxidation states of Pt and Bi. In the high vacuum chamber of the spectrometer, Pt was in the metallic state, with the binding energy of Pt $4f_{7/2}$ at approximately 71 eV while the majority of Bi (86 %) was present as Bi(III). Similar results from XPS were reported by Mallet et al.[27]

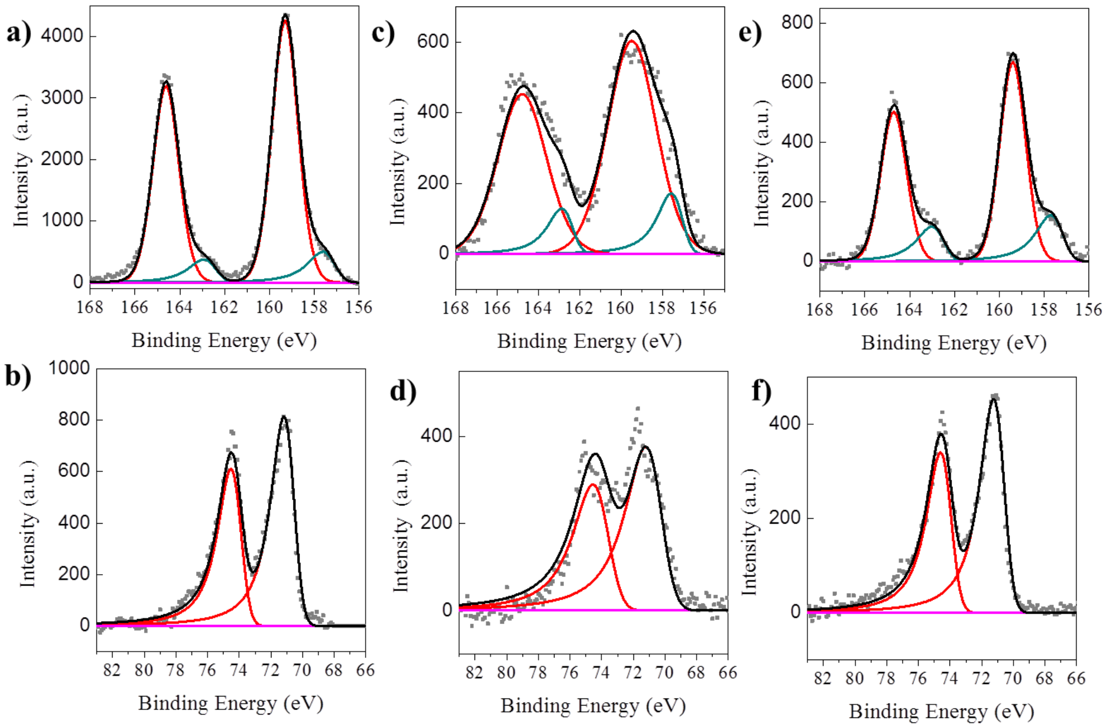

Figure 3. 2. The Bi $4f_{7/2}$ X-ray photoemission spectra of a) 0.6Bi-Pt/C, c) 0.6Bi-Pt/C-P and e) 0.6Bi-Pt/C-R and the Pt $4f_{7/2}$ spectra of b) 0.6Bi-Pt/C, d) 0.6Bi-Pt/C-P and f) 0.6Bi-Pt/C-R. 0.6Bi-Pt/C-P was recovered after 20 min pretreatment in 0.1 M 1,6-hexanediol under He flow at 328 K. 0.6Bi-Pt/C-R was recovered after 4 h reaction of 1,6-hexanediol oxidation under 0.02 MPa O_2 at 328 K. The fitting results are summarized in Table 3.2.

Table 3. 2. XPS binding energies (Pt, Bi) and surface compositions of 0.6Bi-Pt/C, 0.6Bi-Pt/C-P and 0.6Bi-Pt/C-R[a].

Sample	Area	Binding Energy (eV)			Bi(0)	Bi(III)	Pt:C[d]	Bi:Pt[d]
		Bi(0)	Bi(III)	Pt(0)	%	%		
0.6Bi-Pt/C	1	157.0	159.6	70.8	13	87	0.0030	2.4
	2	157.3	159.4	70.8	14	86	0.0028	2.4
	3	157.3	159.3	70.7	14	86	0.0030	2.3
	Avg	–	–	–	14	86	0.0029	2.4
0.6Bi-Pt/C-P[b]	1	157.2	159.5	70.5	16	84	0.0028	0.85
	2	157.0	159.3	70.6	13	87	0.0030	0.95
	3	157.0	159.6	70.6	13	87	0.0033	0.80
	Avg	–	–	–	14	86	0.0030	0.87
0.6Bi-Pt/C-R[c]	1	157.4	159.4	70.5	25	75	0.0034	0.64
	2	157.4	159.5	70.8	16	84	0.0031	0.66
	3	157.0	159.6	70.8	32	68	0.0031	0.69
	Avg	–	–	–	25	75	0.0032	0.66

a: Three different regions of each sample were analyzed. The spectra are shown in Figure 3.2.

b: Catalyst collected after 20 min of pretreatment in 0.1 M 1,6-hexanediol under He flow at 328 K.

c: Catalyst collected after 4 h of 1,6-hexanediol oxidation at 0.02 MPa O_2 at 328 K.

d: Atomic ratio of Bi:Pt was corrected by atomic subshell photoionization cross sections of corresponding element [54].

Table 3. 3 Elemental analysis of 0.6Bi-Pt/C and 0.6Bi-Pt/C-R[a].

Sample	Pt (wt%)	Bi (wt%)	Pt:C (atomic)	Bi:Pt (atomic)
0.6Bi-Pt/C	2.69	1.82	0.0017	0.63
0.6Bi-Pt/C-R[a]	2.42	1.62	0.0015	0.63

a: Analyzed by ICP-AES method.

b: Catalyst was collected after 4 h of 1,6-hexanediol oxidation at 0.02 MPa O_2 at 328 K.

The XAS results of Pt/C and Bi-Pt/C are shown in Figure 3.3. The addition of Bi to the Pt catalyst resulted in a decrease in the relative white line intensity at the Pt L_{III} edge, which was attributed to Bi species deposited on the Pt particles.[21] In contrast to XPS, which was measured in high vacuum, air-exposed Pt/C and 0.3Bi-Pt/C revealed Pt to be partially oxidized, as supported by both a higher relative white line intensity at the Pt L_{III} edge compared to a reference Pt foil (Figure 3.3a) and a Pt-O feature shown in the Fourier transform of the extended X-ray absorption fine structure (EXAFS) (Figures 3.3b and 3.3c). The oxidized Pt measured in XAS was most likely due to chemisorption of oxygen on the Pt nanoparticles. As reported by Gracia et al., the fraction of oxidized Pt increased significantly with the decreasing particle size under oxidizing conditions.[58] Note that although the EXAFS and the relative white line intensity revealed partially oxidized Pt in Pt/C and 0.6Bi-Pt/C, the Pt L_{III} edge threshold energy of Pt/C and 0.6Bi-Pt/C was consistent with the Pt metal foil and significantly shifted from the edge of $(NH_3)_4Pt(NO_3)_2$ in which Pt is in the 2+ oxidation state (Figure 3.3a). The inconsistency of white line intensity and the low edge energy was also reported elsewhere,[28] which may be related to adsorbents on nanoparticles, such as water, resulting in a shift of XANES to a lower energy.[59]

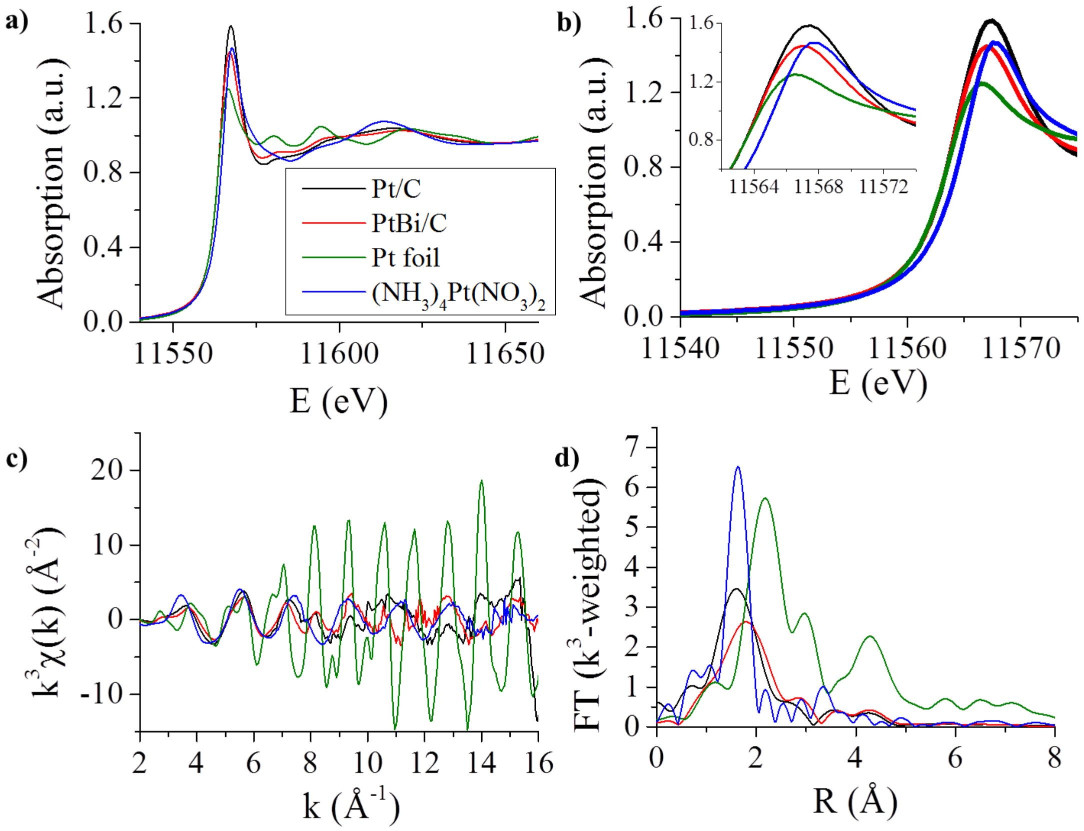

Figure 3. 3. Normalized XAS spectra at the Pt L_{III} edge (a), Normalized XANES spectra at the Pt L_{III} edge (b), k^3-weighted EXAFS data in *k*-space (c) and *r*-space (d) collected during exposure of Pt/C (black), 0.3Bi-Pt/C (red), Pt foil (green) and $(NH_3)_4Pt(NO_3)_2$ (blue) to air.

The metal particle sizes of Pt/C, 0.3Bi-Pt/C and 0.6Bi-Pt/C catalysts were determined by STEM. The dark-field STEM images of carbon-supported Pt and Bi-Pt catalysts showed a narrow size distribution of observed nanoparticles, with the majority of them in the range of 0.5 – 3.0 nm (Figures 3.4 and 3.5). As summarized in Table 3.4, the number average diameter for catalysts with different Bi loading were similar (1.4 ± 0.5 nm for Pt/C and 0.3Bi-Pt/C; 1.5 ± 0.5 nm for 0.6Bi-Pt/C). The similar metal particle sizes in this study eliminated size as a factor that might influence the observed catalytic performance. The surface-weighted average diameters were also similar for Pt/C and Bi-Pt/C (Table 3.4), indicating that the fraction of exposed metal atoms for catalysts with different Bi loadings was similar.

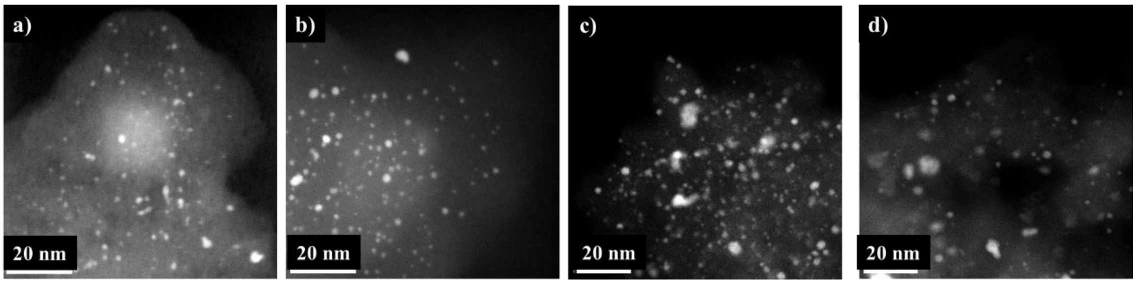

Figure 3. 4. Dark-field STEM images of a) Pt/C, b) 0.3Bi-Pt/C, c) 0.6Bi-Pt/C and d) 0.6Bi-Pt/C-R recovered after 4 h of 1,6-hexanediol oxidation under 0.02 MPa O_2 at 328 K.

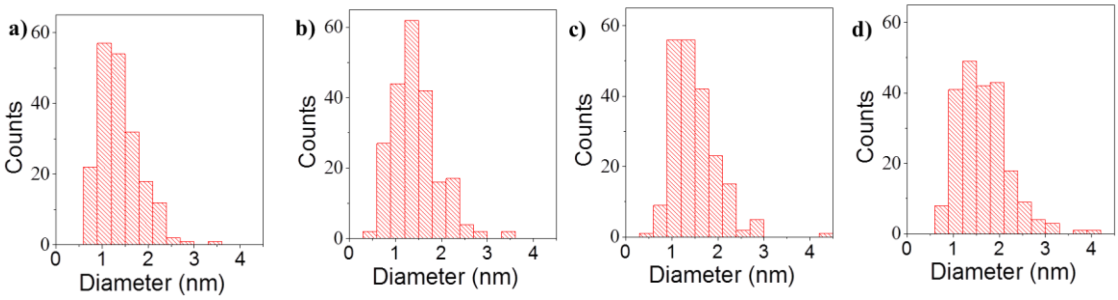

Figure 3. 5. Particle size distributions obtained from STEM of a) Pt/C, b) 0.3Bi-Pt/C, c) 0.6Bi-Pt/C and d) 0.6Bi-Pt/C-R recovered after 4 h of 1,6-hexanediol oxidation under 0.02 MPa O_2 at 328 K.

Table 3. 4 Summary of results from H_2 chemisorption and electron microscopy of Pt/C and Bi-Pt/C catalysts.

Catalysts	H/Pt[a]	Avg diameter (nm)	Surface-weighted Avg diameter[b] (nm)	Fraction of surface atoms[c]
Pt/C	0.63	1.4 ± 0.5	1.7	0.59
0.09Bi-Pt/C	0.52	–	–	–
0.18Bi-Pt/C	0.44	–	–	–
0.3Bi-Pt/C	0.37	1.4 ± 0.5	1.8	0.56
0.45Bi-Pt/C	0.27	–	–	–
0.6Bi-Pt/C	0.18	1.5 ± 0.5	1.8	0.56
0.6Bi-Pt/C-R[d]	–	1.6 ± 0.5	2.0	0.50

a: Determined from H_2-chemisorption, assuming a nominal loading of Pt.

b: Obtained from TEM by calculating $\Sigma d^3/\Sigma d^2$.

c: Estimated from the inverse of surface-weight average diameter ($1/d$) [60].

d: Catalysts collected after 4 h of 1,6-hexanediol oxidation reaction under 0.02 MPa O_2 at 328 K.

The X-ray diffraction patterns of Pt/C and Bi-Pt/C catalysts are presented in Figure 3.6. The peak at around $2\theta = 25^\circ$ was attributed to graphitic carbon (JCPDS 23-0064) while the peak close to $2\theta = 40^\circ$ was attributed to the (111) reflection of Pt (JCPDS 04-802). No significant shift in the diffraction patterns of Bi-Pt/C samples was observed compared to the unpromoted Pt catalyst, suggesting that Pt-Bi alloys were not likely formed under the mild conditions used to prepare the Bi-promoted catalysts. The broad, low-intensity Pt features in the diffraction patterns indicate that Pt particles were well-dispersed on the support, which is in agreement with the small particle sized observed in STEM (Figure 3.4). Although features of Bi_2O_3 and $Bi_2Pt_2O_7$ were observed on 0.9Bi-Pt/C,[61] the diffraction patterns of bismuth metal and bismuth oxide [62] were not detected for xBi-Pt/C (x = 0 – 0.6), indicating that Bi species were well-dispersed over the carbon support and/or Pt particles when the Bi:Pt atomic ratio was less than 0.6.

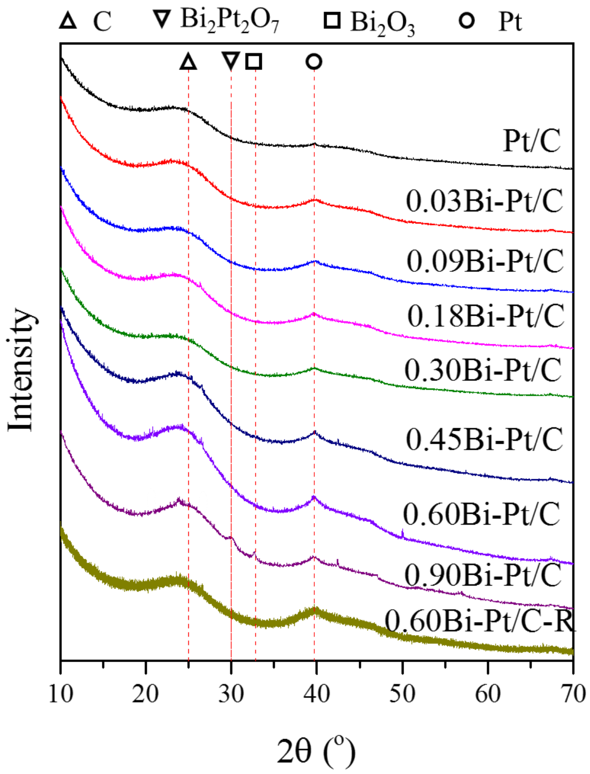

Figure 3. 6. XRD patterns, offset for clarity, of Pt/C and Bi-Pt/C bimetallic catalysts.

Chemisorption of H_2 was utilized to probe the surface composition of the Bi-promoted Pt nanoparticles. The ratio of adsorbed hydrogen atoms to total platinum atoms is shown in Table 3.4. With an increasing amount of Bi, the H/Pt ratio decreased from 0.63 for Pt/C to 0.18 for 0.6Bi-Pt/C (Figure 3.7). Because the fraction of exposed metal atoms, estimated from STEM, was similar for Pt/C and Bi-promoted Pt/C catalysts (Table 3.4), the decrease in H_2 chemisorption capacity indicates that the Bi promoter (Bi metal or Bi oxide) was present on the surface of Pt particles and blocked hydrogen uptake on Pt sites.

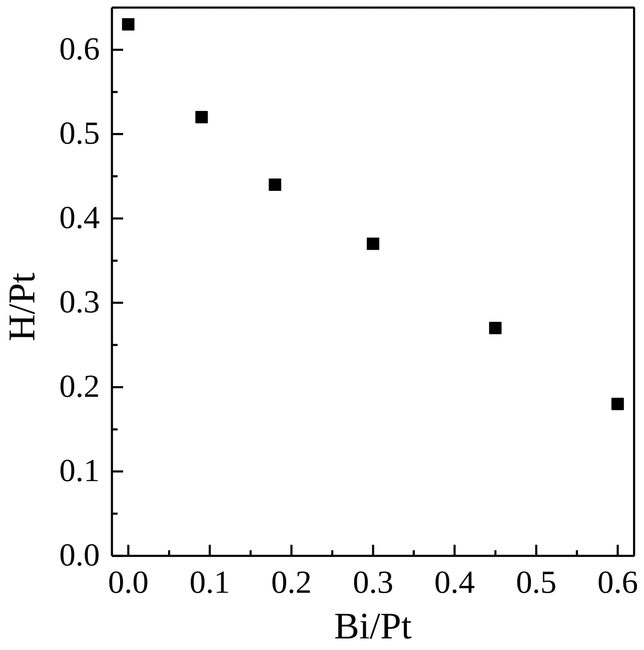

Figure 3. 7. H/Pt ratio of *x*Bi-Pt/C catalyst ($x = 0, 0.09, 0.18, 0.30, 0.45, 0.6$).

To further investigate the composition of nanoparticles, Bi-Pt/C was examined by energy-dispersive X-ray spectroscopy (EDS) in our electron microscope operating in the STEM mode. Single-nanoparticle EDS was first performed on twenty nanoparticles, which were chosen randomly (Figures 3.8a and 3.8b), and the elemental composition of each particle is listed in Table 3.5. As shown in Figure 3.8a and Table 3.5, both Pt and Bi signals were detected in most particles and the average elemental composition of particles on 0.6Bi-Pt/C is 72 ± 15% Pt and 28 ± 15% Bi. The relatively narrow distribution of elemental compositions indicates that during the preparation, the Bi was deposited selectively on the Pt particles rather than the carbon support. The overall elemental composition of 0.6Bi-Pt/C from ICP-AES analysis was 61% Pt and 39% Bi, which is in the confidence interval of elemental composition obtained from EDS. Additional STEM-EDS mapping further supported the conclusion that Bi species were selectively deposited on the Pt particles in Bi-Pt/C. The dark-field image, presented in Figure 3.9a, contained relatively large nanoparticles (~ 3 nm) to ensure sufficient EDS counts. The corresponding EDS map of Pt (blue), Bi (red) and the overlayed map of Pt and Bi are shown in Figures 3.9b, 3.9c and 3.9d, respectively. Both the Pt and Bi EDS maps overlapped well with the dark field image. In the regions where nanoparticles appeared, Pt and Bi EDS signals appeared simultaneously. An STEM-EDS mapping study over a larger area was also performed and confirmed that Pt and Bi signals appeared in the same region (Figure 3.10).

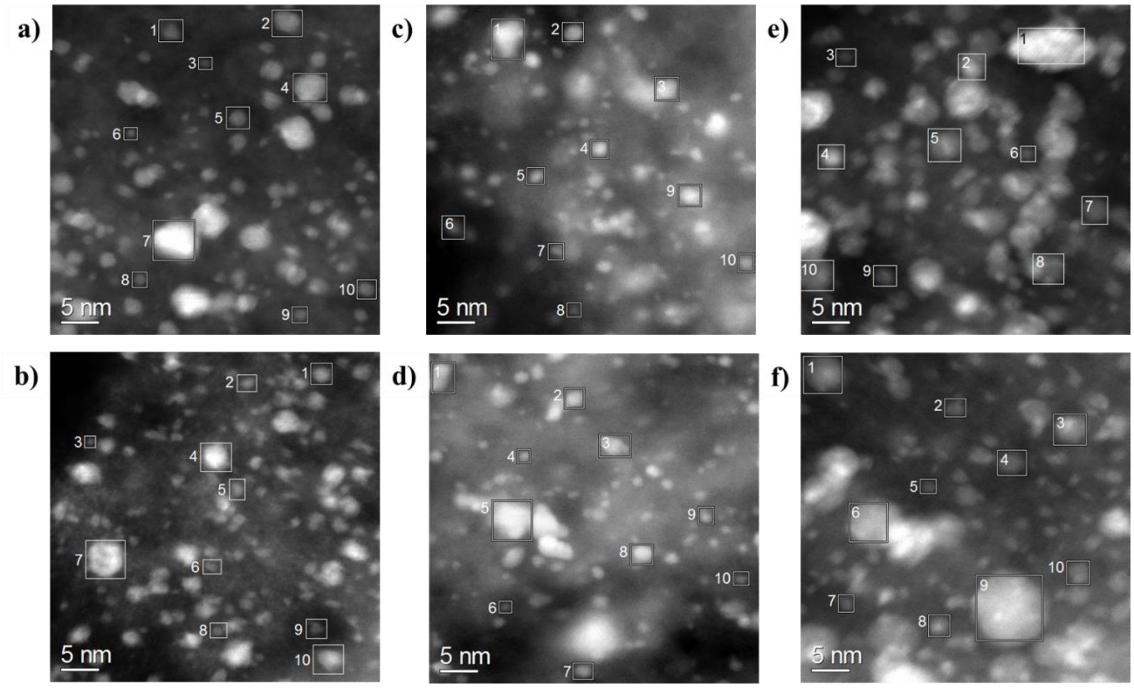

Figure 3. 8. Regions for EDS analysis of a) b) 0.6Bi-Pt/C, c) d) 0.6Bi-Pt/C-P and e) f) 0.6Bi-Pt/C-R. 0.6Bi-Pt/C-P was recovered after 20 min pretreatment in 0.1 M hexanediol under He flow at 328 K. 0.6Bi-Pt/C-R was recovered after 4 h reaction of HDO oxidation under 0.02 MPa O_2 at 328 K. The corresponding compositions of analysis region are shown in Table 3.3.

Table 3. 5 Elemental compositions from EDS of 0.6Bi-Pt/C, 0.6Bi-Pt/C-P and 0.6Bi-Pt/C-R[a].

0.6Bi-Pt/C			0.6Bi-Pt/C-P[b]			0.6Bi-Pt/C-R[b]		
Region	Pt (mol %)	Bi (mol %)	Region	Pt (mol %)	Bi (mol %)	Region	Pt (mol %)	Bi (mol %)
a1	60	40	c1	80	20	e1	75	25
a2	74	26	c2	93	7	e2	76	24
a3	97	3	c3	84	16	e3	55	45
a4	83	17	c4	61	39	e4	82	18
a5	60	40	c5	64	36	e5	61	39
a6	69	31	c6	80	20	e6	49	51
a7	83	17	c7	52	48	e7	0	100
a8	50	50	c8	60	40	e8	79	21
a9	87	13	c9	61	39	e9	25	75
a10	88	12	c10	59	41	e10	76	24
b1	62	38	d1	79	21	f1	0	100
b2	50	50	d2	79	21	f2	0	100
b3	90	10	d3	79	21	f3	38	62
b4	75	25	d4	57	44	f4	0	100
b5	69	31	d5	85	15	f5	43	57
b6	55	45	d6	79	21	f6	11	89
b7	52	38	d7	75	25	f7	49	51
b8	60	40	d8	86	14	f8	68	32
b9	70	30	d9	69	31	f9	59	41
b10	100	0	d10	83	17	f10	46	54
Avg	72±15	28±15	Avg	73±12	27±12	Avg	45±30	55±30

a: The corresponding regions for EDS analysis are shown in Figure 3.8.

b: Catalyst collected after 20 min of pretreatment in 0.1 M 1,6-hexnaediol under He flow at 328 K.

c: Catalyst collected after 4 h of 1,6-hexanediol oxidation under 0.02 MPa O_2 at 328 K.

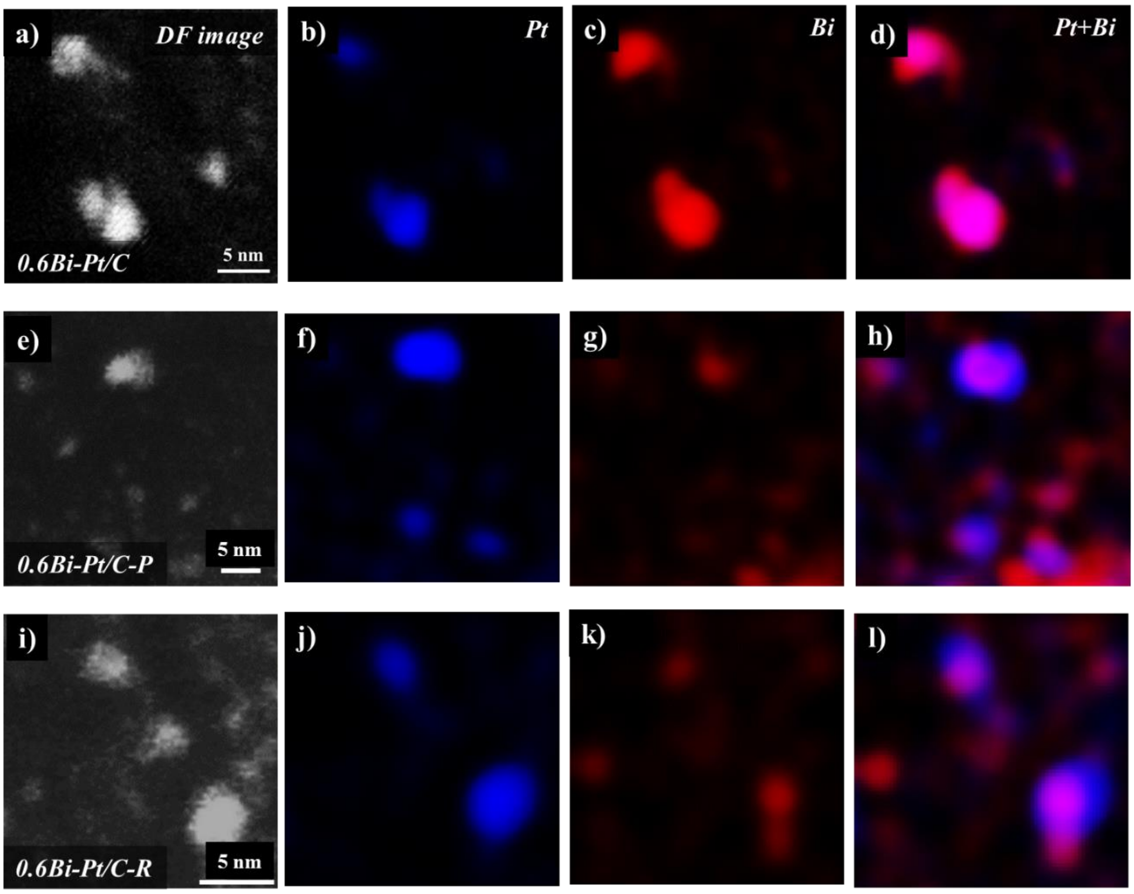

Figure 3. 9. STEM-EDS-map of 0.6Bi-Pt/C (a, b, c, d), 0.6Bi-Pt/C-P (e, f, g, h) and 0.6Bi-Pt/C-R including (i, j, k, l) including dark-field STEM images (a, e, i), EDS map of Pt (b, f, j), EDS map of Bi (c, g, k) and the overlayed map of Pt and Bi (d, h, l). (For interpretation of the references to color in this figure legend, the reader is referred to the web version of this article.)

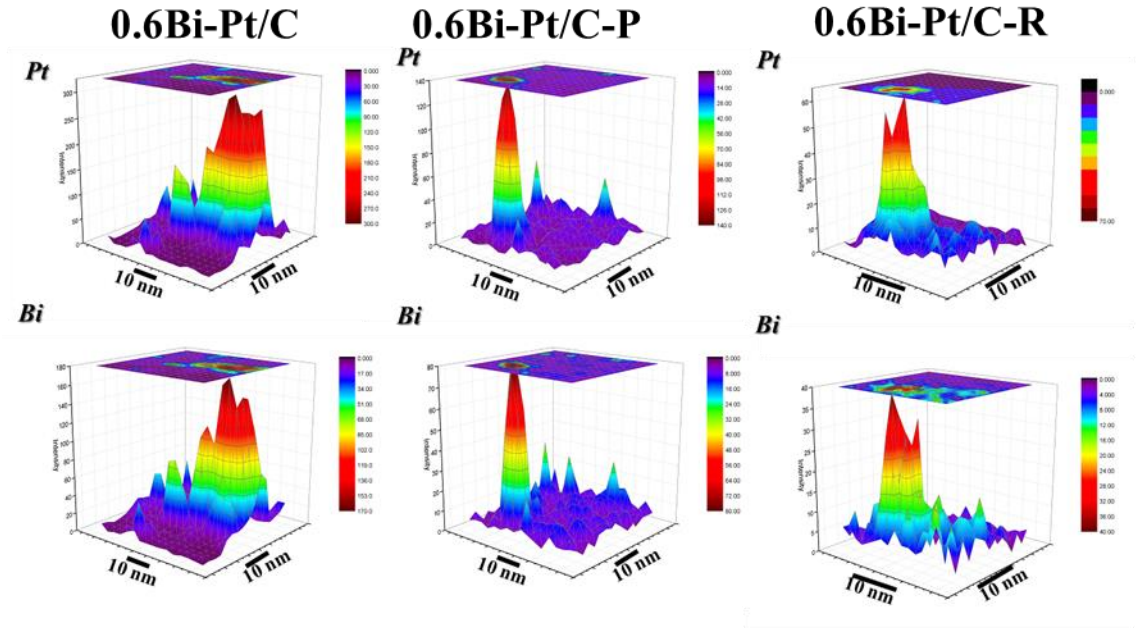

Figure 3. 10. Pt and Bi EDS mapping of 0.6Bi-Pt/C, 0.6Bi-Pt/C-P and 0.6Bi-Pt/C-R in large region. 0.6Bi-Pt/C-P was recovered after 20 min pretreatment in 0.1 M hexanediol under He flow at 328 K. 0.6Bi-Pt/C-R was recovered after 4 h reaction of HDO oxidation under 0.02 MPa O_2 at 328 K.

3.3.1.2 Characterization of the Bi-promoted Pt catalysts after pretreatment and reaction

Extensive characterization suggests that xBi-Pt/C (x = 0 – 0.6) catalysts with oxidized Bi selectively deposited on Pt particles were successfully prepared. As discussed in the Introduction, structural changes of bimetallic catalysts might happen during the reaction. In the current study, a catalyst was first pretreated in alcohol solution under He at 328 K for 20 min to reduce nanoparticles in situ and then reacted in alcohol solution under various O_2 pressures. To investigate the influence of reaction environment on the structure of Bi-Pt/C catalysts, samples recovered after 20 min of the aqueous alcohol pretreatment (0.6Bi-Pt/C-P) and after 4 h of the alcohol oxidation reaction (0.6Bi-Pt/C-R) were extensively characterized.

The stability of the carbon support was examined first. An SEM image together with the measured surface area of 0.6Bi-Pt/C-R is presented in Figure 3.3c. The size of the carbon particles after reaction was similar to the as-prepared sample and the surface area of the recovered catalyst was 9.24×10^2 m^2 g^{-1}, which is slightly lower than the as-prepared 0.6Bi-Pt/C sample (1.10×10^3 m^2 g^{-1}). Evidently, the porous structure of carbon support was relatively stable and was largely maintained under the reaction conditions used in this study.

Fresh 0.6Bi-Pt/C and used 0.6Bi-Pt/C-R were analyzed by ICP-AES to check for leaching. As shown in Table 3.3, the loadings of Pt and Bi measured by ICP-AES were similar to those of the fresh catalyst, but slightly lower on the catalyst recovered from 4 h HDO oxidation. Because the atomic ratio of Bi to Pt remained constant at 0.63, we suspect the slightly lower loadings on the recovered catalyst is the result of adsorbed species on the catalyst after reaction, a conclusion also reached by Wörz et al.[29] The reaction medium was also tested for leached metals after 4 h of reaction. The concentrations of Pt and Bi were both below 6.3 ppm, the detection limit of ICP-AES, confirming that less than 2% of available Pt or Bi leached into the solution.

The 0.6Bi-Pt/C-R was also characterized by STEM to examine whether or not sintering of nanoparticles occurred during the reaction. The STEM image, the corresponding particle size distribution and the statistical analysis of the nanoparticle sizes are presented in Figures 3.4d, 3.5d and Table 3.4, respectively. The mean particle diameter of 0.6Bi-Pt/C-R is 1.6 ± 0.5 nm, which is similar to that of the as-prepared 0.6Bi-Pt/C (1.5 ± 0.5 nm). Likewise, the surface average diameter, which is related to the fraction of exposed metal sites, was also similar for 0.6Bi-Pt/C (1.8 nm) and 0.6Bi-Pt/C-R (2.0 nm). Prior work by Ide et al. has also shown that a monometallic Pt/C catalyst does not sinter during the selective oxidation of alcohols under similar conditions.[20] The negligible aggregation of Pt was also supported by results from XRD, as shown in Figure 3.6. The very weak diffraction peak associated with Pt(111) for 0.6Bi-Pt/C-R was relatively unchanged from that for as-prepared 0.6Bi-Pt/C, indicating the excellent dispersion of the Pt nanoparticles was maintained.

To investigate the oxidation state of Pt and Bi after pretreatment and reaction, 0.6Bi-Pt/C-P and 0.6Bi-Pt/C-R were interrogated by XPS and compared to as-prepared 0.6Bi-Pt/C. The Pt $4f_{7/2}$ and Bi $4f_{5/2}$ core level spectra of 0.6Bi-Pt/C-P and 0.6Bi-Pt/C-R are shown in Figures 3.2c - f and the analysis of the spectra is summarized in Table 3.2. For both 0.6Bi-Pt/C-P and 0.6Bi-Pt/C-R, the Pt remained metallic and the Bi remained oxidized. In addition, the binding energy of the features associated with $4f_{7/2}$ Pt(0), $4f_{5/2}$ Bi(0) and $4f_{5/2}$ Bi(III) were similar among the 0.6Bi-Pt/C, 0.6Bi-Pt/C-P and 0.6Bi-Pt/C-R samples. The XPS results revealed that Pt was not over-oxidized irreversibly and that there was no significant change of the electronic interaction of Pt and Bi after the pretreatment and reaction compared to the as-prepared catalyst.

Although leaching, sintering or change of oxidation state was not detected after the reaction, severe migration of Bi species was revealed by XPS and EDS. The atomic ratio of Pt:C obtained from XPS was similar for fresh 0.6Bi-Pt/C and the catalyst after pretreatment and reaction, suggesting that Pt particles did not substantially migrate on the carbon support. However, a significant decrease in Bi:Pt atomic ratio was observed on 0.6Bi-Pt/C-P (0.87) and 0.6Bi-Pt/C-R (0.66), compared to the fresh 0.6Bi-Pt/C (2.4). The Bi:Pt atomic ratio of 0.6Bi-Pt/C-P and 0.6Bi-Pt/C-R determined by XPS was similar to the overall Bi:Pt ratio (0.63) determined from ICP-AES. Since neither Bi nor Pt leached during the reaction, the results from XPS indicate a substantial migration of Bi on the carbon support and a more uniform distribution of Bi species throughout the carbon particles as a result of pretreatment and reaction.

The migration of Bi on the carbon support was also supported by the EDS study. For fresh 0.6Bi-Pt/C, single-nanoparticle EDS study shows that nanoparticles have a relatively uniform composition of Pt and Bi, indicating the selective deposition of Bi. After the pretreatment, the relatively uniform composition of Pt and Bi in the individual nanoparticles was maintained, as indicated in Figures 3.8c and 3.8d and Table 3.5. The average elemental composition of 0.6Bi-Pt/C-P is 73 ± 12% Pt and 27 ± 12 Bi, which is similar to that of as-prepared 0.6Bi-Pt/C. However, some segregation of Bi and Pt was observed on 0.6Bi-Pt/C-P in the EDS mapping study. As shown in Figures 3.9e-h, although Bi was present in the Pt-rich region, it also appeared in regions without Pt, most notably in the lower right area of the figure. The Pt and Bi EDS maps in a larger region are presented in Figure 3.10. Areas containing only Bi (no Pt) were observed in these maps as well. After 4 h of reaction, the segregation of Pt and Bi was more evident. The single-nanoparticle analysis showed a broader distribution of compositions of individual particles after reaction, which results in 45 ± 30% Pt and 55 ± 30% Bi, as shown in Table 3.5. As with 0.6Bi-Pt/C-P, regions that contained only Bi were detected on 0.6Bi-Pt/C-R, i.e., region 7 in Figure 3.8e and regions 1,2 and 4 in Figure 3.8f. Although Bi species migrated substantially on the carbon support, no diffraction pattern of Bi species was observed by XRD (presented in Figure 3.6) suggesting that Bi species remained well dispersed in the vicinity of the Pt nanoparticles or on the support.

3.3.2. Oxidation of 1,6-hexanediol

3.3.2.1.Tests for transport artifacts

The potential influence of external mass transport limitations on reaction rates was first examined by testing the effect of the stirring rate on initial activity of HDO oxidation over 0.6Bi-Pt/C, the most active catalyst, under 0.02 MPa O_2. As shown in Figure 3.11, the initial activity (TOF) first increased with stirring rate and then reached a plateau when the stirring rate exceeded 1000 rpm. In subsequent work, the stirring rate was chosen to be 1200 rpm. In addition, the maximum O_2 transport rate from the gas phase to the aqueous phase in the pressurized reaction system was determined by the sulfite oxidation method [56] and for the dioxygen pressure used here, the reaction rate did not exceed the O_2 transfer rate. Hence, at 1200 rpm, neither transport of dioxygen from the gas phase into the bulk of the liquid nor the film diffusion of HDO or O_2 to the catalyst surface limited the reaction rate.

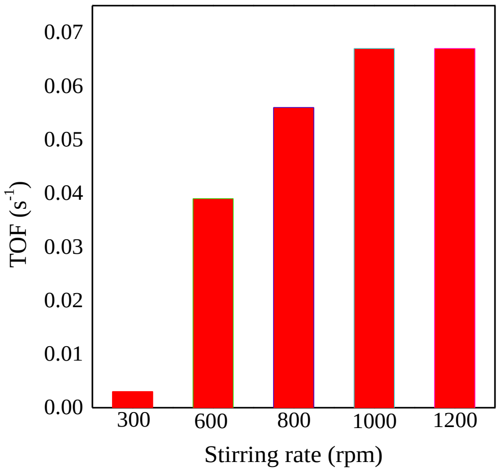

Figure 3. 11. Effect of stirring rate on measured initial activity (TOF) of 1,6-hexanediol oxidation over 0.6Bi-Pt/C. Reaction conditions: 328 K, Pt: 1,6-hexanediol = 1:500 (atomic ratio), 0.1 M 1,6-hexanediol solution, 0.02 MPa O_2.

Internal transport limitations did not affect the measured rates over Bi-Pt/C in the range of 0.02 – 1 MPa O_2 and 0.05 – 0.2 M HDO or Pt/C in the range of 0.05 – 0.2 M HDO under high O_2 pressure (0.2 – 1 MPa) because the reaction order in both HDO and O_2 is close to zero (Figure 3.12a). However, a reaction order of 0.75 with respect to O_2 pressure was observed over Pt/C in the range of 0.02 – 0.2 MPa O_2. The Weisz-Prater criterion was used to estimate the role of internal mass transport of O_2 at 0.02 MPa O_2 on the observed rate,[63] which was adapted from the work on hindered diffusion in liquid-phase glycerol oxidation over a PtBi catalyst by Wörz et al.[29]

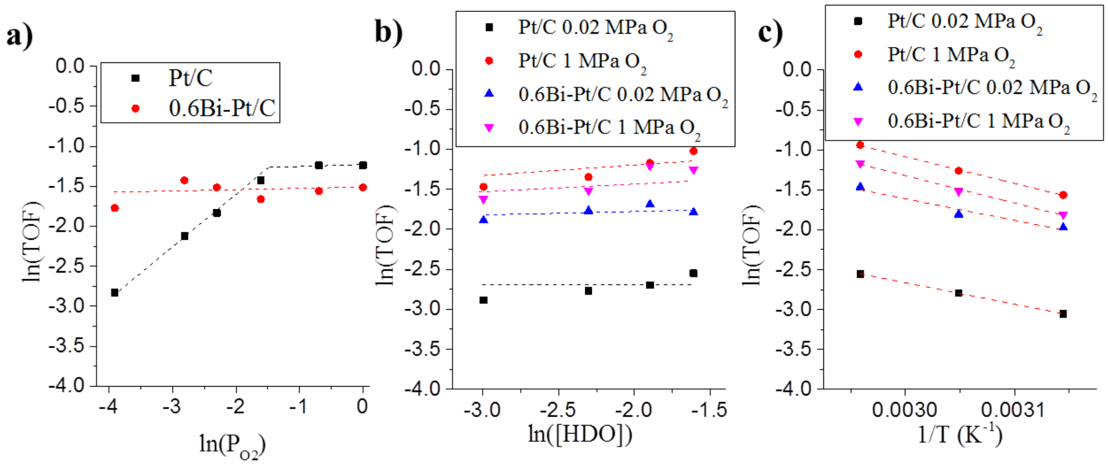

Figure 3. 12. Dependence of initial activity (TOF (s^{-1})) of 1,6-hexanediol (HDO) oxidation over Pt/C and 0.6Bi-Pt/C on a) dioxygen pressure (MPa). Reaction conditions: Pt: 1,6-hexanediol = 1:500 (atomic ratio), 0.1 M 1,6-hexanediol solution, stirring rate = 1200 rpm, 328K; b) concentration of 1,6-hexanediol (HDO) (M). Reaction conditions: 0.02 and 1 MPa O_2, stirring rate = 1200 rpm, 328K and c) inverse temperature (K^{-1}). Reaction conditions: Pt: 1,6-hexanediol = 1:500 (atomic ratio), 0.02 and 1 MPa O_2, 0.1 M 1,6-hexanediol solution, stirring rate = 1200 rpm.

Based on the Weisz-Prater criterion, the diffusion limitations are negligible when

$$\Phi_i = \frac{r^{eff} \cdot r_p^2}{c_{i,s} \cdot D_{i,mix}^{eff}} < 0.3 \qquad \mathit{1}$$

with Φ_i, the dimensionless Weisz-Prater parameter; r^{eff}, effective (observed) rate per volume of catalyst in mol s^{-1} m^{-3}; r_p, radium of the catalyst particle in m; $c_{i,s}$, concentration of i at the surface of the particle in mol m^{-3} and $D_{i,mix}{}^{eff}$, effective diffusivity of i in the mixture in m^2 s^{-1}. The Weisz-Prater parameter of O_2 was calculated under 0.02 MPa O_2 over Pt/C with different HDO concentration (0.05 – 0.2 M) and temperature (318 – 338 K). The r^{eff} was measured as the initial reaction rate (Table 3.6). The r_p was determined from the SEM image, which was estimated to be 4 μm as 1/6 of the particle diameter [64] (Figure 3.1). The $c_{i,s}$ was assumed to be the bulk concentration, $c_{i,l}$. The bulk concentration of HDO was used as the initial concentration and for O_2, Henry's law was applied [65]:

$$P_{O_2} = H_{O_2,mix} \cdot \frac{c_{O_2,l}}{c_{total}} \quad 2$$

with P_{O_2}, saturated vapor pressure of oxygen in Pa; $H_{O_2,mix}$, Henry coefficient of oxygen in the liquid mixture in Pa and c_{total} as the total concentration of liquid, which is 5.10×10^3 mol m^{-3}.[29] As the concentration of HDO is low (0.1 M), $H_{O_2,mix}$ was assumed to be equal to H_{O_2,H_2O}, which was calculated as a function of temperature according to a correlation of Rettich *et al.* [66]. The effective diffusivity, $D_{i,mix}^{eff}$, was calculated by

$$D_{i,mix}^{eff} = D_{i,mix} \cdot \frac{\varepsilon}{\tau} \quad 3$$

where ε and τ are the catalyst porosity and tortuosity, respectively, which were estimated to be 0.4 and 5, as a first approximation. The diffusion coefficient of dioxygen, $D_{O_2,mix}$, was assumed to be equal to D_{O_2,H_2O}, which was measured by Han *et al.* at different temperatures.[67]

Based on Equations 1 – 3, the Weisz-Prater parameters of dioxygen, shown in Table 3.6, were calculated under different conditions and were all below 0.3, indicating a negligible diffusional resistance in our porous catalysts.[63]

Table 3. 6 Calculated Weisz-Prater parameters for 1,6-hexanediol and dioxygen

c(HDO) (mol L^{-1})	P(O$_2$) (MPa)	T (K)	r^{eff} (mol s^{-1} m^{-3})	H_{O_2,H_2O}[66] (10^9 Pa)	c_{O_2} (mol m^{-3})	D_{O_2}[67] (10^{-9} m^2 s^{-1})	Φ_{O_2}
0.05	0.02	328	0.84	6.19	0.16	3.64	0.180
0.1	0.02	328	0.95	6.19	0.16	3.64	0.203
0.15	0.02	328	1.18	6.19	0.16	3.64	0.253
0.1	0.02	318	0.72	5.68	0.18	3.05	0.168
0.1	0.02	338	1.18	6.7	0.15	4.25	0.234

3.3.2.2.Enhanced activity of 1,6-hexanediol oxidation over Bi-promoted Pt catalyst

The series of xBi-Pt/C (x = 0, 0.03, 0.09, 0.18, 0.30, 0.45, 0.60 and 0.90) catalysts was tested in the semi-batch oxidation of HDO under 0.02 MPa O$_2$. The conversion of HDO after 15 min and 4 h is shown in Figure 3.13. Addition of Bi clearly promoted activity for alcohol oxidation relative to Pt/C. For example, the HDO conversion at 15 min increased from 2.2 % over Pt/C to 6.1% over 0.6Bi-Pt/C. A similar promotional trend was also observed after 4 h of reaction.

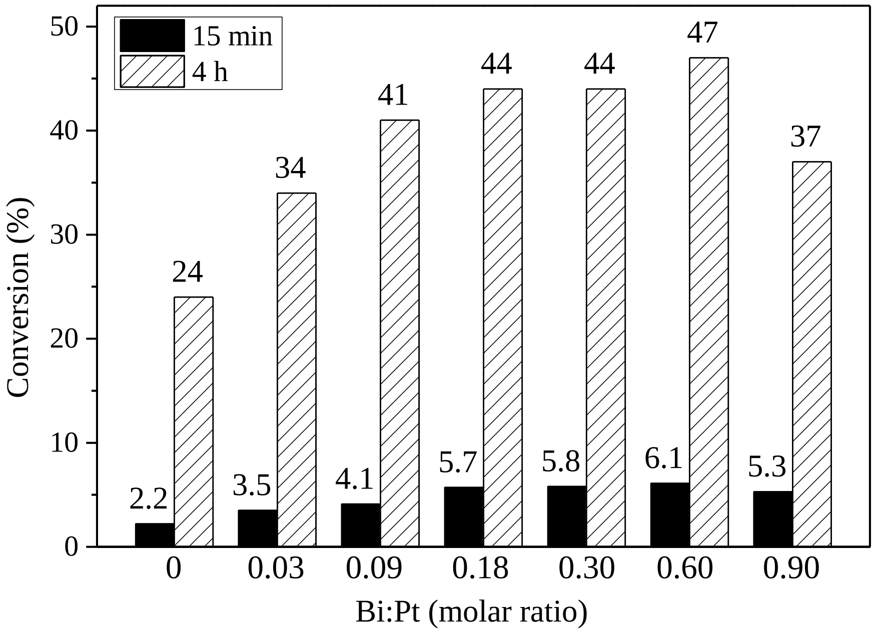

Figure 3. 13. Performance of Bi-Pt/C with different Bi:Pt ratios in oxidation of 1,6-hexanediol. Reaction conditions: 328 K, Pt: 1,6-hexanediol = 1:500 (atomic ratio), 0.1 M 1,6-hexanediol solution, 0.02 MPa O_2, stirring rate = 1200 rpm.

Among the Bi-Pt/C catalysts with different Bi loadings, the highest conversion was obtained over 0.6Bi-Pt/C. At high catalyst loading in the reactor, the 0.6Bi-Pt/C catalyst allowed for nearly stoichiometric conversion of 1,6-hexanediol to adipic acid. More specifically, a 98% yield of adipic acid was obtained after 36 h of reaction over 0.6Bi-Pt/C while the yield of adipic acid was only 43 % over an equivalent loading of Pt/C, as shown in Figure 3.14. The carbon balance was greater than 90% in both runs.

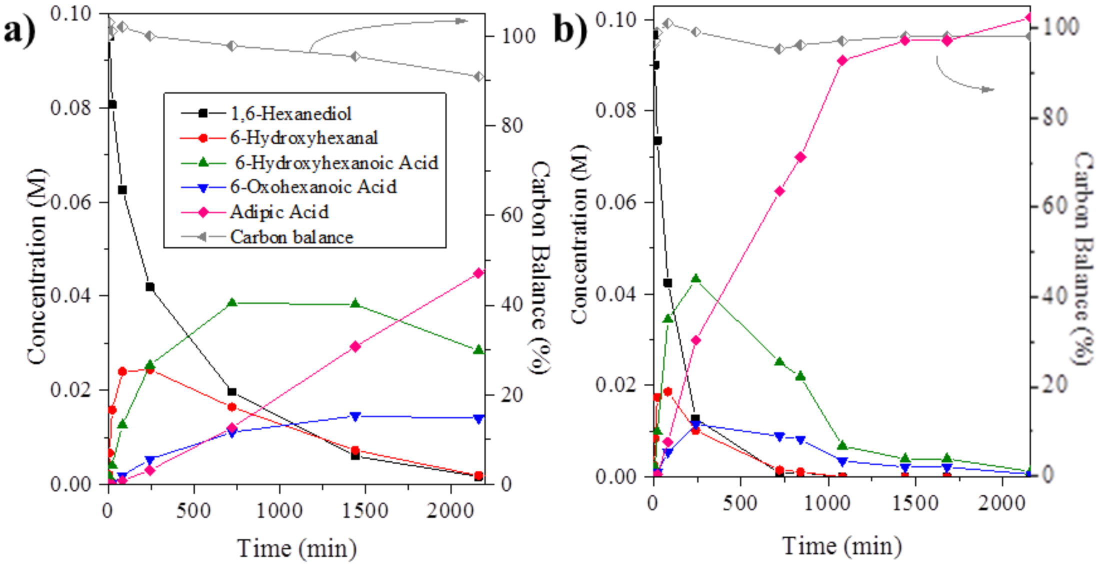

Figure 3. 14. Reaction profiles for 1,6-hexanediol oxidation over a) Pt/C and b) 0.6Bi-Pt/C. Reaction conditions: 328 K, Pt: 1,6-hexanediol = 1:100 (atomic ratio), 0.1 M 1,6-hexanediol solution, 0.02 MPa O_2, stirring rate = 1200 rpm.

The Pt/C and Bi-Pt/C catalysts were also tested under different dioxygen pressures and interestingly the effect of Bi addition on activity appeared to depend on O_2 pressure, as shown in Figure 3.15. Although the addition of Bi had a promotional effect on the rate in 0.02 MPa O_2 (Figure 3.15a), the presence of Bi inhibited the rate on Pt/C under high dioxygen pressure (1 MPa), as shown in Figure 3.15d. The influence of Bi addition on the product distribution was also examined under high (1 MPa) and low (0.02 MPa) pressure of O_2. As shown in Figure 3.16, the selectivities to 6-hydroxyhexanal, 6-hydroxyhexanoic acid and 6-oxohexanoic acid were similar over Pt/C, 0.3Bi-Pt/C and 0.6Bi-Pt/C at similar levels of conversion (20 %), indicating that the main influence of Bi is on the rate of HDO oxidation.

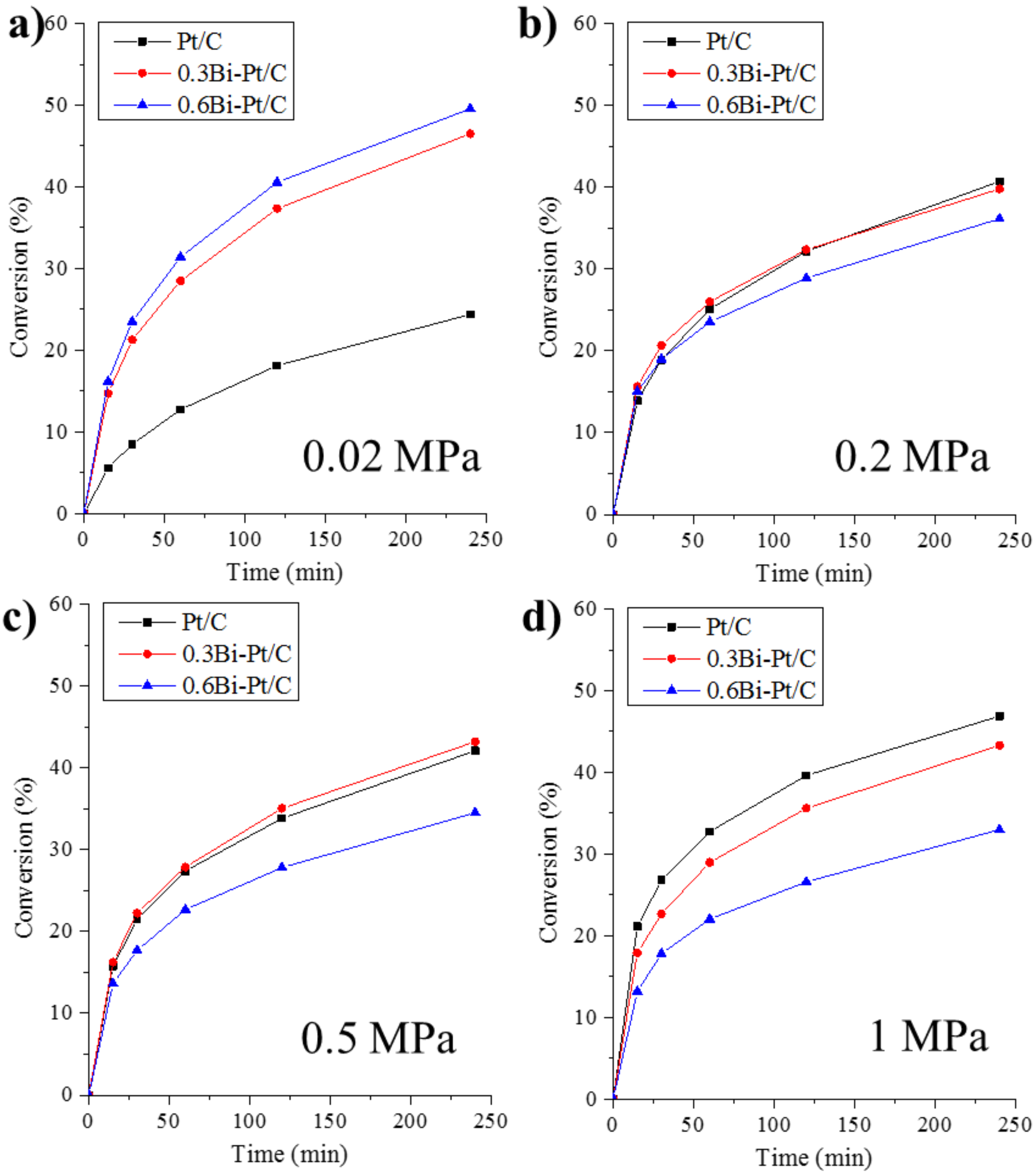

Figure 3. 15. Reaction profiles for 1,6-hexanediol oxidation over Pt/C, 0.3Bi-Pt/C and 0.6Bi-Pt/C under a) 0.02 MPa, b) 0.2 MPa, c) 0.5 MPa and d) 1 MPa dioxygen pressure. Reaction conditions: 328 K, Pt: 1,6-hexanediol = 1:500 (atomic ratio), 0.1 M 1,6-hexanediol solution, stirring rate = 1200 rpm.

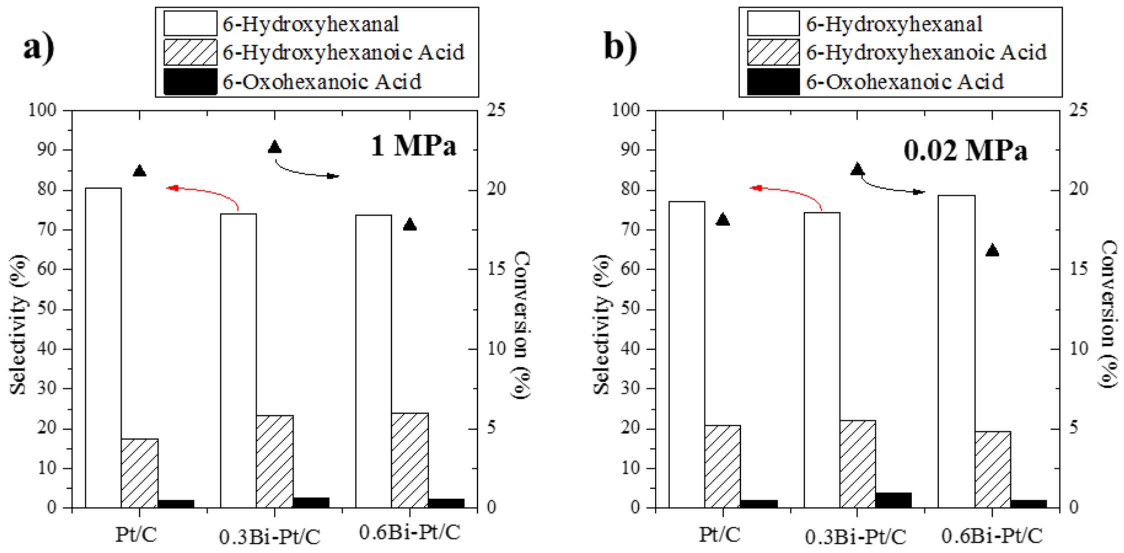

Figure 3. 16. Product distribution during 1,6-hexanediol oxidation over Pt/C, 0.3Bi-Pt/C and 0.6Bi-Pt/C (conversion ≈ 20%) under a) 1 MPa and b) 0.02 MPa O_2. Reaction conditions: 328K, Pt: 1,6-hexanediol = 1:500 (atomic ratio), stirring rate = 1200 rpm. The conversion is indicated by ▲. Only trace amounts of adipic acid were detected.

3.3.2.3.Influence of reaction conditions on HDO oxidation

Figure 3.12a summarizes the promotional effect of Bi on Pt as a function of O_2 pressure. The TOF in Figure 3.12 is based on the surface Pt atoms associated with Pt/C since our characterization indicates that Bi is a highly mobile species during pretreatment and reaction. Under low O_2 pressures, the TOF for HDO oxidation over unpromoted Pt/C increased significantly with O_2 pressure, resulting in a reaction order of 0.75 over the range of 0.02 to 0.2 MPa O_2. At high pressure (0.2 to 1 MPa O_2), the reaction was independent of O_2 (zero order) over Pt/C. When the O_2 pressure exceeds 0.2 MPa, the TOF over Pt/C actually exceeded that over 0.6Bi-Pt/C. The reaction order in O_2 for HDO oxidation over 0.6Bi-Pt/C was close to zero over the whole range of pressures from 0.02 to 1 MPa. Evidently, the observed promotional effect of Bi on Pt-catalyzed HDO oxidation is directly related to the observation that the reaction is zero order in O_2 over the promoted system even at low pressure.

The effect of substrate concentration and temperature on the reaction rate was also investigated, as shown in Figures 3.12b and 3.12c. In the range of 0.05 – 0.2 M, the oxidation of HDO was found to be nearly zero order with respect to HDO concentration at 328 K, under either 0.02 or 1 MPa O_2. Zero order behavior with respect to alcohol was also reported in other studies, indicating the saturated adsorption of HDO on the catalyst surface.[15,17,68] The apparent activation energy of HDO oxidation was also calculated from rates measured from 318 to 338 K, as shown in Figure 3.12c. The apparent activation energies (E_a) reported in Table 3.7 were similar over Pt/C and 0.6Bi-Pt/C. At low O_2 pressure (0.02 MPa), the apparent activation energies were 22 and 23 kJ mol^{-1} over Pt/C and Bi-promoted Pt/C, respectively, which are experimentally indistinguishable. Although the apparent activation energy values were higher at high O_2 pressure (1 MPa O_2), no discernable difference between the promoted and unpromoted Pt catalysts was observed. The similar apparent activation energy of HDO oxidation over Pt/C and Bi-Pt/C suggests a similar reaction path is followed on both catalysts. Previous work by Ide and Davis reported that the kinetics of HDO oxidation at high O_2 pressure over monometallic Pt/C can be explained by the dissociative adsorption of alcohol, the elimination of β-hydrogen, the reaction of surface H and surface OH and the generation of surface OH from O_2 and water, among which β-hydrogen elimination was believed to be the kinetically-relevant step.[15] The apparent activation energy measured in this work is in the same range as the calculated activation barrier of β-hydrogen elimination of alcohol over Pt(111) in water, which was 24 kJ mol^{-1}.[10]

Table 3. 7 Reaction order and apparent activation energy of 1,6-hexanediol (HDO) oxidation over Pt/C and Bi-Pt/C[a]

Catalyst	$\boldsymbol{P_{O_2}}$[b]	$\boldsymbol{n_{O_2}}$[c]	$\boldsymbol{n_{HDO}}$[d]	E_a[e] (kJ mol^{-1})
Pt/C	low	0.75	0	22
Pt/C	high	0	0	28
0.6Bi-Pt/C	low	0	0	23
0.6Bi-Pt/C	high	0	0	29

a. Reaction rates are shown in Figure 3.12.

b. For simplification, low P_{O_2} means O_2 pressure in the region of 0.02 – 0.2 MPa while high P_{O_2} means O_2 pressure in the region of 0.2 – 1 MPa.

c. Reaction conditions: 328 K, 0.1 M HDO, Pt:HDO = 1:500 (atomic ratio), stirring rate = 1200 rpm.

d. Reaction conditions: 328 K, 0.02 MPa or 1 MPa O_2, stirring rate = 1200 rpm, 0.05 – 0.2 M 1,6-hexanediol.

e. Reaction conditions: 0.1 M HDO, Pt:HDO = 1:500 (atomic ratio), stirring rate = 1200 rpm, 0.02 MPa or 1 MPa O_2, 318 – 338 K.

3.3.2.4.Kinetic isotope effect of D_2O over Pt/C and Bi-Pt/C and the promotional effect of Bi

The significantly different O_2 reaction order under low O_2 pressure condition over Pt/C and Bi-Pt/C suggests that the promotional effect of Bi is likely related to the activation of O_2. For Pt/C, the rate of O_2 dissociation is fast so that it can be assumed to be at equilibrium under high O_2 pressure[15] whereas under low O_2 pressure, the dissociation of O_2 might be a kinetically-relevant step. From this perspective, the role of Bi might be to accelerate O_2 dissociation so that the O_2 reaction order is zero, even under low O_2 pressure, as shown in Figure 3.12a.

Zope et al. reported the calculated activation barriers for O_2 dissociation over Pt(111) in water,[10] with E_a for direct dissociative adsorption of O_2 determined to be 64 kJ mol^{-1}, which was lowered to 18 kJ mol^{-1} when O_2 dissociation was assisted by adsorbed water ($O_2 * + H_2O * \rightarrow OOH * + OH *$). A water-assisted O_2 dissociation step was also supported by the detection of peroxide during HDO oxidation over Pt/C as described in our previous work.[15] Since water may be an active participant in the dissociation of O_2, the effect of replacing H_2O with D_2O was evaluated over Pt/C and 0.6Bi-Pt/C.

The initial rates (TOF) of HDO oxidation over Pt/C and 0.6Bi-Pt/C under 0.02 MPa and 1 MPa O_2 were measured in H_2O and D_2O, respectively. The measured TOF and TOF_H/TOF_D ratio are reported in Table 3.8. Under high O_2 pressure, a TOF_H/TOF_D ratio was determined to be 1.1 over both Pt/C and 0.6Bi-Pt/C. The negligible kinetic isotope effect with D_2O under high O_2 pressure was also observed during ethanol oxidation by Ide et al., suggesting that the dissociative adsorption of alcohol and formation of surface hydroxyl species from dioxygen and water are not the kinetically-relevant steps.[15] Under low O_2 pressure (0.02 MPa), however, a modest kinetic isotope effect of D_2O was observed over Pt/C in this work. The initial TOF of HDO oxidation over Pt/C was 0.063 and 0.044 s^{-1} in H_2O and D_2O, respectively, resulting in a TOF_H/TOF_D ratio of 1.4. In contrast to the results over Pt/C, a negligible kinetic isotope effect was observed over 0.6Bi-Pt/C under 0.02 MPa O_2, with the TOF_H and TOF_D measured at 0.17 and 0.20 s^{-1} ($TOF_H/TOF_D = 0.9$). Evidently, the presence of Bi allows the Bi-Pt/C system to have similar reaction kinetics during alcohol oxidation at low and high pressures of O_2. Without Bi, there is a strong dependence of the reaction rates on O_2 pressure at low pressure as well as a key role of water.

Table 3. 8 Effect of D_2O versus H_2O on the rate of 1,6-hexanediol oxidation over Pt/C and 0.6Bi-Pt/C[a]

$P_{dioygen}$	Solvent and catalyst	TOF (s^{-1})	TOF_H/TOF_D
0.02 MPa	H_2O + Pt/C	0.063	–
	D_2O + Pt/C	0.044	1.4
	H_2O + 0.6Bi-Pt/C	0.17	–
	D_2O + 0.6Bi-Pt/C	0.20	0.9
1 MPa	H_2O + Pt/C	0.29	–
	D_2O + Pt/C	0.26	1.1
	H_2O + 0.6Bi-Pt/C	0.22	–
	D_2O + 0.6Bi-Pt/C	0.20	1.1

a: Reaction conditions: 328 K, Pt:HDO = 1:500 (atomic ratio), 0.1 M 1,6-hexanediol in H_2O or D_2O, 0.02 MPa or 1 MPa O_2, stirring rate = 1200 rpm.

3.3.3. Influence of Bi on the stability of Pt catalyst during 1,6-hexanediol oxidation

Others have reported that Bi might promote the stability of the catalyst in alcohol oxidation by suppressing the formation or adsorption of contaminating species or preventing Pt from over-oxidation.[21,23,24,28,32,38] Ide et al. suggested that severe deactivation of Pt catalysts during alcohol oxidation was possibly related to strongly bonded species generated from intermediates.[20] However, the nature of the deactivating species remains unknown. In an attempt to quantitatively compare the deactivation behavior of our Pt/C and Bi-Pt/C catalysts, the experimental results were fitted by an empirical deactivation model proposed by Froment and Bischoff, which was applied to the deactivation caused by continuous formation of carbon on active sites.[69] As shown in Figure 3.17, the following model fit the results well:

$$r = \frac{r_0}{1+k_d \cdot t} \qquad 4$$

with r as the measured reaction rate; r_0 as the initial reaction rate; k_d as the deactivation factor and t as reaction time. The deactivation factors, k_d, for HDO oxidation over Pt/C and 0.6Bi-Pt/C at 328 K under different O_2 pressure (0.02 – 1 MPa) are shown in Figure 3.17. Under different O_2 pressures, k_d varied from 0.007 to 0.07 s^{-1}. However, no obvious trend in k_d with O_2 pressure was observed over Bi-Pt/C and Pt/C.

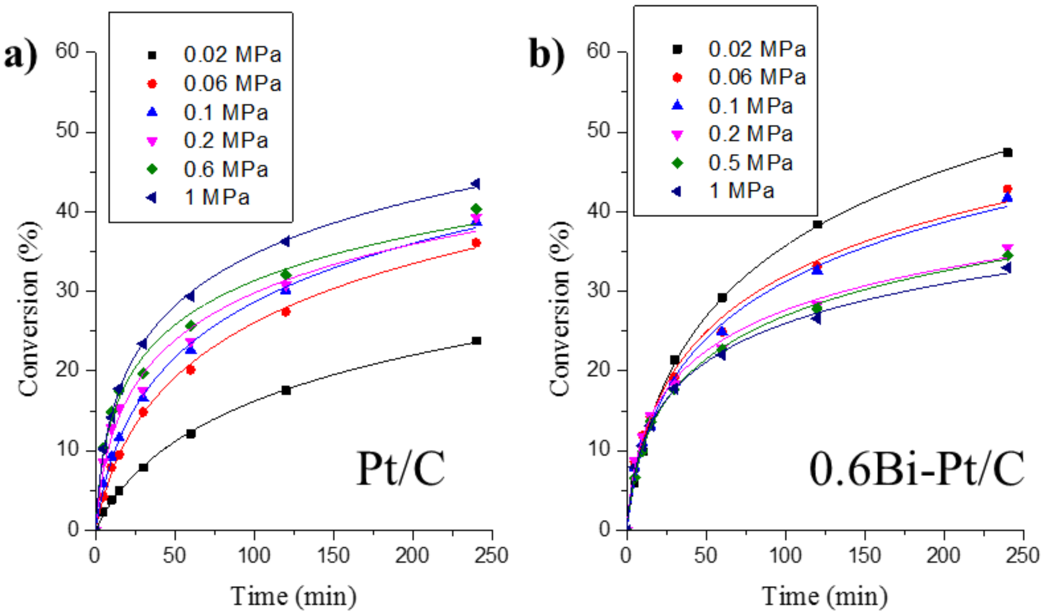

Figure 3. 17. Curve fitting of HDO oxidation deactivation model over Pt/C and 0.6Bi-Pt/C under different O_2 pressure (dot: measured data; line: fitted curve).

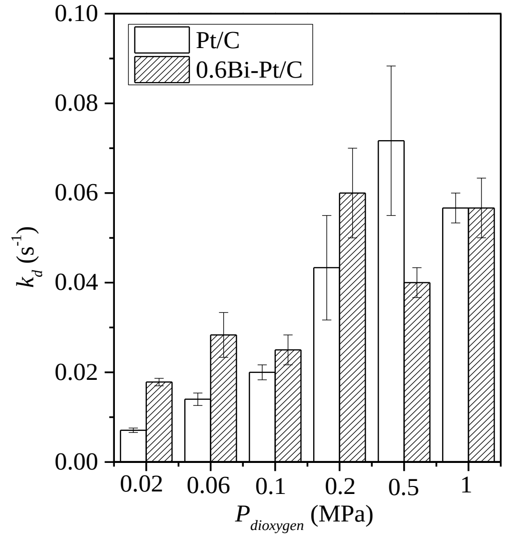

Figure 3. 18. Deactivation factor (k_d) of 1,6-hexanediol oxidation over Pt/C and 0.6Bi-Pt/C under different O_2 pressure.

3.4. Discussion

Extensive characterization of 0.6Bi-Pt/C, 0.6Bi-Pt/C-P and 0.6Bi-Pt/C-R revealed a significant structural change of Bi-Pt/C under pretreatment and reaction conditions. A schematic model for the evolution of Bi-Pt/C during alcohol pretreatment and alcohol oxidation is summarized in Figure 3.19. During catalyst preparation, Bi was selectively deposited on Pt particles in the outer layer of the carbon support (Figure 3.19a). However, under conditions of pretreatment and reaction, substantial migration of Bi species on the carbon support was observed. Although some areas on the carbon support containing only Pt or Bi were detected on Bi-Pt/C after pretreatment and reaction, Bi and Pt were still in the vicinity of each other in most regions, even after a long reaction time.

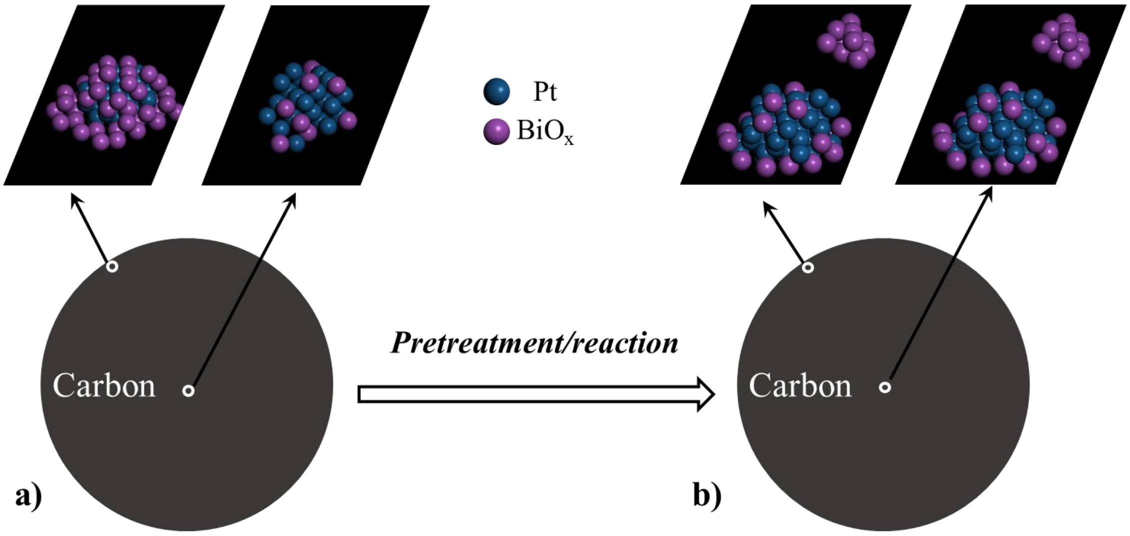

Figure 3. 19. Illustration of restructuring between a) as-prepared Bi-Pt/C and b) Bi-Pt/C after pretreatment or reaction. Pretreatment conditions: catalyst in 0.1 M 1,6-hexanediol under He at 328 K; Reaction conditions: catalyst in 0.1 M 1,6-hexanediol under 0.02 MPa O_2 at 328 K. Pt and BiO_x are blue and pink, respectively.

Most importantly, the addition of Bi only increased the rate of HDO oxidation under low O_2 pressure. The increased rate was related to fact that the promoted system was zero order in O_2 whereas the unpromoted catalyst was 0.75 order in O_2 under the same conditions. Evidently, O_2 activation became kinetically-relevant over Pt/C at low O_2 pressure and promotion with Bi facilitated O_2 activation. The promotional effect of Bi is likely to involve a water-assisted O_2 dissociation path. This speculation was supported by the the moderate kinetic isotope effect of D_2O on HDO oxidation over Pt/C at low O_2 pressure, with TOF_H/TOF_D being 1.4, which is substantially higher than TOF_H/TOF_D = 0.9 seen over 0.6Bi-Pt/C. Bismuth is reportedly oxidized faster than Pt under alcohol oxidation conditions[28] and BiO_x is readily reduced when it is in contact with Pt,[57] which may enable Bi to act as a redox site to facilitate O_2 activation and subsequent transfer to the Pt surface. In addition, Feliu et al. proposed that BiO_x on a Pt surface is likely to change the water adsorption on the surface and favor the formation of oxygenated species.[40,70] Combining our reaction kinetics and characterization results, we propose that the BiO_x species adjacent to Pt nanoparticles form active sites that accelerate the water-assisted dissociation of O_2 in liquid water and the subsequent formation of hydroxyl species on Pt surface, which in turn promotes the rate of HDO oxidation. Since no alloys of Bi and Pt were detected by XRD before and after reaction, we do not expect there to be a significant electronic effect associated with the Bi species on the Pt. Indeed, the similar apparent activation energy, product distribution and deactivation factor are consistent with the active Pt phase remaining fairly unperturbed after promotion with Bi.

3.5. Conclusions

Bismuth was successfully deposited onto carbon-supported Pt nanoparticles, but liquid phase pretreatment of the Bi-promoted Pt catalyst caused migration of Bi. The presence of Bi adjacent to Pt significantly promoted the rate of 1,6-hexanediol oxidation under low O_2 pressure without influencing the product distribution or catalyst deactivation. In the range of 0.02 to 0.2 MPa O_2, the order of reaction in O_2 changed from 0.75 over Pt/C to zero over Bi-promoted Pt/C, which accounts for the observed promotion in rate at low O_2 pressure. Results from the kinetic isotope effect with D_2O vs H_2O suggest that water-assisted O_2 activation is not kinetically-relevant on Bi-promoted Pt at low O_2 pressure whereas it is relevant on unpromoted Pt. All of the promotional effects of Bi disappear at higher O_2 pressure.

References for Chapter 3

(1) Besson, M.; Gallezot, P. Selective Oxidation of Alcohols and Aldehydes on Metal Catalysts. *Catal. Today* **2000**, *57*, 127–141.

(2) Mallat, T.; Baiker, A. Oxidation of Alcohols with Molecular Oxygen on Solid Catalysts. *Chem. Rev.* **2004**, *104*, 3037–3058.

(3) Corma, A.; Iborra, S.; Velty, A. Chemical Routes for the Transformation of Biomass into Chemicals. *Chem. Rev.* **2007**, *107*, 2411–2502.

(4) Kroger, M.; Prußе, U.; Vorlop, K. D. A New Approach for the Production of 2,5-Furandicarboxylic Acid by in Situ Oxidation of 5-Hydroxymethylfurfural Starting from Fructose. *Top. Catal.* **2000**, *13*, 237–242.

(5) Carrettin, S.; McMorn, P.; Johnston, P.; Griffin, K.; Hutchings, G. J. Selective Oxidation of Glycerol to Glyceric Acid Using a Gold Catalyst in Aqueous Sodium Hydroxide. *Chem. Commun.* **2002**, 696–697.

(6) Carrettin, S.; McMorn, P.; Johnston, P.; Griffin, K.; Kiely, C. J.; Hutchings, G. J. Oxidation of Glycerol Using Supported Pt, Pd and Au Catalysts. *Phys. Chem. Chem. Phys.* **2003**, *5*, 1329–1336.

(7) Porta, F.; Prati, L. Selective Oxidation of Glycerol to Sodium Glycerate with Gold-on-Carbon Catalyst: An Insight into Reaction Selectivity. *J. Catal.* **2004**, *224*, 397–403.

(8) Demirel, S.; Lehnert, K.; Lucas, M.; Claus, P. Use of Renewables for the Production of Chemicals: Glycerol Oxidation over Carbon Supported Gold Catalysts. *Appl. Catal. B Environ.* **2007**, *70*, 637–643.

(9) Casanova, O.; Iborra, S.; Corma, A. Biomass into Chemicals: Aerobic Oxidation of 5-Hydroxymethyl-2-Furfural into 2,5-Furandicarboxylic Acid with Gold Nanoparticle Catalysts. *ChemSusChem* **2009**, *2*, 1138–1144.

(10) Zope, B. N.; Hibbitts, D. D.; Neurock, M.; Davis, R. J. Reactivity of the Gold/water Interface during Selective Oxidation Catalysis. *Science.* **2010**, *330*, 74–78.

(11) Davis, S. E.; Houk, L. R.; Tamargo, E. C.; Datye, A. K.; Davis, R. J. Oxidation of

5-Hydroxymethylfurfural over Supported Pt, Pd and Au Catalysts. *Catal. Today* **2011**, *160*, 55–60.

(12) Gupta, N. K.; Nishimura, S.; Takagaki, A.; Ebitani, K. Hydrotalcite-Supported Gold-Nanoparticle-Catalyzed Highly Efficient Base-Free Aqueous Oxidation of 5-Hydroxymethylfurfural into 2,5-Furandicarboxylic Acid under Atmospheric Oxygen Pressure. *Green Chem.* **2011**, *13*, 824–827.

(13) Zope, B. N.; Davis, R. J. Inhibition of Gold and Platinum Catalysts by Reactive Intermediates Produced in the Selective Oxidation of Alcohols in Liquid Water. *Green Chem.* **2011**, *13*, 3484–3491.

(14) Davis, S. E.; Zope, B. N.; Davis, R. J. On the Mechanism of Selective Oxidation of 5-Hydroxymethylfurfural to 2,5-Furandicarboxylic Acid over Supported Pt and Au Catalysts. *Green Chem.* **2012**, *14*, 143–147.

(15) Ide, M. S.; Davis, R. J. Perspectives on the Kinetics of Diol Oxidation over Supported Platinum Catalysts in Aqueous Solution. *J. Catal.* **2013**, *308*, 50–59.

(16) Davis, S. E.; Ide, M. S.; Davis, R. J. Selective Oxidation of Alcohols and Aldehydes over Supported Metal Nanoparticles. *Green Chem.* **2013**, *15*, 17–45.

(17) Nie, J.; Xie, J.; Liu, H. Efficient Aerobic Oxidation of 5-Hydroxymethylfurfural to 2,5-Diformylfuran on Supported Ru Catalysts. *J. Catal.* **2013**, *301*, 83–91.

(18) Xie, J.; Nie, J.; Liu, H. Aqueous-Phase Selective Aerobic Oxidation of 5-Hydroxymethylfurfural on Ru/C in the Presence of Base. *Chinese J. Catal.* **2014**, *35*, 937–944.

(19) Zope, B. N.; Davis, S. E.; Davis, R. J. Influence of Reaction Conditions on Diacid Formation During Au-Catalyzed Oxidation of Glycerol and Hydroxymethylfurfural. *Top. Catal.* **2012**, *55*, 24–32.

(20) Ide, M. S.; Falcone, D. D.; Davis, R. J. On the Deactivation of Supported Platinum

Catalysts for Selective Oxidation of Alcohols. *J. Catal.* **2014**, *311*, 295–305.

(21) Keresszegi, C.; Mallat, T.; Grunwaldt, J. D.; Baiker, A. A Simple Discrimination of the Promoter Effect in Alcohol Oxidation and Dehydrogenation over Platinum and Palladium. *J. Catal.* **2004**, *225*, 138–146.

(22) Chapman, A. O.; Akien, G. R.; Arrowsmith, N. J.; Licence, P.; Poliakoff, M. Continuous Heterogeneous Catalytic Oxidation of Primary and Secondary Alcohols in scCO2. *Green Chem.* **2010**, *12*, 310.

(23) Mallat, T.; Bodnar, Z.; Maciejewski, M.; Baiker, A. Partial Oxidation of Cinnamyl Alcohol on Bimetallic Catalysts of Improved Resistance to Self-Poisoning. *Stud. Surf. Sci. Catal.* **1994**, *82*, 561–570.

(24) Mallat, T.; Bodnar, Z.; Baiker, A. Partial Oxidation of Water - Insoluble Alcohols over Bi - Promoted Pt on Alumina . Electrochemical Characterization of the Catalyst in Its Working State. *Stud. Surf. Sci. Catal.* **1993**, *78*, 377–384.

(25) Mallat, T.; Bronnimann, C.; Baiker, A. Platinum-Catalyzed Oxidation of Alcohols in Aqueous Solutions. The Role of Bi-Promotion in Suppression of Catalyst Deactivation. *Stud. Surf. Sci. Catal.* **1994**, *88*, 385–392.

(26) Anderson, R.; Griffin, K.; Johnston, P.; Alsters, P. L. Selective Oxidation of Alcohols to Carbonyl Compounds and Carboxylic Acids with Platinum Group Metal Catalysts. *Adv. Synth. Catal.* **2003**, *345*, 517–523.

(27) Mallat, T.; Bodnar, Z.; Hug, P.; Baiker, A. Selective Oxidation of Cinnamyl Alcohol to Cinnamaldehyde with Air over Bi-Pt/Alumina Catalysts. *Journal of Catalysis*, 1995, *153*, 131–143.

(28) Mondelli, C.; Grunwaldt, J.; Ferri, D.; Baiker, A. Role of Bi Promotion and Solvent in Platinum-Catalyzed Alcohol Oxidation Probed by in Situ X-Ray Absorption and ATR-IR Spectroscopy. *Phys. Chem. Chem. Phys.* **2010**, *12*, 5307–5316.

(29) Wörz, N.; Brandner, A.; Claus, P. Platinum-Bismuth-Catalyzed Oxidation of Glycerol: Kinetics and the Origin of Selective Deactivation. *J. Phys. Chem. C* **2010**, *114*, 1164–1172.

(30) Mounzer, H. N.; Wood, J.; Stitt, E. H. Heterogeneous Oxidation of 2-Octanol on 5wt%Pt–1wt%Bi/Carbon Catalyst. *Chem. Eng. Sci.* **2010**, *65*, 179–185.

(31) Gallezot, P. Selective Oxidation with Air on Metal Catalysts. *Catal. Today* **1997**, *37*, 405–418.

(32) Besson, M.; Gallezot, P. Deactivation of Metal Catalysts in Liquid Phase Organic Reactions. *Catal. Today* **2003**, *81*, 547–559.

(33) Kwon, Y.; Birdja, Y.; Spanos, I.; Rodriguez, P.; Koper, M. T. M. Highly Selective Electro-Oxidation of Glycerol to Dihydroxyacetone on Platinum in the Presence of Bismuth. *ACS Catal.* **2012**, *2*, 759–764.

(34) Kimura, H. Selective Oxidation of Glycerol on a Platinum-Bismuth Catalyst by Using a Fixed Bed Reactor. *Appl. Catal. A Gen.* **1993**, *105*, 147–158.

(35) Frassoldati, A.; Pinel, C.; Besson, M. Aerobic Oxidation of Secondary Pyridine-Derivative Alcohols in the Presence of Carbon-Supported Noble Metal Catalysts. *Catal. Today* **2013**, *203*, 133–138.

(36) Bowman, R. K.; Brown, A. D.; Cobb, J. H.; Eaddy, J. F.; Hatcher, M. a.; Leivers, M. R.; Miller, J. F.; Mitchell, M. B.; Patterson, D. E.; Toczko, M. a.; *et al.* Synthesis of HCV Replicase Inhibitors: Base-Catalyzed Synthesis of Protected α-Hydrazino Esters and Selective Aerobic Oxidation with Catalytic Pt/Bi/C for Synthesis of Imidazole-4,5-Dicarbaldehyde. *J. Org. Chem.* **2013**, *78*, 11680–11690.

(37) Figueiredo, M. C.; Sorsa, O.; Doan, N.; Pohjalainen, E.; Hildebrand, H.; Schmuki, P.; Wilson, B. P.; Kallio, T. Direct Alcohol Fuel Cells: Increasing Platinum Performance by Modification with Sp-Group Metals. *J. Power Sources* **2015**, *275*, 341–350.

(38) Figueiredo, M. C.; Santasalo-aarnio, A.; Vidal-Iglesias, F. J.; Solla-Gullón, J.; Feliu, J. M.; Kontturi, K.; Kallio, T. Tailoring Properties of Platinum Supported Catalysts by Irreversible Adsorbed Adatoms toward Ethanol Oxidation for Direct Ethanol Fuel Cells. *Appl. Catal. B Environ.* **2013**, *140–141*, 378–385.

(39) Climent, V.; Garcia-Araez, N.; Compton, R. G.; Feliu, J. M.; Garcia-Araez, N.; Compton, R. G.; Feliu, J. M. Effect of Deposited Bismuth on the Potential of Maximum Entropy of Pt(111) Single-Crystal Electrodes. *J. Phys. Chem. B* **2006**, *110*, 21092–21100.

(40) García-Aráez, N.; Climent, V.; Feliu, J. M. Evidence of Water Reorientation on Model Electrocatalytic Surfaces from Nanosecond-Laser-Pulsed Experiments. *J. Am. Chem. Soc.* **2008**, *130*, 3824–3833.

(41) Purgato, F. L. S.; Pronier, S.; Olivi, P.; De Andrade, a. R.; Léger, J. M.; Tremiliosi-Filho, G.; Kokoh, K. B. Direct Ethanol Fuel Cell: Electrochemical Performance at 90 °c on Pt and PtSn/C Electrocatalysts. *J. Power Sources* **2012**, *198*, 95–99.

(42) Ramos, S. G.; Calafiore, A.; Bonesi, A. R.; Triaca, W. E.; Castro Luna, A. M.; Moreno, M. S.; Zampieri, G.; Bengio, S. Supported Catalysts for Alcohol Oxidation Synthesis and Analysis of Their Catalytic Activity. *Int. J. Hydrogen Energy* **2012**, *37*, 14849–14853.

(43) Tanaka, K. I. Chemical Reconstruction and Catalysis of Metal and Bimetallic Surfaces. *Surf. Sci.* **1996**, *357–358*, 721–728.

(44) Tao, F.; Grass, M. E.; Zhang, Y.; Butcher, D. R.; Aksoy, F.; Aloni, S.; Altoe, V.; Alayoglu, S.; Renzas, J. R.; Tsung, C. K.; *et al.* Evolution of Structure and Chemistry of Bimetallic Nanoparticle Catalysts under Reaction Conditions. *J Am Chem Soc* **2010**, *132*, 8697–8703.

(45) Stanley, J. N. G.; Worthington, K.; Heinroth, F.; Masters, A. F.; Maschmeyer, T. Designing Nanoscopic, Fluxional Bimetallic Pt–Ru Alloy Hydrogenation Catalysts for Improved Sulfur Tolerance. *Catal. Today* **2011**, *178*, 164–171.

(46) Nagamatsu, S.; Arai, T.; Yamamoto, M.; Ohkura, T.; Oyanagi, H.; Ishizaka, T.; Kawanami, H.; Uruga, T.; Tada, M.; Iwasawa, Y. Potential-Dependent Restructuring and Hysteresis in the Structural and Electronic Transformations of Pt/C, Au(Core)-Pt(Shell)/C, and Pd(Core)-Pt(Shell)/C Cathode Catalysts in Polymer Electrolyte Fuel Cells Characterized by in Situ X-Ray Absorption Fine St. *J. Chem. Phys. C* **2013**, *117*, 13094–13107.

(47) Michalka, J. R.; Gezelter, J. D. Island Formation on Pt/Pd(557) Surface Alloys in the Presence of Adsorbed CO: A Molecular Dynamics Study. *J. Phys. Chem. C* **2015**, 150611154824003.

(48) Silva, D. O.; Luza, L.; Gual, A.; Baptista, D. L.; Bernardi, F.; Zapata, M. J. M.; Morais, J.; Dupont, J. Straightforward Synthesis of Bimetallic Co/Pt Nanoparticles in Ionic Liquid: Atomic Rearrangement Driven by Reduction–sulfidation Processes and Fischer–Tropsch Catalysis. *Nanoscale* **2014**, *6*, 9085.

(49) Alayoglu, S.; Somorjai, G. a. Nanocatalysis II: In Situ Surface Probes of Nano-Catalysts and Correlative Structure–Reactivity Studies. *Catal. Letters* **2015**, *145*, 249–271.

(50) Coloma, F.; Llorca, J.; Homs, N.; Ramírez de la Piscina, P.; Rodríguez-Reinoso, F.; Sepúlveda-Escribano, A. Crotonaldehyde Hydrogenation over Alumina- and Silica-Supported Pt–Sn Catalysts of Different Composition. In Situ DRIFT Study. *Phys. Chem. Chem. Phys.* **2000**, *2*, 3063–3069.

(51) Michalak, W. D.; Krier, J. M.; Alayoglu, S.; Shin, J.-Y.; An, K.; Komvopoulos, K.; Liu, Z.; Somorjai, G. A. CO Oxidation on PtSn Nanoparticle Catalysts Occurs at the

Interface of Pt and Sn Oxide Domains Formed under Reaction Conditions. *J. Catal.* **2014**, *312*, 17–25.

(52) Xie, J.; Falcone, D. D.; Davis, R. J. Restructuring of Supported PtSn Bimetallic Catalysts during Aqueous Phase Oxidation of 1,6-Hexanediol. *J. Catal.* **2015**, *332*, 38–50.

(53) Kim, J. H.; Choi, S. H. M.; Nam, S. H.; Seo, M. H.; Choi, S. H. M.; Kim, W. B. Influence of Sn Content on PtSn/C Catalysts for Electrooxidation of C1-C3 Alcohols: Synthesis, Characterization, and Electrocatalytic Activity. *Appl. Catal. B Environ.* **2008**, *82*, 89–102.

(54) Yeh, J. J.; Lindau, I. Atomic Subshell Photoionization Cross Sections and Asymmetry Parameters: $1 \leqslant Z \leqslant 103$. *At. Data Nucl. Data Tables* **1985**, *32*, 1–155.

(55) Ravel, B., Newville, M. ATHENA, ARTEMIS, HEPHAESTUS: Data Analysis for X-Ray Absorption Spectroscopy Using IFEFFIT. *J. Synchrotron Radiat.* **2005**, *12*, 537–541.

(56) Maier, B.; Dietrich, C.; Büchs, J. Correct Application of the Sulphite Oxidation Methodology of Measuring the Volumetric Mass Transfer Coefficient kLa Under Non-Pressurized and Pressurized Conditions. *Food Bioprod. Process.* **2001**, *79*, 107–113.

(57) Szabó, S. Underpotential Deposition of Metals on Foreign Metal Substrates. *Int. Rev. Phys. Chem.* **1991**, *10*, 207–248.

(58) Gracia, F. .; Bollmann, L.; Wolf, E. .; Miller, J. .; Kropf, A. . In Situ FTIR, EXAFS, and Activity Studies of the Effect of Crystallite Size on Silica-Supported Pt Oxidation Catalysts. *J. Catal.* **2003**, *220*, 382–391.

(59) Guo, N.; Fingland, B. R.; Williams, W. D.; Kispersky, V. F.; Jelic, J.; Delgass, W. N.; Ribeiro, F. H.; Meyer, R. J.; Miller, J. T. Determination of CO, H2O and H2 Coverage

by XANES and EXAFS on Pt and Au during Water Gas Shift Reaction. *Phys. Chem. Chem. Phys.* **2010**, *12*, 5678.

(60) Boudart, M. Solubility of Hydrogen in Small Particles of Palladium. *J. Catal.* **1975**, *39*, 44–52.

(61) Dawood, F.; Leonard, B. M.; Schaak, R. E. Oxidative Transformation of Intermetallic Nanoparticles: An Alternative Pathway to Metal/oxide Nanocomposites, Textured Ceramics, and Nanocrystalline Multimetal. *Chem. Mater.* **2007**, *19*, 4545–4550.

(62) Jayachandran, K. *Electrical, Optical and Structural Studies in Bismuth, Antimony, Bismuth Oxide and Antimony Oxide Thin Films*; School of Pure and Applied Physics, 1997.

(63) Weisz, P. B.; Prater, C. D. Interpretation of Measurements in Experimental Catalysis. *Adv. Catal.* **1954**, *6*, 143–196.

(64) Díaz, E.; Casas, J. A.; Mohedano, A. F.; Calvo, L.; Gilarranz, M. A.; Rodríguez, J. J. Kinetics of 4-Chlorophenol Hydrodechlorination with Alumina and Activated Carbon-Supported Pd and Rh Catalysts. *Ind. Eng. Chem. Res.* **2009**, *48*, 3351–3358.

(65) Henry, W. Experiments on the Quantity of Gases Absorbed by Water, at Different Temperatures, and under Different Pressures. *Philos. Trans. R. Soc. London* **1803**, 29–42.

(66) Rettich, T. R.; Battino, R.; Wilhelm, E. Solubility of Gases in Liquids. 22. High-Precision Determination of Henry's Law Constants of Oxygen in Liquid Water fromT=274 K toT=328 K. *J. Chem. Thermodyn.* **2000**, *32*, 1145–1156.

(67) Han, P.; Bartels, D. M. Temperature Dependence of Oxygen Diffusion in H 2 O and D 2 O †. *J. Phys. Chem.* **1996**, *100*, 5597–5602.

(68) Vleeming, J. H.; Kuster, B. F. M.; Marin, G. B. Selective Oxidation of Methyl α- D -Glucopyranoside with Oxygen over Supported Platinum: Kinetic Modeling in the

Presence of Deactivation by Overoxidation of the Catalyst. *Ind. Eng. Chem. Res.* **1997**, *36*, 3541–3553.

(69) Froment, G. F.; Bischoff, K. B. Non-Steady State Behaviour of Fixed Bed Catalytic Reactors due to Catalyst Fouling. *Chem. Eng. Sci.* **1961**, *16*, 189–201.

(70) Climent, V.; Garcia-Araez, N.; Compton, R. G.; Feliu, J. M. Effect of Deposited Bismuth on the Potential of Maximum Entropy of Pt(111) Single-Crystal Electrodes. *J. Phys. Chem. B* **2006**, *110*, 21092–21100.

Chapter 4. Alcohol oxidation reaction over non-precious metal atoms

A portion of this thesis was previously published as Xie, J. et al. Selective Aerobic Oxidation of Alcohols over Atomically-Dispersed Non-Precious Metal Catalysts. ChemSusChem 10, 359–362

4.1. Introduction

Precious metal catalysts are widely used in petrochemical refineries, pharmaceutical production facilities and environmental radiation devices.[1] In particular, the aerobic oxidation of biomass-derived alcohols to corresponding aldehydes and acids in the aqueous phase using heterogeneous precious metal catalysts, such as Au, Pt, Pd and Ru, has received growing attention because it offers a green and sustainable route to value-added chemicals.[2,3] The limited annual production and very high price of the metals, however, can be a significant barrier to commercialization of new processes.[4] Therefore, replacement of precious metals with more earth-abundant metals would be quite advantageous.

Recently, non-precious metal catalysts confined in a nitrogen-containing carbon matrix, which were prepared by pyrolysis or a ball milling method, exhibited decent activity in electrochemical reactions[5–10] and organic synthesis.[11–16] For example, the efficient activation of dioxygen has been reported with Fe-containing, nitrogen-doped carbon (Fe-N-C) in the electrochemical O_2 reduction reaction (ORR), with a comparable activity to the well-known Pt ORR catalysts.[8] Alcohol oxidation reactions can also be catalyzed by the Fe-based catalysts, such as Fe-containing polyoxometalates,[17] nano-Fe_2O_3 particles[18,19] and encapsulated or supported Fe complexes,[20–24] but these catalysts often require the addition of peroxides，which is likely the consequence of the poor ability of the catalyst to activate dioxygen. As an Fe-N-C catalyst has previously demonstrated excellent ORR performance, we hypothesized that it might also be a promising catalyst for the aerobic oxidation of alcohols. In fact, Jagadeesh *et al.* have reported the aerobic oxidative nitrification of various alcohols over Fe-N-C and identified aldehydes as intermediates.[25] To the best of our knowledge, however, the exploration of Fe-N-C and other platinum group metal-free analogues as potential catalysts for alcohol oxidation in water to produce aldehyde or acid products has not been reported and the mechanism of alcohol oxidation remains unclear. The current study relates extensive materials characterization results to catalytic performance, explores the kinetics of alcohol oxidation in liquid water, examines the regenerability of the catalysts and compares a variety of non-precious metal, atomically-dispersed M-N-C catalysts.

4.2. Experimental methods

4.2.1. Preparation of M-N-C catalysts

The M-N-C catalysts were prepared by a modified sacrificial support method.[9] First, a calculated amount of silica (Cab-O-Sil® M5P, surface area 125 m^2 g^{-1}) was dispersed in water using a high energy ultrasound probe. Then, a suspension of nicarbazin (Sigma-Aldrich) in acetone was added to silica and sonicated for 20 minutes in an ultrasonic bath. Finally, a solution of metal nitrate ($Fe(NO_3)_3$•$9H_2O$, $Cr(NO_3)_3$•$9H_2O$, $Co(NO_3)_2$•$6H_2O$, $Ni(NO_3)_2$•$6H_2O$, $Cu(NO_3)_2$•$3H_2O$, as received from Sigma-Aldrich) was added to SiO_2-nicarbazin solution and ultra-sonicated for 8 hours (the total metal loading on silica was calculated to be ~20 wt%). After ultrasonic treatment, the viscous gel of silica，metal nitrate and nicarbazin was dried overnight at 358 K. The obtained solid was ground to a fine powder in an agate mortar and then subjected toheat treatment at 1173 K with ultra-high purity N_2 (GT&S 99.999%) flow (100 cm^3 min^{-1}) for 45 min. After heat treatment, silica was leached using 25 wt% HF overnight. Finally, the M-N-C catalyst was washed with deionized water until neutral pH was achieved and then dried at 358 K. A second heat treatment was performed at T = 1223 K in reactive (NH_3) atmosphere. A metal-free N-C material was synthesized by the same method as described above without addition of metal salt.

A 2 wt% Fe supported on activated carbon (Norit, SX ultra) (Fe/C) was prepared by incipient wetness impregnation of iron nitrate ($Fe(NO_3)_3•9H_2O$, Sigma-Aldrich). The Fe/C was dried in air for 12 h at 393 K, reduced in 100 cm^3 min^{-1} of flowing H_2 (GTS-Welco, 99.999%) for 4 h at 673 K, cooled, exposed to air, and stored at ambient temperature.

To study the deactivation behavior of M-N-C, a used catalyst was recovered after 8 h of benzyl alcohol oxidation at 358 K under 1 MPa O_2, washed with deionized water and dried in a 343 K oven for 8 h. To test whether the activity can be regenerated, the used M-N-C was treated with H_2 (GTS-Welco, 99.999%) at 573 K. The catalyst was placed in a ceramic boat located in a horizontal quartz tube. The samples were then heated to 573 K at 10 K min^{-1} under 100 cm^3 min^{-1} of flowing H_2, held for 3 h and cooled to room temperature under H_2 flow.

4.2.2. Characterization of M-N-C catalysts

The transmission electron microscopy (TEM) and scanning transmission electron microscopy (STEM) were performed on an FEI Titan 80-300 operating at 300 kV that is equipped with a Gatan 794 Multi-scan Camera (EFTEM) and an energy dispersive spectrometer (EDS) for elemental X-ray analysis. Aberration-corrected STEM imaging was performed using a Nion UltraSTEM which is equipped with a cold-field emission gun operated at 60 kV. The dispersion of fresh and used Fe-N-C was characterized using high angle annular dark field (HAADF) STEM imaging using a convergence semi-angle of 31 mrad and collection angle of 86 to 200 mrad.

Elemental analysis was used to determine the Fe loading on fresh and used Fe-N-C and the concentration of Fe in the reaction medium after 8 h of alcohol oxidation. Elemental analysis was performed by Galbraith Laboratories (2323 Sycamore Drive, Knoxville, TN

37921) using inductively coupled plasma – atomic emission spectroscopy (ICP-AES).

XPS spectra were acquired on a Kratos Axis Ultra DLD X-ray photoelectron spectrometer using a Al Kα source monochromatic operating at 150W with no charge compensation. The base pressure was about 2×10^{-10} Torr, and operating pressure was around 2×10^{-9} torr. Survey and high-resolution spectra were acquired at pass energies of 80 eV and 20 eV, respectively. Data analysis and quantification were performed using CasaXPS software. A linear background subtraction was used for quantification of C1s, O1s and N1s spectra, while a Shirley background was applied to metal 2p spectra. Sensitivity factors provided by the manufacturer were utilized.

4.2.3. Oxidation of benzyl alcohol over M-N-C

The high-pressure, semi-batch alcohol oxidation reactions were performed in a 50 cm^3 Parr Instrument Company 4592 batch reactor with a 30 cm^3 glass liner. An aqueous alcohol (benzyl alcohol (99.8%), 5-hydroxymethylfurfural (99%), ethanol (>99.5%), glycerol (>99%), 1,6-hexnaediol (99%), as received from Sigma-Aldrich) solution (10 mL) and catalyst were added to the glass liner with or without the addition of 1 mM *tert*-butanol (>99.5%, Sigma-Aldrich), 1,4-benzoquinone (98%, Sigma-Aldrich) or 2,2,6,6-Tetramethyl-1-piperidinyloxy (98%, Sigma-Aldrich). The glass liner was inserted into the reactor, sealed, purged with He (GTS Welco, 99.999%), heated to 328 K and initiated by pressurizing the reactor with O_2 (GTS Welco, 99.993%) in the range of 0.25 – 1 MPa. The conversion of alcohol during the set-up was negligible (less than 10% of the conversion at 30 min, which was used to calculate the initial rate and activity). Liquid samples were periodically removed and the catalyst was recovered using a 0.2 μm PTFE filter before product analysis with a Waters e2695 high performance liquid chromatograph (HPLC) equipped with refractive index detector. Product separation in the HPLC was accomplished on an Aminex HPX-87H column (Bio-Rad) operating at 318 K with an aqueous 5 mM H_2SO_4 solution as the mobile phase flowing at 5 cm^3 min^{-1}. The retention times and calibration curves were determined by injecting known concentrations of standards. The carbon balance was greater than 90 %.

The maximum O_2 transport rate from the gas phase to the aqueous phase in the pressurized reaction system was determined by the sulfite oxidation method.[26] The amount of catalyst added to the reactor was chosen so that the alcohol oxidation rate would not be limited by O_2 mass transfer from the gas to the liquid. Selectivity to a specific product is defined as moles of that product formed divided by moles of all products produced. The initial rate was calculated from the initial conversion of the alcohol by performing a linear fit of the conversion after 30 min of reaction. The turnover frequency (TOF) [mol alcohol converted (mol metal)$^{-1}$ s^{-1}] was derived from the initial rate calculated from conversion after 30 min of reaction, which was below 10% in all cases.

4.3. Results

4.3.1. Catalyst characterization

An Fe-N-C catalyst synthesized by pyrolysis of $Fe(NO_3)_3$ and nicarbazin (details provided in the supplementary information) was investigated in the aqueous-phase aerobic alcohol oxidation reaction. Although the catalyst has been leached with acid to remove Fe or Fe_3C nanoparticles, some nanoparticles (5 – 30 nm) were still observed (Figure 4.1a), which has also been observed by others using similar synthesis methods and shown to be covered by a graphitic carbon shell.[12,27] Extensive prior characterization of our Fe-N-C catalyst by X-ray photoelectron spectroscopy (XPS), Mössbauer spectroscopy and in situ X-ray absorption spectroscopy indicates that ~90% of the iron is atomically-dispersed as nitrogen-coordinated Fe (Fe-N_x) species and are proposed to be the ORR active sites.[9] The predominant existence of atomically-dispersed Fe in the sample used here was confirmed by aberration-corrected scanning transmission electron microscopy (AC-STEM) (Figure 4.2a). The weight loading of Fe was determined to be 1.2 wt% from XPS (Table 4.1) and 1.5 wt% from inductively coupled plasma atomic emission spectroscopy (ICP-AES) (Table 4.2), respectively. A similar metal loading from XPS (surface-sensitive) and ICP-AES (bulk) is consistent with the atomically-dispersed iron species composing a large fraction of the total iron on the catalyst.

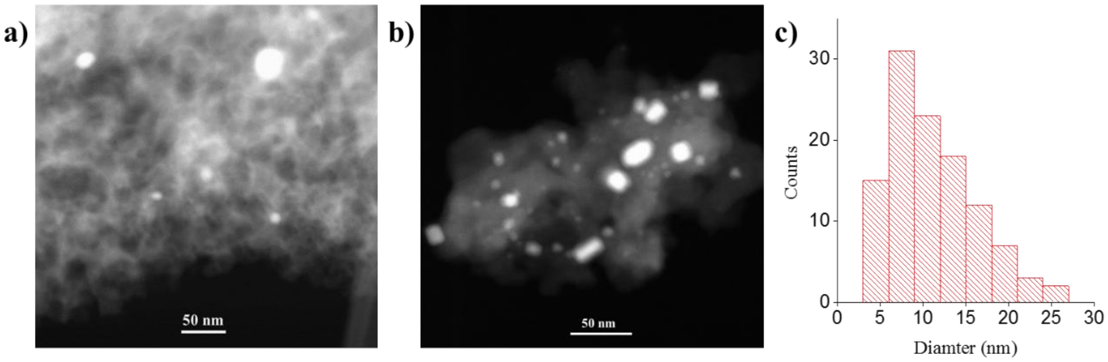

Figure 4. 1. STEM image of a) Fe-N-C, b) Fe/C and c) particle size analysis of Fe/C.

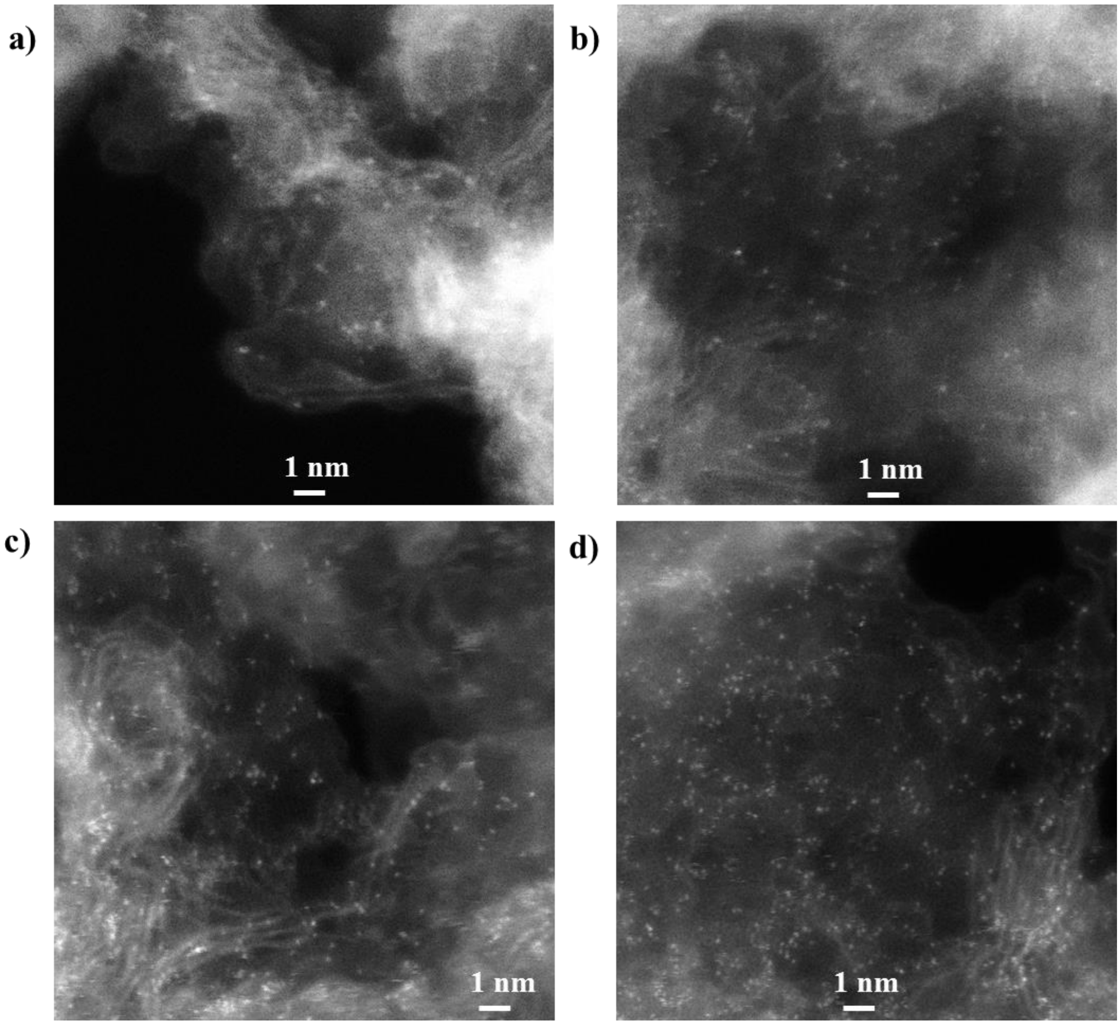

Figure 4. 2. Aberration-corrected STEM images of a) fresh Fe-N-C, b) used Fe-N-C, c) fresh Cu-N-C and d) used Cu-N-C-R. Used catalysts were recovered after 8 h of benzyl alcohol oxidation reaction, washed and dried.

Table 4. 1. Metal loadings of M-N-C catalysts from XPS analysis

Catalyst	Weight loadings (wt%)			
	metal	N	O	C
Cr-N-C	0.7	5.6	3.7	90.0
Fe-N-C	1.2	6.4	3.4	89.1
Co-N-C	0.7	4.4	7.6	90.8
Ni-N-C	1.2	3.0	5.6	90.4
Cu-N-C	0.4	4.4	7.6	87.7

Table 4. 2. Elemental analysis of fresh and used Fe-N-C and the recovered reaction medium after alcohol oxidation reaction over Fe-N-C or Cu-N-C[a].

Sample	Metal loading
Fresh Fe-N-C	1.5 wt% Fe
Used Fe-N-C[b]	1.5 wt% Fe
Filtered reaction medium (Fe-N-C)[c]	<0.03 mM Fe
Filtered reaction medium (Cu-N-C)[c]	<0.02 mM Cu

a: Analyzed by ICP-AES method.

b: The used Fe-N-C catalyst was recovered after 8 h of benzyl alcohol oxidation reaction by washing thoroughly with water and drying for 8 h at 343 K.

c: The reaction medium was collected after 8 h of benzyl alcohol oxidation reaction over Fe-N-C or Cu-N-C.

4.3.2. Benzyl alcohol oxidation over Fe-N-C

The rate of benzyl alcohol oxidation over Fe-N-C under mild conditions (353 K, 1 MPa O_2, aqueous solution) was measured to be 1.7×10^{-7} mol s^{-1} g_{cat}^{-1} (Table 4.3, Entry 2), which is equivalent to a turnover frequency of 0.00078 s^{-1} based on total Fe atoms. As control experiments, the conversion of benzyl alcohol was evaluated under identical conditions in the presence of Norit activated carbon and activated-carbon-supported Fe (Fe/C) with similar Fe loading and nanoparticle size compared to Fe-N-C (Figures 4.1). In addition, metal-free nitrogen-containing carbon (N-C) was evaluated for benzyl alcohol oxidation in the absence and presence of soluble Fe^{3+} ($Fe(NO_3)_3$) (Table 4.4). The conversion of benzyl alcohol over activated carbon and supported Fe nanoparticles was negligible whereas the reaction rate over N-C (with or without the presence of Fe^{3+} ion) is ~20 % of that observed with the equivalent amount of Fe-N-C. The low observed catalytic activity of N-C, compared with Fe-N-C, is likely related to the nitrogen sites on the carbon, which have been reported to participate in the partial reduction of O_2.[28–30] Considering the molar loading of nitrogen in the carbon matrix is much larger than that of Fe (4.7 mol% of N *versus* 0.4 mol% of Fe[9]) and Fe-N-C is about 500% more active than N-C, we propose that the Fe-N_x sites are the primary active sites for benzyl alcohol oxidation.

Table 4. 3. Rates of benzyl alcohol oxidation over fresh, used and regenerated M-N-C catalysts[a]

Entry	Catalyst	Treatment[b]	Rate (10^{-8} mol s^{-1} g_{cat}^{-1})	TOF (10^{-3} s^{-1})[c]
1	Cr-N-C	Fresh	84	6.5
2	Fe-N-C	Fresh	17	0.78
3	Co-N-C	Fresh	180	15
4	Ni-N-C	Fresh	64	3.1
5	Cu-N-C	Fresh	204	34
6	Cr-N-C	Used	46	3.6
7	Fe-N-C	Used	11	0.52
8	Co-N-C	Used	21	1.7
9	Ni-N-C	Used	7.3	0.36
10	Cu-N-C	Used	21	3.5
11	Cr-N-C	Regenerated	67	5.2
12	Fe-N-C	Regenerated	19	0.90
13	Co-N-C	Regenerated	133	11
14	Ni-N-C	Regenerated	14	0.70
15	Cu-N-C	Regenerated	31	5.0

a: Reaction conditions: 353 K, 10 mL 0.05 M benzyl alcohol aqueous solution, 0.0400 g Fe-N-C or 0.0130 g M-N-C (M = Cr, Co, Ni, Cu), 1 MPa O_2.

b: The used catalysts were recovered after 8 h of benzyl alcohol oxidation reaction, washed and dried; The regenerated catalysts were recovered after 8 h of oxidation reaction, washed, dried and treated in dihydrogen flow at 573 K for 3 h.

c: The turnover frequency (TOF) [mol alcohol converted (mol metal)$^{-1}$ s^{-1}] was derived from the initial rate calculated from conversion after 30 min of reaction, which was below 10% in all cases.

Table 4. 4. Rates of benzyl alcohol oxidation over different materials[a]

Materials	Rate (10^{-8} mol s^{-1} g_{cat}^{-1})[c]
Norit activated carbon	0.70
1.5 wt% Fe/C	1.2
N-C	3.4
N-C + $Fe(NO_3)_3$[b]	2.4

a: Reaction conditions: 353 K, 10 mL 0.05 M benzyl alcohol in aqueous solution, 0.0400 g catalyst, 1 MPa O_2.

b: The amount of Fe is 14 μmol, similar to the that of Fe-N-C and Fe/C.

c: The reaction rate was calculated from the conversion of benzyl alcohol after 30 min of reaction.

The reaction orders with respect to O_2 and benzyl alcohol were evaluated over the range of 0.3 – 1 MPa O_2 and 0.025 – 0.1 M benzyl alcohol. As illustrated in Figures 4.3a and 4.3b, the reaction orders were close to zero, indicating the saturated adsorption of O_2 and benzyl alcohol. To further explore the reaction mechanism, the kinetic isotope effect utilizing deuterated alcohol ($C_6H_5CD_2OH$) was evaluated. As summarized in Table 4.5, a significant kinetic isotope effect of 4.9 was observed, indicating β-H elimination is a kinetically-relevant step during benzyl alcohol oxidation over Fe-N-C. For comparison, the KIE was measured to be 1.8 over commercial carbon-supported Pt catalyst (Pt/C), which is a well-studied material for alcohol oxidation.[31] Moreover, the influence of *tert*-butanol and 1,4-benzoquinone, known scavengers for hydroxyl and superoxide radicals,[32] on the rate of benzyl alcohol oxidation was examined over Fe-N-C and Pt/C. As revealed in Table 4.6, the introduction of the radical scavengers did not substantially change the rate of alcohol oxidation over either Fe-N-C or Pt/C. These results suggest that radical intermediates are not involved in the benzyl alcohol oxidation over Fe-N-C.

Table 4. 5. Kinetics isotope effect and orders of reaction for benzyl alcohol oxidation

Catalyst	TOF_D (10^{-3} s^{-1})[a]	TOF_H/TOF_D	n_{O_2}[b]		$n_{benzyl\ alcohol}$[c]
			0.3 – 1 MPa	1 – 2 MPa	
Fe-N-C	0.16	4.9	0	0	0
Cu-N-C	16	2.2	0.7	0	0

a: The turnover frequency (TOF) [mol alcohol converted (mol metal)$^{-1}$ s^{-1}] was derived from the initial rate calculated from conversion after 30 min of reaction, which was below 10% in all cases. Reaction conditions: 353 K, 10 mL 0.05 M deuterated benzyl alcohol ($C_6H_5CD_2OH$) aqueous solution, 0.0400 g Fe-N-C or 0.0130 g M-N-C (M = Cr, Co, Ni, Cu), 1 MPa O_2.

b: Reaction conditions: 353 K, 10 mL 0.05 M benzyl alcohol aqueous solution, 0.0400 g Fe-N-C or 0.0130 g Cu-N-C, 0.3 – 2 MPa O_2.

c: 353 K, 10 mL benzyl alcohol aqueous solution (0.025 – 0.1 M), 0.0400 g Fe-N-C or 0.0130 g Cu-N-C, 1 MPa O_2.

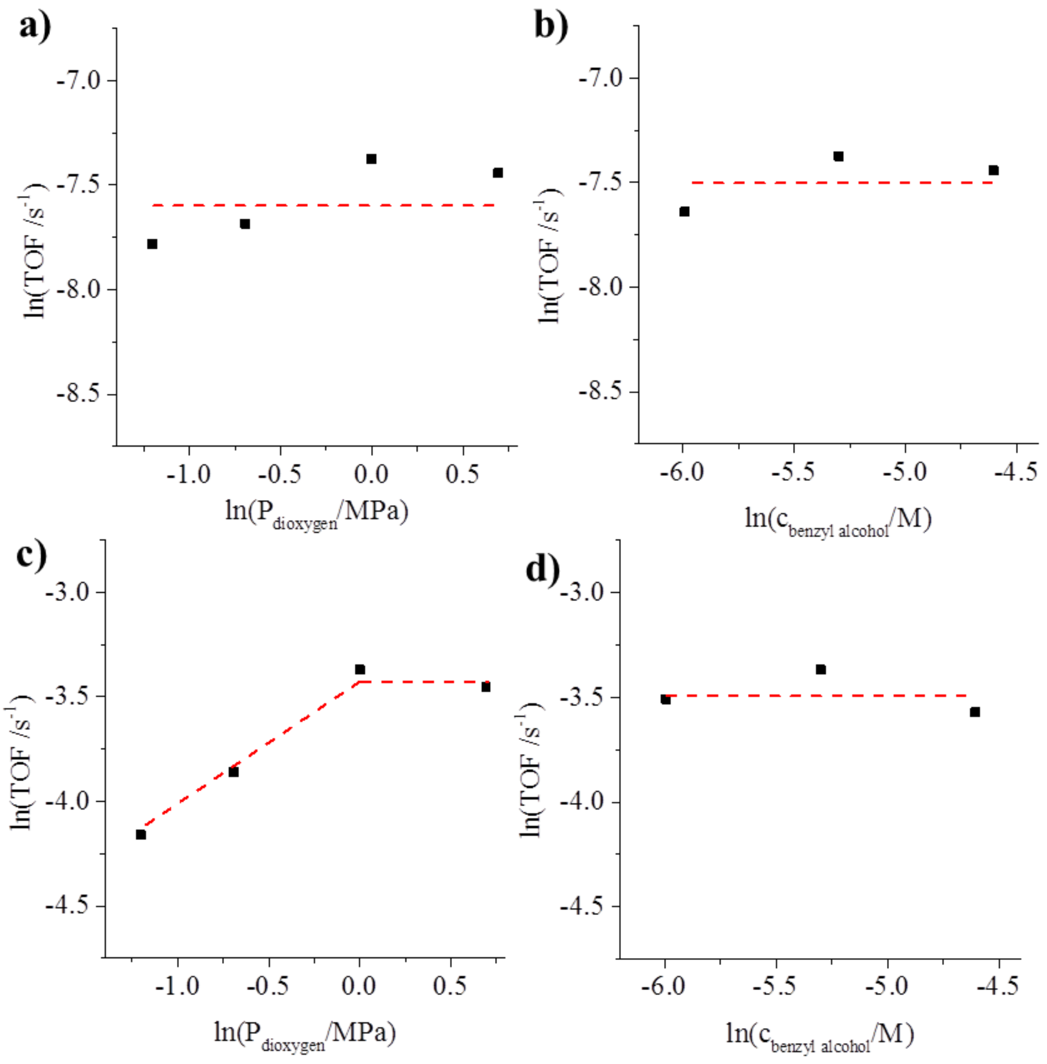

Figure 4. 3. Dependence of initial alcohol oxidation turnover frequencies (TOF (s^{-1})) on dioxygen pressure in the range of 0.3 – 2 MPa over a) Fe-N-C and c) Cu-N-C. Reaction conditions: 353 K, 10 mL 0.05 M benzyl alcohol aqueous solution, 0.0400 g Fe-N-C or 0.0130 g Cu-N-C; and concentration of benzyl alcohol in the range of 0.025 – 0.1 M over b) Fe-N-C and d) Cu-N-C. Reaction conditions: 353 K, 10 mL benzyl alcohol aqueous solution, 0.0400 g Fe-N-C or 0.0130 g Cu-N-C, 1 MPa O_2.

Table 4. 6. Influence of radical trap addition on benzyl alcohol oxidation over Fe-N-C and Pt/C[a]

Catalyst	Radical trap	TOF (10^{-3} s^{-1})[b]
Fe-N-C	--	0.78
	Tert-butanol	0.83
	1,4-Benzoquinone	0.64
Pt/C	--	330
	Tert-butanol	310
	1,4-Benzoquinone	230

a: Reaction conditions: 353 K, 10 mL 0.05 M benzyl alcohol in aqueous solution, 0.0400 g Fe-N-C or 0.0020 g Pt/C, 1 MPa O_2, 1 mM tert-butanol or 1,4-benzoquinone.

b: The turnover frequency (TOF) [mol alcohol converted (mol metal)$^{-1}$ s^{-1}] was derived from the initial rate calculated from conversion after 30 min of reaction.

Slight deactivation was observed after 8 h of reaction. As shown in Table 4.3, Entries 2 and 7, ~35% of the initial activity of Fe-N-C was lost after recovery from the reactor compared to the fresh catalyst. To investigate the cause of deactivation, the used catalyst was characterized by AC-STEM and ICP-AES. High-resolution electron microscopy (Figure 4.2b) revealed atomically-dispersed Fe-N_x sites remained on the used catalyst and elemental analysis of the fresh and recovered catalysts confirmed that the Fe loading was unaffected by reaction (Table 4.2). Moreover, the concentration of Fe in the reaction medium after 8 h was less than 0.03 mM, consistent with less than 2% of available iron being leached into the solution. Indeed, the catalytic activity can be almost fully regenerated by a reductive treatment in H_2 (Table 4.2, Entries 2, 7, 12). These results suggest that the Fe-N_x sites are stable under the reaction conditions and the deactivation is likely the result of strongly adsorbed species on active sites, which were removed during the H_2 treatment. A similar deactivation behavior was also observed during alcohol oxidation over a Pt catalyst.[33]

The oxidation of other alcohols, including 5-hydroxymethylfurfural (HMF), ethanol, 1,6-hexanediol and glycerol, was also investigated over the Fe-N-C catalyst. As shown in Figure 4.4, benzyl alcohol and HMF were efficiently and selectively converted to benzyl aldehyde and 2,5-diformylfuran (DFF), respectively. The selectivity to benzyl aldehyde and DFF was 92% and 82% at the conversion of 79% and 49%, respectively. Less than 3% conversion of ethanol, 1,6-hexanediol and glycerol was observed under the same conditions, which is likely the result of either more difficult activation of β-H in the aliphatic alcohols or severe catalyst deactivation.

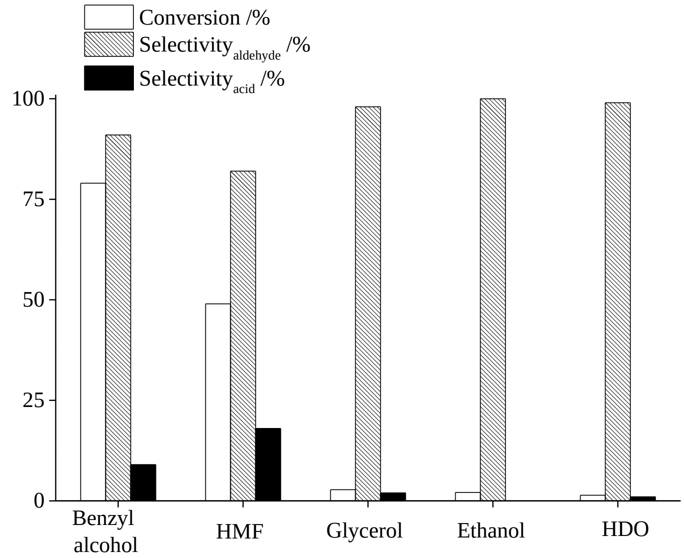

Figure 4. 4. Conversion and product distribution from oxidation of benzyl alcohol, 5-hydroxymethylfurfural (HMF), glycerol and ethanol over Fe-N-C. Reaction conditions: 353 K, 10 mL 0.05 M benzyl alcohol aqueous solution, 0.167 g Fe-N-C, 1 MPa O_2, 8 h reaction time.

In an attempt to improve the rate of alcohol oxidation over Fe-N-C, 2,2,6,6-tetramethyl-1-piperidinyloxy (TEMPO) was added to the reaction medium, which has been reported to catalyze the oxidation of both aromatic and aliphatic alcohols when combined with homogeneous first-row transition metal co-catalysts.[34,35] As shown in Table 4.7, the catalytic amount of additive TEMPO (1 mM) significantly increased the rate of benzyl alcohol oxidation. The conversion of benzyl alcohol after 30 min increased from 2.4 % to 12.2% with the addition of TEMPO. More importantly, the oxidation of 1,6-hexanediol, an aliphatic diol, was significantly promoted by TEMPO, with 6.3% conversion after 30 min, compared to 0.5% conversion without the addition of TEMPO.

Table 4. 7. Influence of TEMPO of benzyl alcohol and 1,6-hexanediol oxidation over Fe-N-C[a]

Substrate	Additive	Conversion (%)	Selectivity (%)	
			Aldehyde[b]	Acid[c]
Benzyl alcohol	--	2.4	100	0
	1 mM TEMPO	12.2	100	0
1,6-Hexanediol	--	0.5	98	2
	1 mM TEMPO	6.3	78	22

a: Reaction conditions: 353 K, 10 mL 0.05 M benzyl alcohol or 1,6-hexnaediol aqueous solution, 0.0400 g Fe-N-C, with or without 1 mM TEMPO, reaction time = 30 min.

4.3.3. Benzyl alcohol oxidation over M-N-C (M = Cr, Co, Ni and Cu)

A series of M-N-C catalysts containing other metals (M = Cr, Co, Ni, Cu) was also prepared by the same method used to synthesize Fe-N-C and evaluated in the benzyl alcohol oxidation. A related study on the oxidative nitrification of alcohols by Jagadeesh *et al.* revealed Fe and Co catalysts exhibited the best activity and selectivity.[25] As shown in Table 4.3, Entries 1-5, benzyl alcohol was also efficiently converted over all of the M-N-C catalysts in this work. The activity of these M-N-C (M = Cr, Co, Ni, Cu) catalysts was much greater than that of Fe-N-C, among which Cu-N-C was the most active catalyst with a TOF of 0.034 s^{-1} (~50 times greater than that of Fe-N-C and about one order of magnitude lower than Pt). As shown in Figure 4.2c, the high-resolution STEM image confirmed the atomic dispersion of Cu, which likely resides in nitrogen-coordinated sites. Similar to Fe-N-C, the reaction order with respect of O_2 and benzyl alcohol was close to 0 in the range of 1 – 2 MPa O_2 and 0.025 – 0.1 M benzyl alcohol over Cu-N-C (Figures 4.3c and 4.3d). However, at lower O_2 pressure (0.3 – 1 MPa), the O_2 reaction order was ~0.7. The higher O_2 reaction order over Cu-N-C versus Fe-N-C is possibly correlated to the observed lower activity of Cu-N-C in ORR as reported by Serov *et al.*[36] Interestingly, a much weaker kinetic isotope effect was observed during oxidation of deuterated benzyl alcohol over Cu-N-C compared to Fe-N-C (2.2 versus 4.9) (Table 4.5), which might be related to a more facile β-H elimination on the Cu catalyst.

The stability of M-N-C catalysts was also investigated. Similar to the behavior of Fe-N-C, loss of activity was observed over M-N-C (M = Cr, Co, Ni, Cu) after 8 h of benzyl alcohol oxidation (Table 4.3, Entries 1-10). More specifically, only ~10% of the initial activity was observed with recycled Co-N-C, Ni-N-C and Cu-N-C catalysts. Microscopy revealed that Cu remained atomically dispersed throughout the reaction (Figure 4.2d) and negligible Cu leaching was observed by ICP-AES (Table 4.2). In an attempt to regenerate the activity of used M-N-C, H_2 treatment at 573 K was performed on the recovered catalysts. Whereas the majority of catalytic activity was recovered from Cr-N-C, Fe-N-C and Co-N-C, the Ni-N-C and Cu-N-C samples were not efficiently regenerated (Table 4.3).

4.4. Conclusion

Materials with atomically-dispersed metal present in a highly porous nitrogen-containing carbon matrix were synthesized by a sacrificial support method and demonstrated to catalyze alcohol oxidation reactions at mild conditions. Benzyl alcohol and 5-(hydroxymethyl)furfural were selectively oxidized to aldehyde products by O_2 in the aqueous phase at 353 K over an Fe-containing catalyst. Individual nitrogen-coordinated iron moieties are proposed to be the active sites for the alcohol oxidation. Rate measurements with deuterated benzyl alcohol revealed a strong kinetic isotope effect, indicating β-H elimination from the alcohol is a kinetically-relevant step in the reaction. Although some deactivation was observed, the original activity was completely regenerated by treatment in H_2 at 573 K. Whereas the rate of 1,6-hexanediol oxidation was substantially slower than that of benzyl alcohol oxidation, addition of 2,2,6,6-tetramethyl-1-piperidinyloxy as a co-catalyst improved the rate of 1,6-hexanediol oxidation by more than an order of magnitude. The rate of benzyl alcohol oxidation was improved when Fe was substituted by other non-precious metals, such as Cr, Co, Ni and Cu. The higher rate of oxidation observed over the Cu catalyst was attributed to faster β-H elimination as the kinetic isotope effect with deuterated benzyl alcohol was much weaker than that observed over Fe catalyst.

References for Chapter 4

(1) Muroi, T. Role of Precious Metal Catalysts. In *Noble Metals*; Su, Y., Ed.; InTech, 2012; pp. 301–334.

(2) Nie, J.; Xie, J.; Liu, H. Efficient Aerobic Oxidation of 5-Hydroxymethylfurfural to 2,5-Diformylfuran on Supported Ru Catalysts. *J. Catal.* **2013**, *301*, 83–91.

(3) Davis, S. E.; Ide, M. S.; Davis, R. J. Selective Oxidation of Alcohols and Aldehydes over Supported Metal Nanoparticles. *Green Chem.* **2013**, *15*, 17–45.

(4) Vesborg, P. C. K.; Jaramillo, T. F. Addressing the Terawatt Challenge: Scalability in the Supply of Chemical Elements for Renewable Energy. *RSC Adv.* **2012**, *2*, 7933–

7947.

(5) Zheng, X.; Deng, J.; Wang, N.; Deng, D.; Zhang, W. H.; Bao, X.; Li, C. Podlike N-Doped Carbon Nanotubes Encapsulating FeNi Alloy Nanoparticles: High-Performance Counter Electrode Materials for Dye-Sensitized Solar Cells. *Angew. Chemie - Int. Ed.* **2014**, *53*, 7023–7027.

(6) Cui, X.; Xiao, J.; Wu, Y.; Du, P.; Si, R.; Yang, H.; Tian, H.; Li, J.; Zhang, W. H.; Deng, D.; *et al.* A Graphene Composite Material with Single Cobalt Active Sites: A Highly Efficient Counter Electrode for Dye-Sensitized Solar Cells. *Angew. Chemie - Int. Ed.* **2016**, *100190*, 6708–6712.

(7) Zou, X.; Huang, X.; Goswami, A.; Silva, R.; Sathe, B. R.; Mikmeková, E.; Asefa, T. Cobalt-Embedded Nitrogen-Rich Carbon Nanotubes Efficiently Catalyze Hydrogen Evolution Reaction at All pH Values. *Angew. Chemie Int. Ed.* **2014**, *53*, 4372–4376.

(8) Shao, M.; Chang, Q.; Dodelet, J.-P.; Chenitz, R. Recent Advances in Electrocatalysts for Oxygen Reduction Reaction. *Chem. Rev.* **2016**, *116*, 3594–365.

(9) Serov, A.; Artyushkova, K.; Niangar, E.; Wang, C.; Dale, N.; Jaouen, F.; Sougrati, M.-T.; Jia, Q.; Mukerjee, S.; Atanassov, P. Nano-Structured Non-Platinum Catalysts for Automotive Fuel Cell Application. *Nano Energy* **2015**, *16*, 293–300.

(10) Wang, J.; Wu, H.; Gao, D.; Miao, S.; Wang, G.; Bao, X. High-Density Iron Nanoparticles Encapsulated within Nitrogen-Doped Carbon Nanoshell as Efficient Oxygen Electrocatalyst for Zinc-Air Battery. *Nano Energy* **2015**, *13*, 387–396.

(11) Jagadeesh, R. V; Junge, H.; Pohl, M.; Radnik, J.; Brückner, A.; Beller, M. Selective Oxidation of Alcohols to Esters Using Heterogeneous Co3O4–N@C Catalysts under Mild Conditions. *J. Am. Chem. Soc.* **2013**, *135*, 10776–10782.

(12) Cui, X.; Li, Y.; Bachmann, S.; Scalone, M.; Surkus, A. E.; Junge, K.; Topf, C.; Beller, M. Synthesis and Characterization of Iron-Nitrogen-Doped Graphene/Core-Shell

Catalysts: Efficient Oxidative Dehydrogenation of N-Heterocycles. *J. Am. Chem. Soc.* **2015**, *137*, 10652–10658.

(13) Jagadeesh, R. V; Stemmler, T.; Surkus, A.; Junge, H.; Junge, K.; Beller, M. Hydrogenation Using Iron Oxide – Based Nanocatalysts for the Synthesis of Amines. *Nat. Protoc.* **2015**, *10*, 548–557.

(14) Matanovic, I.; Babanova, S.; Iii, P.; Serov, A. Bio-Inspired Design of Electrocatalysts for Oxalate Oxidation : A Combined Experimental and Computational Study of Mn-N-C Catalysts. *Phys. Chem. Chem. Phys.* **2015**, *17*, 13235–13244.

(15) Jagadeesh, R. V.; Surkus, A.-E.; Junge, H.; Pohl, M.-M.; Radnik, J.; Rabeah, J.; Huan, H.; Schunemann, V.; Bruckner, A.; Beller, M. Nanoscale Fe2O3-Based Catalysts for Selective Hydrogenation of Nitroarenes to Anilines. *Science.* **2013**, *342*, 1073–1076.

(16) Deng, D.; Chen, X.; Yu, L.; Wu, X.; Liu, Q.; Liu, Y.; Yang, H.; Tian, H.; Hu, Y.; Du, P.; *et al.* A Single Iron Site Confined in a Graphene Matrix for the Catalytic Oxidation of Benzene at Room Temperature. *Sci. Adv.* **2015**, *1*, e1500462.

(17) Farsani, M. R.; Yadollahi, B. Synthesis, Characterization and Catalytic Performance of a Fe Polyoxometalate/silica Composite in the Oxidation of Alcohols with Hydrogen Peroxide. *J. Mol. Catal. A Chem.* **2014**, *392*, 8–15.

(18) Shi, F.; Tse, M. K.; Pohl, M. M.; Brückner, A.; Zhang, S.; Beller, M. Tuning Catalytic Activity between Homogeneous and Heterogeneous Catalysis: Improved Activity and Selectivity of Free Nano-Fe2O3 in Selective Oxidations. *Angew. Chemie - Int. Ed.* **2007**, *46*, 8866–8868.

(19) Gao, Y.; Ma, D.; Hu, G.; Zhai, P.; Bao, X.; Zhu, B.; Zhang, B.; Su, D. S. Layered-Carbon-Stabilized Iron Oxide Nanostructures as Oxidation Catalysts. *Angew. Chem. Int. Ed. Engl.* **2011**, *50*, 10236–10240.

(20) Modak, A.; Mondal, J.; Bhaumik, A. Porphyrin Based Porous Organic Polymer as

Bi-Functional Catalyst for Selective Oxidation and Knoevenagel Condensation Reactions. *Appl. Catal. A Gen.* **2013**, *459*, 41–51.

(21) Fidalgo-Marijuan, A.; Barandika, G.; Bazán, B.; Urtiaga, M. K.; Larrea, E. S.; Iglesias, M.; Lezama, L.; Arriortua, M. I. Heterogeneous Catalytic Properties of Unprecedented μ-O-[FeTCPP]2 Dimers (H2TCPP = Meso-tetra(4-Carboxyphenyl)porphyrin): An Unusual Superhyperfine EPR Structure. *Dalt. Trans.* **2015**, *44*, 213–222.

(22) Bilis, G.; Christoforidis, K. C.; Deligiannakis, Y.; Louloudi, M. Hydrocarbon Oxidation by Homogeneous and Heterogeneous Non-Heme Iron (III) Catalysts with H2O2. *Catal. Today* **2010**, *157*, 101–106.

(23) Rahimi, R.; Ghoreishi, S. Z.; Dekamin, M. G. Immobilized Metalloporphyrins on 3-Aminopropyl-Functionalized Silica Support as Heterogeneous Catalysts for Selective Oxidation of Primary and Secondary Alcohols. *Monatshefte für Chemie* **2012**, *143*, 1031–1038.

(24) Oveisi, A. R.; Zhang, K.; Khorramabadi-Zad, A.; Farha, O. K.; Hupp, J. T. Stable and Catalytically Active Iron Porphyrin-Based Porous Organic Polymer: Activity as Both a Redox and Lewis Acid Catalyst. *Sci. Rep.* **2015**, *5*, 10621.

(25) Jagadeesh, R. V; Junge, H.; Beller, M. Green Synthesis of Nitriles Using Non-Noble Metal Oxides-Based Nanocatalysts. *Nat. Commun.* **2014**, *5*, 4123.

(26) Maier, B.; Dietrich, C.; Büchs, J. Correct Application of the Sulphite Oxidation Methodology of Measuring the Volumetric Mass Transfer Coefficient kLa Under Non-Pressurized and Pressurized Conditions. *Food Bioprod. Process.* **2001**, *79*, 107–113.

(27) Zhu, Y.; Zhang, B.; Liu, X.; Wang, D. W.; Su, D. S. Unravelling the Structure of Electrocatalytically Active Fe-N Complexes in Carbon for the Oxygen Reduction Reaction. *Angew. Chemie - Int. Ed.* **2014**, *53*, 10673–10677.

(28) Artyushkova, K.; Serov, A.; Rojas-Carbonell, S.; Atanassov, P. Chemistry of Multitudinous Active Sites for Oxygen Reduction Reaction in Transition Metal-Nitrogen-Carbon Electrocatalysts. *J. Phys. Chem. C* **2015**, *119*, 25917–25928.

(29) Martinez, U.; Dumont, J. H.; Holby, E. F.; Artyushkova, K.; Purdy, G. M.; Singh, A.; Mack, N. H.; Atanassov, P.; Cullen, D. A.; More, K. L.; *et al.* Critical Role of Intercalated Water for Electrocatalytically Active Nitrogen-Doped Graphitic Systems. *Sci. Adv.* **2016**, *2*, 1–7.

(30) Strelko, V. V.; Kartel, N. T.; Dukhno, I. N.; Kuts, V. S.; Clarkson, R. B.; Odintsov, B. M. Mechanism of Reductive Oxygen Adsorption on Active Carbons with Various Surface Chemistry. *Surf. Sci.* **2004**, *548*, 281–290.

(31) Ide, M. S.; Davis, R. J. Perspectives on the Kinetics of Diol Oxidation over Supported Platinum Catalysts in Aqueous Solution. *J. Catal.* **2013**, *308*, 50–59.

(32) Yang, M.-Q.; Zhang, Y.; Zhang, N.; Tang, Z.-R.; Xu, Y.-J. Visible-Light-Driven Oxidation of Primary C-H Bonds over CdS with Dual Co-Catalysts Graphene and TiO2. *Sci. Rep.* **2013**, *3*, 3314.

(33) Ide, M. S.; Falcone, D. D.; Davis, R. J. On the Deactivation of Supported Platinum Catalysts for Selective Oxidation of Alcohols. *J. Catal.* **2014**, *311*, 295–305.

(34) Hoover, J. M.; Ryland, B. L.; Stahl, S. S. Mechanism of copper(I)/TEMPO-Catalyzed Aerobic Alcohol Oxidation. *J. Am. Chem. Soc.* **2013**, *135*, 2357–2367.

(35) Cao, Q.; Dornan, L. M.; Rogan, L.; Hughes, N. L.; Muldoon, M. J. Aerobic Oxidation Catalysis with Stable Radicals. *Chem. Commun.* **2014**, *50*, 4524–4543.

(36) Serov, A.; Robson, M. H.; Smolnik, M.; Atanassov, P. Templated Bi-Metallic Non-PGM Catalysts for Oxygen Reduction. *Electrochim. Acta* **2012**, *80*, 213–218.

Chapter 5. Atomically-dispersed Co and Cu on N-doped Carbon for Reactions involving C-H activation

5.1. Introduction

The catalytic transformation of carbon feedstocks to liquid fuels and useful chemicals usually involves the activation of C-H bonds, regardless of the feedstock source such as petroleum, natural gas or biomass.[1–3] For nearly a century, heterogeneous precious-metal catalysts have been recognized as possessing the features needed to activate C-H bonds.[4,5] However, high cost limits their application in large scale and distributed systems.[6] Therefore, a strong motivation exists to discover or engineer earth-abundant elements in chemical environments that catalyze desired chemical transformations similar to those typical of precious metals. Recently, non-precious metals confined in a nitrogen-containing carbon matrix (M-N-C) were developed for electro-catalytic oxygen reduction (ORR) and water splitting reaction, in which comparable activity and stability to the well-known Pt catalysts were observed.[7–10] Considering its demonstrated redox activity, M-N-C catalysts were further applied in organic reactions involving oxidative C-H activation at mild temperature (usually lower than 400 K), such as dehydrogenation, coupling, esterification and nitrification.[11–21]

The M-N-C catalysts are commonly prepared by a high-temperature pyrolysis method, which usually produces a variety of metal environments simultaneously, such as exposed or encapsulated metal nanoparticles along with the atomically-dispersed metals in a variety of coordination environments. The co-existence of these sites complicates investigations into the nature of the catalytically active sites. Catalysts containing predominantly atomically-dispersed Fe and Co, which also exhibited catalytic activity in ORR or C-H activation, were utilized to study the coordination environment and chemical state around the metal.[15,17,20,22–40] Atomic dispersion of the metals on these catalysts has been verified by aberration-corrected scanning transmission electron microscopy (AC-STEM) and X-ray absorption spectroscopy (XAS). The chemical state and coordination environment were also probed by XAS, along with X-ray photoelectron spectroscopy (XPS), Mössbauer spectroscopy, electron energy loss spectroscopy (EELS) and density-functional theory (DFT).[15,17,27–29,31,35,36,38,40,41] Although the existence of nitrogen-coordinated metal sites (MN_x) has been well documented, the coordination number of N atoms to the active metal center is still unresolved.[21,37,38,40,42] Additionally, in situ XAS and XPS have been used to study Fe-based catalysts for ORR,[29,31,34,36] but in situ characterization of materials for chemical catalysis is lacking.

In a recently-published work,[19] atomically-dispersed Co and Cu in N-containing carbon exhibited the highest activity for catalytic alcohol oxidation among a series of M-N-C catalysts. In the current work, Co and Cu catalysts were comprehensively characterized and correlated with reaction rates to identify and quantify the active sites. In situ XAS was performed to investigate the evolution of Co and Cu sites under oxidizing and reducing conditions at different temperatures (up to 750 K). In addition to oxidative dehydrogenation of benzyl alcohol at mild temperature (353 K), the dehydrogenation of propane to propene was demonstrated over Co-N-C.

5.2. Experimental methods

5.2.1. Preparation of M-N-C catalysts

Black Pearls 2000 from Cabot Corporation and Davisil 636 silica from Sigma-Aldrich were used as the carbon and silica supports in this study. The aqueous ammonia was purchased from Fisher Scientific. All other chemicals were purchased from Sigma-Aldrich Corporation or Alfa Aesar and gases were from Praxair Inc. distributed by GTS-Welco. The M-N-C catalysts were prepared by a modified pyrolysis method.[11,43] First, an ethanol solution of 1,10-phenanthroline was mixed with an aqueous solution of $Co(NO_3)_2{\cdot}6H_2O$ or $Cu(NO_3)_2{\cdot}3H_2O$ with a 1:2 molar ratio of metal to 1,10-phenanthroline. The mixture was stirred for 20 min at 353 K and added dropwise to slurry of carbon black in a 0.1 M NaOH aqueous solution under vigorous stirring at 353 K. After 2 h, the slurry was cooled, filtered, washed thoroughly with distilled, deionized water (DI water) and dried overnight at 343 K. The filtered medium was colorless, indicating the efficient adsorption of metal complex onto the carbon support. The prepared materials were subsequently impregnated with an acetone solution of dicyandiamide and dried at 343 K overnight. The amount of impregnated dicyandiamide relative to carbon support was 40 wt% for samples with 1 wt% metal loading or 80 wt% for catalysts with 3 or 5 wt% metal loading. The obtained solid was pyrolyzed at 873, 973 or 1073 K for 2 h with a ramping rate of 10 K min^{-1} under ultra-high purity N_2 flow (100 cm^3 min^{-1}). To investigate the influence of ammonia treatment, Co and Cu catalysts pyrolyzed at 973 K with 1 wt% nominal metal loading were treated at 1223 K in NH_3 with a ramping rate of 10 K min^{-1} for 2 h under NH_3 flow (100 cm^3 min^{-1}). To remove the nanoparticles that were observed on the optimized Co-N-C, the catalyst was treated in 1 M HCl solution overnight at room temperature, filtered, washed thoroughly and dried at 393 K. The acid-treated catalyst was denoted as Co-N-C-HCl. To prepare a metal-free nitrogen-doped carbon (N-C), an acetone solution of dicyandiamide (0.4 g) was impregnated into carbon black (0.5 g) followed by a pyrolysis step at 973 K for 2 h under a dinitrogen flow of 100 cm^3 min^{-1}. As references, supported Co (5 wt%) and Cu (1.5 wt%) nanoparticles were prepared by incipient wetness impregnation using an aqueous solution of $Co(NO_3)_2{\cdot}6H_2O$ or $Cu(NO_3)_2{\cdot}3H_2O$ as the metal precursor and silica, carbon black or N-C as the support. After impregnation, the Co precursors on carbon or N-doped carbon were decomposed by thermal treatment in N_2 flow (100 cm^3 min^{-1}) at 973 K. The C or N-C-supported Cu nanoparticles were prepared by reducing the impregnated $Cu(NO_3)_2$ under

H_2 flow at 623 K. The nanoparticles on Co/SiO_2 were prepared by reducing the impregnated support under H_2 flow at 923 K. Nitrogen-doped carbon layers were subsequently added to carbon-supported Co and Cu nanoparticle by a modified pyrolysis methods using 4-aminoantipyrine as the N-C precursor.[44,45] Additionally, an atomically-dispersed 2.5 nominal wt% Co/SiO_2 catalyst was synthesized by an ion exchange method described elsewhere (denoted as CoO_x-SiO_2).[46,47] Briefly, 4.875 g of acid-washed silica was dispersed in 98 cm^3 of DI water under vigorous stirring and then heating to 373 K. A solution containing 0.573 g $Co(NH_3)_6Cl_3$, 2.765 cm^3 aqueous ammonia, and 104 cm^3 DI water was added dropwise over 10 min to the SiO_2 slurry, followed by stirring at 373 K for 1 h. Afterwards, the mixture was cooled to room temperature, washed in DI water, dried, and calcined in 100 cm^3 min^{-1} air at 573 K for 2 h after heating with a 1 K min^{-1} ramp rate.

5.2.2. Characterization of M-N-C catalysts

The XRD patterns were recorded using a PANalytical X'Pert Pro MPD (Multi-Purpose Diffractometer) instrument with Cu Kα radiation (45 kV, 40 mA) and scanning of 2θ from 10° to 70° with a step size of 0.0025° at a rate of 0.5° min^{-1}.

The STEM was performed on an FEI Titan 80-300 operating at 300 kV or a JEOL 2010 F instrument operating at 200 kV.

The metal loading on Cu-N-C and Co-N-C-HCl was determined by ICP-AES (performed by Galbraith Laboratories (2323 Sycamore Drive, Knoxville, TN 37921)).

The XPS was performed on a Thermo Scientific ESCALAB 250 spectrometer equipped with a focused monochromatic Al Kα X-ray radiation source (1486.6 eV) and a hemispherical analyzer with a 6-element multichannel detector. The incident X-ray beam was 45° off normal to the sample while the X-ray photoelectron detector was normal to the sample. A large area magnetic lens with a 500 μm spot size in constant analyzer energy mode was utilized with a pass energy of 20 eV for region scans. Charge compensation was employed during data collection with an internal electron flood gun (2 eV) and a low energy external Ar ion flood gun. The binding energy of the C 1s peak assigned at 284.5 eV, which is attributed to the support, was used to reference the peak positions.[48]

X-ray absorption spectroscopy (XAS) at the Co *K* and Cu *K* edges was collected at beamline 8-ID at the National Synchrotron Light Source II, Brookhaven National Laboratory. The Cu and Co metal foils (Goodfellow Corporation) were used as reference. Chemical standards including CoO, $Co(NO_3)_2{\cdot}6H_2O$, Co_3O_4, $(NH_3)CoCl_3$, Co(II) phthalocyanine, CuO, $Cu(NO_3)_2{\cdot}3H_2O$, and Cu(II) phthalocyanine were pelletized with boron nitride to provide appropriate absorption thickness. The XAS data were processed using the Demeter software package.[49]

5.2.3. Oxidation of benzyl alcohol over M-N-C

The high-pressure, semi-batch alcohol oxidation reactions were performed in a 50 cm^3 Parr Instrument Company 4592 batch reactor with a 30 cm^3 glass liner. An aqueous benzyl alcohol solution (10 cm^3) and catalyst were added to the glass liner. The glass liner was inserted into the reactor, sealed, purged with Ar, heated to 353 K and initiated by pressurizing the reactor with O_2. The conversion of alcohol during the initial heating stage was negligible. Liquid samples were periodically removed and the catalyst was removed using a 0.2 μm PTFE filter before product analysis with a Waters e2695 high performance liquid chromatograph (HPLC) equipped with refractive index detector. Product separation in the HPLC was accomplished on an Aminex HPX-87H column (Bio-Rad) operating at 318 K with an aqueous 5 mM H_2SO_4 solution as the mobile phase flowing at 5 cm^3 min^{-1}. The retention times and calibration curves were determined by injecting known concentrations of standards. The carbon balance was greater than 90 % unless otherwise stated.

The amount of catalyst added to the reactor was chosen so that the alcohol oxidation rate would not be limited by O_2 mass transfer from the gas to the liquid.[50] Selectivity to a specific product is defined as moles of that product formed divided by moles of all products produced. The initial reaction rates were calculated from the initial conversion of the alcohol by performing a linear fit of the conversion after 15 min of reaction.

For poisoning experiments, 10 mg of catalysts (Co-N-C and Cu-N-C) and 10 cm^3 aqueous solution of benzoic acid or KSCN were added to the glass liner. The glass liner was inserted into the reactor, sealed, purged with Ar and heated to 353 K for 20 min. Subsequently, the catalyst was recovered by filtration, washed thoroughly and dried in R.T. overnight. The filtered medium was analyzed by HPLC to calculate the amount of adsorbed benzoic acid. The recovered catalyst was then evaluated in the benzyl alcohol oxidation reaction as described above.

5.2.4. Propane Dehydrogenation

Dehydrogenation experiments were conducted in a continuous downward flow reactor consisting of a 0.64 cm OD x 0.089 cm wall thickness stainless steel tube 15 cm in length. A 10 cm pre-heating section of the same material was above the reactor. The catalyst bed was supported by glass wool. Catalysts were diluted with silica such that the total catalyst and diluent mass was 300 mg. The Co-N-C-HCl catalyst was treated in 5 M NH_4OH aqueous solution overnight, washed and dried at room temperature before the reaction. This treatment was performed since HCl treatment was shown to inhibit alcohol oxidation activity that can be recovered by mild base (Tabls S5). Other catalysts were used after the synthesis. The carbon-supported catalysts were pre-treated in situ in 100 cm^3 min^{-1} N_2 at 923 K for 3 h and the silica-supported catalysts were pre-treated in N_2 at 773 K for 3 h. Propane and N_2 were then fed to the reactor with flow rates of 10 cm^3 min^{-1} and 30 cm^3 min^{-1}. Reactor effluent was fed to an online Agilent 7890A equipped with an Agilent HP-PLOT/Q column and a flame ionization detector (FID). Samples were taken every 15 min, starting with the sample after 5 minutes on stream.

5.3. Results

5.3.1. Optimization of Co-N-C and Cu-N-C for benzyl alcohol oxidation

By pyrolyzing carbon-supported 1,10-phenanthroline–metal complexes (MPhen/C (M = Co, Cu)), a series of Co and Cu catalysts prepared at different pyrolysis temperatures was obtained and evaluated in the aerobic oxidation of benzyl alcohol. As shown in Table 5. 1, alcohol oxidation rates over unpyrolyzed CoPhen/C and CuPhen/C were both less than 0.015×10^{-6} mol s^{-1} g_{cat}^{-1}, respectively. A significant increase in reaction rate (by more than an order of magnitude) was observed after the pyrolysis. Over the most active Co and Cu catalysts pyrolyzed at 973 K, reaction rates of 2.1×10^{-6} and 0.92×10^{-6} mol s^{-1} g_{cat}^{-1} were measured (Table 5. 2). Whereas pyrolysis at elevated temperature is necessary for the formation of active sites,[20,28,51] we observed a decrease in reaction rate when pyrolysis temperature increased to 1073 K, which was likely related to the formation of catalytically-inactive metal nanoparticles. As shown in Figure 5.1, negligible diffraction pattern of metal or metal oxide nanoparticles were observed over catalysts pyrolyzed up to 973 K. In contrast, metal nanoparticles were formed during the pyrolysis at 1073 K, as evidenced by the X-ray diffraction pattern of Cu(111) at $2\theta=43^{o}$ (Figures 5. 1) and a predominant Co-Co EXAFS feature over a catalyst pyrolyzed at 1073 K (Figure 5.2b). Further increase in Co loading over Co catalyst pyrolyzed 973 K from 1 wt% to 5 wt% increased the reaction rate but negligible change in rate was observed when Cu loading increased from 1 wt% to 3 wt% (Table 5. 2).

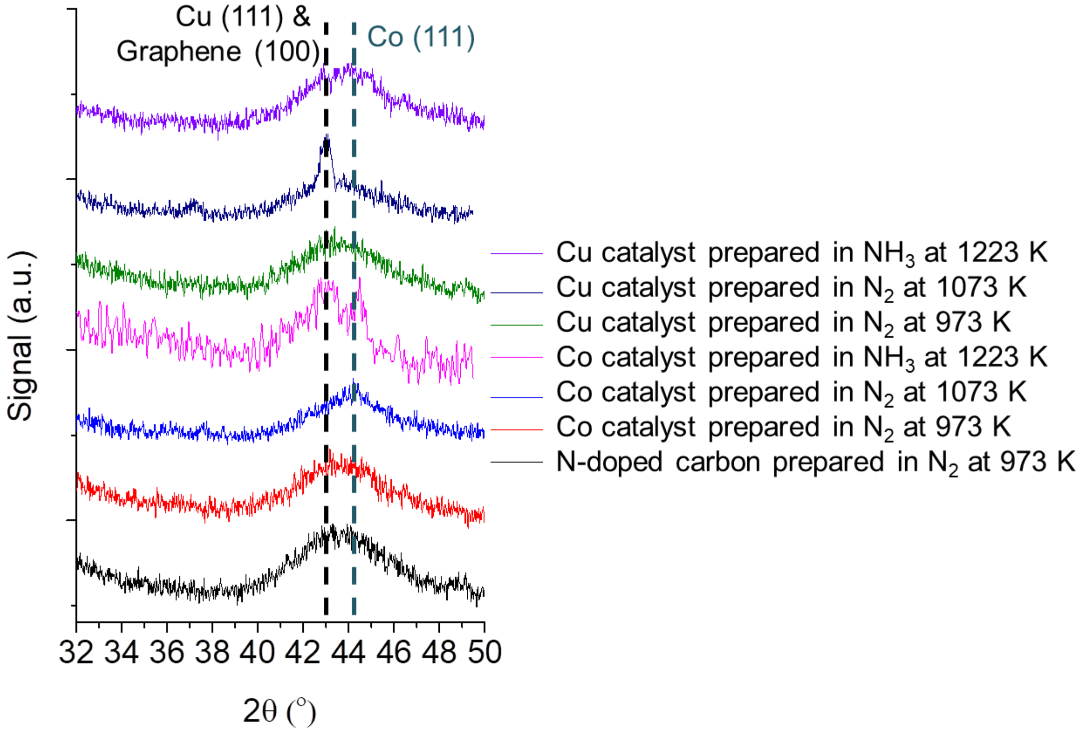

Figure 5. 1. XRD patterns, offset for clarity of Cu and Co catalysts prepared under different conditions and the metal-free N-doped carbon pyrolyzed at 973 K.

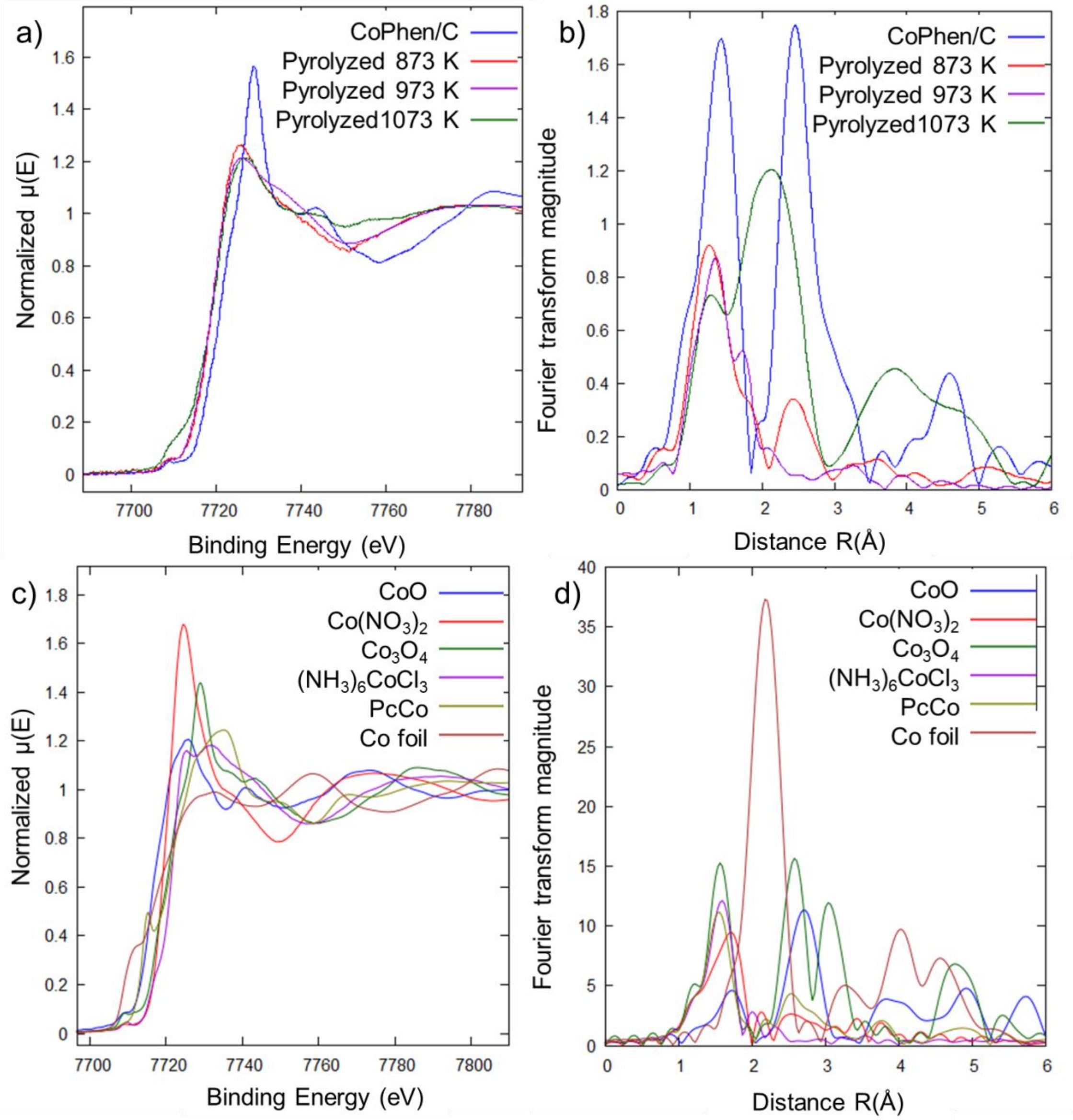

Figure 5. 2. Normalized XANES at the Co K-edge of a) carbon-supported 1,10-phenanthroline Co complex (CoPhen/C) and Co catalysts prepared by pyrolysis at 873, 973 and 1073 K and c) cobalt standards (PcCo is Co(II) phthalocyanine); The k^2-weighted Fourier transform (not corrected for phase shift) of Co EXAFS associated with b) CoPhen/C and Co catalysts at 873, 973 and 1073 K and d) cobalt standards.

Table 5. 1. Rates of benzyl alcohol oxidation over reference materials[a]

Entry	Catalyst	Metal loading[b] (wt%)	Rate (10^{-6} mol s^{-1} g_{cat}^{-1})
1	CoPhen/C	1	0.013
2	CuPhen/C	1	0.010
3	N-C	–	0.041
4	Cu/C	1.5	0.035
5	Cu/N-C	1	0.022
6	N-C-Cu/C	1.5	0.024
7	Co/C	5	0.040
8	Co/N-C	5	0.085
9	N-C-Co/C	5	0.062
10	Co/SiO_2	5	0.0026
11	CoO_x-SiO_2	2.5	0.0025
12	Co/N-C	5	0.085

a. Reaction conditions: 10 mL 0.05 M benzyl alcohol aqueous solution, 10 mg catalyst, 1 MPa O_2, 353 K.

b. The nominal metal loadings are calculated based on the amounts of precursors for catalyst preparation unless otherwise stated.

Table 5. 2. Rates of benzyl alcohol oxidation over Co and Cu catalysts[a]

Metal	Metal loading (wt%)[b]	Pyrolysis temperature (K)	Post-treatment	Rate (10^{-6} mol s^{-1} g_{cat}^{-1})
Cu	1	873	–	0.35
	1	973	–	0.92
	1	1073	–	0.42
	3	973	–	0.88
	1.2[c]	973	NH_3, 1223 K	1.6
Co	1	873	–	0.93
	1	973	–	2.1
	1	1073	–	1.3
	5	973	–	7.8
	1	1073	NH_3, 1223 K	0.17

a. Co and Cu catalysts were prepared by a pyrolyzing carbon-supported Co and Cu complexs. Details of catalyst preparation are described in Method. Reaction conditions: 10 mL 0.05 M benzyl alcohol aqueous solution, 10 mg catalyst, 1 MPa O_2, 353 K.

b. The nominal metal loadings are calculated based on the amounts of precursors for catalyst preparation unless otherwise stated.

c. The metal loading measured by ICP-AES.

To further promote the activity, an NH_3 post-treatment at 1223 K was additionally performed on Co and Cu catalysts after pyrolysis at 973 K.[10,31] The Cu catalyst remained mostly atomically-dispersed, as evidenced by the negligible formation of Cu metal particles observed in STEM (Figure 5.3a) and EXAFS (Figure 5.2). The reaction rate of the

NH_3-treated Cu catalyst increased to 1.6×10^{-6} mol s^{-1} g_{cat}^{-1}, compared to a rate of 0.92×10^{-6} mol s^{-1} g_{cat}^{-1} over the Cu catalyst before NH_3 treatment. Over NH_3-treated Co catalyst, however, a diffraction peak from Co(111) at $2\theta = 44.2^{o}$ was observed by XRD (Figure 5.1). The reaction rate of the NH_3-treated Co catalyst decreased by more than an order of magnitude compared to that measured over the Co catalyst before NH_3 treatment. Using the catalytic activities in aqueous benzyl alcohol oxidation as the property to maximize, the optimized Co-N-C is prepared by pyrolysis of CoPhen/C with impregnated dicyandiamide at 973 K and the optimized Cu-N-C is prepared by pyrolyzing CuPhen/C with impregnated dicyandiamide at 973 K followed by NH_3 treatment at 1223 K. The kinetic isotope effect (KIE), evaluated by using $C_6H_5CD_2OH$, ranged from 1.6 to 2.9, depending on the metal in the catalyst and the presence of base in the reaction (see Table 5. 3). The normal KIE observed here indicates that C-H activation of the alcohol is a kinetically-relevant elementary step.

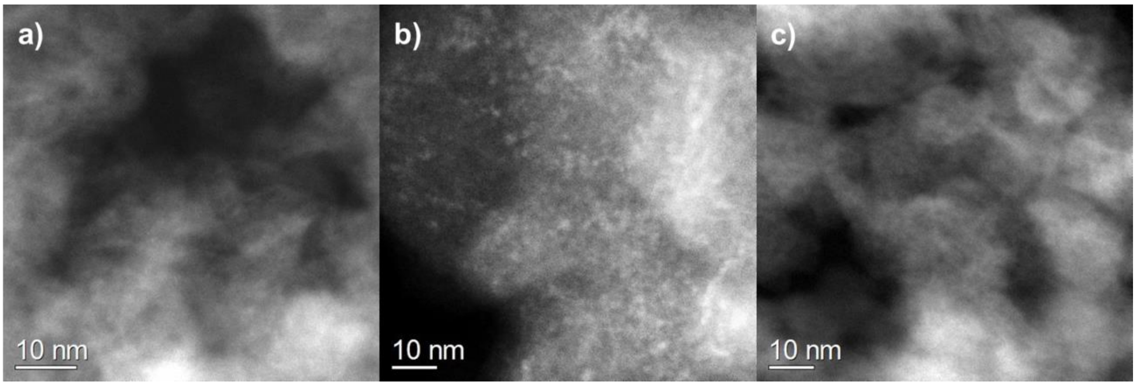

Figure 5. 3. Dark-field STEM images of a) Cu-N-C (prepared by pyrolysis at 973 K followed by NH_3 treatement at 1223 K), b) Co-N-C (prepared by pyrolysis at 973 K) and c) Co-N-C-HCl (prepared by HCl treatment of Co-N-C).

Table 5. 3. Kinetic isotope effect for benzyl alcohol oxidation[a]

Catalyst	Reaction	$Rate_D$ (10^{-6} mol s^{-1} g_{cat}^{-1})	$Rate_H$/ $Rate_D$
Co-N-C	$C_6H_5CD_2OH+H_2O$	2.3	2.9
	$C_6H_5CD_2OH+H_2O$+0.1 M NaOH	10	1.6
Cu-N-C	$C_6H_5CD_2OH+H_2O$	0.57	2.8
	$C_6H_5CD_2OH+H_2O$+0.1 M NaOH	3.9	1.8

a: Reaction conditions: 10 mL 0.05 M benzyl alcohol aqueous solution, 10 mg catalyst, 1 MPa O_2, 353 K. Conversion was less than 20 % when calculating the rate.

5.3.2. Quantification of active sites for low-temperature C-H activation

The quantification of active sites in these materials remains a challenge since some of the metal atoms may be "buried" in the carbon matrix and therefore unavailable for catalysis, or the local environment around some of the metal atoms may not optimal for catalysis. A titration method to selectively poison active sites would be quite useful to estimate the actual number of metal sites participating in the reaction. Potassium thiocyanate has been reported to poison atomically-dispersed metal sites,[21,42] but it turns out to be an unsuitable poison under the reaction conditions in this study. As shown in Table 5. 4, addition of KSCN to the reaction solution at a level of more than 5 times that of metal caused a decrease in rate by less than 30% over the Co and Cu catalysts. In contrast, addition of benzoic acid decreased the reaction rate by ~90% and therefore was utilized to estimate the active site density in Co-N-C and Cu-N-C catalysts.

Table 5. 4. Reaction rate of benzyl alcohol oxidation over M-N-C with additives[a]

Catalyst	Additive	Reaction rate (10^{-6} mol s^{-1} g_{cat}^{-1})	Decreased %
Co-N-C	KSCN	5.5	29
	Benzoic acid	0.92	88
Cu-N-C	KSCN	1.2	25
	Benzoic acid	0.15	91

a: Reaction conditions: 10 mL 0.1 M benzyl alcohol aqueous solution with 0.005 M additive, 10 mg catalyst, 1 MPa O_2, 353 K. The reaction rates with additives were compared to those without additive to calculate the percentages of decreased reaction rate.

A very small amount of acid can poison a substantial fraction of the observed activity, especially for Co-N-C (Figure 5.4). The oxidation rate decreased by 65% with adsorption of 0.24×10^{-6} mol of benzoic acid, which corresponds to 0.03 equivalents relative to total Co. Over Cu-N-C, adsorption of 0.34×10^{-6} mol of acids (0.18 equivalents relative to Cu), a 40% decrease in oxidation activity. Adsorption of higher acid amounts did not proportionally decrease the rate, indicating the presence of active sites that are not readily poisoned by acid. A similar non-linear dependence of reaction rate on the amount of poisoning species has also been reported recently.[42] Since it is possible that acid molecules could also adsorb on the carbon support, the ratio of adsorbed acid to catalytically active sites has an assumed upper bound of 1:1. The effect of acid poisoning on the highly active sites can be correlated with the following equation:

$$r_{add} = r_0 - \frac{r_0 \times poisoned\ sites}{total\ sites} \geq r_0 - \frac{r_0 \times Adsorbed\ acids}{total\ sites} \quad (1)$$

where r_{add} is the measured oxidation rate and r_0 is the oxidation rate without any acid poison. The initial linear region (first four points) in Figures 5. 4a and 5. 4b were fitted with Equation

(1) to estimate an upper bound of the highly active metal sites that were poisoned. As shown in Table 5. 5, the upper bound of the highly active sites in 10 mg of sample were 0.32×10^{-6} mol in Co-N-C and 0.70×10^{-6} mol in Cu-N-C, which correspond to 0.19 wt% Co and 0.45 wt% of Cu. Accordingly, the lower bound of benzyl alcohol oxidation turnover frequency (TOF) over the highly active Co and Cu sites was 0.24 s^{-1} and 0.023 s^{-1}, respectively. Carbon-supported Pt nanoparticles have a turnover frequency of 0.33 s^{-1} under identical conditions, indicating the highly active sites of Co-N-C exhibit nearly the same rate as Pt nanoparticles.

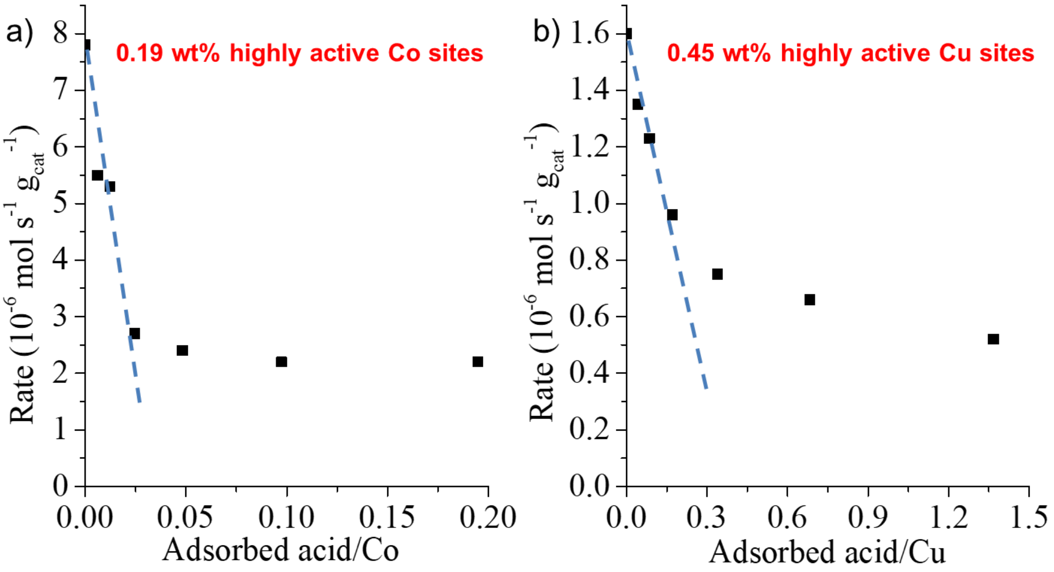

Figure 5. 4. Influence of adsorbed acids on metal sites on the reaction rate of benzyl alcohol oxidation over a) Co-N-C and b) Cu-N-C catalysts. Reaction conditions: 10 mL 0.1 M benzyl alcohol aqueous solution, 10 mg catalyst, 353 K, 1 MPa O_2, the reaction rates were calculated from the conversion after 15 min of reaction. The results from linear fit of first four points (dashed lines) are presented in Table 5. 5.

Table 5. 5. Amount of active sites from linear fit of alcohol oxidation rate with acid additives[a]

Catalyst	Intercept r_0, 10^{-6} mol s^{-1} g_{cat}^{-1}	Slope $\frac{r_0}{Active\ sites}$ s^{-1} g_{cat}^{-1}	Active sites in 10 mg catalyst (10^{-6} mol)
Co-N-C	7.4	23	0.32
Cu-N-C	1.6	2.3	0.70

a: The experimental data and fitting range were presented in Figure 5.4.

5.3.3. Discrimination of active sites

The optimized Co-N-C and Cu-N-C catalysts were characterized and compared to the reference materials in an attempt to identify the active sites. As shown in Figures 5. 1, 5. 2 and 5. 3, metal nanoparticle was not observed on the optimized Cu-N-C by XRD, XAS or STEM, suggesting the atomic dispersion of Cu sites. The elemental analysis by ICP-AES showed a Cu loading of 1.2 wt% (Table 5. 6). The Co-N-C catalyst, on the other hand, contains nanoparticles with a diameter of ~2 nm, as revealed by STEM (Figure 5. 3b). The Co nanoparticles were successfully removed by a mild acid wash with 1 M HCl (Figure 5. 3c).[21] The atomically-dispersed Co that remained on the sample (denoted as Co-N-C-HCl), has a loading of 1.5 wt% from ICP-AES (Table 5. 6), compared to a nominal loading of 5 wt% Co before the acid wash. Since the reaction rates of benzyl alcohol oxidation under basic conditions were the same over Co-N-C before and after acid-washing of catalyst (Table 5. 7), catalytic activity is not associated with the nanoparticles. Moreover, comparing the rates over supported or encapsulated nanoparticles (Figure 5. 5) as well as N-C without any metal (Table 5. 1), the much higher activity of the atomically-dispersed metal sites confirms their participation in the catalysis for oxidative dehydrogenation of benzyl alcohol. Additionally, negligible activity of carbon-supported 1,10-phenanthroline–metal complexes or highly-dispersed CoO_x on silica (Figure 5. 6) indicates the importance of the unique chemical environment around the metal atoms in M-N-C catalysts (Table 5. 1).

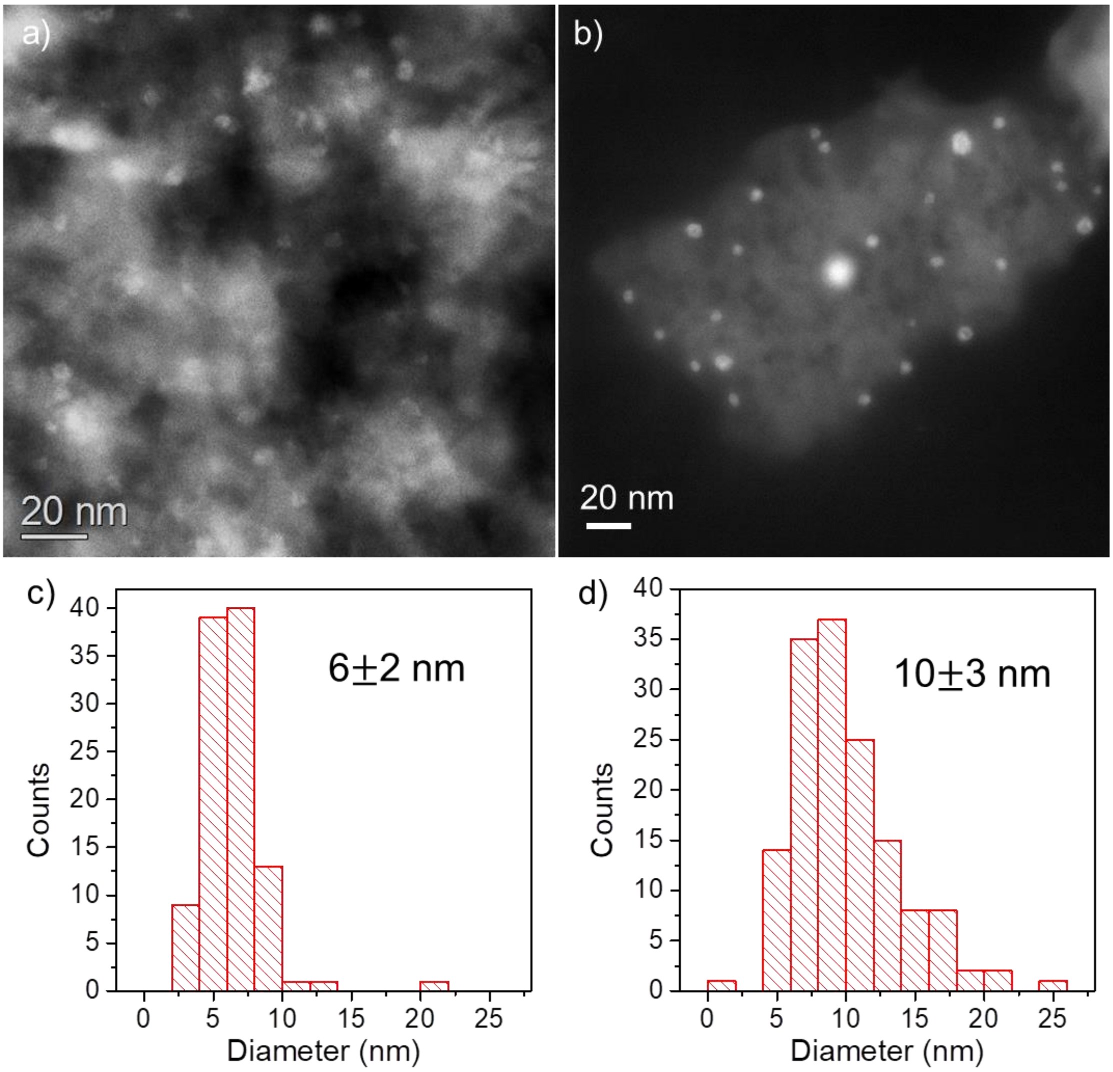

Figure 5. 5. Dark-field STEM images of a) Co/C and b) Cu/C and particle size distribution of c) Co/C and d) Cu/C. Co/C and Cu/C were prepared by incipient-wetness impregnation method using metal nitrates as precursor.

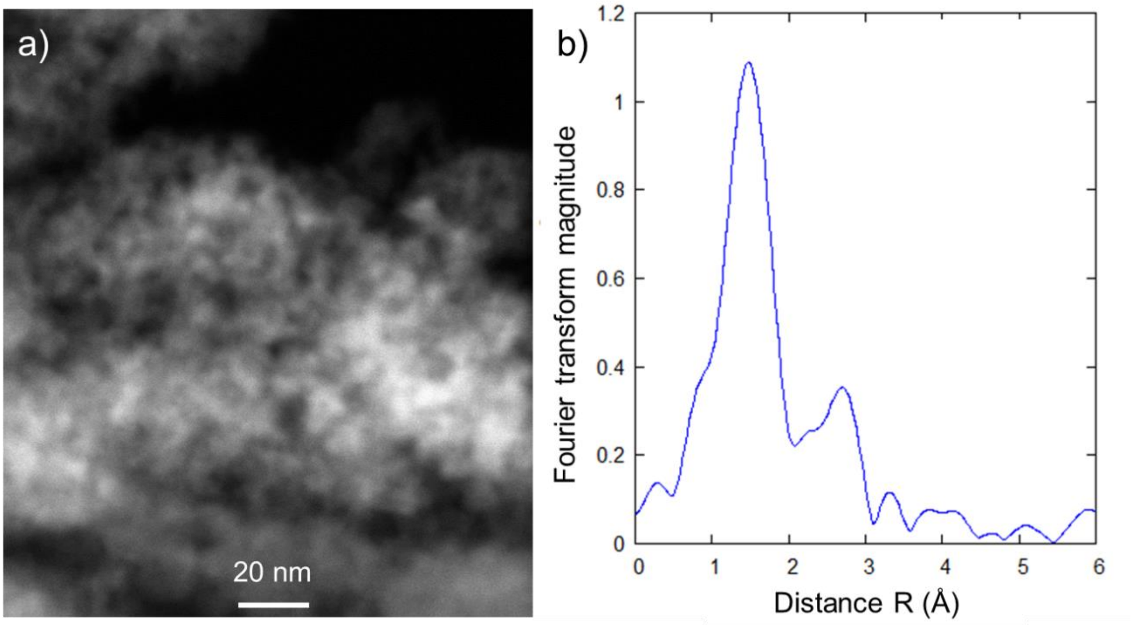

Figure 5. 6. a) Dark-field STEM image and b) k^2-weighted Fourier transform (not corrected for phase shift) of Co-K edge EXAFS associated with CoO_x-SiO_2 in air. CoO_x-SiO_2 was prepared by an ion-exchanged method followed by calcination at 573 K in air.

Table 5. 6. Weight loadings of metal sites associated with atomically-dispersed Co and Cu catalysts

Catalyst	Overall metal loading (wt%)	
	ICP-AES	XPS
Co-N-C-HCl	1.5	1.3
Cu-N-C	1.2	0.51

Table 5. 7. Rates of benzyl alcohol oxidation over Co-N-C before and after acid wash[a]

Catalyst	Metal loading (wt%)	Rate (10^{-6} mol s^{-1} g_{cat}^{-1})
Co-N-C	5[b]	16
Co-N-C-HCl	1.5[c]	16

a. Co-N-C after HCl wash is nominated as Co-N-C-HCl. Reaction conditions: 10 mL 0.05 M benzyl alcohol aqueous solution, 10 mg catalyst, 1 MPa O_2, 353 K, 0.1 M NaOH.

b. Nominal metal loading

c. The metal loading measured by ICP-AES.

5.3.4. Characterization of atomically-dispersed metal sites

The coordination environment around the metal atoms and the oxidation state in Co-N-C-HCl and Cu-N-C were also investigated. Results from XPS were used to characterize the loading and chemical state of the metal and nitrogen. As shown in Figure 5.7a, a major peak for Co $2p_{3/2}$ was observed at 780.7 eV, together with a satellite peak at 786.4 eV having 1/3 intensity of the main peak, consistent with the presence of Co(II).[52,53] The Cu $2p_{3/2}$ XPS spectrum showed only one peak at 933.5 eV, which is characteristic of Cu(II).[54] The N 1s XPS spectra of Co-N-C-HCl and Cu-N-C can be deconvoluted into a graphitic N peak at ~400.7 eV and pyridinic N peak at ~398.8 eV. Pyridinic N atoms have been reported to act as coordinating sites for metal cations to form active MN_x sites.[42,47,52] Over both atomically-dispersed Co and Cu catalysts, excess pyridinic N exists relative to metal, as determined by XPS (Tabls S5). The molar ratios of metal:pyridinic N are ~ 1:11 over Co-N-C-HCl and ~1:2 over Cu-N-C (Table 5. 8). Notably, 1.3 wt% Co loading in Co-N-C-HCl measured from surface-sensitive XPS is quite close to the bulk Co loading determined by ICP-AES, which suggests a homogeneous distribution of Co throughout the catalyst. In the Cu-N-C catalyst, 0.51 wt% of Cu was measured by XPS compared to 1.2 wt% Cu by ICP-AES (Table 5. 6), indicating a higher fraction of CuN_x moieties were buried in the support rather than being present on the surface.

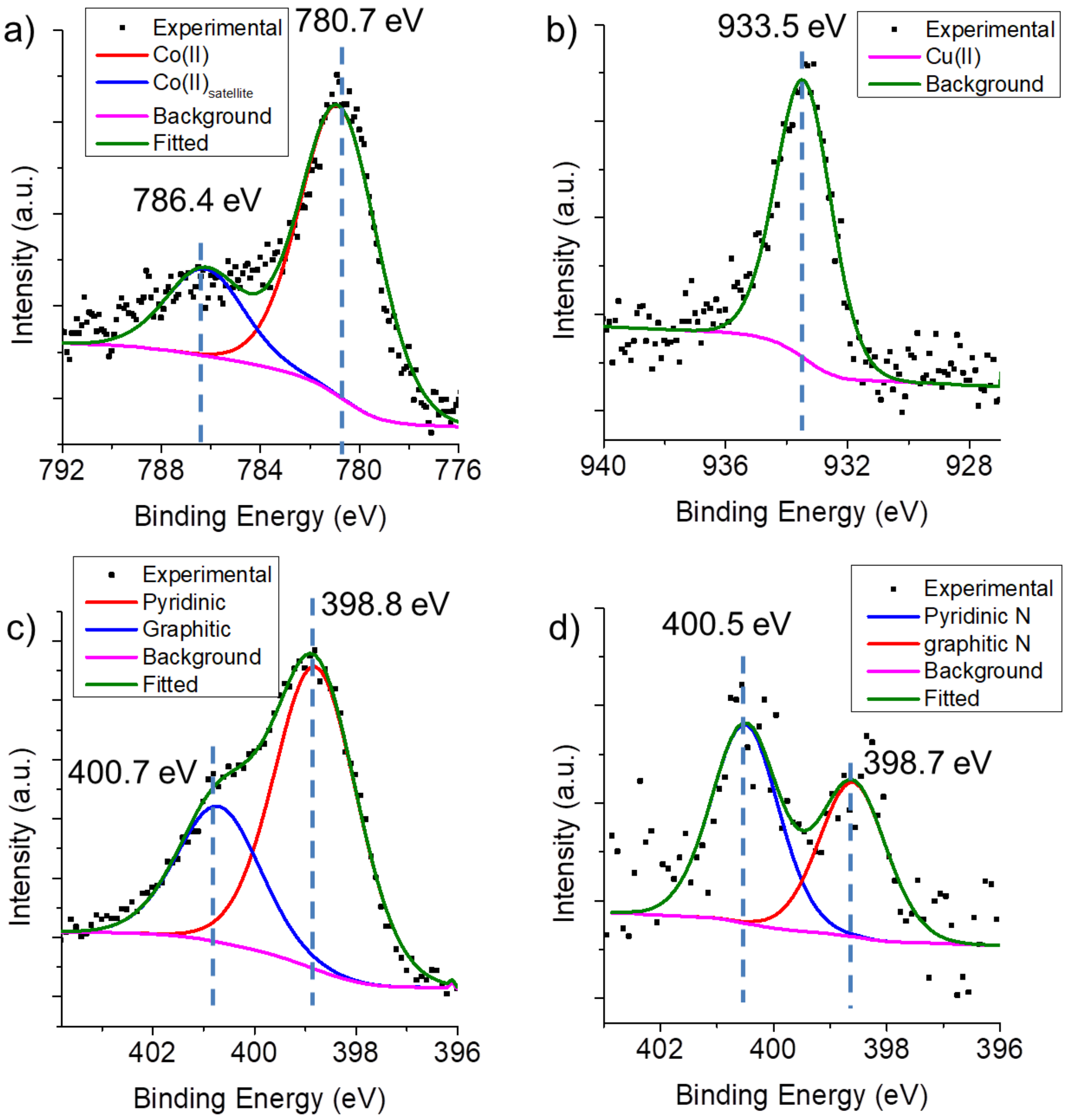

Figure 5. 7. a) Co $2p_{3/2}$ X-ray photoelectron spectrum of Co-N-C-HCl and b) Cu $2p_{3/2}$ X-ray photoelectron spectrum of Cu-N-C.

Table 5. 8. Core level binding energies and compositions determined by XPS[a]

Sample	Area	Binding energies (eV)			Relative amount (mol%)				
		Metal	N_I[b]	N_{II}[c]	Metal	N_I[b]	N_{II}[c]	O	C
N-C	1	–	398.8	400.7	–	0.80	0.66	1.8	97
	2	–	398.8	400.7	–	0.88	0.78	2.0	96
	3	–	398.8	400.6	–	0.65	0.60	1.5	97
	Avg	–	–	–	–	0.78	0.68	1.8	97
Co-N-C-HCl	1	780.7	398.8	400.7	0.31	3.0	1.3	2.4	93
	2	780.7	398.8	400.9	0.23	3.1	1.4	2.3	93
	3	780.7	398.9	400.8	0.24	2.6	1.4	2.4	94
	Avg	–	–	–	0.26	2.9	1.4	2.4	93
Cu-N-C	1	933.5	398.6	400.5	0.12	0.20	0.25	1.8	98
	2	933.3	398.8	400.7	0.10	0.17	0.18	1.5	98
	3	933.3	398.8	400.6	0.09	0.20	0.23	1.5	98
	Avg	–	–	–	0.10	0.19	0.22	1.6	98

a. The N 1s and metal 2p spectra are presented in Figure 5.7 and Figure 5.8. All spectra were deconvoluted with a curve fitting routine in CasaXPS software. The full width at half maximum of N_I and N_{II} species were kept the same during the fitting using a combination of 70% Gaussian and 30% Lorentzian curves after subtracting a Shirley background. The molar percentages of each species were calculated from peak areas normalized by atomic subshell photoionization cross sections of the corresponding element.[55]

b. The N_I at ~398.8 eV was assigned to graphitic N.

c. The N_{II} at ~400.7 eV was assigned to pyridinic N.

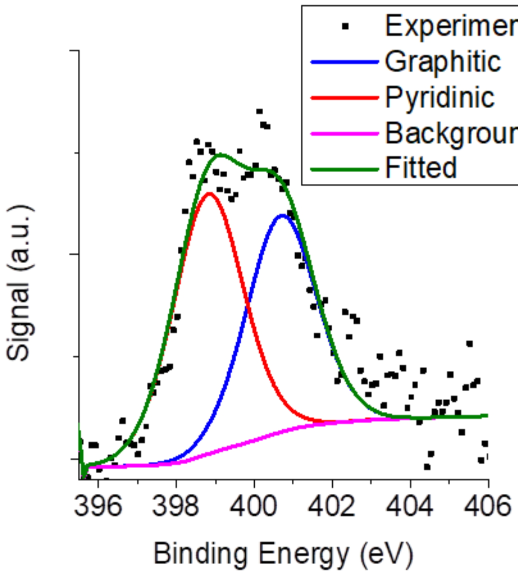

Figure 5. 8. N 1s X-ray photoelectron spectrum of N-C. The binding energies and quantification results are presented in Table 5. 10.

X-ray absorption spectroscopy at the K-edge of Co and Cu was also used to investigate the atomically-dispersed Co and Cu catalysts. A characteristic near-edge feature associated with square-planar MN_4 is present at 7715 eV for CoN_4 and 8986 eV for CuN_4, which originates from the 1s – $4p_z$ transition with simultaneous ligand-to-metal charge transfer.[52,56] This feature is present in the X-ray Absorption Near Edge Structure (XANES) of Co(II) phthalocyanine and Cu(II) phthalocyanine standards (Figures 5. 2c and 5. 9c). The Co-N-C-HCl and Cu-N-C catalysts did not exhibit this pre-edge feature (Figures 5. 10a, 10c, 11a and 11c), suggesting a non-planar structure of CoN_x and CuN_x sites in the catalytic samples. Attempts were also made to analyze the oxidation state of the metals by comparing the Co and Cu K edge XANES based on spectra of standard materials, but the correlation of oxidation state to the white line intensity or edge position was not obvious because of changes in line shape among the standards. The Extended X-ray Absorption Fine Structure (EXAFS) was used to analyze the coordination environment around the Co and Cu atoms. As shown in Figures 5. 10b and 11b, a predominant peak in the radial structure function associated with Co-N and a less intense feature attributed to Co-O were observed on Co-N-C-HCl catalyst. There was no significant Co-Co contribution, which is consistent with the atomic dispersion of Co. The coordination numbers (CN), interatomic distances (r), and Debye–Waller factors (σ^2) obtained from EXAFS curve fitting of Co-N-C-HCl after heating in H_2 and cooled to 313 K are present in Table 5. 9. A Co-N shell at a distance of 1.90 Å with a coordination number of 3.0 and a Co-O shell at 2.07 Å, with a coordination number of 0.8 fit the data well (Figure 5.12). Similar Co-N and Co-O distances have been reported previously for a Co-N-C material exposed to air with a coordination number of 3.7 for Co-N and 1.7 for Co-O.[52] The Cu-N-C sample had a minor feature in the EXAFS that might be attributed to Cu-Cu, but a strong feature of either Cu-N or Cu-O was observed (Figure 5.10d). Similar interatomic distances of Cu-N and Cu-O in EXAFS were observed on the standard samples shown in Figure 5. 9d. The fitting results suggest a Cu-N/O bonding length of 1.97 Å with a total coordination number of 3.6 in Cu-N-C (Table 5. 10).

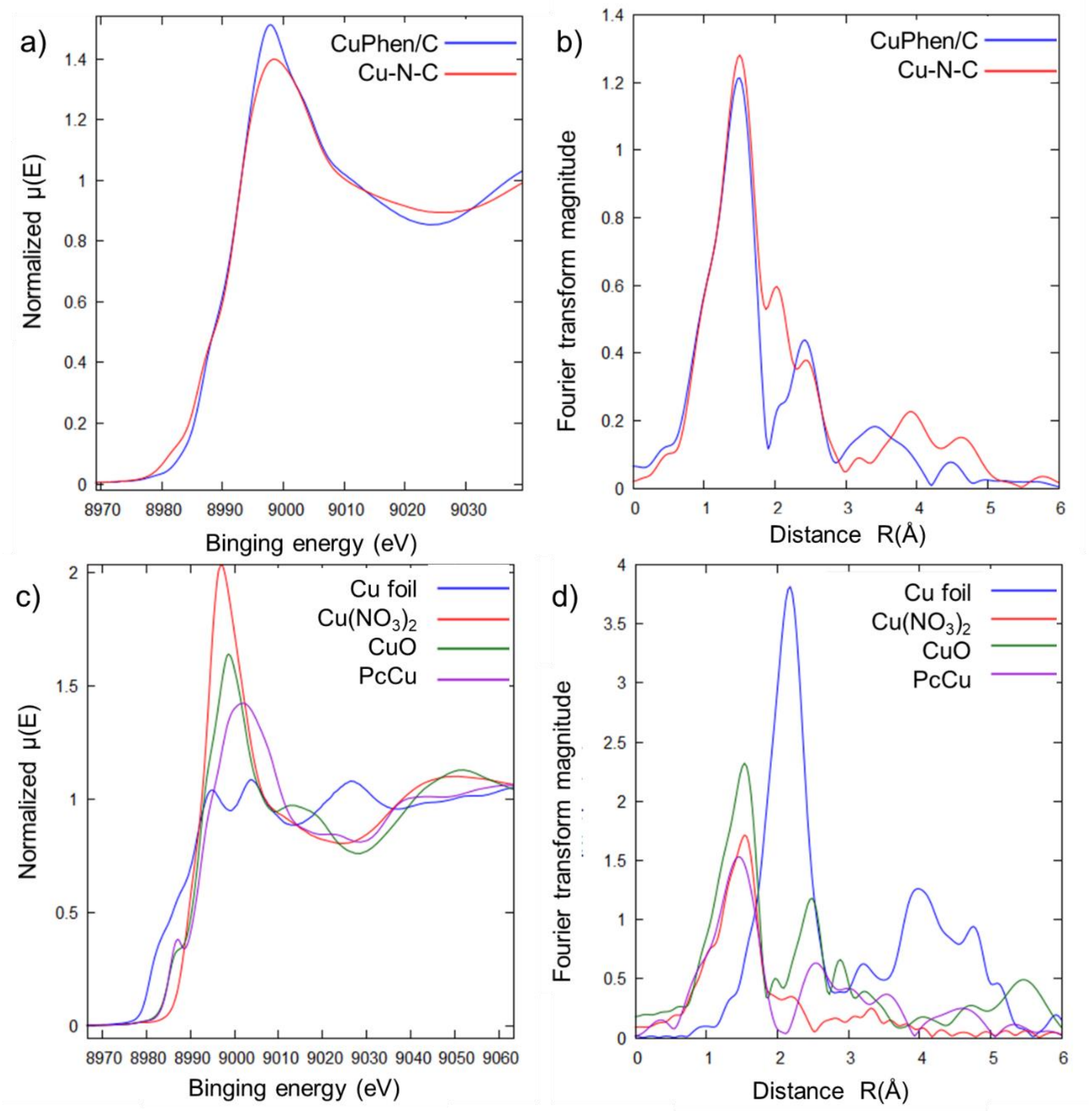

Figure 5. 9. Normalized XANES at the Cu K-edge of a) carbon-supported 1,10-phenanthroline Cu complex (CuPhen/C) and Cu-N-C catalysts prepared by 973 K pyrolysis followed by NH_3 treatment at 1223 K and c) copper standards (PcCu is Cu(II) phthalocyanine); The k^2-weighted Fourier transforms (not corrected for phase shift) of Cu EXAFS associated with b) CuPhen/C and Cu-N-C and d) copper standards.

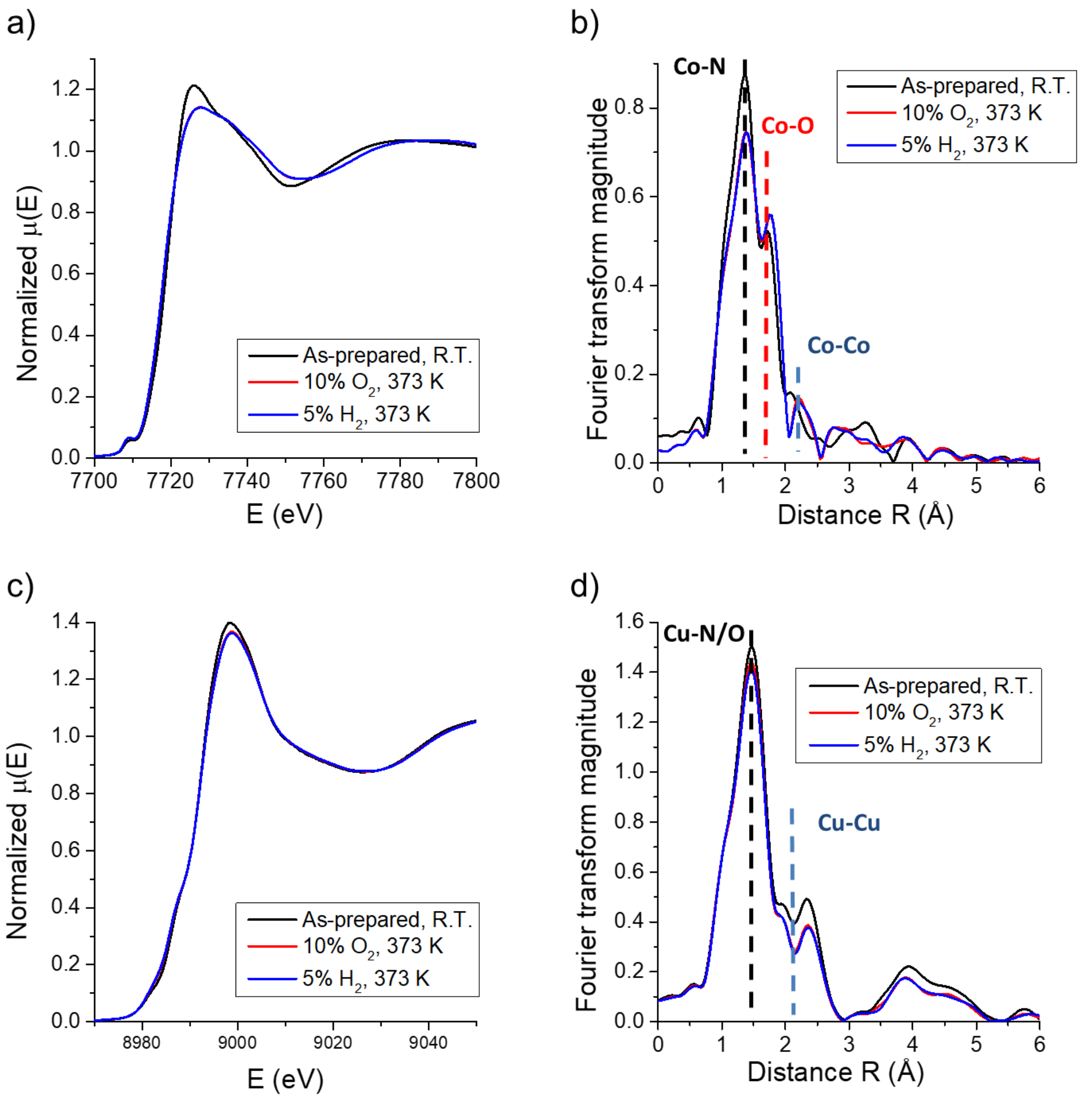

Figure 5. 10. a) Normalized XANES at the Co K-edge and b) the k^2-weighted Fourier transform (not corrected for phase shift) of Co EXAFS associated with Co-N-C-HCl at room temperature, at 373 K under 10% O_2 and at 373 K under 5% H_2; and c) normalized XANES at the Cu K-edge and d) the k^2-weighted Fourier transform (not corrected for phase shift) of Cu EXAFS associated with Cu-N-C at room temperature, at 373 K under 10% O_2 and at 373 K under 5% H_2.

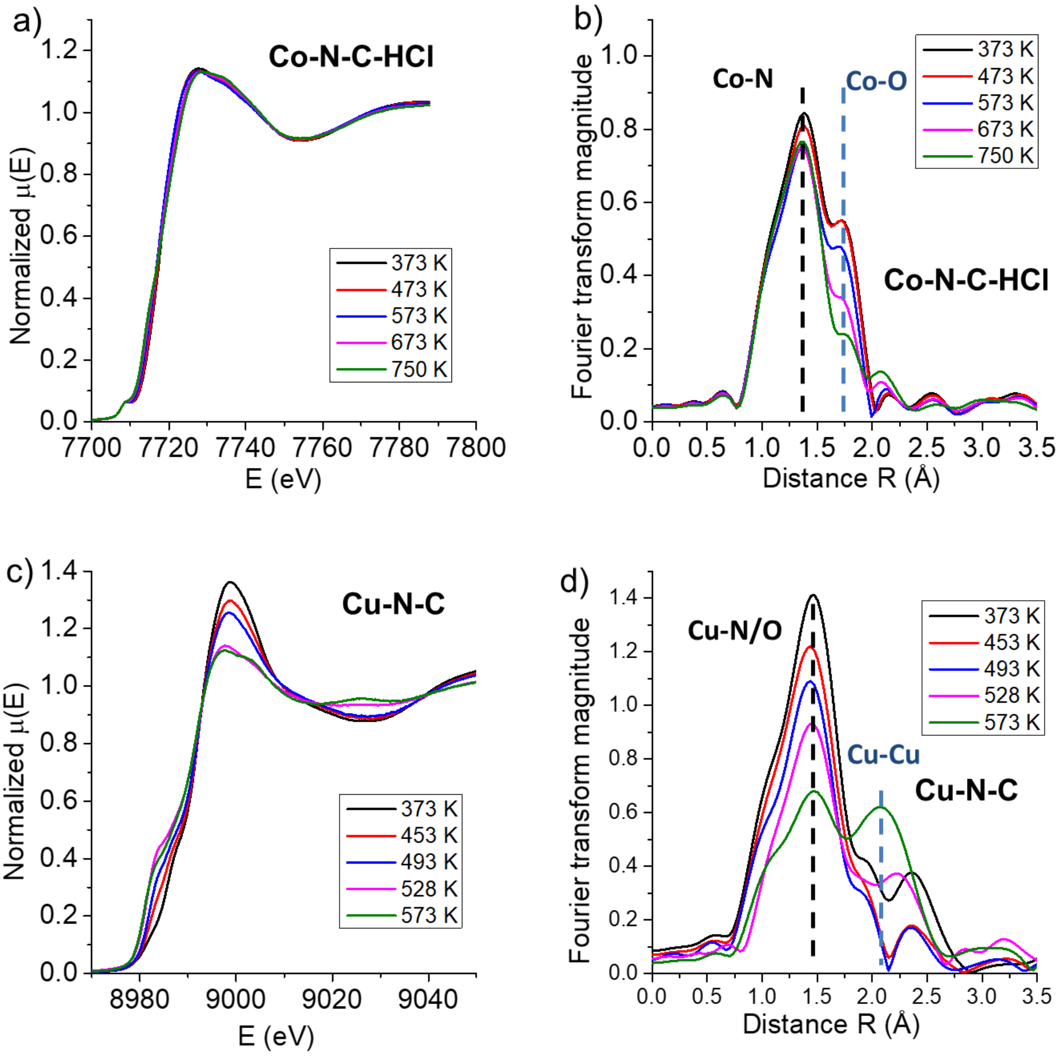

Figure 5. 11. a) Normalized XANES at the Co K-edge and b) the k^2-weighted Fourier transform (not corrected for phase shift) of Co EXAFS associated with Co-N-C-HCl under 5% H_2 flow from 373 to 750 K and c) normalized XANES at the Cu K-edge and d) the k^2-weighted Fourier transform (not corrected for phase shift) of the Cu EXAFS associated with Cu-N-C under 5% H_2 flow from 373 to 573 K

a) Co-N-C-HCl H_2 750 K, cool to 313 K

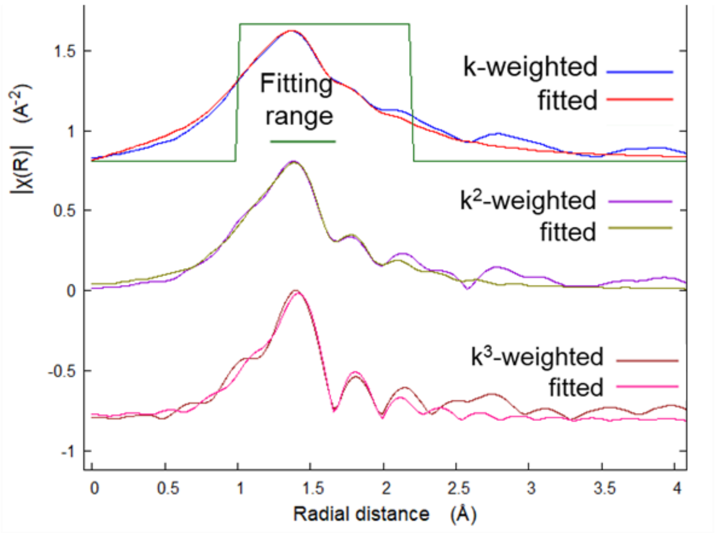

b) Cu-N-C as-synthesized R.T.

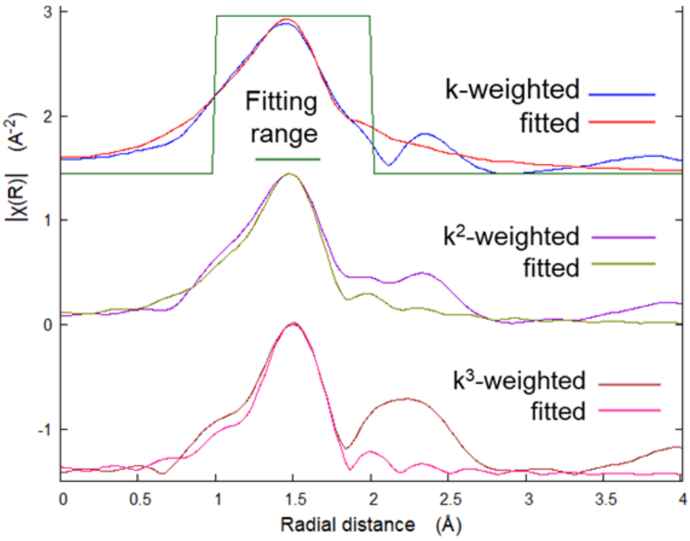

Figure 5. 12. The k, k^2 and k^3-weighted experimental and fitted Fourier transforms of a) the Co EXAFS associated with Co-N-C-HCl after the thermal treatment up to 750 K in H_2 and cooling to 313 K and b) the Cu EXAFS associated with as-synthesized Cu-N-C at room temperature. The fitting parameters are presented in Tables 5. 9 and 5.10.

Table 5. 9. Results from the analysis of Co EXAFS from Co-N-C-HCl catalyst after H_2 treatment[a]

Shell	Coordination number	r (Å)	$\Delta\sigma$ (Å^2)	ΔE_0 (eV)	R factor
Co-N	3.0	1.90	0.0057	-0.73	0.0056
Co-O	0.8	2.07	0.0025	-0.73	

a: Co-N-C-HCl catalyst was treated in H_2 from room temperature to 750 K and then cooled to 313 K. Fitting parameters: Fourier transform range, Δk, 2-14 Å^{-1}; fitting range ΔR, 1-2.2 Å; k^2-weighting, S_0^2(Co-N/O) = 0.775 (Calibrated from Co phthalocyanine). The fitted Fourier transforms are present in Figure 5.12.

Table 5. 10. Results from the analysis of Cu EXAFS from Cu-N-C catalyst[a]

Shell	Coordination number	r (Å)	$\Delta\sigma$ (Å^2)	ΔE_0 (eV)	R factor
Cu-N/O	3.6	1.94	0.0049	1.30	0.039

a: Fitting parameters: Fourier transform range, Δk, 2 – 10 Å^{-1}; fitting range ΔR, 1 – 2.0 Å; k^2-weighting, S_0^2(Cu-N/O) = 0.825 (Calibrated from Cu phthalocyanine). The fitted Fourier transforms are present in Figure 5.12.

The Co and Cu catalysts were explored under both oxidative and reductive environments at 373 K, which is similar to the alcohol oxidation reaction temperature of 353 K. Catalysts were first treated with 10% O_2 in N_2 flow at 373 K for 30 min, followed by purging with N_2 and treatment in 5% H_2 in N_2 at 373 K. As shown in Figures 5. 10a and 10b, the XANES and EXAFS of Co and Cu catalysts under the oxidizing and reducing environments are almost identical. The negligible change of atomic structure or chemical state around Co and Cu under oxidative and reductive conditions at 373 K indicates that Co and Cu likely do not directly activate dioxygen or C-H during the oxidative dehydrogenation of alcohol at 353 K. Since our recently published kinetic isotope study showed that metal sites of MN_x can significantly influence the kinetically-relevant β-H elimination step during alcohol oxidation,[19] we tentatively propose that the C-H is likely activated by MN_x-bonded oxygen (M-O) or peroxide (M-O-O·). The existence of peroxide radicals has been observed by electron paramagnetic resonance spectroscopy during oxidative C-H activation.[17,57] The importance of the N bonded to metal center is also critical for dioxygen activation.[36]

5.3.5. Evolution of M-N-C under reducing condition at elevated temperature

To investigate the evolution of oxygen-bonded CoN_x sites at elevated temperature under reducing conditions, Co-N-C-HCl was subsequently ramped to 750 K in 5% H_2 balanced with N_2. Figure 5. 11a illustrates the XANES at the Co K edge during the thermal treatment. Only very subtle variations in the edge position and line shape were observed, indicating the atomic structure and chemical state around the Co did not vary significantly with treatment and remained atomically-dispersed as charged cations, even at 750 K in 5% H_2. From EXAFS analysis shown in Figure 5. 11b, the Co-N feature in the radial structure function was relatively unaffected by the thermal ramp in H_2. No evidence for the growth of nanoparticles was observed, which suggests that the Co atoms remained atomically dispersed throughout the thermal treatment. In contrast, the Co-O contribution in the radial structure function significantly decreased in intensity with increasing temperature, indicating the continuous removal of coordinated oxygen from Co above 473 K (Figure 5.11b).

In contrast to Co-N-C-HCl, the influence of H_2 on the chemical state of Cu in Cu-N-C was clearly evident. The XANES of Cu-N-C in 5% H_2 at different temperatures is shown in Figure 5.11c. A significant decrease in the white line intensity was observed with increasing temperature, indicating reduction of Cu cations in the N-doped carbon matrix. Additionally, the thermal treatment in H_2 induced the emergence of the pre-edge at ~8983 eV, which is the characteristic feature of Cu metal (Figure 5. 9c). Simultaneously, the intensity of Cu-N/O feature in the radial structure function decreased, which is consistent with the reduction of isolated Cu cations into metallic Cu metal clusters during the H_2 treatment. The very different thermal stability of atomically-dispersed Co and Cu sites might explain the H_2 regeneration experiments reported in our previous work,[43] during which H_2 treatment at 573 K could effectively regenerate the activity of a poisoned Co-N-C catalyst but only regenerated ~30% of the original activity of Cu-N-C. The aggregation of atomically-dispersed Cu sites to inactive Cu nanoparticles for alcohol oxidation reaction could account for the problem with Cu-N-C regeneration.

5.3.6. Propane dehydrogenation over CoN_x sites

The very high stability of cationic Co coordinated to nitrogen offers an opportunity to explore Co-N-C as a catalyst for propane dehydrogenation, which is well-recognized to occur over Sn-promoted Pt particles (and other variants of promoted Pt) at elevated temperatures.[58] Propane can also be converted on Co(II) cations loaded into H-ZSM-5 zeolites, but the product distribution is complex because the acid sites of the zeolite can catalyze cracking and oligomerization reactions.[59,60] In 2015, Hu et al. reported that Co(II) ions on silica gel catalyzed the dehydrogenation of propane to propene at temperatures of 823 K and greater with high selectivity.[61] In this study, both atomically-dispersed Co-N-C-HCl and SiO_2-supported CoO_x catalysts were evaluated in a flow reactor. As shown in Figure 5.13, an initial TOF normalized by the total number of Co sites (giving a lower bound of the TOF) was measured to be 0.028 s^{-1} over the Co-N-C-HCl after 5 min on stream. Some deactivation was observed, and the TOF decreased to 0.015 s^{-1} after 3.1 h on stream (Figure 5.13b), which is one order of magnitude lower than the TOF associated with supported Pt nanoparticles (0.14 s^{-1}). Highly-dispersed CoO_x on silica has a measured TOF of ~0.005 s^{-1} under the same reaction conditions. The selectivity to propene is higher than 98% over both Co-N-C-HCl and CoO_x-SiO_2. In comparison, the metallic Co nanoparticles supported on carbon or SiO_2 exhibited significantly lower activity and conversion of propane was not measured after 5 min on stream. Our results indicate that the propane dehydrogenation reaction can be efficiently catalyzed by cationic Co atoms and high activity can be obtained by replacing coordinated oxygen with coordinated nitrogen. Since our TOF over Co-N-C-HCl is a lower bound, it is quite possible that the active Co sites could be similar in rate to Pt, as illustrated earlier for benzyl alcohol oxidation. More detailed investigations on Co-N-C-HCl including the quantification of active sites and mechanistic study are currently underway.

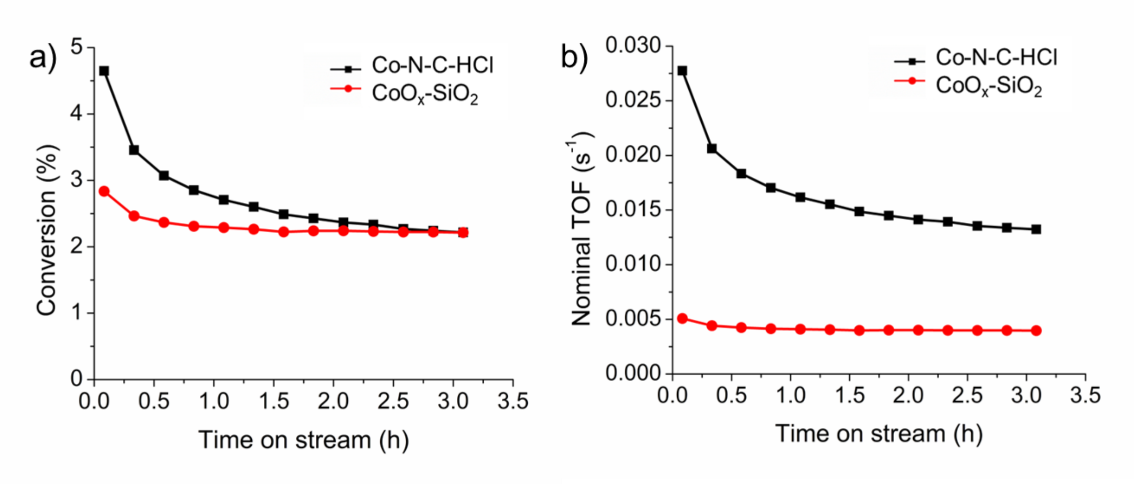

Figure 5. 13. a) Conversion of propane and b) nominal TOF during propane dehydrogenation over 0.05 g Co-N-C-HCl and 0.1 g CoO_x-SiO_2. TOF was based on total Co loading in the sample. Reaction conditions: 773 K, 0.1 MPa, N_2:propane = 3:1.

5.4. Conclusion

This work demonstrates that atomically-dispersed Co confined in nitrogen-doped carbon catalyzes C-H activation during oxidative alcohol dehydrogenation at 353 K and alkane dehydrogenation at 773 K. The selective poisoning of highly active Co sites for benzyl alcohol oxidative dehydrogenation allowed for the estimation of a turnover frequency, which was determined to be nearly the same as that over Pt nanoparticles under identical conditions. Nitrogen-coordinated Co(II) cations bound to oxygen are proposed as active sites for C-H activation based on comprehensive characterization methods of the sample. Whereas oxygen bound to the Co(II) can be removed by dihydrogen treatment at elevated temperature (>473 K), the Co(II) cations remained atomically-dispersed and coordinated to nitrogen in the carbon at up to 750 K. The stable Co(II) cations in N-doped carbon catalyze the propane dehydrogenation reaction at 773 K. Copper (II) cations confined in nitrogen-doped carbon also catalyze aerobic alcohol oxidation at 353 K but the turnover frequency of the highly active CuN_x sites is an order of magnitude lower than that associated with CoN_x. Although Cu(II) cations remained in the N-doped carbon matric at 373 K under reducing conditions, partial reduction of the Cu was observed above 473 K.

References for Chapter 5

(1) Sousa-Aguiar, E. F.; Appel, L. G.; Mota, C. Natural Gas Chemical Transformations: The Path to Refining in the Future. In *Catalysis Today*; Elsevier, 2005; Vol. 101, pp. 3–7.

(2) Matar, S.; Hatch, L. F. *Chemistry of Petrochemical Processes*; Second Edi.; Gulf Publishing Company: Houston, Texas, 2000.

(3) Corma, A.; Iborra, S.; Velty, A. Chemical Routes for the Transformation of Biomass into Chemicals. *Chem. Rev.* **2007**, *107*, 2411–2502.

(4) Santoro, S.; Kozhushkov, S. I.; Ackermann, L.; Vaccaro, L. Heterogeneous Catalytic Approaches in C–H Activation Reactions. *Green Chem.* **2016**, *18*, 3471–3493.

(5) Santen, R. A. V.; Neurock, M.; Shetty, S. G. Reactivity Theory of Transition-Metal Surfaces: A Brønsted-Evans-Polanyi Linear Activation Energy-Free-Energy Analysis. *Chem. Rev.* **2010**, *110*, 2005–2048.

(6) Vesborg, P. C. K.; Jaramillo, T. F. Addressing the Terawatt Challenge: Scalability in the Supply of Chemical Elements for Renewable Energy. *RSC Adv.* **2012**, *2*, 7933–7947.

(7) Zou, X.; Zhang, Y. Noble Metal-Free Hydrogen Evolution Catalysts for Water Splitting. *Chem. Soc. Rev* **2015**, *44*, 5148–5180.

(8) Zhu, Y. P.; Guo, C.; Zheng, Y.; Qiao, S.-Z. Surface and Interface Engineering of Noble-Metal-Free Electrocatalysts for Efficient Energy Conversion Processes. *Acc. Chem. Res.* **2017**, *50*, 915–923.

(9) Shao, M.; Chang, Q.; Dodelet, J.-P.; Chenitz, R. Recent Advances in Electrocatalysts for Oxygen Reduction Reaction. *Chem. Rev.* **2016**, *116*, 3594–365.

(10) Jaouen, F.; Lefèvre, M.; Dodelet, J. P.; Cai, M. Heat-Treated Fe/N/C Catalysts for O2 Electroreduction: Are Active Sites Hosted in Micropores? *J. Phys. Chem. B* **2006**, *110*, 5553–5558.

(11) Jagadeesh, R. V; Junge, H.; Pohl, M.; Radnik, J.; Brückner, A.; Beller, M. Selective Oxidation of Alcohols to Esters Using Heterogeneous Co3O4–N@C Catalysts under Mild Conditions. *J. Am. Chem. Soc.* **2013**, *135*, 10776–10782.

(12) Cui, X.; Li, Y.; Bachmann, S.; Scalone, M.; Surkus, A. E.; Junge, K.; Topf, C.; Beller, M. Synthesis and Characterization of Iron-Nitrogen-Doped Graphene/Core-Shell Catalysts: Efficient Oxidative Dehydrogenation of N-Heterocycles. *J. Am. Chem. Soc.* **2015**, *137*, 10652–10658.

(13) Jagadeesh, R. V; Stemmler, T.; Surkus, A. E.; Bauer, M.; Pohl, M. M.; Radnik, J.; Junge, K.; Junge, H.; Bruckner, A.; Beller, M. Cobalt-Based Nanocatalysts for Green

Oxidation and Hydrogenation Processes. *Nat. Protoc.* **2015**, *10*, 916–926.

(14) Jagadeesh, R. V; Junge, H.; Beller, M. Green Synthesis of Nitriles Using Non-Noble Metal Oxides-Based Nanocatalysts. *Nat. Commun.* **2014**, *5*, 4123.

(15) Zhang, L.; Wang, A.; Wang, W.; Huang, Y.; Liu, X.; Miao, S.; Liu, J.; Zhang, T. Co-N-C Catalyst for C-C Coupling Reactions: On the Catalytic Performance and Active Sites. *ACS Catal.* **2015**, *5*, 6563–6572.

(16) Slot, T. K.; Eisenberg, D.; van Noordenne, D.; Jungbacker, P.; Rothenberg, G. Cooperative Catalysis for Selective Alcohol Oxidation with Molecular Oxygen. *Chem. - A Eur. J.* **2016**, *22*, 12307–12311.

(17) Liu, W.; Zhang, L.; Liu, X. X.; Liu, X. X.; Yang, X.; Miao, S.; Wang, W.; Wang, A.; Zhang, T. Discriminating Catalytically Active FeNx Species of Atomically Dispersed Fe-N-C Catalyst for Selective Oxidation of the C-H Bond. *J. Am. Chem. Soc.* **2017**, *139*, 10790–10798.

(18) Li, M.; Wu, S.; Yang, X.; Hu, J.; Peng, L.; Bai, L.; Huo, Q.; Guan, J. Highly Efficient Single Atom Cobalt Catalyst for Selective Oxidation of Alcohols. *Appl. Catal. A Gen.* **2017**, *543*, 61–66.

(19) Xie, J.; Yin, K.; Serov, A.; Artyushkova, K.; Pham, H. N.; Sang, X.; Unocic, R. R.; Atanassov, P.; Datye, A. K.; Davis, R. J. Selective Aerobic Oxidation of Alcohols over Atomically-Dispersed Non-Precious Metal Catalysts. *ChemSusChem 10*, 359–362.

(20) Nakatsuka, K.; Yoshii, T.; Kuwahara, Y.; Mori, K.; Yamashita, H. Controlled Synthesis of Carbon-Supported Co Catalysts from Single-Sites to Nanoparticles: Characterization of the Structural Transformation and Investigation of Their Oxidation Catalysis. *Phys. Chem. Chem. Phys.* **2017**, *19*, 4967–4974.

(21) Cheng, T.; Yu, H.; Peng, F.; Wang, H.; Zhang, B.; Su, D. Identifying Active Sites of CoNC/CNT from Pyrolysis of Molecularly Defined Complexes for Oxidative

Esterification and Hydrogenation Reactions. *Catal. Sci. Technol.* **2016**, *6*, 1007–1015.

(22) Kattel, S.; Atanassov, P.; Kiefer, B. Stability, Electronic and Magnetic Properties of in-Plane Defects in Graphene: A First-Principles Study. *J. Phys. Chem. C* **2012**, *116*, 8161–8166.

(23) Kattel, S.; Atanassov, P.; Kiefer, B. Catalytic Activity of Co-N(x)/C Electrocatalysts for Oxygen Reduction Reaction: A Density Functional Theory Study. *Phys. Chem. Chem. Phys.* **2013**, *15*, 148–153.

(24) Kamiya, K.; Koshikawa, H.; Kiuchi, H.; Harada, Y.; Oshima, M.; Hashimoto, K.; Nakanishi, S. Iron-Nitrogen Coordination in Modified Graphene Catalyzes a Four-Electron-Transfer Oxygen Reduction Reaction. *ChemElectroChem* **2014**, *1*, 877–884.

(25) Liang, W.; Chen, J.; Liu, Y.; Chen, S. Density-Functional-Theory Calculation Analysis of Active Sites for Four-Electron Reduction of O2 on Fe/N-Doped Graphene. *ACS Catal.* **2014**, *4*, 4170–4177.

(26) Serov, A.; Artyushkova, K.; Atanassov, P. Fe-N-C Oxygen Reduction Fuel Cell Catalyst Derived from Carbendazim: Synthesis, Structure, and Reactivity. *Adv. Energy Mater.* **2014**, *4*, 1–7.

(27) Zhou, J.; Duchesne, P. N.; Hu, Y.; Wang, J.; Zhang, P.; Li, Y.; Regier, T.; Dai, H. Fe-N Bonding in a Carbon Nanotube-Graphene Complex for Oxygen Reduction: An XAS Study. *Phys. Chem. Chem. Phys.* **2014**, *16*, 15787–15791.

(28) Artyushkova, K.; Serov, A.; Rojas-Carbonell, S.; Atanassov, P. Chemistry of Multitudinous Active Sites for Oxygen Reduction Reaction in Transition Metal-Nitrogen-Carbon Electrocatalysts. *J. Phys. Chem. C* **2015**, *119*, 25917–25928.

(29) Jia, Q.; Ramaswamy, N.; Hafiz, H.; Tylus, U.; Strickland, K.; Wu, G.; Barbiellini, B.; Bansil, A.; Holby, E. F.; Zelenay, P.; *et al.* Experimental Observation of

Redox-Induced Fe-N Switching Behavior as a Determinant Role for Oxygen Reduction Activity. *ACS Nano* **2015**, *9*, 12496–12505.

(30) Kabir, S.; Artyushkova, K.; Kiefer, B.; Atanassov, P. Computational and Experimental Evidence for a New TM–N 3 /C Moiety Family in Non-PGM Electrocatalysts. *Phys. Chem. Chem. Phys.* **2015**, *17*, 17785–17789.

(31) Serov, A.; Artyushkova, K.; Niangar, E.; Wang, C.; Dale, N.; Jaouen, F.; Sougrati, M.-T.; Jia, Q.; Mukerjee, S.; Atanassov, P. Nano-Structured Non-Platinum Catalysts for Automotive Fuel Cell Application. *Nano Energy* **2015**, *16*, 293–300.

(32) Cui, X.; Ren, P.; Deng, D.; Deng, J.; Bao, X. Single Layer Graphene Encapsulating Non-Precious Metals as High-Performance Electrocatalysts for Water Oxidation. *Energy Environ. Sci.* **2016**, *9*, 123–129.

(33) Cui, X.; Xiao, J.; Wu, Y.; Du, P.; Si, R.; Yang, H.; Tian, H.; Li, J.; Zhang, W. H.; Deng, D.; *et al.* A Graphene Composite Material with Single Cobalt Active Sites: A Highly Efficient Counter Electrode for Dye-Sensitized Solar Cells. *Angew. Chemie - Int. Ed.* **2016**, *100190*, 6708–6712.

(34) Jia, Q.; Ramaswamy, N.; Tylus, U.; Strickland, K.; Li, J.; Serov, A.; Artyushkova, K.; Atanassov, P.; Anibal, J.; Gumeci, C.; *et al.* Spectroscopic Insights into the Nature of Active Sites in Iron–nitrogen–carbon Electrocatalysts for Oxygen Reduction in Acid. *Nano Energy* **2016**, *29*, 65–82.

(35) Liu, W.; Zhang, L.; Yan, W.; Liu, X.; Yang, X.; Miao, S.; Wang, W.; Wang, A.; Zhang, T. Single-Atom Dispersed Co–N–C Catalyst: Structure Identification and Performance for Hydrogenative Coupling of Nitroarenes. *Chem. Sci.* **2016**, *7*, 5758–5764.

(36) Artyushkova, K.; Matanovic, I.; Halevi, B.; Atanassov, P. Oxygen Binding to Active Sites of Fe-N-C ORR Electrocatalysts Observed by Ambient-Pressure XPS. *J. Phys.*

Chem. C **2017**, *121*, 2836–2843.

(37) Chen, X.; Yu, L.; Wang, S.; Deng, D.; Bao, X. Highly Active and Stable Single Iron Site Confined in Graphene Nanosheets for Oxygen Reduction Reaction. *Nano Energy* **2017**, *32*, 353–358.

(38) Chung, H. T.; Cullen, D. A.; Higgins, D.; Sneed, B. T.; Holby, E. F.; More, K. L.; Zelenay, P. Direct Atomic-Level Insight into the Active Sites of a High-Performance PGM-Free ORR Catalyst. *Science.* **2017**, *357*, 479–484.

(39) Guo, S.; Yuan, P.; Zhang, J.; Jin, P.; Sun, H.; Lei, K.; Pang, X.; Xu, Q.; Cheng, F. Atomic-Scaled Cobalt Encapsulated in P,N-Doped Carbon Sheaths over Carbon Nanotubes for Enhanced Oxygen Reduction Electrocatalysis under Acidic and Alkaline Media. *Chem. Commun.* **2017**, *53*, 9862–9865.

(40) Shen, H.; Gracia-Espino, E.; Ma, J.; Tang, H.; Mamat, X.; Wagberg, T.; Hu, G.; Guo, S. Atomically FeN2 Moieties Dispersed on Mesoporous Carbon: A New Atomic Catalyst for Efficient Oxygen Reduction Catalysis. *Nano Energy* **2017**, *35*, 9–16.

(41) Artyushkova, K.; Kiefer, B.; Halevi, B.; Knop-Gericke, A.; Schlogl, R.; Atanassov, P. Density Functional Theory Calculations of XPS Binding Energy Shift for Nitrogen-Containing Graphene-like Structures. *Chem. Commun.* **2013**, *49*, 2539.

(42) Liu, W.; Zhang, L.; Liu, X.; Liu, X.; Yang, X.; Miao, S.; Wang, W.; Wang, A.; Zhang, T. Discriminating Catalytically Active FeNx Species of Atomically Dispersed Fe-N-C Catalyst for Selective Oxidation of the C-H Bond. *J. Am. Chem. Soc.* **2017**, *139*, 10790–10798.

(43) Xie, J.; Yin, K.; Serov, A.; Artyushkova, K.; Pham, H. N.; Sang, X.; Unocic, R. R.; Atanassov, P.; Datye, A. K.; Davis, R. J. Selective Aerobic Oxidation of Alcohols over Atomically-Dispersed Non-Precious Metal Catalysts. *ChemSusChem* **2017**, *10*, 359–362.

(44) Pham, H. N.; Anderson, A. E.; Johnson, R. L.; Schwartz, T. J.; O'Neill, B. J.; Duan, P.; Schmidt-Rohr, K.; Dumesic, J. A.; Datye, A. K. Carbon Overcoating of Supported Metal Catalysts for Improved Hydrothermal Stability. *ACS Catal.* **2015**, *5*, 4546–4555.

(45) Pham, H. N.; Anderson, A. E.; Johnson, R. L.; Schmidt-Rohr, K.; Datye, A. K. Improved Hydrothermal Stability of Mesoporous Oxides for Reactions in the Aqueous Phase. *Angew. Chemie Int. Ed.* **2012**, *51*, 13163–13167.

(46) Kaylor, N.; Xie, J.; Kim, Y.-S.; Pham, H. N.; Datye, A. K.; Lee, Y.-K.; Davis, R. J. Vapor Phase Deoxygenation of Heptanoic Acid over Silica-Supported Palladium and Palladium-Tin Catalysts. *J. Catal.* **2016**, *344*, 202–212.

(47) Lam, Y. M.; Boudart, M. Preparation of Small Au-Pd Particles on Silica. *J. Catal.* **1977**, *50*, 530–540.

(48) Xie, J.; Falcone, D. D.; Davis, R. J. Restructuring of Supported PtSn Bimetallic Catalysts during Aqueous Phase Oxidation of 1,6-Hexanediol. *J. Catal.* **2015**, *332*, 38–50.

(49) Ravel, B., Newville, M. ATHENA, ARTEMIS, HEPHAESTUS: Data Analysis for X-Ray Absorption Spectroscopy Using IFEFFIT. *J. Synchrotron Radiat.* **2005**, *12*, 537–541.

(50) Xie, J.; Huang, B.; Yin, K.; Pham, H. N.; Unocic, R. R.; Datye, A. K.; Davis, R. J. Influence of Dioxygen on the Promotional Effect of Bi during Pt-Catalyzed Oxidation of 1,6-Hexanediol. *ACS Catal.* **2016**, *6*, 4206–4217.

(51) Serov, A.; Robson, M. H.; Halevi, B.; Artyushkova, K.; Atanassov, P. Highly Active and Durable Templated Non-PGM Cathod Catalysts Derived from Iron and Amino. *Electrochem. commun.* **2012**, *22*, 53–56.

(52) Liu, W.; Zhang, L.; Yan, W.; Liu, X.; Yang, X.; Miao, S.; Wang, W.; Wang, A.; Zhang, T. Single-Atom Dispersed Co–N–C Catalyst: Structure Identification and

Performance for Hydrogenative Coupling of Nitroarenes. *Chem. Sci.* **2016**, *7*, 5758–5764.

(53) Biesinger, M. C.; Payne, B. P.; Grosvenor, A. P.; Lau, L. W. M.; Gerson, A. R.; Smart, R. S. C. Resolving Surface Chemical States in XPS Analysis of First Row Transition Metals, Oxides and Hydroxides: Cr, Mn, Fe, Co and Ni. *Appl. Surf. Sci.* **2011**, *257*, 2717–2730.

(54) Biesinger, M. C.; Lau, L. W. M.; Gerson, A. R.; Smart, R. S. C. Resolving Surface Chemical States in XPS Analysis of First Row Transition Metals, Oxides and Hydroxides: Sc, Ti, V, Cu and Zn. *Appl. Surf. Sci.* **2010**, *257*, 887–898.

(55) Yeh, J. J.; Lindau, I. Atomic Subshell Photoionization Cross Sections and Asymmetry Parameters: $1 \leqslant Z \leqslant 103$. *At. Data Nucl. Data Tables* **1985**, *32*, 1–155.

(56) Yokoyama, T. Metastable Photoinduced Phase of Cu (II) Ethylenediamine Complexes Studied by X-Ray-Absorption Fine-Structure Spectroscopy. *Phys. Rev. B* **2003**, *67*, 1–4.

(57) Zhang, L.; Wang, A.; Wang, W.; Huang, Y.; Liu, X.; Miao, S.; Liu, J.; Zhang, T. Co–N–C Catalyst for C–C Coupling Reactions: On the Catalytic Performance and Active Sites. *ACS Catal.* **2015**, *5*, 6563–6572.

(58) Sattler, J. J. H. B.; Ruiz-Martinez, J.; Santillan-Jimenez, E.; Weckhuysen, B. M. Catalytic Dehydrogenation of Light Alkanes on Metals and Metal Oxides. *Chemical Reviews*, 2014, *114*, 10613–10653.

(59) Li, W.; Yu, S. Y.; Meitzner, G. D.; Iglesia, E. Structure and Properties of Cobalt-Exchanged H-ZSM5 Catalysts for Dehydrogenation and Dehydrocyclization of Alkanes. *J. Phys. Chem. B* **2001**, *105*, 1176–1184.

(60) Yu, S. Y.; Yu, G. J.; Li, W.; Iglesia, E. Kinetics and Reaction Pathways for Propane Dehydrogenation and Aromatization on Co/H-ZSM5 and H-ZSM5. *J. Phys. Chem. B*

2002, *106*, 4714–4720.

(61) Hu, B.; Bean Getsoian, A.; Schweitzer, N. M.; Das, U.; Kim, H.; Niklas, J.; Poluektov, O.; Curtiss, L. A.; Stair, P. C.; Miller, J. T.; *et al.* Selective Propane Dehydrogenation with Single-Site CoII on SiO2 by a Non-Redox Mechanism. *J. Catal.* **2015**, *322*, 24–37.

Chapter 6: Concluding Remarks

6.1. Conclusions

Selective alcohol oxidation, which is an important reaction in chemical synthesis and biomass upgrading, can be efficiently catalyzed by Pt catalysts. The high price of Pt and the deactivation, however, can be a main barrier for the application of this process. In this study, deactivation of Pt during oxidation of 1,6-hexanediol was comprehensively studied by kinetic, spectroscopic and microscopic methods. Kinetic measurements indicate the generation of strongly-adsorbed poisoning species. In situ surface-enhanced Raman spectroscopy of adsorbates produced during 1,6-hexanediol oxidation over Pt revealed characteristic features of a di-σ-bonded olefinic species. Consistent with SERS, solid-state ^{13}C NMR spectroscopy of deactivated Pt/silica after oxidation of ^{13}C-enriched 1,4-butanediol showed a single C=C signal at 125 ppm, which was assigned to ethylene. The observed weakly bound ethylene was likely derived from strongly adsorbed species on Pt, which would give only a non-distinct broad and low-intensity NMR feature. Kinetic measurements with various additives demonstrated that species containing olefinic groups were strongly adsorbed on Pt and significantly inhibited the alcohol oxidation reaction. The poisoning olefinic species are likely generated from the decarbonylation of aldehyde products, as evidenced by significant decrease of activity after aldehyde pretreatment as well as the similar amount of CO_2 generated after alcohol oxidation reaction and aldehyde pretreatment.

To suppress the poisoning decarbonylation path that is very sensitive to assemble size and increase the activity, we further explored the bimetallic Bi-Pt catalysts for alcohol oxidation reaction prepared by selective deposition of Bi on Pt. The presence of Bi adjacent to Pt significantly promoted the rate of 1,6-hexanediol oxidation under low O_2 pressure without influencing the product distribution or catalyst deactivation. In the range of 0.02 to 0.2 MPa O_2, the order of reaction in O_2 changed from 0.75 over Pt/C to zero over

Bi-promoted Pt/C, which accounts for the observed promotion in rate at low O_2 pressure. Results from the kinetic isotope effect with D_2O *vs* H_2O suggest that water-assisted O_2 activation is not kinetically-relevant on Bi-promoted Pt at low O_2 pressure whereas it is relevant on unpromoted Pt. All of the promotional effects of Bi disappear at higher O_2 pressure. However, a similar deactivation was observed over Bi-promoted Pt catalyst during the reaction. The STEM-EDS and XPS characterization showed that whereas bismuth was successfully deposited onto carbon-supported Pt nanoparticles after the synthesis, liquid phase pretreatment of the Bi-promoted Pt catalyst caused migration of Bi. Because of the high mobility of Bi, relatively large Pt ensembles can still be exposed and catalyze the formation of poisoning olefinic species through aldehyde decarbonylation.

From the perspective of replacing expensive Pt, non-precious-metal M-N-C catalysts were evaluated in the aqueous-phase aerobic alcohol oxidation at mild temperature. Benzyl alcohol and HMF were efficiently and selectively converted to the aldehyde products over the earth-abundant Fe-N-C catalyst with a slight loss of activity that could be fully regenerated by simple H_2 treatment. The rate of aliphatic alcohol oxidation was quite slow over Fe-N-C but can be significantly promoted by adding a catalytic amount of TEMPO. The kinetic isotope effect, evaluated by using $C_6H_5CD_2OH$, was ~4.9 over Fe-N-C, indicating the β-H elimination as a kinetically-relevant step. Replacing Fe with other metals significantly increased the reactivity and decreased the kinetic isotope effect. The highest reaction rates for benzyl alcohol oxidation were obtained over Cu-N-C and Co-N-C, which is tentatively attributed to a faster β-H elimination step. The selective poisoning of highly active Co sites for benzyl alcohol oxidative dehydrogenation allowed for the estimation of a turnover frequency, which was determined to be nearly the same as that over Pt nanoparticles under identical conditions. Nitrogen-coordinated Co(II) cations bound to oxygen are proposed to be active sites for C-H activation based on comprehensive characterization methods of the sample. Whereas oxygen bound to the Co(II) can be removed by dihydrogen treatment at elevated temperature (>473 K), the Co(II) cations remained atomically-dispersed and coordinated to nitrogen in the carbon at up to 750 K. The stable Co(II) cations in N-doped carbon catalyze the propane dehydrogenation reaction at 773 K. Copper (II) cations confined in nitrogen-doped carbon also catalyze aerobic alcohol oxidation at 353 K but the turnover frequency of the highly active CuN_x sites is an order of magnitude lower than that associated with CoN_x. Although Cu(II) cations remained in the N-doped carbon matric at 373 K under reducing conditions, partial reduction of the Cu was observed above 473 K.

6.2. Outlook

6.2.1. Kinetics Study of Catalyst Deactivation in the Flow Reactor

As introduced in Chapter 1, kinetics is commonly used to investigate the deactivation process.[1] However, in the batch reactor, the concentration of substrate and products is constantly changing, which adds complexity to the kinetic modeling. In contrast to a batch reactor, a quasi-stationary state could possibly be reached in a fixed bed continuous flow reactor, which would be ideal for the modeling of deactivation. Additionally, the alcohol oxidation reaction in the flow reactor might be significantly different from that in batch reactor because of the limited contact time of the substrate with the catalyst.[2] Since industrial processes are commonly performed in a flow system, it would be important to understand the Pt-catalyzed alcohol oxidation reaction in fixed-bed reactors.

6.2.2. Bimetallic catalyst synthesis

The key to inhibit the deactivation is to shut down the C-C cleavage path while at the same time maintaining activity for O-H and C-H activation required for alcohol oxidation reaction. Because C-C cleavage is more sensitive to the exposed Pt ensemble size, it is possible to promote the stability of catalysts by precisely modifying the Pt surface. One strategy is to control the surface environment of the catalyst by self-assembly of thiol monolayers, which has been proven to inhibit the deactivation of Pt-group catalysts during the alcohol oxidation reaction.[3–5] However, the thiol layer is not stable when exposed to air. Another promising approach is to develop Pt-based bimetallic catalysts that can tune the ensemble size and electronic properties of the catalyst. However, the addition of Sn and Bi to Pt has been shown to have negligible influence on the stability, which is likely related to the high mobility of the added metals or metal oxides when exposed to O_2 and H_2O.[6,7] Therefore, a strong interaction of Pt and added metal (M) is necessary so that a stable structure of Pt-M alloy or Pt-MO_x interface maintains under the reaction and the C-C cleavage can be eliminated by tuned electronic property of PtM alloy or confined Pt ensemble size by MO_x. From the phase diagram,[8] PtRu, PtAg and PtNi have stable alloyed structure at ~373 K (close to reaction temperature), which might be worthy of further exploration.

6.2.3. Mechanistic study of C-H activation over Co-N-C

The Co-N-C catalyst with atomically-dispersed Co coordinated with nitrogen has been shown to catalyze C-H activation under both oxidizing environment at mild temperature as well as reducing environment at high temperature. Additionally, the in situ XAS demonstrated that active sites for mild-temperature alcohol oxidation is CoN_x bound to oxygen whereas during high-temperature propane dehydrogenation, it is likely that the bound oxygen has been removed. To understand the reaction path of C-H activation over CoN_x, mechanistic studies including kinetics, spectroscopy, microscopy and computational simulation would be very helpful. For example, EPR spectroscopy can be used to detect the possible radical intermediates; Mass spectrometer can be used to evaluate the dioxygen exchange rates; Steady State Isotopic Transient Kinetic Analysis (SSITKA) can provide insights on the amount of active sites as well as the activity in gas-phase; the in situ XAS, XPS and STEM-EELS can illustrate the evolution of active sites during catalytic cycles; and computational simulation can be applied to help understand the energy barrier of possible steps.

6.2.4. Optimization of M-N-C catalysts for C-H activation

The preliminary XAS results showed that atomically-dispersed CoN_x sites are active for C-H activation with a coordination number less than 4, indicating that the Co atoms are likely bound to the defects of N-doped carbon. Therefore, to further optimize M-N-C catalysts, efforts can be made to: 1) prepare carbon or N-doped carbon with more defects or directly purchased well-dispersed graphene oxide; 2) vary metal centers in addition to the first-row transition metals. Additionally, it is also interesting to explore M-N-C catalysts in other important reactions involving C-H activation, such as oxidation, alkylation or coupling reactions of carbon feedstocks from biomass or natural gas.

References for Chapter 6

1. Froment, G. F. & Bischoff, K. B. Non-steady state behaviour of fixed bed catalytic reactors due to catalyst fouling. *Chem. Eng. Sci.* **16,** 189–201 (1961).
2. Zope, B. N., Davis, S. E. & Davis, R. J. Influence of reaction conditions on diacid formation during Au-catalyzed oxidation of glycerol and hydroxymethylfurfural. *Top. Catal.* **55,** 24–32 (2012).
3. Kahsar, K. R., Schwartz, D. K. & Medlin, J. W. Control of Metal Catalyst Selectivity through Specific Noncovalent Molecular Interactions. *J. Am. Chem. Soc.* **134,** 520–526 (2014).
4. Hao, P., Pylypenko, S., Schwartz, D. K. & Medlin, J. W. Application of thiolate

self-assembled monolayers in selective alcohol oxidation for suppression of Pd catalyst deactivation. *J. Catal.* **344,** 722–728 (2016).

5. Schoenbaum, C. A., Schwartz, D. K. & Medlin, J. W. Controlling the surface environment of heterogeneous catalysts using self-assembled monolayers. *Acc. Chem. Res.* **47,** 1438–1445 (2014).
6. Xie, J. *et al.* Influence of Dioxygen on the Promotional Effect of Bi during Pt-Catalyzed Oxidation of 1,6-Hexanediol. *ACS Catal.* **6,** 4206–4217 (2016).
7. Xie, J., Falcone, D. D. & Davis, R. J. Restructuring of supported PtSn bimetallic catalysts during aqueous phase oxidation of 1,6-hexanediol. *J. Catal.* **332,** 38–50 (2015).
8. Okamoto, H. & Massalski, T. B. Binary alloy phase diagrams requiring further studies. *J. Phase Equilibria* **15,** 500–521 (1994).